

## 1 Study of corium/steel interaction at high temperature

Seeing as one of the construction materials of the reactor is steel, the study of the reactor core melt properties, the composition of which includes stainless steel elements, is strongly urgently. In view of high chemical activity of stainless steel components at corium melting point it was decided to perform steel-containing corium tests in graphite crucibles with ZrC coating. Amount of steel added in corium fits with the evaluated amount according to the reactor design and is equal to ~10% of corium mass.

This group of tests was conducted in three scenarios, and correction was made by the results obtained from the previous experiments (in performance order):

- simultaneous loading of burden containing mixture of core and steel components, and heating up to corium melt point (W-75, W-76, W-78);
- discharge of steel sample in liquid corium melt (W-79);
- simultaneous loading of corium and steel components mixture with heating up to steel melt point (S-2, S-3).

The experiments were performed in the VCG-135 test facility using the graphite crucible with ZrC coating applied previously. Temperature was measured by thermocouples W-Re5/20 and spectral ratio pyrometer focused on "melt mirror". Initial burden components used are as follows: uranium dioxide pellets chips, fine zirconium dioxide powder, fragments of zirconium FE tube, stainless steel 12X18H10T (tube sections 12×1), steel rods of low-carbon steel of 4 mm diameter.

Main parameters of the group of tests carried out are included in Table A2.1.1.

Table A2.1.1– Tests parameters

Parameter	Value							
	W-75	W-76	W-77 <sup>1</sup>	W-78	W-79	S-1	S-2	S-3
1 Loading of burden components, g								
UO <sub>2</sub>	84,0	76,2	84,0	98,2 (W-77)	76,2	-	10,63	5,2
ZrO <sub>2</sub>	10,63	9,36	10,63		9,5	-	-	-
Zr	15,80	14,49	15,76		14,48	-	-	-
Corium		-	-	-	-	-	-	(TT-9) 9,53
12X18H10T	11,05	-	-	-	-	-	-	-
Steel (Fe)	-	10	-	9,83	10	113,9	105,6	99,2
2 Burden mass, g	121,48	110,08	110,4	108,02	207,5	211,8	213	212
3 Graphite grade	R4340	R4340	R4340	R4340	R-4340	APB-1	APB-1	APB-1
4 Crucible mass, g	67,55	63,19	67,55	62,695	63,22	66,32	64,83	65,44
5 Mass of Zr in coating, g	6,0	5,05	5,0		4,37	9,05	7,95	7,92
7 Max. voltage of generator, kV	3,0	3,0	3,0	3,0	3,5	2,0	2,0	2,0
8 Max. temperature T, °C	2385	2320	2530	2350	2388	1550	1700	1800

<sup>1</sup> Corium for test W-78 was produced in test W-77,

<sup>2</sup> In test S-1 the resistance of ZrC coating against steel melt was studied.

### 1.1 The tests on melting components of corium with steel

#### 1.1.1 Test W-75

The composition loaded for Test W-75 was corresponded to corium C-30 and contained 10% mass steel 12X18H10T.

On heating the experimental assembly, when temperature 2350°C was reached, the temperature was suddenly dropped. The figure below demonstrates the plot of the temperature measured by the color pyrometer (Figure A2.1.1). Probably, the temperature drop was resulted from the start of physic-chemical process of melt components/crucible graphite interaction.

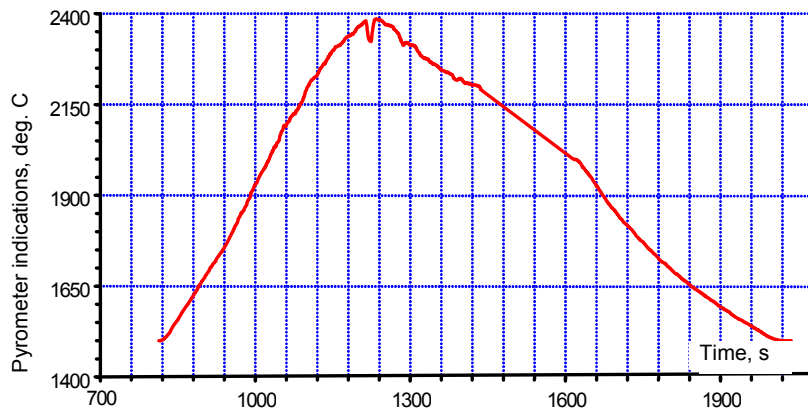


Figure A2.1.1 – Temperature plot of corium in Test W-75

Analysis of data resulted from cutting crucible represented in Figure A2.1.2, confirmed interaction of melt with crucible graphite.



Figure A2.1.2– Surface of crucible cut after Test W-75

Different ingot fragments were used for producing powder samples to perform X-ray phase analysis. The analysis showed that two unmixed melts, one of which is called "oxide" with basic component  $(U,Zr,(Fe,Cr,Ni))O_{2-x}$ , and other ("carbide") consisting of carbides of group  $UMeC_2$  and solid solution  $(Zr,U,(Fe,...))(C,O)$  with zirconium carbide lattice, were available in the ingot. In addition, there were non-melted fragments of the original uranium dioxide (mainly in its top part) and variable composition phase based on  $\alpha$ -iron VCC - lattice in the ingot. Separate phases with content of stainless steel chrome were not detected.

### 1.1.2 Test W-76

In the next experiments, for simplicity of the results analysis, the carbon steel was used instead of stainless steel (that allowed the interaction of "corium-nickel" and "corium-chrome" to be left of any consideration). In Test W-76 the steel was loaded in the melting volume inside zirconium tubes that will admittedly allow postponing the moment of liquid steel contact with uranium dioxide (Figure A2.1.3).

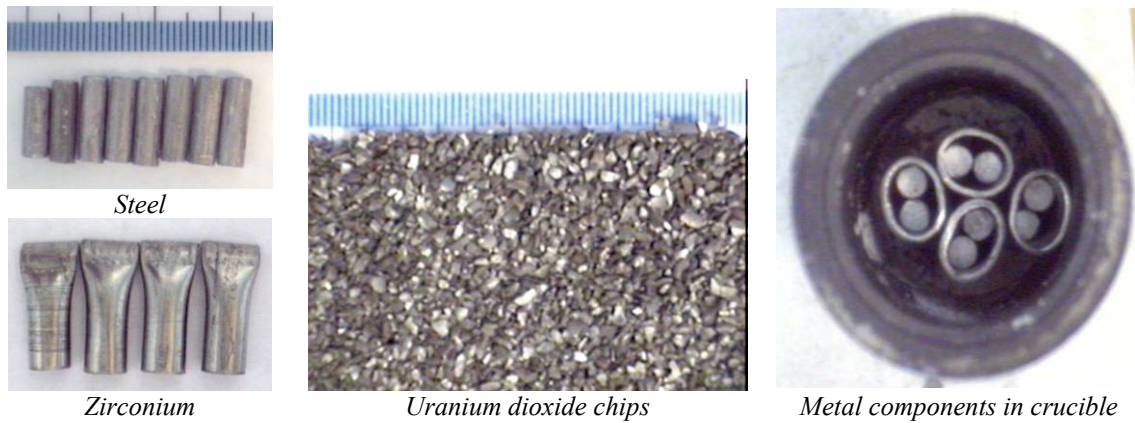


Figure A2.1.3 – Stages of the experimental assembly W-76 preparation

On heating crucible in the induction furnace, following the analogy of the previous test when temperature  $\sim 2300$  °C was reached, temperature reduction was registered and gas release from the melting volume was observed. The surface of the crucible cut after the test is illustrated in Figure A2.1.4.



Figure A2.1.4 – Section of the cut surface, Test W 76

The sections for the X-ray phase analysis were produced from the ingot fragments. The radiographic analysis was performed on the diffractometer DRON-3 with Bragg-Brentano geometry on copper emission. The samples diffractograms were got from sections surface containing mainly dark or light material. The resulted X-ray phase analysis is included in Table A2.1.2.

The main phase in the dark ingot material is solid solution  $(U,Zr,(Fe))O_{2-x}$  with FCC - lattice of  $CaF_2$  type. Measured averaged lattice parameter of the given phase for samples is 0,534 nm, that corresponds to the calculated composition  $U_{\sim 0,6}Zr_{\sim 0,4}O_2$ . The content of other phases in the material is low.

The main phase in the light ingot material is bicarbide  $UFeC_2$  and solid solution on the basis of zirconium carbide FCC - lattice  $(Zr,U,(Fe))(C,O)$  with lattice parameter 0,476 nm corresponding to approximate calculated composition  $Zr_{\sim 0,7}U_{\sim 0,3}C$ .

Consequently, two unmixed melts, one of which is called "oxide" with basic component  $(U,Zr,(Fe))O_{2-x}$ , and other ("carbide") consisting of carbide  $UFeC_2$  and solid solution  $(Zr,U,(Fe))(C,O)$  with zirconium carbide lattice, were available in the ingot.

There were non-melted fragments of the initial uranium dioxide (mainly in its top part) and variable composition phase based on  $\alpha$ -iron bcc lattice in the ingot. The phase composition of light material on the section of that start-up did not differ essentially from the previous one.

Table A2.1.2– Test parameters

Sample	Basic phase	Other phase
W-76. dark	$((U,Zr,(Fe))O_{2-x})$ ( $a_0=0,534nm$ )	$(U,Zr)(C,O)$
W-76. light	$UFeC_2, (U,Zr)(C,O)$ ( $a_0=0,476nm$ )	$\alpha$ -Fe, $(U,Zr,(Fe))O_{2-x}$

### 1.1.3 Test W-78

In Test W-78, the corium produced in the course of Test W-77 with the composition corresponding to C-30 was used for crucible loading. The grinded ingot chips were put into the ZrC-coated crucible, and steel cylinders were put on the top of the chips. Some moments of the experimental assembly preparation are seen in Figure A2.1.5.

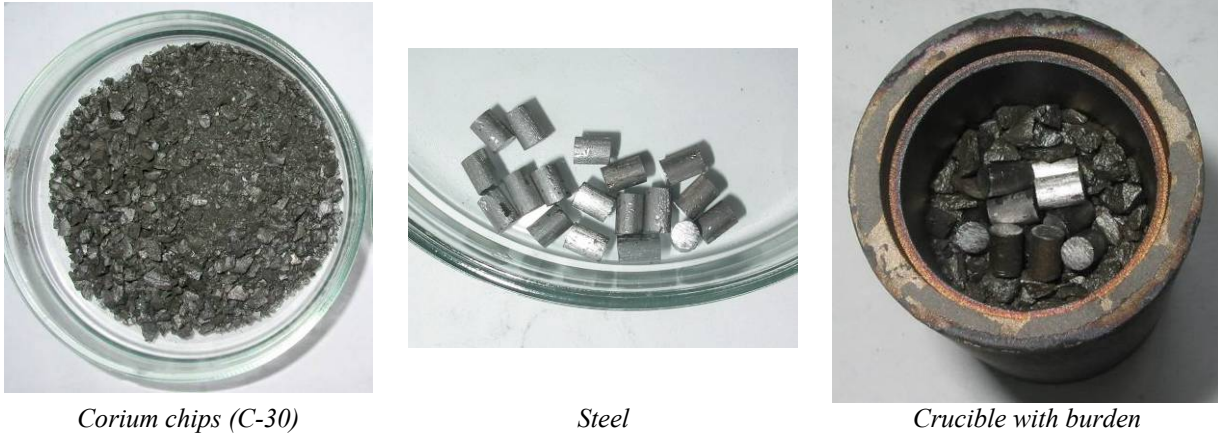


Figure A2.1.5 – Stages of the experimental assembly preparation

The actions undertaken had not come to favorable results. The test scenario was repeated, i.e. at temperature about 2300 °C the interaction of melt with the loss-of-protective-coating crucible wall was started. The surface of the crucible cut in Test W-78 with illustration of this effect is given in Figure A2.1.6.



Figure A2.1.6 – Section of the cut surface, Test W - 78.

Evidently, that the presence of stainless steel components in corium melt degrades distinctly the protective characteristics of zirconium (or other) coating. This fact is explained with powerful overheating of steel components at the melting point of the oxide corium components and, consequently, with their chemical over activity.

The ingot fragments were used for producing the sections to perform the X-ray phase analysis. The samples diffractograms were taken from sections surface and powder samples. The phase analysis points are given in Figure A2.1.7.





Figure A2.1.7– Areas of phase composition study

The basis phase of the ingot dark material is solid solution  $(U,Zr,(Fe))O_{2-x}$  with FCC - lattice of  $CaF_2$  type. For most samples the measured lattice parameters of the given phase have expressed maximums on values 0,547 nm and 0,534 nm as well as intermediate values (about 540 nm) that corresponds to the calculated contents from  $UO_2$  to  $U_{-0,6}Zr_{-0,4}O_2$  ( $U_{-0,8}Zr_{-0,2}O_2$ ). The given phase content in samples is not less than 70% by weight. In sample W-78.2 the peaks of solid solutions and uranium dioxide are least resolved between themselves, and intensity maximum corresponds to the lattice spacing 0,540 nm ( $U_{-0,8}Zr_{-0,2}O_2$ ), that points to more uniform distribution of the stoichiometrical composition of this phase in the sample material. The presence of  $UO_2$  in the ingot should be noted in the light of the fact that the material loaded in the crucible contained uranium dioxide only in the solutions from  $U_{-0,85}Zr_{-0,15}O_2$  to  $U_{-0,9}Zr_{-0,1}O_2$ . Uranium dioxide lines are well found in samples W-78.3 and 78.4.

The second phase in the ingot material is bicarbide  $UF_2C_2$  that is well-located both on the surface and on powder samples W-78.1 and W-78.4.

Solid solution based upon the zirconium carbide FCC - lattice  $(Zr,U,(Fe))(C,O)$  with lattice parameter 0,474 nm, corresponding to approximate calculation composition  $Zr_{-0,8}U_{-0,2}C$ , is present in samples W-78.1 and W-78.4. In the powder sample W-78.3 there was observed a group of solid solutions  $(Zr,U,(Fe))(C,O)$  within the range from UC to ZrC with maximum concentration for composition  $Zr_{-0,8}U_{-0,2}C$ . The above phase was not found on the section surface of the sample and also on the section surface and in powder sample of sampling W-78.2.

The diffractograms of powder samples W-78.2 and W-78.3 involve characteristic line of low intensity at  $2\theta$ -angle  $42,2^\circ$ . For sampling W-78.2 the above line was found also on the section surface diffractogram. Amongst the candidate phases, the phase  $Fe_2ZrO_x$  is emphasized, however, the lines of which were failed to identify surely owing to their superposition on the lines of other present phases. Likewise, the phase  $Zr_2Fe$  (tetragonal) and intermetallic compound  $(U,Zr)Fe_2$  with the crystal lattice of the spatial group  $Fd_3m$  and lattice spacing  $a_0 \approx 0.71$  nm may be considered as the candidate phases the reference lines of which are in close agreement with main controversial lines on the samples diffractograms.

In sampling W-78.2 and W-78.3 element of phase  $\alpha$ -Zr(O) was detected as well.

Consequently, the ingot represents rather complicated phase picture for which the change with regard to homogeneous stoichiometric composition of the loaded original solid solution and, in particular, the phase  $UO_2$  occurrence in the ingot samples is typical. Presence of carbide phases  $UF_2C_2$  and solid solution  $(Zr,U,(Fe))(C,O)$  is typical for the top sampling. In the bottom samples the phase  $\alpha$ -Zr(O) as well as new phases, presumably  $Fe_2ZrO_x$  and  $(U,Zr)Fe_2$ , are detected. The data from the qualitative X-ray phase analysis are included in Table A2.1.3.

Table A2.1.3 – Phase composition of samples according to RPA data

Sample	Basic phase	Other phase
W-78.1	$U_{-0,5}Zr_{-0,5}O_2(a_0=0,533 \text{ nm}), (U,Zr)(C,O)$ ( $a_0=0,472 \text{ nm}$ )	$U_{-0,8}Zr_{-0,2}O_2(a_0=0,542 \text{ nm}), UO_2,$ $UFeC_2,$
W-78.2	$U_{-0,75}Zr_{-0,35}O_2 \div U_{-0,5}Zr_{-0,5}O_2$ ( $a_0=0,540 \text{ nm} \div 0,533 \text{ nm}$ )	$UO_2, \alpha-Zr(O), Fe_2ZrO_x,$
W-78.3	$(U,Zr)O_2 (a_0=0,540 \text{ nm}; a_0=0,533 \text{ nm}), (U,Zr)(C,O)$ ( $a_0=0,472 \div 0,480 \text{ nm}$ )	$(U,Zr)Fe_2(a_0=0,710 \text{ nm}); UO_2,$ $UFeC_2$
W-78.4	$UO_2 \div U_{-0,6}Zr_{-0,4}O_2 (a_0=0,547 \text{ nm} \div 0,540 \text{ nm})$ $((U,Zr)(C,O) (a_0=0,474 \text{ nm}))$	$UFeC_2, (U,Zr); Fe_2(a_0=0,703 \text{ nm})$

## 1.2 Experiments on steel discharge in the corium melt

### 1.2.1 Test W-79

In the given test, in the course of heating steel was discharged in the molten corium by means of the device specially developed. That gave the ability to stop the experiment at the stage of interaction of steel with the corium melt and coating.

The device specially manufactured for discharging steel in the melting volume (Figure A2.1.8) is a graphite tube 1 installed at angle of crucible axis. The graphite tube is equipped with a sliding shutter 2 that is rod-connected 3 with electromagnet 4 and is controlled from the VCG-135 operator console.

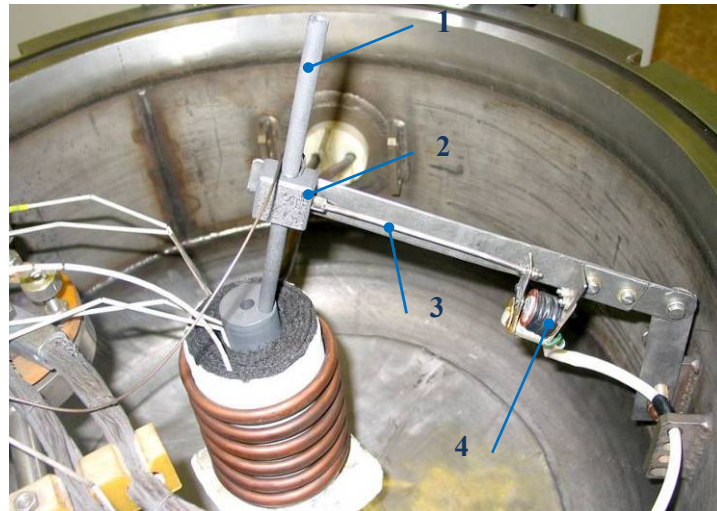


Figure A2.1.8 – Device for steel discharge in the crucible

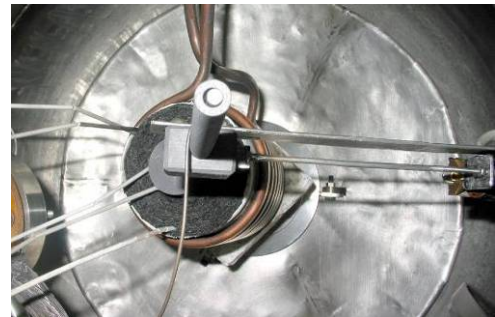
In the standard ZrC-coated crucible, corium components were located and the steel, in the form of rod segments of 5-7 mm, was put in the discharging device. Some stages of the experimental assembly preparation are demonstrated in Figure A2.1.9.



Mixture of  $UO_2$  chips and  $ZrO_2$  powder



Crucible with burden



The device before test

Figure A2.1.9 – Stages of experimental assembly preparation

In view of impossibility of producing corium melt with content of steel components in the offered configuration, it was decided to perform the experiments on melting steel in the

graphite crucible with ZrC coating. Location of corium components in the molten steel allows studying their interaction.

To support the possibility of steel melt production in the graphite crucible, the VCG-135 test was carried out. Steel rods with diameter 4 mm and height 35 mm were installed in the ZrC-coated crucible.

The temperature curve in the course of the test is represented in Figure A2.1.10.

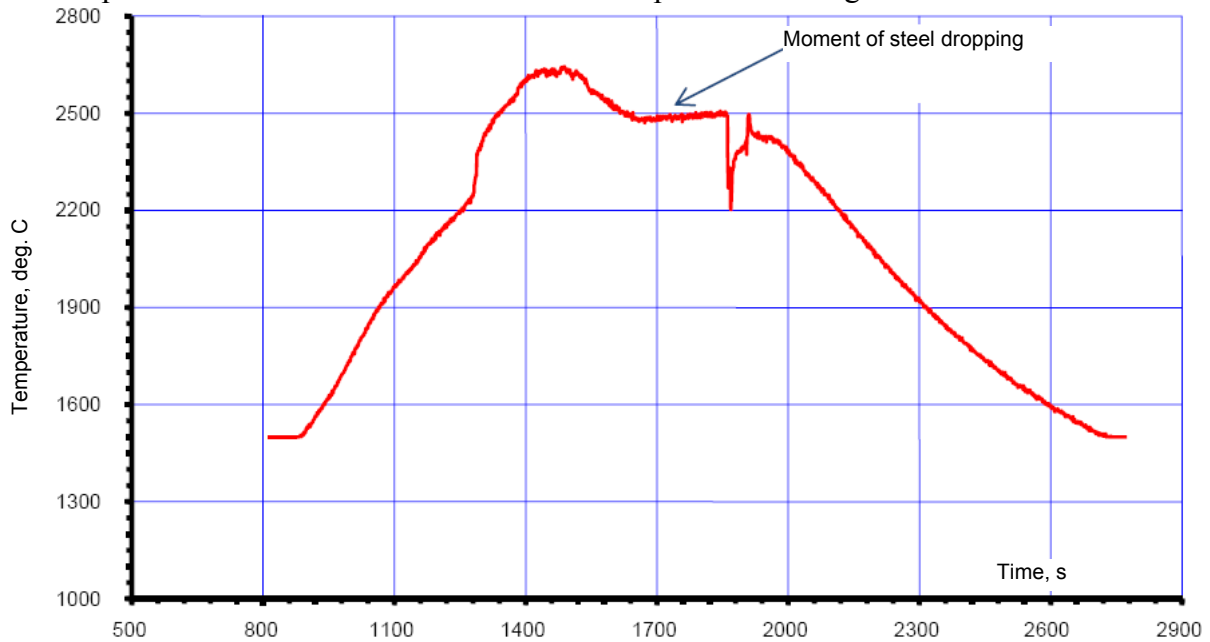


Figure A2.1.10 – Pyrometer readings

The X-ray phase analysis was made from the section surface, the survey regions are given in Figure A2.1.11.



Figure A2.1.11 – Area of phase content study

The results of the qualitative phase analysis of the ingot cut surface are included in Table A2.1.4.

Table A2.1.4 – Phase content of samples according to RPA data

Sample	Basic phase	Other phase
1	$U_{-0,5}Zr_{-0,5}O_2(a_0=0,533nm)$	$U_{-0,8}Zr_{-0,2}O_2(a_0=0,542nm)$ ; $(U,Zr)Fe_2(a_0=0,708nm)$ ; $ZrC(a_0=0,468nm)$
2	$U_{-0,9}Zr_{-0,1}O_2 \div U_{-0,5}Zr_{-0,5}O_2$ $(a_0=0,545nm \div 0,533nm)$ ;	$(U,Zr)Fe_2(a_0=0,703nm)$ ; $ZrC(a_0=0,468nm)$
2_1	$U_{-0,9}Zr_{-0,1}O_2 \div U_{-0,5}Zr_{-0,5}O_2$ $(a_0=0,544nm \div 0,532nm)$ ;	$(U,Zr)Fe_2(a_0=0,703 \div 0,706nm)$ ; $ZrC(a_0=0,468nm)$
3	$U_{-0,9}Zr_{-0,1}O_2 \div U_{-0,5}Zr_{-0,5}O_2$ $(a_0=0,544nm \div 0,532nm)$ ;	$(U,Zr)Fe_2(a_0=0,704 \div 0,708nm)$ ; $ZrC(a_0=0,468nm)$
4	$U_{-0,9}Zr_{-0,1}O_2; U_{-0,5}Zr_{-0,5}O_2$ $(a_0=0,544nm; 0,533nm)$ ;	Ingot $(U,Zr)Fe_2(a_0=0,703nm)$

### 1.2.2 Test S-1 (auxiliary)

The objective of the first test was to produce steel melt in the ZrC-coated graphite crucible, which was needed for confirmation of realizability of the posed tasks. The test favorable results are considered the absence of considerable carbonization of steel melt that is usually observed in the free-of-coating tests.

The steel rods were placed in the coated crucible (Figure A2.1.12), the assembly was heated to the steel melting point and maintained for 5-7 minutes.



Figure A2.1.12 – Stages of experimental assembly preparation

The section of the cut surface after Test S-1 is illustrated in Figure A2.1.13. There was no appreciable erosion of the wall; the section surface differed only from the bottom crucible part that, probably, was resulted from the presence of zirconium excess on the crucible bottom before melting.



Figure A2.1.13 – Section of the cut surface in Test S-1

To determine phase content of the melt material resulted from the given experiment, the section surface areas microstructure was studied and X-ray phase analysis was performed (Figure A2.1.14).



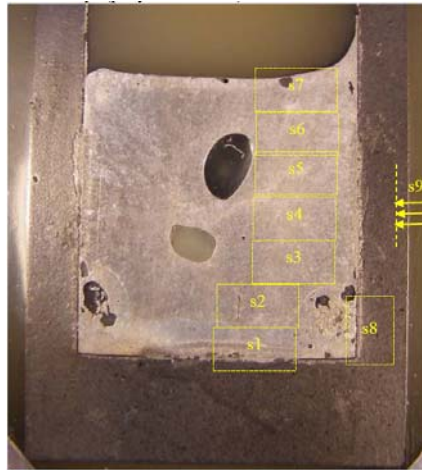


Figure A2.1.14 – Areas of phase content study

For determination of the phase basic ingot material structure, the radiographic examination of the areas was performed s(2÷7). To study phase structure of the ingot regions in the vicinity of the graphite erosion zones as well as in the rich of zirconium regions, the areas s1, s8, s9 were studied. The radiographic analysis was performed on the diffractometer DRON-3 with Bragg-Brentano focusing in copper  $K\alpha$  emission using the flat graphite monochromator on the reflected beam. The resulted diffractograms were analyzed through the qualitative phase analysis using the crystallographic database.

The phase analysis results are included in Table A2.1.5.

The measured values of the lattice spacing  $a_0$  and their approximate component composition are included in the table of phases. The phase succession in the table columns corresponds to decreasing of their volumetric content in samples.

Table A2.1.5 - Results of qualitative analysis of samples phase content

Sample	Basic phase	Other phase
s1	$\alpha$ -Fe	ZrC( $a_0=0.470$ nm), ing. ZrFe <sub>2</sub>
s2	$\alpha$ -Fe	ZrC( $a_0=0.470$ nm)
s3	$\alpha$ -Fe	ZrC( $a_0=0.470$ nm)
s4	$\alpha$ -Fe	ZrC( $a_0=0.470$ nm)
s5	$\alpha$ -Fe	ZrC( $a_0=0.470$ nm)
s6	$\alpha$ -Fe	ZrC( $a_0=0.470$ nm)
s7	$\alpha$ -Fe	ZrC( $a_0=0.468$ nm), ing. ZrFe <sub>2</sub>
s8	$\alpha$ -Fe	ZrFe <sub>2</sub> (0.704 nm), ZrC( $a_0=0.468\div 0,470$ nm)
s9	$\alpha$ -Fe	ZrC( $a_0=0.469$ nm)

Metal iron identified as  $\alpha$ -phase (ferrite) is the basis of the phase samples composition, has strong magnetic properties and characteristic ferrite microstructure. The lattice spacing ( $a_0=0.868\pm 0.002$  nm) and its zero distortions indicates to  $\alpha$ -phase. Presence of the variable composition phase ZrC<sub>1-x</sub> with zirconium carbide FCC - lattice implies dissolution of carbon and zirconium in the iron melt. The lattice spacing of the given phase varies over the range  $0,468\pm 0,002$  nm that may meet the entire homogeneity region of the phase composition. Note that the microstructure appearance of the phase extraction, especially in the vicinity of the regions meeting with the original coating position, imply the possible formation of the carbide phase of mixed composition (Fe,Zr)C<sub>x</sub>. However, we are free of the data on diagram of the system status Zr-Fe-C. Percentage of the zirconium carbide phase extraction in the ingot was not determined; however as per the lines intensity of the given phase we may conclude that there was homogeneous distribution along the ingot height. This is with the exception of the ingot regions s7 and, particularly s1, when zirconium carbide concentration is higher than in the ingot at the average.

Description of the phase composition of the region with high original content of metal zirconium merits separate attention. This region is least carbonized and its phase composition should reflect the phase composition of the system Fe-Zr. According to the X-ray phase analysis results the main phase composition component of the solidified melt samples is  $\alpha$ -iron, phase of variable composition close to FCC - lattice parameter to zirconium carbide and a phase, specifically a set of phases that are most closely identified as  $ZrFe_2$  with the lattice of spacing group Fd3m or P63/mmc. For the cubic lattice of the given phase the lattice spacing values are within the range of  $0,702 \div 0,706$  nm.

The rentgenography of region s9, the most carbonized, did not bring to detecting new carbide phases, and, particularly, carbides on the basis of iron. That fact complicates the performance of the phase analysis of the system Fe-Zr-C. The optical metallographic data indicate the formation of cast iron structure in that region, and presence of carbide phases of iron is very expected here.

Presence of metal zirconium in the melt promotes reduction of dissolved carbon content due to formation of zirconium carbide extraction.

Interaction of metal iron melt with zirconium was very active with formation of intermetalloids  $ZrFe_2$  after crystallization.

### 1.3 Experiments on simultaneous loading and heating up to the steel melting point

#### 1.3.1 Test S-2

Then the test on steel burden melting with presence of uranium dioxide was conducted. At the crucible bottom four dioxide pellets were put so as to have further possibility of diametrical cut in such a way that the cutting plane would be at right angle to the pellets axis (Figure A2.1.15).

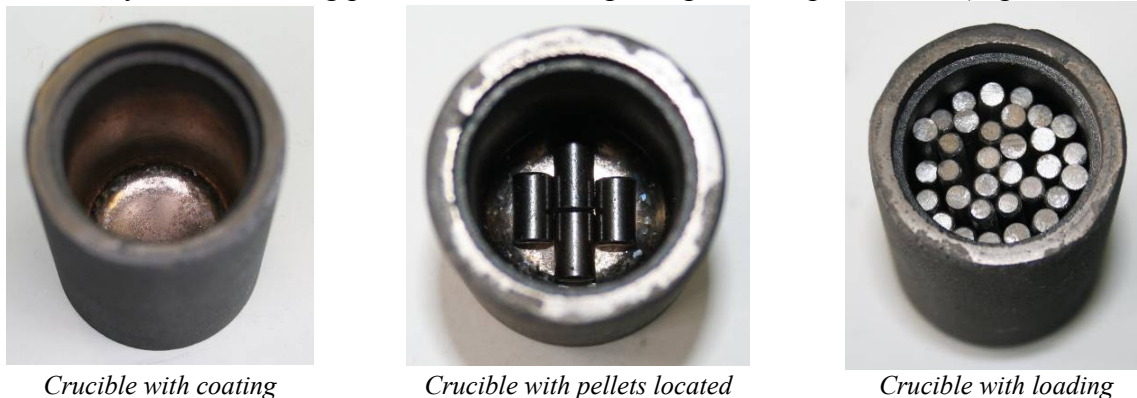


Figure A2.1.15 - Stages of experimental assembly preparation

The section of the crucible cut surface after Test S-2 is illustrated in Figure A2.1.16. There was visual evidence of hollows between the pellets that may be resulted from poor wettability of uranium dioxide with steel melt.



Figure A2.1.16 – Section of the cut surface in Test S-2

However, the metallographic study discovered the availability of wetting areas and impregnation of uranium dioxide surface layer with steel melt (Figure A2.1.17) at a depth of 100 microns.

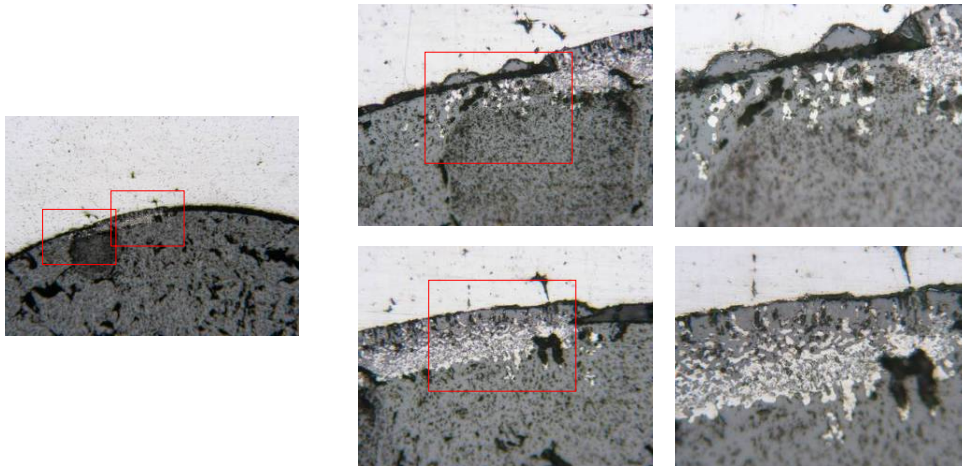
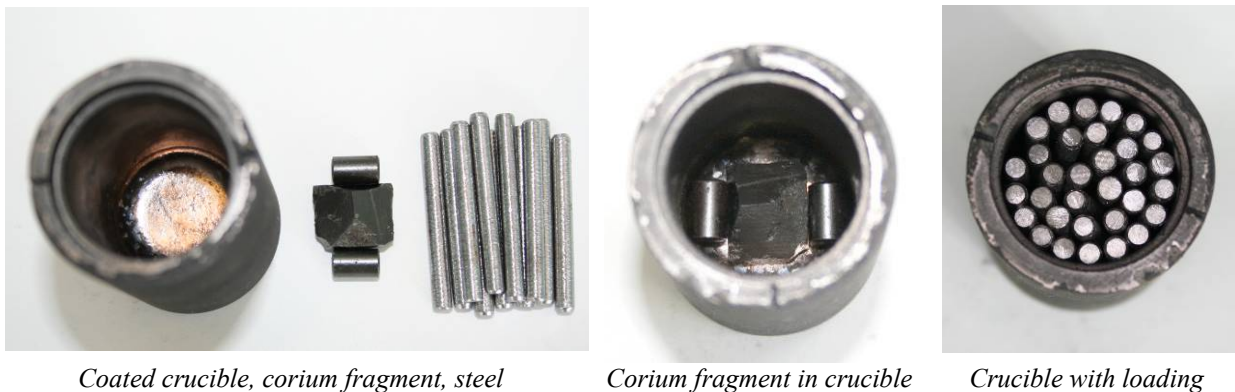


Figure A2.1.17 – Section regions in points of dioxide impregnation with steel

### 1.3.2 Test S-3

In the given experiment a fragment of the solidified corium melt from Test TT-9 (composition:  $m(\text{UO}_2)=62,4 \text{ g.}$ ;  $m(\text{ZrO}_2)= 5,6 \text{ g.}$ ;  $(\text{Zr})= 12,0 \text{ g}$ ) as a cylinder segment fixed with two uranium dioxide pellets, was loaded in the standard crucible. Some stages of crucible preparation are represented in Figure A2.1.18.



*Coated crucible, corium fragment, steel*

*Corium fragment in crucible*

*Crucible with loading*

Figure A2.1.18 – Stages of experimental assembly preparation

After the test the crucible was potted with compound and cut in the plane perpendicularly to the corium ingot axis. The section of the cut surface is represented in Figure A2.1.19.



Figure A2.1.19 – Section of the cut surface of Test S-3

The phase composition of the melt material produced in the given test was studied through

investigation of microstructure and X-ray phase analysis of the section surface regions (Figure A2.1.20).

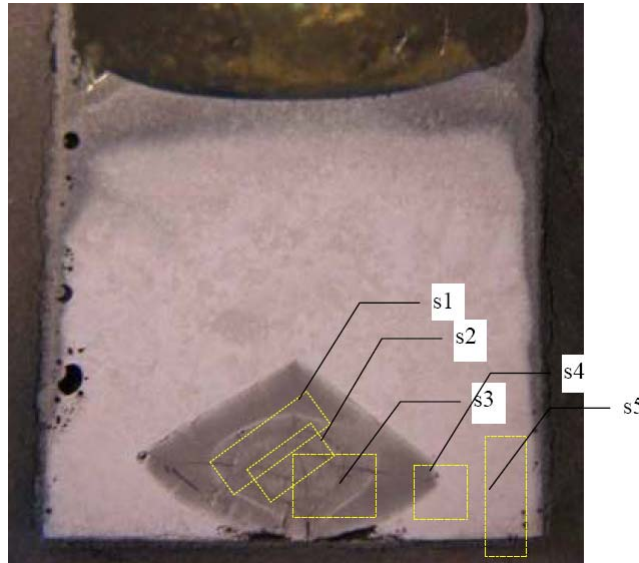


Figure A2.1.20 – Areas of phase content study

The phase composition of the main ingot material was not identified owing to its full coincidence with the ingot microstructure studied after Test S-1 on iron melting in the coated crucible.

A special emphasis of the study laid on the investigation of phase composition in different corium regions discovered on the section macrograph as well as on investigating microstructure of these regions through the method of optical metallography. The ingot fragment resulted from Test TT-9 on melting corium materials composition in the tungsten crucible was used as corium in the given test. To trace variations occurred with corium material, the results of corium ingot study after Test TT-9 were represented as well.

The radiographic analysis was performed on the diffractometer DRON-3 with Bragg-Brentano focusing in copper  $K\alpha$  emission using the flat graphite monochromator on the reflected beam. The resulted diffractograms were analyzed through the qualitative phase analysis using the crystallographic database. The phase analysis results are included in Tables A2.1.6 and A2.1.7. The measured values of the lattice spacing  $a_0$  and their approximate component composition are included in the tables of the phases with cubic lattice. The phase succession in the table columns corresponds to decreasing of their volumetric content in samples

Table A2.1.6 - Results of qualitative analysis of corium samples phase content TT-9

Sample	Basic phase	Other phase
1	$U_{\sim 0,8}Zr_{\sim 0,2}O_2(a_0=0,541 \text{ nm}); \alpha\text{-Zr(O)}$	Ingot $Zr(C,O)_{1-x}(a_0=0.464 \text{ nm})$
2	$U_{\sim 0,9}Zr_{\sim 0,1}O_2(a_0=0,544 \text{ nm}); \alpha\text{-Zr(O)}$	ingot $\alpha\text{-U}; \text{сл. } Zr(C,O)_{1-x}(a_0=0.464 \text{ nm})$
3	$U_{\sim 0,9}Zr_{\sim 0,1}O_2(a_0=0,544 \text{ nm}); \alpha\text{-Zr(O)}$	ingot $\alpha\text{-U}; \text{сл. } Zr(C,O)_{1-x}(a_0=0.464 \text{ nm})$
4	$U_{\sim 0,85}Zr_{\sim 0,15}O_2(a_0=0,543 \text{ nm}); \alpha\text{-Zr(O)}$	Ingot $Zr(C,O)_{1-x}(a_0=0.464 \text{ nm});$ ingot $\alpha\text{-U}$

Table A2.1.7 - Results of qualitative analysis of corium areas phase content S-3

Sample	Basic phase	Other phase
s1	$U_{\sim 0,75}Zr_{\sim 0,25}O_2(a_0=0,540 \text{ nm});$ $U_{\sim 0,5}Zr_{\sim 0,5}O_2(a_0=0,532 \text{ nm})$	$ZrFe_2(0.703 \text{ nm}); (U,Zr)Fe_2(0.708 \text{ nm});$ $\alpha\text{-Fe}, Zr_3Fe; Zr(C,O)_{1-x}(a_0=0.467 \text{ nm})$
s2	$U_{\sim 0,75}Zr_{\sim 0,25}O_2(a_0=0,541 \text{ nm});$ $U_{\sim 0,5}Zr_{\sim 0,5}O_2(a_0=0,533 \text{ nm})$	$(U,Zr)Fe_2(0.708 \text{ nm}); ZrFe_2(0.704 \text{ nm});$ ingot $Zr(C,O)_{1-x}(a_0=0.464 \div 0,467 \text{ nm});$ ing. $\alpha\text{-Fe}; \text{сл. } \alpha\text{-Zr(O)}$ ;
s3	$U_{\sim 0,8}Zr_{\sim 0,2}O_2(a_0=0,542 \text{ nm});$ $U_{\sim 0,6}Zr_{\sim 0,4}O_2(a_0=0,535 \text{ nm})$	$Zr(C,O)_{1-x}(a_0=0.464 \div 0,467 \text{ nm}); \alpha\text{-Zr(O)}$ ; ingot $(U,Zr)Fe_2(0.708 \text{ nm})$
s4	$U_{\sim 0,75}Zr_{\sim 0,25}O_2(a_0=0,540 \text{ nm});$ $U_{\sim 0,5}Zr_{\sim 0,5}O_2(a_0=0,533 \text{ nm})$	$(U,Zr)Fe_2(0.708 \text{ nm}); ZrFe_2(0.704 \text{ nm});$ $Zr(C,O)_{1-x}(a_0=0.467 \text{ nm}),$ ing. $\alpha\text{-Fe}$
s5	$\alpha\text{-Fe}$	$ZrFe_2(0.704 \text{ nm}), ZrFe_3(a_0=1,173 \text{ nm}); ZrC(a_0=0.467 \text{ nm})$



The basis of the phase composition in all corium fragment regions are solid solutions  $(U,Zr)O_2$ . The table presents evaluated stoichiometric composition of the given phase. Availability of two solid solutions with evaluated compositions  $U_{\sim 0,75}Zr_{\sim 0,25}O_2$  ( $a_0=0,541$  nm) and  $U_{\sim 0,5}Zr_{\sim 0,5}O_2$  ( $a_0=0,533$  nm) is typical. This is a distinctive feature of the phase corium composition after its interaction with steel, i.e. appearance of the phase with minor lattice parameter is considered the interaction result. It should be noted that new phase lines are unusually narrow for the solutions of the given concentration, thereby testifying to the lattice ordering of this phase, and, consequently, to the composition stability. At the same time the lines of the phase close to initial solution correspond to a number of phases with lattice parameters from original uranium dioxide to composition  $U_{\sim 0,7}Zr_{\sim 0,3}O_2$  ( $a_0=0,547\div 0,538$  nm). According to the results of the X-ray phase analysis, a new component of the phase material composition in corium zone is the phase of variable composition, and specifically a set of phases that are most closely identified as  $(U,Zr)Fe_2$  with spatial group lattice Fd3m or P63/mmc. For the cubic lattice of the given phase the lattice spacing values are within the range of  $0,703\div 0,711$  nm. Note that the content of the given phases decreases naturally to the corium fragment center with simultaneous increasing of phase portion of large lattice parameter. The lattice parameter of the given phase increases from  $0,705$  nm for  $ZrFe_2$  to  $0,707$  for  $UFe_2$ .

Other phases represented in the table, are identified without full confidence. Among these phases we should specify the phases close to uranium dioxide, tetragonal zirconium dioxide, intermetallic compound  $Fe_3Zr$  (Fd3m,  $a_0=1,170$  nm), the lines of which are the most intensive on diffractograms of regions S1 and S4.

The ingot regions phase composition was changed in comparison with initial one.

The interaction of metallic iron melt with corium is rather active with formation after crystallization of intermetalides  $(U,Zr)Fe_x$  and formation of ceramic solid solution  $(U,Zr)O_2$  with more high content of zirconium. Dissolution, apparently, occurs, first of all, through inclusion of metallic zirconium available in the initial corium.

Generally, corium separation at its dissolution into ceramic oxide and metallic components may be followed.

The presence of two solid solutions based on uranium dioxide lattice, one of which meets lattice parameter of the solution with high content of the dissolved zirconium to composition  $U_{\sim 0,5}Zr_{\sim 0,5}O_2$  deserves close attention. Formation of solid solutions with high zirconium concentration requires either increasing of oxygen content in the solution or reduction of uranium concentration (e.g. at the expense of its extraction to the metal phase), or at the expense of solid solution formation with involving iron atoms.

The phase composition of interaction products is very complicated and requires refinement and correction through correlation of optical metallography results.

So as to find out penetration depth of steel in the corium, the element analysis of section surface was carried out. The scanning was performed through a leaden gap with diameter 3 mm, in all 3 measurements S-1, S-2 and S-3 respectively (Figure A2.1.21) were performed. In addition there was resulted a qualitative spectrum of the TT-9 original corium material, the spectrum of analytical lines of which is given in Figure A2.1.22.

The scanning was performed over the range of wave-lengths  $1500 - 1980$  mÅ (in this range there are maximums of analytical lines of characteristic X-ray radiation of Zr and U on the second reflection order and Fe on the first one). Line spectrums of the specified elements are given in Figures A2.1.23 and A2.1.24.

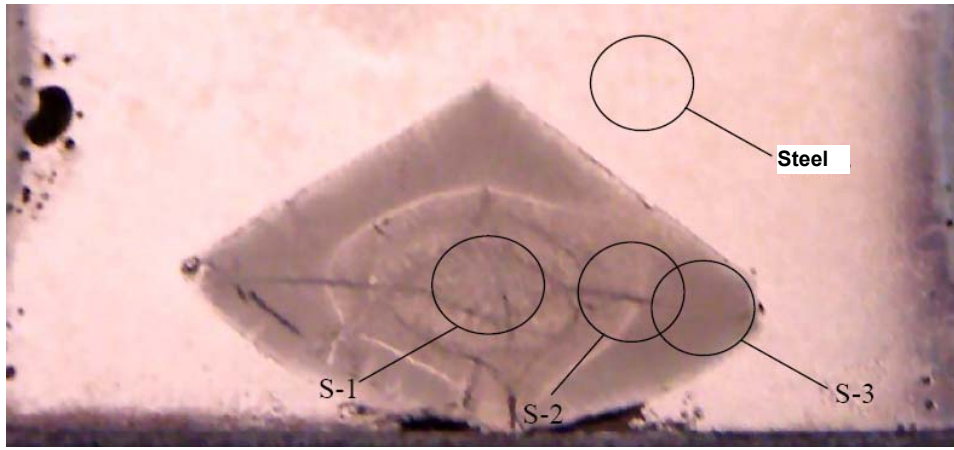


Figure A2.1.21 – Spectrum locations  
Zr-U

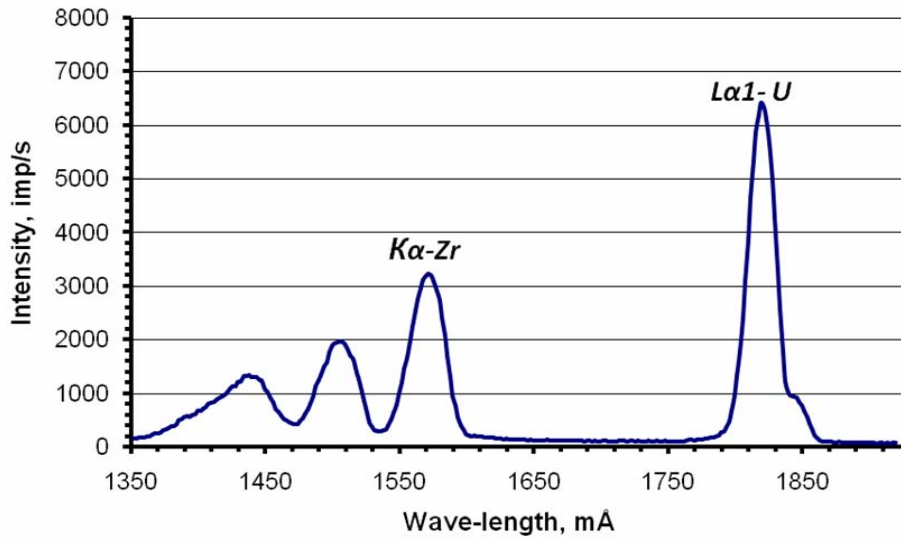


Figure A2.1.22 – Spectrum of elements  
Zr-U

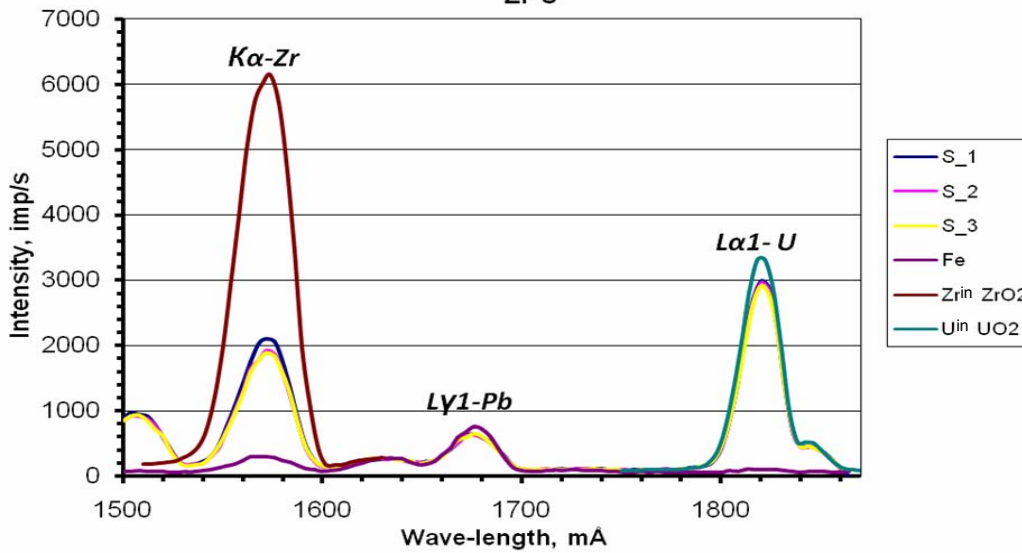


Figure A2.1.23 - Spectrum of elements

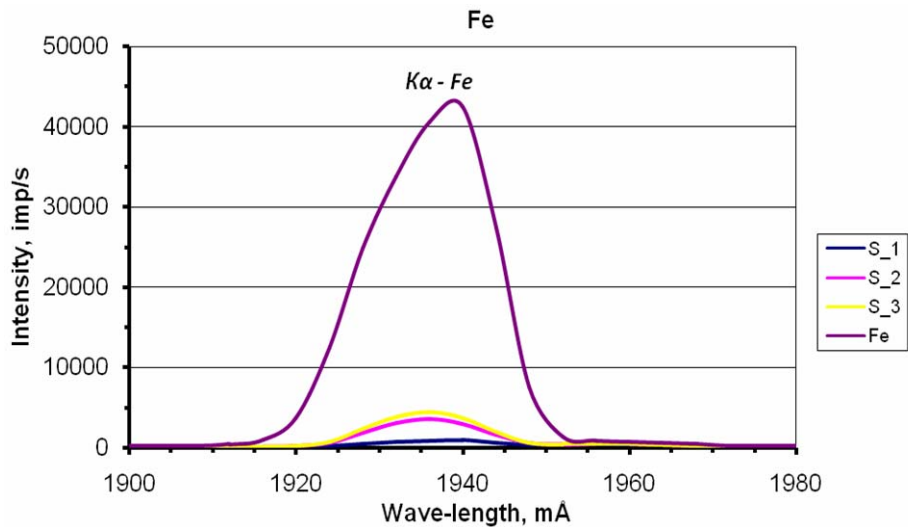


Figure A2.1.24 - Spectrum of elements

From the resulted roentgen fluorescent analysis, there was calculated relative concentration of elements. The results of the calculated relative concentrations are included in Table A2.1.8.

Table A2.1.8 – Results of the relative element analysis

№	Elements content		
	in relation to steel	(in relation to mixture ZrO <sub>2</sub> and UO <sub>2</sub> )	
	Fe	Zr	U
S_1	2,2%	25,9%	79,5%
S_2	8,7%	25,3%	78,6%
S_3	10,8%	21,9%	77,5%
		(in relation to TT-9 ingot (C-30 corium))	
S_1		25,84%	62,98%
S_2		24,45%	64,37%
S_3		24,33%	64,49%

The metallographic study was also used for confirmation of iron presence in the corium ingot. The pictures of the microstructure of the upper crucible part are represented in Figures A2.1.25...A2.1.28.

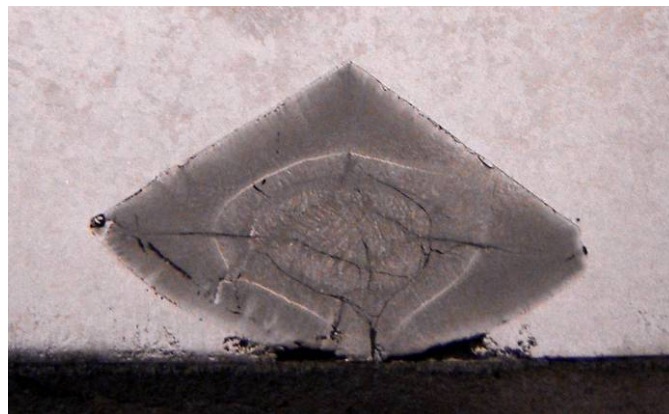


Figure A2.1.25 – Section of corium ingot in the steel

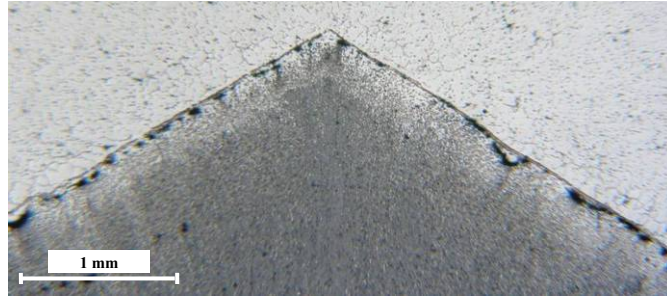


Figure A2.1.26 – Section fragment in steel-corium transition region

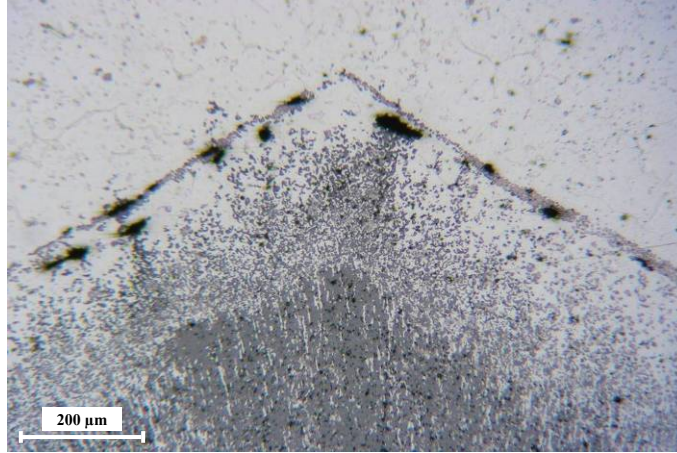


Figure A2.1.27 – Section fragment in steel-corium transition region

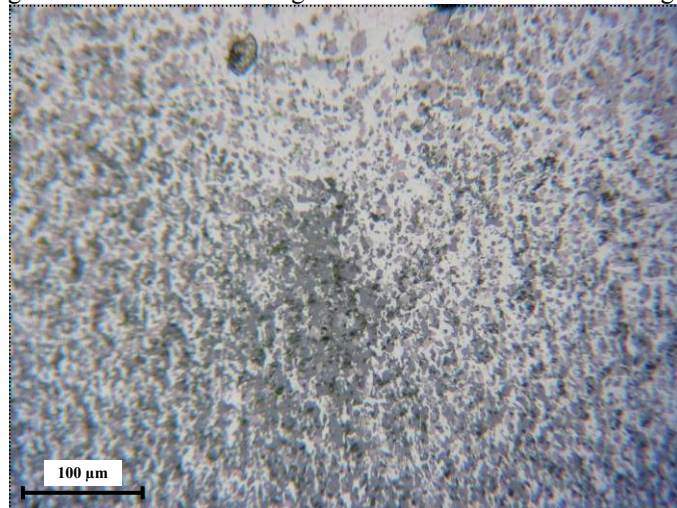


Figure A2.1.28 – Section fragment in steel-corium transition region

The interaction occurs as intensive wetting of solid uranium dioxide (corium) with steel melt. According to the results from Tests S2 and S3 comparison we may conclude that the steel melt moistens corium ingot much faster than uranium dioxide. Presence of a larger contact surface will promote more intensive chemical interaction between iron and corium components. To specify the mechanism of solidified melt/steel interaction, the samples holding time at high temperature during the tests should be increased.



## 2 Large-scale calibration tests on heating and melting of initial components of prototypic corium using single plasmatrons (TOP)

### 2.1 TOP-6 test

2.1.1 Subject of investigation is the plasmatrons melt heating system in the RPV lower head model.

2.1.2 Objective and goals of the test

2.1.2.1 The objective of the experiment was to test the resistance of the graphite nozzle of the outer electrode of the plasmatrons made from R4340 graphite with protective carbide zirconium layer against oxide medium attack at high temperature.

2.1.2.2 The goals of the experiment were:

- production of melt from the loading consisting of zirconium dioxide powder ( $ZrO_2$ ), uranium dioxide pellets ( $UO_2$ ) and metal zirconium in the steel vessel;
- evaluation of resistance of the protective carbide zirconium layer during 150 minutes;
- comparison of the erosion rate of the graphite nozzle made of graphite R4340 with results of nozzles tests made of ARV-1 graphite.

2.1.3 General provisions

2.1.3.1 The plasmatrons melt heating system in the RPV model (drawing #DKIG.681.613.001.SB) was designed for simulating of decay heat in the melt situated in the RPV model. The RPV model with the plasmatrons installed is located in the "LAVA-B" facility pressure vessel.

2.1.3.2 The test was carried out in the "ANGARA" heat engineering test facility.

2.1.3.3 The experiment was performed in conformity with the program and procedure "Testing of the melt heating system in the reactor vessel lower head model in the "LAVA-B" test facility" reg. No. 1652 of 10.08.2005 as well as in compliance with the resolution on performance of tests in the melt heating system with plasmatrons reg. No. 240-02/68 of 29.05.2008 and functional program reg. No. D-319 of 30.07.2007.

2.1.4 Test conditions

2.1.4.1 Magnetic medium recording and data display were performed by means of the "ANGARA" test facility data acquisition (DAS).

2.1.4.2 The test facility automatic control systems were managed manually.

2.1.4.3 Nominal parameters of the melt heating system in the RPV model are as follows:

- maximum value of the plasmatrons working current, A – to 400;
- plasmatrons arc volts, V – to 70;
- open circuit volts on the plasmatrons, V – to 140;
- water flow rate through the plasmatrons cooling path, kg/s – to 0,08;
- consumption of argon supplied to inter-electrode space, kg/s – 0,001;
- consumption of nitrogen supplied to inter-electrode space, kg/s – 0,00008.

2.1.4.4 The work was done using the plasmatrons "A" installed on the concrete support. The plasmatrons construction is illustrated in Figure A2.2.1. The plasmatrons was installed vertically on the concrete support. The concrete support was placed inside the facility pressure vessel. There was an experimental cell inside the concrete support, see Figure A2.2.2, item 6. The vessel outer surface (Figure A2.2.2, item 5), was covered with two glass fabric layers at a distance of 100 mm from the upper vessel end and one glass fabric layer at a distance of 90 mm from the sleeve bottom (total sleeve height – 190 mm), which was used as a thermo- and electro-insulation. Mass of the thermo-insulated vessel with thermocouples was equal to 2,552 kg. The burden heating vessel was loaded with burden consisting of the following materials: zirconium dioxide powder – total weight 1,116 kg, uranium dioxide pellets – 9,144 kg, metal zirconium – 1,74 kg (including zirconium plates with total weight 0,200 kg). Metal zirconium was used in the form of grains. The scheme of burden loading in the vessel is shown in Figure A2.2.2. The burden heating vessel was cooled from the

reverse water system from the supply head through the tank THW-3 reservoir with further water removal to the dump header.

A cylindrical nozzle of the internal electrode and lower part of the composite nozzle of the outer electrode made of graphite R4340 were installed on the plasmatrons. The upper composite nozzle part of the outer electrode was made of graphite ARV-1. Nozzles drawing is represented in Figure A2.2.3. The external surface of the outer electrode nozzle bottom was coated with protective carbide zirconium layer. To improve zirconium spreading, from the outside the screw M90×1.5 was made on the lateral surface of the nozzle bottom, and on the end of the nozzle bottom the grooves of concentric-form rings were cut. Mass of the lower and upper parts of the outer electrode graphite nozzle was 0,6625 kg and 0,735 kg, and the mass of the internal electrode graphite nozzle - 0,3157 kg. The distance between the internal electrode nozzle end and the outer electrode nozzle bottom was equaled to 22 mm.

In the burden located in the experimental cell 4 thermocouples W-Re5/20: c.p. MDT.04, MDT.14, MDT.34, MDT.103 were installed. Five thermocouples CA, represented in Figure A2.2.4, were installed on the outer surface of the vessel for the purpose of measuring temperature of the wall and vessel bottom. Their designations are as follows: c.p. L.T.31, MDT.44, MDT.02, MDT.22, MDT.24. On the protective shield, from the top, see Figure A2.2.4, item 2, three thermocouples CA c.p. TCJ4, TCJ 5, TCJ 6 for measuring temperature of gas released through the gap between the protective shield and outer electrode nozzle, were installed. On the outer electrode nozzle, a thermocouple CA c.p. CLT.01 was installed at a distance of 148 mm from the lower end of the outer electrode nozzle (1 mm over the screen). The thermocouples layout is given in Figure A2.2.4.

2.1.4.5 Electric power was supplied to the plasmatrons from welding apparatus of Group "A". In the plasmatrons power-supply circuit, the reactance was switched off.

2.1.4.6 Plasmatrons voltage was measured by the standard normalizing converter 73G-IV10 (c.p. NN.01A).

2.1.4.7 Plasmatrons current strength was measured by the standard normalizing converter 73G-IV100M (c.p. TN.01A).

2.1.4.8 Working medium and facility elements temperature was measured by the standard thermocouples of the "LAVA-B" test facility.

2.1.4.9 Working medium pressure was measured with the standard pressure gauges DDM.

2.1.4.10 Electric arc ignition was performed with supply of argon in the inter-electrode opening with further, after ignition, nitrogen supply to produce gas mixtures.

2.1.4.11 In the working medium supply paths, the nozzles were installed in the plasmatrons:

- argon supply path- nozzle diameter 0,7 mm;
- nitrogen supply path - hollow needle with effective open area  $\phi F = 5,667 \times 10^{-8} \text{ m}^2$ .

2.1.4.12 The functional program reg. No. D-319 of 30.07.07 was changed and supplemented as follows:

- Item 6 – adjust reducer B.6.03 to pressure  $P = 8$  gage atm;
- Item 7 – adjust reducer K.6.04 to pressure  $P = 7,5$  gage atm;
- Item 19 – plasmatrons run time has been changed from 1 for 2,5 hours.

2.1.5 Scope of the work performed

2.1.5.1 On June 23, 2008 the start-up of TOP-6 was began. The plasmatrons "A" was ignited from the first push.

At 10 minutes after 10, after analyzing voltage and current readings taken from the plasmatrons electric arc, there was concluded that nitrogen came into the plasmatrons inter-electrode space insufficiently. It was decided to increase reducer setting K.R.04 up to pressure 15 gage atm in order to avoid blocking of needle channel.

At 10:12, the instruction for increasing reducer setting K.R.04 up to pressure 20 gage atm was received.

At 10:14, for the purpose of arc power increase, the instruction for coming welding apparatus

VD306E to the maximum running current was received.

At 10:52, to increase plasmatrons power, it was decided to increase pressure in the facility pressure vessel up to 1,7 gage atm.

From 11:05 to 11:08, there was made an attempt to clean the nitrogen supply path by means of nitrogen pressure increase after the hollow needle, and that attempt didn't bring to any results ex fact. At the same time argon was supplied to the plasmatrons inter-electrode space.

At 11 minutes after 12, it was found that the test facility DAS parameters were not registered.

At 12:11:50 the registration of the test facility DAS parameters was restarted.

At 12:15:35, after analyzing of the arc current and voltage as well as the outer electrode nozzle temperature, it was decided to stop testing to prevent burning-out of the inner electrode copper part. Total arc burning period was 2 hours 20 minutes and 40 seconds. Changes for plasmatrons running parameters, such as voltage, current, power, argon and nitrogen pressure, as well as the outer electrode nozzle temperature are graphically represented in Figure A2.2.5.

Changes of cooling water flow rate and temperature of the plasmatrons and experimental cell during the experiment are shown in Figure A2.2.6. The gas pressure change in the facility pressure vessel is in Figure A2.2.7. Validity of gauges c.p. A.R.11 and A.R.19 demonstrated that values were overpressured by ~1,2 – 1,4 atm (gauges indications are in "zero" position), but they were within the margin of error. Change of temperature of gas released from the melt, vessel wall temperature and the temperature of the burden itself during the experiment are shown in Figures A.2.2.8, A.2.2.9 and A.2.2.10. In all diagrams within the time lag from 11:33:13 to 12:1:50 these parameter values absent owing to the test facility DAS failure.

After completion of the test the graphite nozzles of the outer and internal electrodes and burden in the experimental cell were examined. In the result of the examination and required measurement there was detected as follows:

- a) the cylindrical part of the internal electrode graphite nozzle was burnt out by 12÷15 mm, maximum length of the remaining part was 48 mm. Total length of the remaining nozzle was equal to 143 mm (before the test the total nozzle length was 155 mm). Appearance of the internal electrode graphite nozzle after the test is represented in Figures A2.2.12 and A2.2.13;
- b) diameter of the cylindrical part of the internal electrode graphite nozzle was increased in the region of arc burning from 50 mm to 51,5mm.
- c) there were no visible damages on the internal surface of the composite graphite nozzle bottom of the outer electrode. The nozzle bottom had no burnout and traces of interaction with melt. Appearance of the internal surface of the nozzle bottom is seen in Figure A2.2.14;
- d) upper part of the outer graphite nozzle had also no visible damages. Appearance of the outer surface of the nozzle top is seen in Figure A2.2.15.

Appearance of the outer electrode nozzle and the melt after cutting the experimental device vessel is represented in the attachment, Figure A2.2.16. In order to keep the melt location in the device the latter was filled with sulfur (blue arrows in Figure A2.2.16).

5.2. Table A2.2.1 includes averaged voltage, current, plasmatrons power, water heating in the cooling paths, heat losses with cooling water, outer electrode nozzle temperature, obtained during the plasmatrons "A" run, and also includes the temperature in different points of the burden heating vessel. Averaged voltage, current and power are given for three time intervals: from the start of the test at 9:54:55 to the moment of pressure increase in the facility vessel up to 1,7 gage atm at 10:52:00; from 10:52:01 to parameters registration stoppage at 11:33:13 and from the moment of parameters registration continuation at 12:11:50 to the completion of the experiment at 12:15:35.

Table A2.2.1 - Parameter values resulted from the plasmatrongs "A" running

Parameter	Value
Time of the plasmatrongs run, h : min : s.	2 : 20 : 40
Averaged voltage of the electric arc, V	38,8 – 45,4 – 72,2
Averaged current of the electric arc, A	354 – 344 – 256
Averaged plasmatrongs power, kW	13,7 – 15,6 – 18,2
Maximum heating of water in the plasmatrongs cooling path, °C	7,62
Heat losses with plasmatrongs cooling water, %	13,2
Maximum water heating in the water cooling jacket of the burden heating device, °C	3,68
Heat losses with cooling water of the burden heating device, %	54,1
Maximum temperature of the outer electrode nozzle, °C (c.p. CLT.01)	590
Maximum temperature of gas released from the burden (melt), °C	
- c.p. TCJ4	611
- c.p. TCJ5	683
- c.p. TCJ6	530
Maximum temperature of vessel wall, °C	
- at a distance of 131 mm from the vessel bottom, c.p. L.T.31	869
- at a distance of 91 mm from the vessel bottom, c.p. MDT.44	963
- at a distance of 61 mm from the vessel bottom, c.p. MDT.02	774
- at a distance of 31 mm from the vessel bottom, c.p. MDT.22	384
- on the vessel bottom, c.p. MDT.24	229
Maximum temperature of melt, °C	
- at a distance of 50 mm from the vessel bottom, c.p. MDT.04	1970*
- at a distance of 75 mm from the vessel bottom, c.p. MDT.14	2401*
- at a distance of 100 mm from the vessel bottom, c.p. MDT.34	2584
- at a distance of 125 mm from the vessel bottom, c.p. MDT.103	1979
Distance from the lower end of the internal electrode nozzle to the outer electrode nozzle bottom, mm	
- before the test	22
- after the test (minor distance)	34
Mass of the internal electrode graphite nozzle, kg:	
- before the test	0,3157
- after the test	0,275

Note: \* - indicated temperature at the moment of thermocouple failure

According to the data represented in Table A2.2.1 it is seen that electrical plasmatrongs parameters were changed during the experiment. Nitrogen percentage in gases mixture supplied to the inter-electrode space did not exceed ~10 % (at the end of the tests to ~20 %). Most likely, at the initial stage of the test, open flow area of the hollow needle (by means of which nitrogen flow rate was set in the inter-electrode space of the plasmatrongs) was closed partially. The hollow needle flow area was cleaned at the completion stage of the test and that is indirectly confirmed with increasing of the plasmatrongs power to ~18,2 kW.

## 2.1.6 Conclusions on the testing results

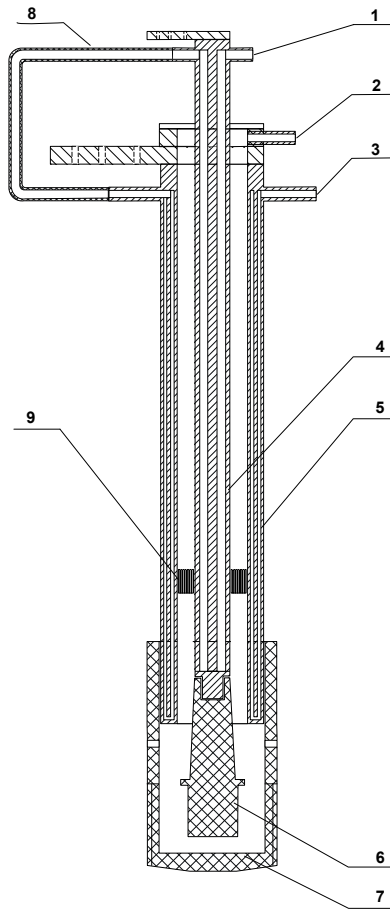
2.1.6.1 As a consequence of the ~141-minute experiment performed the burden melt was produced but the burden was not molten completely. Maximum burden temperature registered by the thermocouples was equal to 2584 °C. The plasmatrongs energy release was 138,4 MJ.

2.1.6.2 Within the experiment performance, ~20 % of consumable part of the internal electrode nozzle was used. Graphite burning out rate was 0,29 g/min.

2.1.6.3 In the course of the test there was no through fracture of the outer electrode graphite nozzle wall. But the protective coating on the most part of the outer electrode graphite nozzle surface was damaged. Minor thickness of the lateral nozzle wall didn't exceed 2 mm.

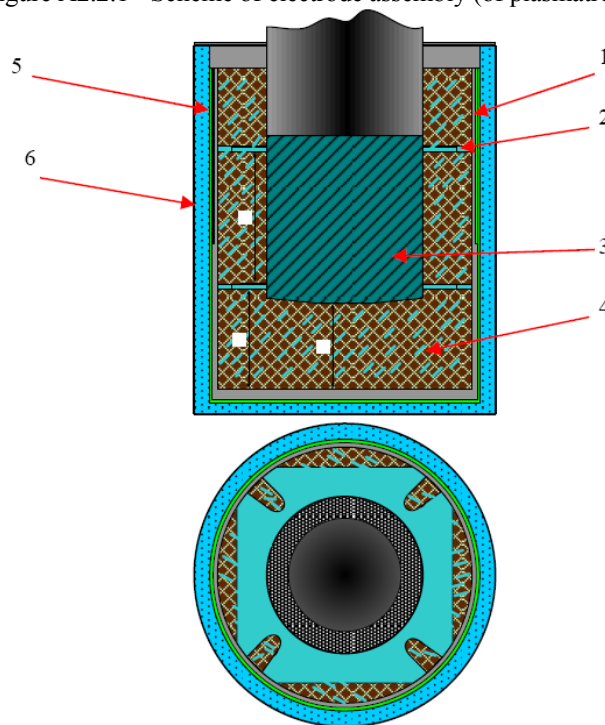
2.1.6.4 The analysis of the test results shows that in the course of the start-up mainly argon was supplied to the inter-electrode plasmatrongs space. Most likely, at the initial stage of the test the hollow needle open area was partially closed that was cleaned at the end of the test. Thus measures should be made to prevent blockage of the hollow needle installed in the nitrogen supply path.





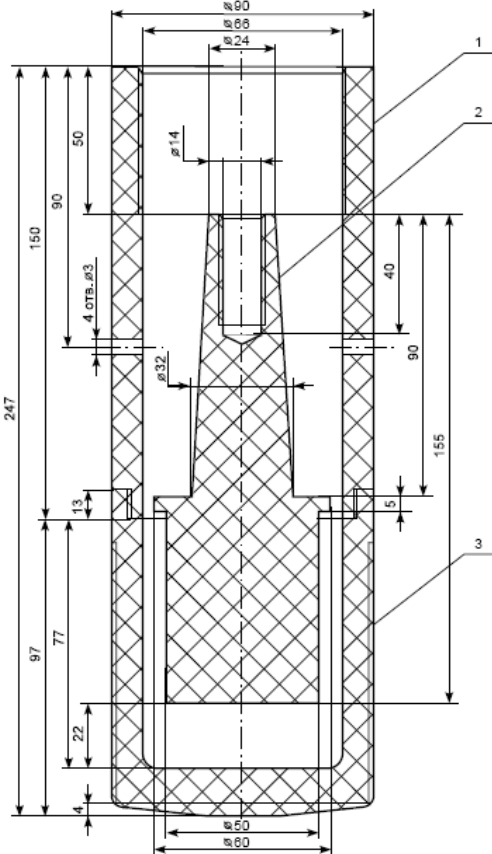
1 – cooling water release; 2 – argon (nitrogen) supply to the inter-electrode space; 3 – cooling water supply; 4 – internal electrode; 5 – outer electrode; 6 – cylindrical graphite nozzle of the internal electrode; 7 – composite graphite nozzle of the outer electrode; 8 – rubber hose; 9 – center sleeve.

Figure A2.2.1 - Scheme of electrode assembly (of plasmatrons)



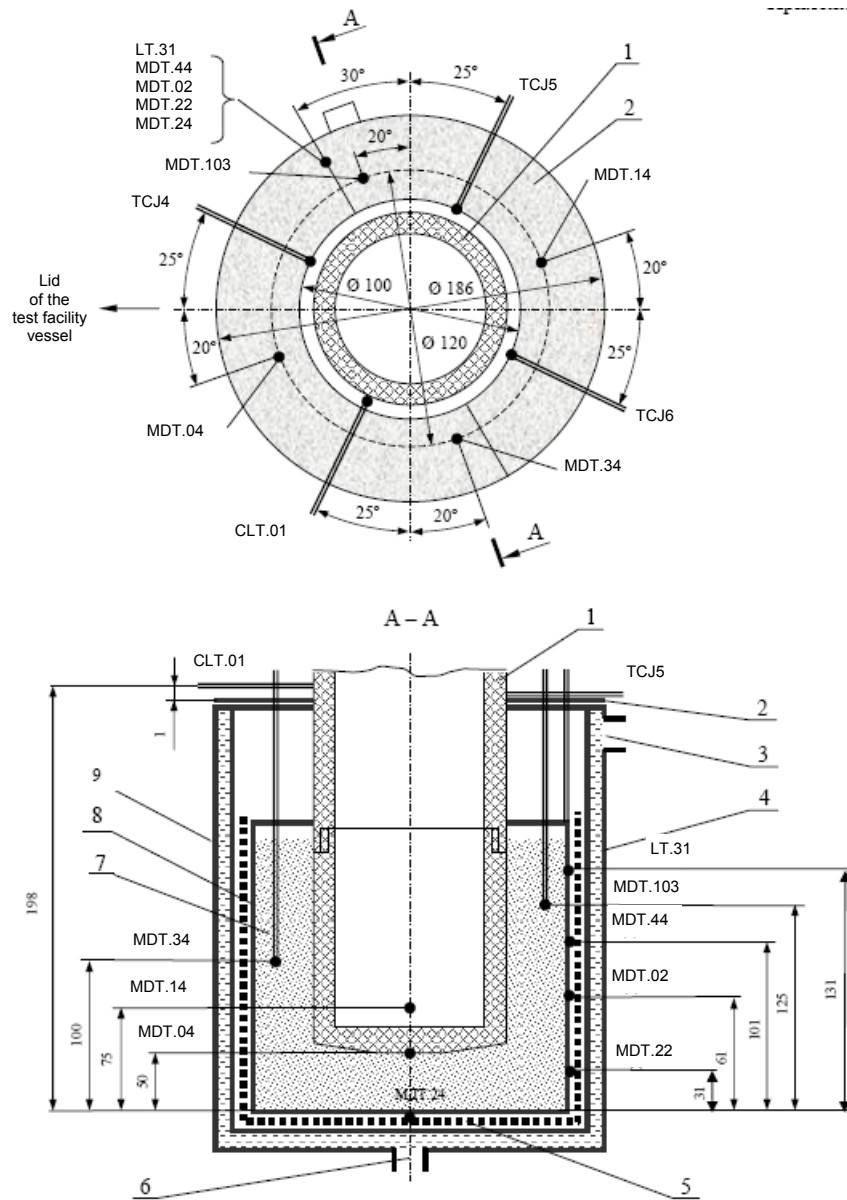
1 – glass fiber cloth; 2 – center rings; 3 – nozzle coated; 4 – burden ( $UO_2$  (pellets)  $ZrO_2$  (powder) + Zr (grains)); 5 – vessel; 6 – experimental cell.

Figure A2.2.2 - Scheme of burden loading



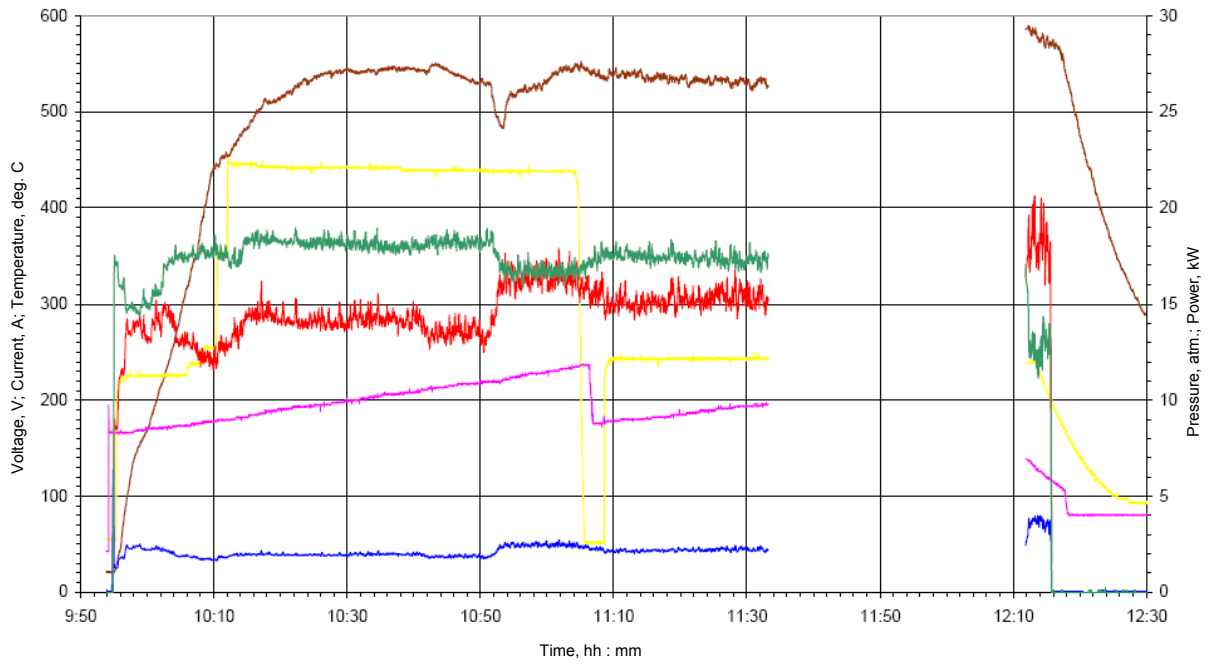
1 – composite graphite nozzle top; 2 – outer electrode nozzle; 3 – composite graphite nozzle bottom

Figure A2.2.3 - Graphite plasmatrons nozzles



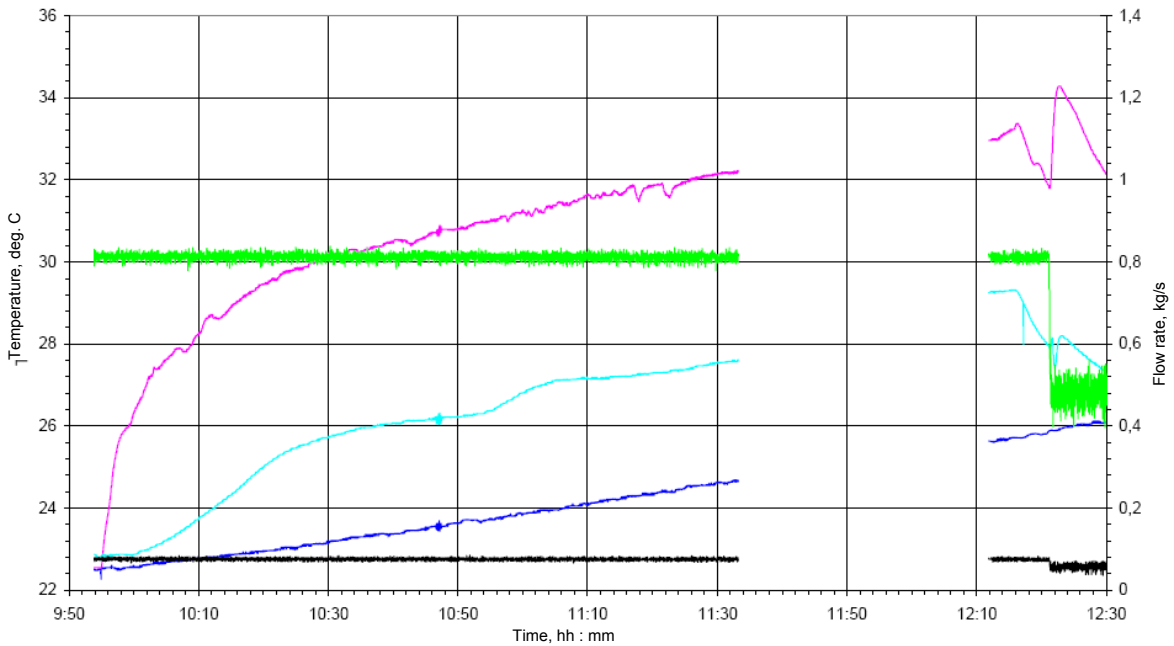
1 – composite graphite nozzle of outer electrode; 2 – protective shield; 3 – cooling water outlet; 4 – cooling water jacket; 5 – glass fiber cloth; 6 – cooling water inlet; 7 – uranium dioxide pellets, metal zirconium and zirconium dioxide powder mixture; 8 – vessel; 9 – experimental cell.

Figure A2.2.4 - Thermocouples layout in the experimental cell



— Temperature of the outer nozzle – CLT.01 (148 mm from the bottom)      — Nitrogen pressure supplied in the plasmatrone – A.R.04  
— Argon pressure supplied in the plasmatrone – B.R.04      — Plasmatrone "A" power  
— Voltage of the plasmatrone A – NN.01.A      — Current in the plasmatrone "A" – T.N.01A

Figure A2.2.5 - Plasmatrone parameters change



— Water temperature in the input collector – LTP.00      — Water temperature in the output from plasmatrone "A" – LTP.01  
— Water temperature in the output from test cell – LTP.04      — Water flow rate for the plasmatrone cooling – LG.16  
— Water flow rate for the test cell cooling – LG.18

Figure A2.2.6 - Change of cooling water parameters of the plasmatrone and experimental cell

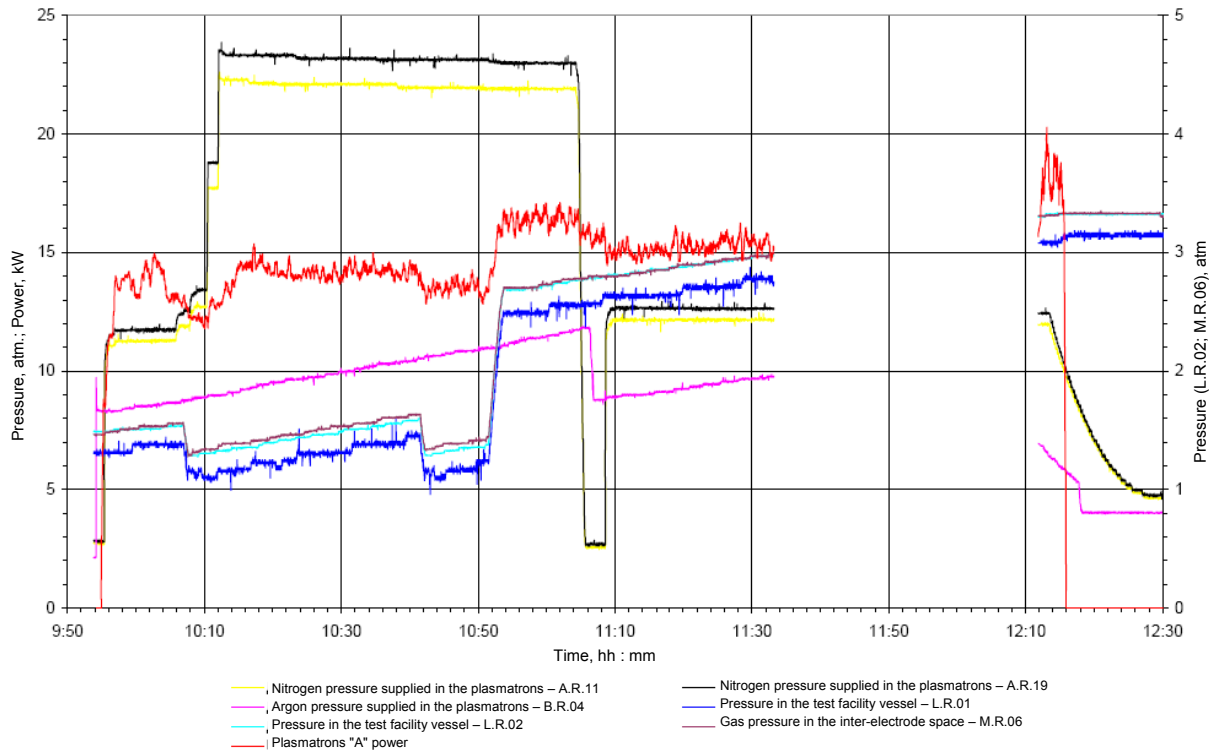


Figure A2.2.7 - Change of medium pressure in the facility pressure vessel and in the inter-electrode space of the plasmatrons

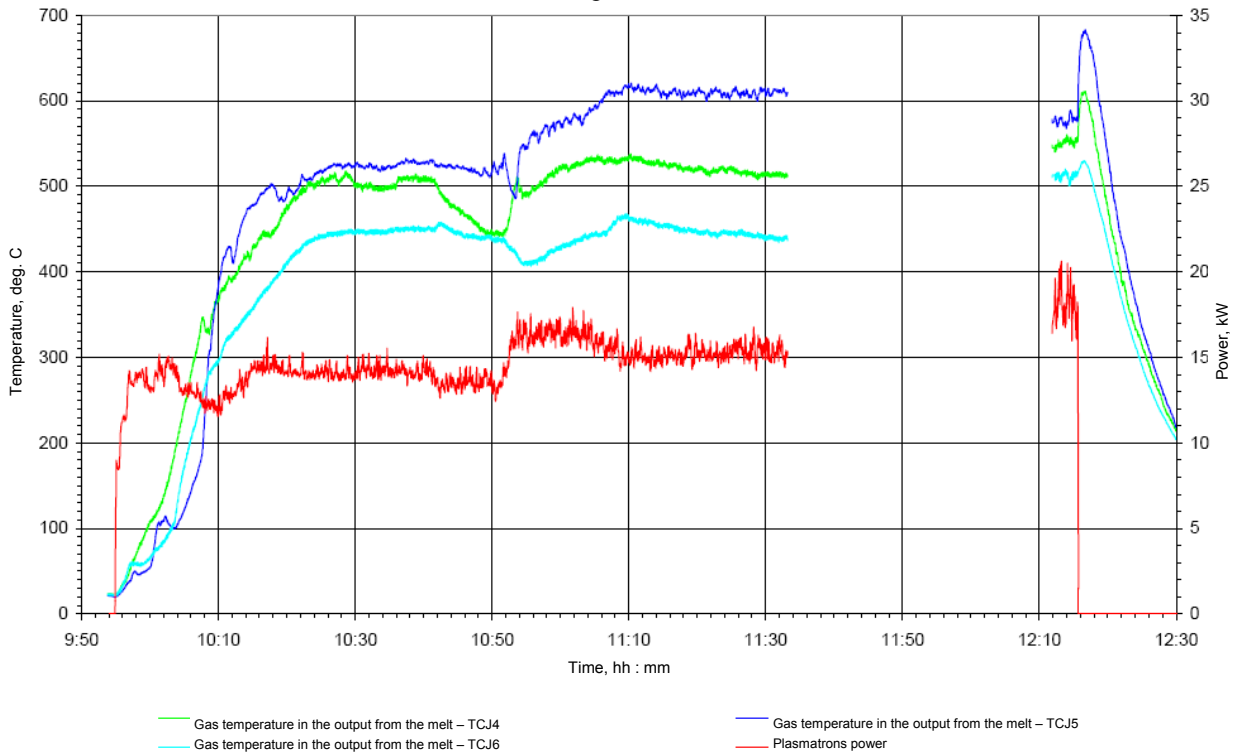


Figure A2.2.8 - Change of temperature of gas released from the melt



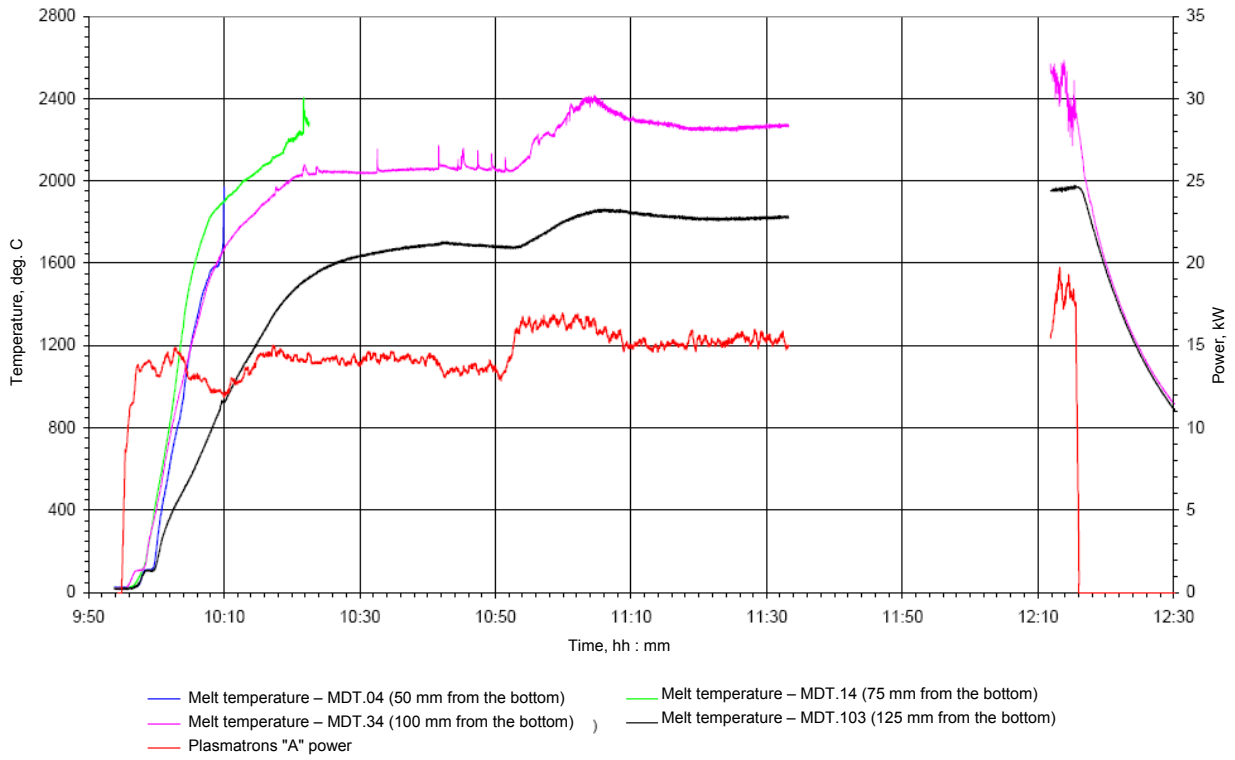


Figure A2.2.9 - Change of burden temperature

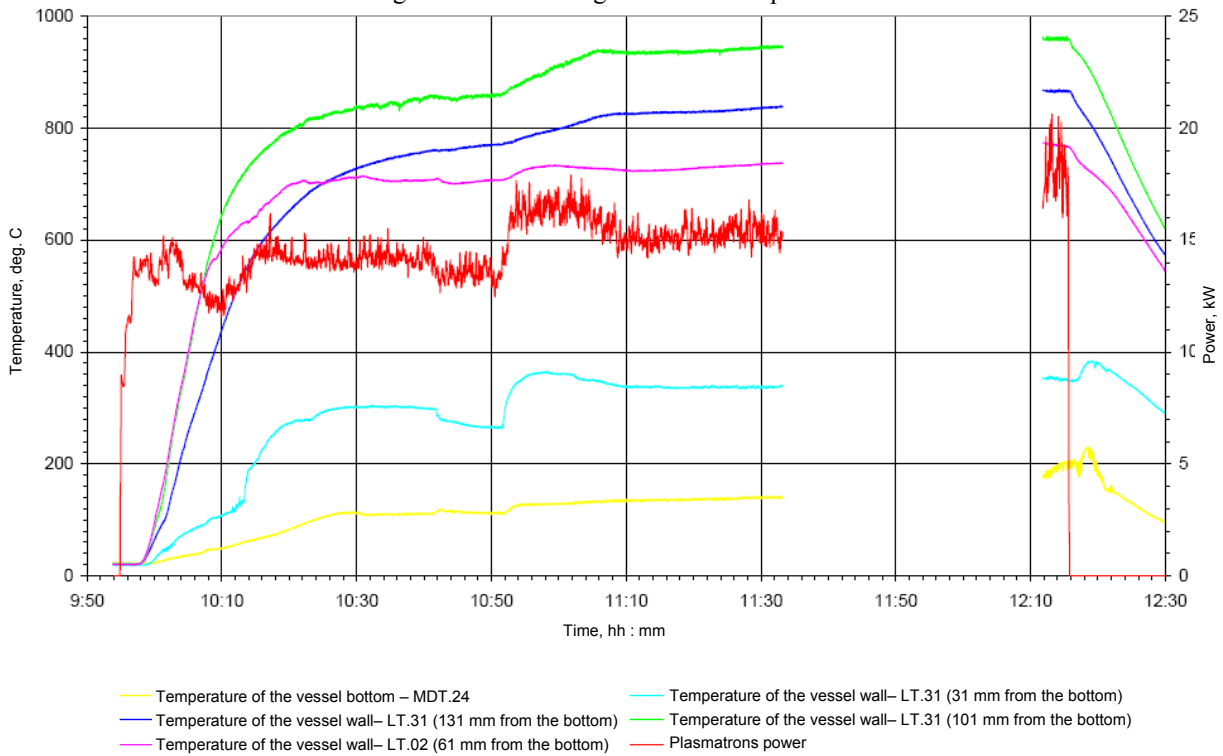


Figure A2.2.10 - Change of vessel material temperature

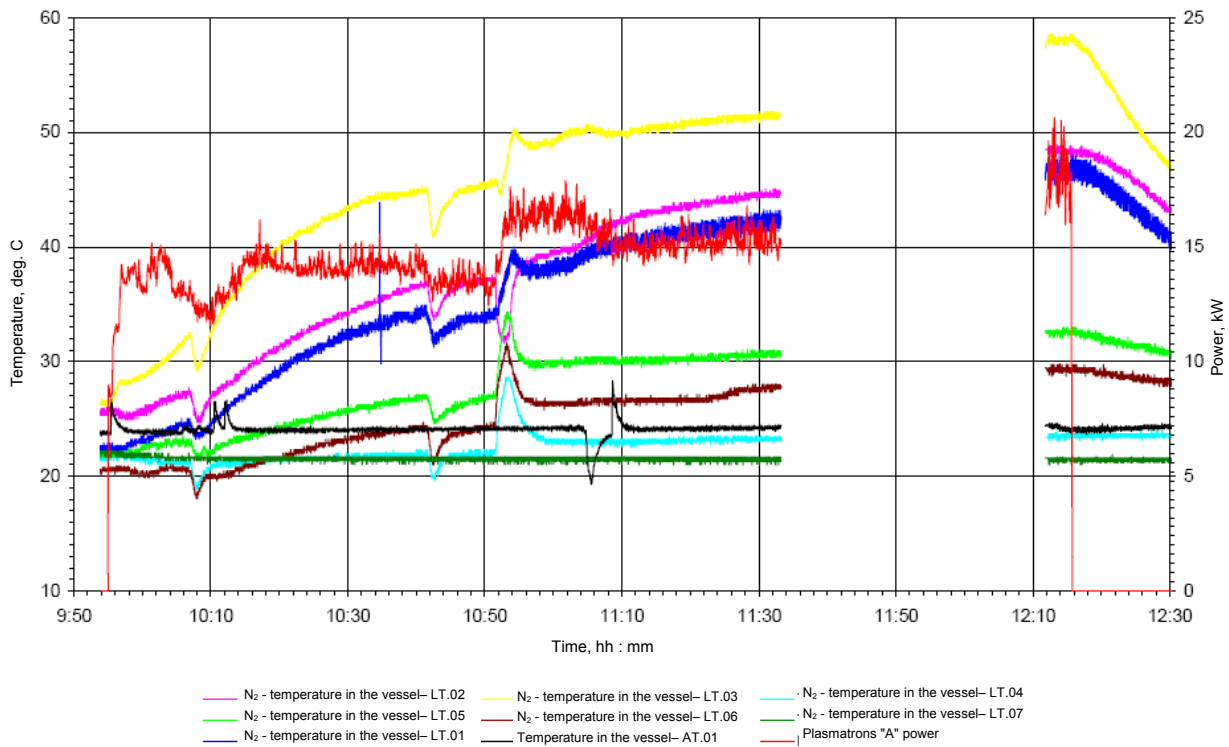


Figure A2.2.11 - Change of medium temperature in the facility pressure vessel



Figure A2.2.12 - Graphite nozzle of the internal electrode after the test. Side view



Figure A2.2.13 - Graphite nozzle of the internal electrode after the test. Top view



Figure A2.2.14 - Internal surface of the composite graphite outer electrode nozzle bottom and burden in the vessel after removal of a burden part



Figure A2.2.15 - Outer surface of the composite graphite outer electrode nozzle top after the test

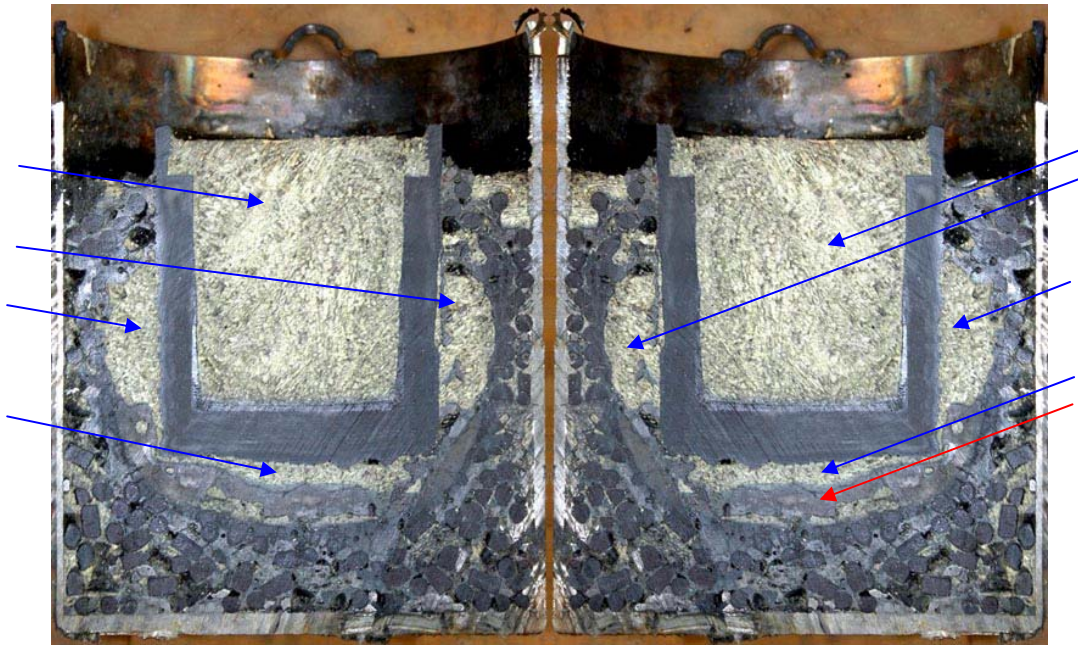


Figure A2.2.16 - Appearance of the vessel, composite graphite nozzle bottom of the outer electrode and caked burden after cutting of the vessel with burden. Blue arrows – sulfur, red arrows - melt

### 2.1.7 Post-test research

The experimental cell was dismantled according to the scheme used in the previous tests. After removal of easily painted burden fragments the vessel with residual conglomerate and outer plasmatrons nozzle was filled with sulfur and cut vertically in a diametrical direction.

From the cuts inspection, we may conclude as follows:

1) The degree of thermal influence on burden material is comparable to the previous tests. The burden went through melting and conversions incompletely. A part of the simulator material in the vicinity of the nozzle was molten and solidified, having formed a crust of the solidified melt around the nozzle. The solidified melt material has generally no contact with the plasmatrons nozzle. From the melt crust outside we observe uranium dioxide pellet fragments enclosed with melt or with caked uranium dioxide powder. Such a case is founded over the entire experimental cell section.

2) The melt crust over the entire cell section has a representative layer structure that corresponds to different phases of melt components interaction with different extent of thermal and temperature effect of the plasmatrons nozzle. The internal layer is brown and in complete adequacy with the molten burden components. Then a darker layer of the melt crust is located with partially dissolved fragments of uranium dioxide pellets. This layer adequates to the dissolution stage of uranium dioxide pellets material on the boundary with liquid melt. The next conditional material layer consists of relatively intact uranium dioxide pellets immersed in the matrix of light material in the breaks of which we see metal impurities. This layer adequates to the impregnation stage of powder uranium dioxide with molten metal zirconium of the burden and their eutectic interaction. The last material layer contains uranium dioxide pellets, dense caked material of zirconium dioxide and non-fused fragments of the burden metal zirconium. This layer adequates to the cake stage of burden material when melting point of the most fusible components of the loading was not reached.

3) The lateral surface of the nozzle as a whole is corroded with the melt. The most significant erosion of the lateral nozzle surface is seen in the bottom plasmatrons part in the form of the zone of deep surrounding erosion of graphite. Depth of erosion is near 10 mm. The protective coating in this region is broken completely, and solidified products of graphite/melt interaction are in the vicinity.

4) The bottom part of the plasmatrons nozzle is also corroded from the corium simulator melt side. A cavity was appeared between the corroded surface of the nozzle and simulator melt

surface. The melt/graphite interaction products are concentrated in the surface layer of the melt crust and has expressed boundary with the remaining melt.

5) Under the nozzle a melt ingot was produced with cross-section height about 10 mm. There is a dark-grey layer, admittedly is a product of decomposition of carbide melt components with water, on the ingot surface. Ingot structure as a whole corresponds to ingots structure in Tests TOP-4, TOP-1.

To define phase composition of the melt produced in the experiment, the melt solidified on the plasmatrons units, protective coating and materials from different assembly areas were sampled. The phase composition was studied by the method of the X-ray phase analysis on powder samples. A group of melt fragments were used for producing of sections for metallographic investigation. Samples designation, sampling points are included in Table A2.2.2 and Figure A2.2.17.

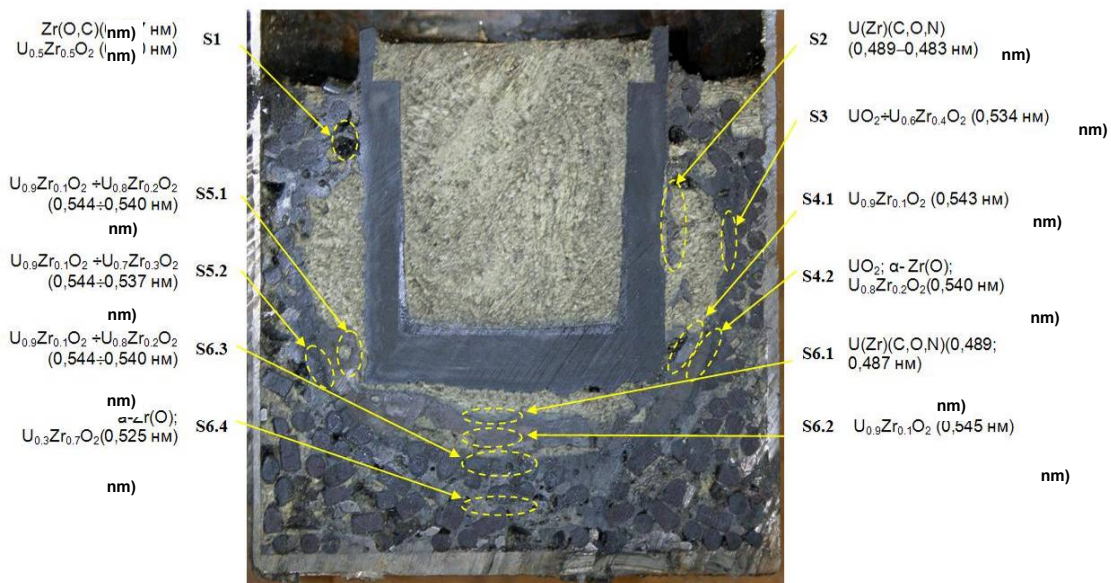


Figure A2.2.17 - Sampling points for investigation

Table A2.2.2 – Samples for investigation

Sample	Sample shape and sampling point	Section	Phase
S1	Melt fragment in the vicinity of the nozzle in the assembly upper part		+
S2	Material fragments in the vicinity of the sidewall erosion area		+
S3	Melt fragment in the vicinity of the steel sleeve		+
S4.1	Fragment of homogeneous melt in the vicinity of the sidewall erosion area		+
S4.2	Fragment of homogeneous melt away from the sidewall erosion area		+
S5.1	Fragment of homogeneous melt in the vicinity of the sidewall erosion area	+	+
S5.2	Fragment of homogeneous melt away from the sidewall erosion area		+
S6.1	Upper layer (carbide)		+
S6.2	Homogeneous melt layer	+	+
S6.3	Layer of uranium dioxide pellets dissolution		+
S6.4	Layer of powder uranium dioxide impregnation with molten metal zirconium		+
S6.5	Caked material of zirconium dioxide		+

The phase analysis was performed with the methods of X-ray diffractometry of polycrystals on powder samples prepared from the material sampled for investigation. X-ray was carried out on the diffractometer DRON-3 with Bragg-Brentano focus in copper  $K\alpha$  emission. The resulted diffractograms were analyzed as per the method of qualitative phase analysis using the crystallographic data library and special methods for identification of phases, variable composition.

According to the X-ray phase analysis, the main components of phase composition of the most samples of solidified melt are oxide phases  $(U, Zr)O_2$  with FCC – uranium dioxide lattice, carbide phases of variable composition, general formula of which may be represented in the



form of (Zr,U)(C, O) and uranium dicarbide. The main feature of phase material composition of this test is the presence in the phase composition of carbidization products of burden components. Uranium dicarbide and oxycarbides with high contents of uranium being in the samples in the vicinity of nozzle erosion areas, are products of oxide burden components/graphite nozzle interaction (samples S2, S4.1, S5.1, S6.1). The fact of very insignificant contents of uranium dicarbide in the carbidized ingot material layer under the nozzle attracts our attention. Here the basic phase is solid solution U(Zr)(O, C, N) with FCC lattice and high contents of uranium atoms. Similar phase composition of the products points to not complete melt carbidization.

Oxide solid solutions (U,Zr)O<sub>2</sub> are characteristic of the experimental cell material samples where partial or full melting of components is taken place. The common feature of this material is its melting without contact with nozzle graphite and carbide melt due to emission and thermal convection.

Metal zirconium ( $\alpha$ -Zr(O)) is present considerably only in the external samples regions (samples S4.2, S5.2) and in the basic melt ingot under the nozzle (samples S6.(2-5)). As a rule, presence of this phase shows low-level of melt carburizing before its solidification. On the contrary, presence of the variable content phase Zr(U)(C, O) with FCC lattice of zirconium carbide indicates increased concentration of carbon in the melt. Particularly, presence of these phases is characteristic of the solidified melt material located in the vicinity of erosion damage of the external electrode nozzle surface. In most cases, propagation of carbon specified according to this character, is limited with the layer in the solidified melt structure where uranium dioxide pellets were dissolved.

The resulted phase analysis is included in Table A2.2.3. The lattice period data  $a_0$  of oxide and oxycarbide phases and their approximate components composition are tabled below. Phases sequence in the table columns corresponds to reduction of their volume content in the samples.

Table 3 The resulted qualitative analysis of the sample phase analysis

Sample	Main phases	Other phases	Sample shape and points of sampling
S1	Zr(O,C)(0,467 nm); U <sub>0,5</sub> Zr <sub>0,5</sub> O <sub>2</sub> (0,530 nm)	UO <sub>2</sub> ; ZrO <sub>2</sub> <sup>mkl</sup> ; ZrO <sub>2</sub> <sup>tetr</sup> ; Zr (O,C,N) ( 0,464 nm);	Melt fragment near the nozzle in the upper assembly part
S2	U(Zr)(C,O,N) (0,489–0,483 nm);	UO <sub>2</sub> ; U <sub>0,8</sub> Zr <sub>0,2</sub> O <sub>2</sub> (0,540 nm); (Zr,U)(C,O)(0,468÷0,471 nm); UC <sub>2</sub>	Material fragments in the vicinity of the lateral wall erosion area
S3	UO <sub>2</sub> ÷U <sub>0,6</sub> Zr <sub>0,4</sub> O <sub>2</sub> (0,534 nm);	Zr (C,O,N) ( 0,467 nm);ZrO <sub>2</sub> <sup>tetr</sup>	Material fragments near the steel barrel wall
S4.1	U <sub>0,9</sub> Zr <sub>0,1</sub> O <sub>2</sub> (0,543 nm);	(Zr)(C,O)(0,465÷0,469 nm); U(Zr)(C,O,N) (0,486 ; 0,476 nm); $\alpha$ - Zr(O); UO <sub>2</sub>	Fragment of the melt in the vicinity of the lateral wall erosion area
S4.2	UO <sub>2</sub> ; $\alpha$ - Zr(O); U <sub>0,8</sub> Zr <sub>0,2</sub> O <sub>2</sub> (0,540 nm)	U <sub>0,8</sub> Zr <sub>0,2</sub> O <sub>2</sub> ÷U <sub>0,3</sub> Zr <sub>0,7</sub> O <sub>2</sub> (0,540÷0,525 nm)	Material fragment away from the lateral wall erosion area
S5.1	U <sub>0,9</sub> Zr <sub>0,1</sub> O <sub>2</sub> ÷U <sub>0,8</sub> Zr <sub>0,2</sub> O <sub>2</sub> (0,544÷0,540 nm)	(Zr,U)(O,C,N)(0,466÷0,467 nm); U <sub>0,7</sub> Zr <sub>0,3</sub> O <sub>2</sub> (0,537 nm); UO <sub>2</sub> ; (Zr,U)(C,O,N) (0,476 nm); $\alpha$ - Zr(O)	Fragment of homogeneous melt near the lateral wall erosion area
S5.2	U <sub>0,9</sub> Zr <sub>0,1</sub> O <sub>2</sub> ÷U <sub>0,7</sub> Zr <sub>0,3</sub> O <sub>2</sub> (0,544÷0,537 nm)	UO <sub>2</sub> ; $\alpha$ - Zr(O) (Zr,U)(O,C,N)(0,464÷0,466 nm)	Fragment of homogeneous melt away from the lateral wall erosion area
S6.1	U(Zr)(C,O,N)(0,489; 0,487 nm);	UO <sub>2</sub> ; U <sub>0,9</sub> Zr <sub>0,1</sub> O <sub>2</sub> (0,544 nm); U <sub>0,8</sub> Zr <sub>0,2</sub> O <sub>2</sub> (0,541 nm)	Upper layer (carbide)
S6.2	U <sub>0,9</sub> Zr <sub>0,1</sub> O <sub>2</sub> (0,545 nm);	Zr(O,C)(0,467nm); UO <sub>2</sub> ; $\alpha$ -Zr(O)	Homogeneous melt layer
S6.3	U <sub>0,9</sub> Zr <sub>0,1</sub> O <sub>2</sub> ÷U <sub>0,8</sub> Zr <sub>0,2</sub> O <sub>2</sub> (0,544÷0,540 nm)	$\alpha$ -Zr(O); Zr(O,C)(0,467nm); UO <sub>2</sub>	Layer of uranium dioxide pellets dissolution
S6.4	$\alpha$ -Zr(O); U <sub>0,3</sub> Zr <sub>0,7</sub> O <sub>2</sub> (0,525 nm)	UO <sub>2</sub> ; U <sub>0,9</sub> Zr <sub>0,1</sub> O <sub>2</sub> (0,544 nm)	Layer of ZrO <sub>2</sub> powder impreg- nation with molted metal Zr
S6.5	$\alpha$ -Zr(O); ZrO <sub>2</sub> <sup>mkl</sup>		Caked material of ZrO <sub>2</sub>



Microstructures of the ingot samples S5.1 and S6.2 are shown in Figures A2.2.18 and A2.2.19 correspondently.

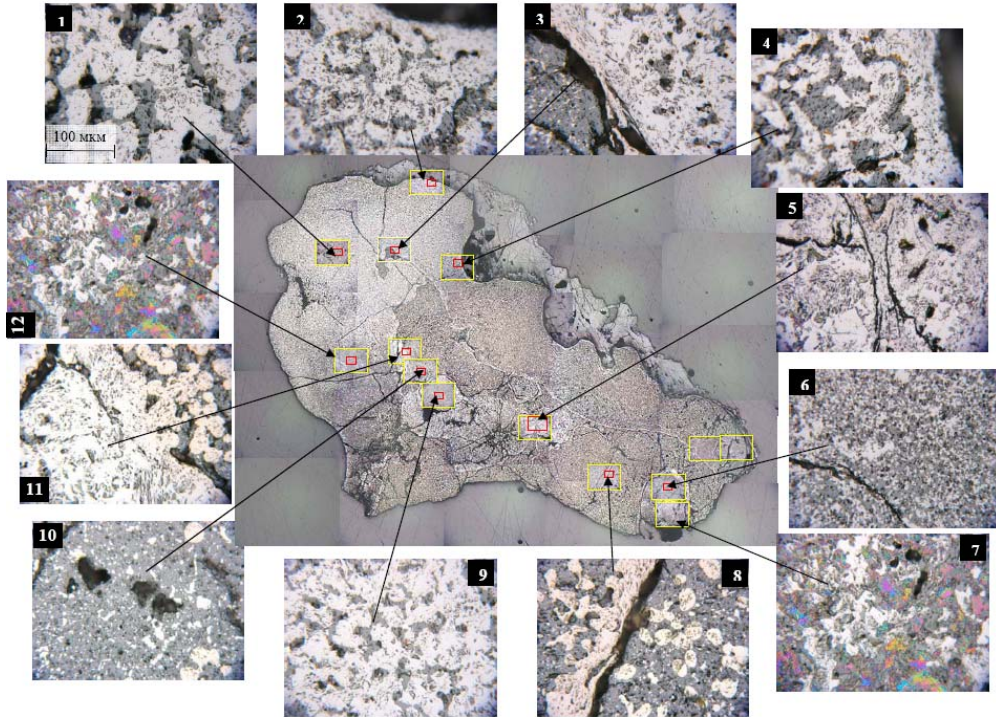


Figure A2.2.18 – Microstructures of the ingot sample S5.1

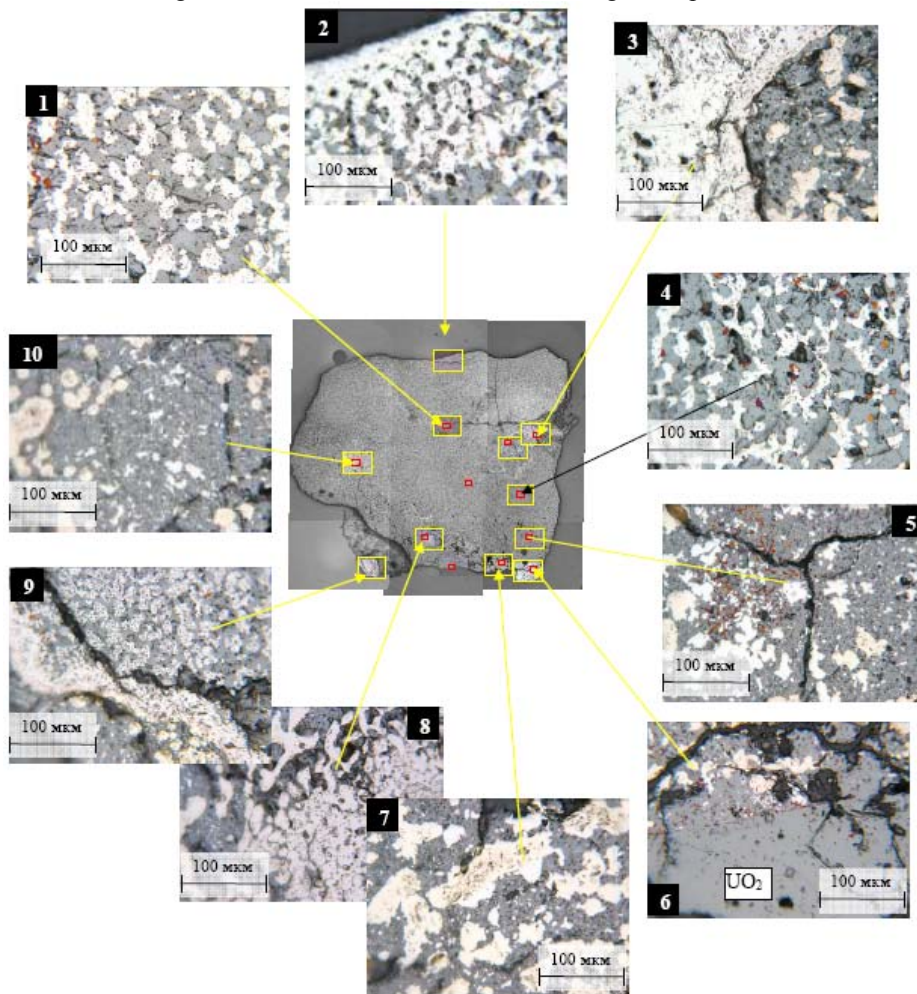


Figure A2.2.19 – Microstructures of the ingot sample S6.2

### 2.1.8 Conclusion

The phase content of the samples is characterized with preferential presence of high temperature burden components interaction products in the course of heating. Degree of melt carbonization near the nozzle and degree of graphite erosion shows that the melt was in contact with graphite during considerably long period but insufficient for full carbonization of the graphite contacting with melt. The cause of the coating zone damage and graphite erosion in the lower nozzle part is considered a local overheating of the nozzle area located opposite narrow zone of arch burning. The origin of coating damage may be thermal stresses in heating or coating overheating. Further growth of the coating damage was taken place due to penetration of the carbonized melt in discontinuity flaws and hollow spaces under the melt. Both chemical dissolving of zirconium carbide in carbide melt and its mechanical detachment play an important role in these processes.

As a consequence of apparent absence of melt/plasmatrons nozzle contact, the mechanism of melt supply to the zone of erosion damage of coating and graphite is not clear completely so far. One of the options may be as follows:

1. Gradual bottom-up fusing of the melt along the assembly and its draining along the nozzle walls due to wetting;
2. Foaming of melt due to generation of gaseous interaction products;
3. Accumulation of molten material in the areas of minor erosion damage.

The products of carbidization are mainly located near the erosion damage zones and upper ingot layers. Such location favors the assumption that graphite erosion leaked at the last stages of heating and occurred mainly as far as material supply along the nozzle walls in the course of heating of the upper burden parts contacting with the nozzle.

## 2.2 TOP-6 test

2.2.1 Subject of investigation is the plasmatrons melt heating system in the RPV lower head model.

2.2.2 Objective and goals of the test

2.2.2.1 The objective of the experiment was to test oxide medium resistance of the graphite nozzle made from R4340 graphite of the outer electrode of the plasmatrons with protective carbide zirconium layer at high temperature.

2.2.2.2 The goals of the experiment were:

- production of melt from the burden consisting of zirconium dioxide powder ( $ZrO_2$ ), uranium dioxide pellets ( $UO_2$ ) and metal zirconium in the vessel for heating burden;
- evaluation of resistance of the protective carbide zirconium layer during 150 minutes;
- comparison of the erosion rate of the graphite nozzle made of graphite R4340 with results of nozzles tests made of ARV-1 graphite.

2.2.3 General provisions

2.2.3.1 The plasmatrons melt heating system in the reactor vessel lower head model (drawing #DKIG.681.613.001.SB) was designed for simulating of heat decay in the melt situated in the lower head model. The lower head model with the plasmatrons installed is located in the pressure vessel of the "LAVA-B" facility.

2.2.3.2 The test was carried out in the "ANGARA" heat engineering test facility.

2.2.3.3 The experiment was performed in conformity with the program and procedure "Testing of the melt heating system in the reactor vessel lower head model in the "LAVA-B" test facility" reg. No. 1652 of 10.08.2005 as well as in compliance with the resolution on performance of tests in the melt heating system with plasmatrons reg. No. 240-02/68 of 29.05.2008 and functional program reg. No. D-319 of 30.07.2007.

2.2.4 Test conditions

2.2.4.1 Magnetic medium recording and data display were performed by means of the

"ANGARA" test facility data acquisition system (DAS).

2.2.4.2 The test facility automatic control systems were managed manually.

2.2.4.3 Nominal parameters of the melt heating system in the reactor vessel lower head model are as follows:

- maximum value of the plasmatrons working current, A – to 400;
- plasmatrons arc volts, V – to 70;
- open circuit volts on the plasmatrons, V – to 140;
- water flow rate through the plasmatrons cooling path, kg/s – to 0,08;
- consumption of argon supplied to inter-electrode space, kg/s – 0,001;
- consumption of nitrogen supplied to inter-electrode space, kg/s – 0,00008.

2.2.4.4 The work was done using the plasmatrons "A" installed on the concrete support. The plasmatrons construction is illustrated in Figure A2.2.20. The plasmatrons was installed vertically on the concrete support. The concrete support was placed inside the MR. There was a vessel for burden heating inside the concrete support, see Figure A2.2.21 item 6. The vessel outer surface, see Figure A2.2.21, item 5, was covered with two glass cloth layers at a distance of 100 mm from the upper vessel end and one glass cloth layer at a distance of 90 mm from the sleeve bottom (total sleeve height – 190 mm), which was used as a thermo- and electro-insulation. Mass of the thermally insulated vessel with thermocouples was equal to 2,597 kg. The burden heating vessel was loaded with burden consisting of the following materials: zirconium dioxide powder – total weight 1,116 kg, uranium dioxide pellets – 9,144 kg, metal zirconium – 1,74 kg. Metal zirconium consisted of zirconium plates of 0,195 kg, zirconium rings – 0,420 kg and grains – 1,125 kg. Metal zirconium was used in the form of grains. The scheme of burden loading in the vessel is shown in Figure A2.2.21. The burden heating vessel was cooled from the reverse water system from the supply head through the tank THW-3 reservoir with further water removal to the dump header.

A cylindrical nozzle of the internal electrode and lower part of the composite nozzle of the outer electrode made of graphite R4340 were installed on the plasmatrons. The upper composite nozzle part of the outer electrode was made of graphite ARV-1. The nozzle drawing is represented in Figure A2.2.22. The external surface of the outer electrode nozzle bottom was coated with protective carbide zirconium layer. To improve zirconium flowing, from the outside the screw M90×1.5 was made on the lateral surface of the nozzle bottom, and on the end of the nozzle bottom the grooves of concentric-form rings were cut. Mass of the lower and upper parts of the outer electrode graphite nozzle was 0,674 kg and 0,735 kg, and the mass of the internal electrode graphite nozzle 0,3086 kg. The distance between the internal electrode nozzle end and the outer electrode nozzle bottom was equaled to 30 mm.

In the burden located in the experimental cell 4 thermocouples W-Re5/20: c.p. MDT.04, MDT.14, MDT.34, MDT.103 were installed. Five thermocouples CA, represented in Figure A2.2.23, were installed on the outer surface of the vessel for the purpose of measuring temperature of the wall and vessel bottom. Their designations are as follows: c.p. L.T.31, MDT.44, MDT.02, MDT.22, MDT.24. On the protective shield, from the top, see Figure A2.2.23, item 2, three thermocouples CA c.p. TCJ4, TCJ5, TCJ6 for measuring temperature of gas released through the gap between the protective shield and outer electrode nozzle, were installed. On the outer electrode nozzle, a thermocouple CA c.p. CLT.01 was installed at a distance of 148 mm from the lower end of the outer electrode nozzle (1 mm over the screen). The thermocouples layout is given in Figure A2.2.23.

2.2.4.5 Electric power was supplied to the plasmatrons from welding apparatus of Group "A". In the plasmatrons power-supply circuit, the reactance was switched off.

2.2.4.6 Plasmatrons voltage was measured by the standard normalizing converter 73G-IV10 (c.p. NN.01A).

2.2.4.7 Plasmatrons current strength was measured by the standard normalizing converter 73G-IV100M (c.p. TN.01A).

2.2.4.8 Working medium and facility elements temperature was measured by the standard thermocouples of the "LAVA-B" test facility.

2.2.4.9 Working medium pressure was measured with the standard pressure gauges DDM.

2.2.4.10 Electric arc ignition was performed with supply of argon in the inter-electrode opening with further, after ignition, nitrogen supply to produce gas mixtures.

2.2.4.11 To provide uninterrupted nitrogen supply to inter-electrode plasmatrons space, additional path of nitrogen supply (bypass path) to the plasmatrons was arranged.

2.2.4.12 In the working medium supply paths, the nozzles were installed in the plasmatrons:

- argon supply path - nozzle diameter 0,7 mm;
- nitrogen supply path - hollow needle with effective open area  $\phi F = 5,667 \times 10^{-8} \text{ m}^2$ ;
- additional nitrogen supply path - nozzle diameter 0,52 mm.

2.2.4.13 The functional program reg. No Д-319 of 30.07.07 was changed and supplemented as follows:

Item 6 – adjust reducer Б.6.03 to pressure  $P = 5$  gage atm;

Item 7 – adjust reducer К.6.04 and reducer А.6.17 to pressure  $P = 16$  gage atm;

Item 16 – open valves А.2.27 and А.2.35 – supply nitrogen to plasmatrons;

Item 19 – plasmatrons run time has been changed from 1 for 2,5 hours.

2.2.5 Scope of the work performed

2.2.5.1 On August 23, 2008 the start-up of TP-36 (TOP-7) was began. The plasmatrons "A" was launched from the first push at 10:21:34.

At 10:23, nitrogen was supplied to inter-electrode space through main and additional paths by means of opening valves А.2.27 and А.2.35.

At 10:32, after analyzing voltage and current readings taken from the plasmatrons electric arc, it was decided to decrease the reducer Б.6.03 setting from pressure 5 to 4 gage atm in order to reduce nitrogen flow rate to the plasmatrons inter-electrode space to increase plasmatrons power.

At 10:39, the instruction to reduce Б.6.03 setting to pressure 3 gage atm in order to increase plasmatrons power.

At 11:18:06, unknown cause, there was a failure in pressure gages readings А.Р.11, А.Р.19, Б.Р.04 and М.Р.06.

At 11:21:05, readings of the above gages were recovered, the origin of the pressure gages failure was not detected.

At 12:03:27, the arc was extinguished spontaneously, the attempt to start the plasmatrons with nitrogen supply to inter-electrode space was failed. It was decided to stop nitrogen supply. Argon supply was not stopped.

At 12:04:37, the plasmatrons was launched.

At 12:12, after analyzing arc current and voltage, for the purpose of plasmatrons power increase and debarring of arc disruption, it was decided to supply nitrogen to inter-electrode space only through the main supply path by means of valve А.2.27 opening.

At 12:21, for the purpose of further plasmatrons power increase, it was decided to supply nitrogen to inter-electrode space through the additional path by means of opening valve А.2.35 and closing valve А.2.27.

At 12:22:23, the arc was extinguished spontaneously, it was decided to stop nitrogen supply through the additional supply path.

At 12:22:38, plasmatrons was launched with argon.

At 12:25, nitrogen supply to inter-electrode space through the main supply path was restarted.

At 12:52, as preset time of the plasmatrons run passed, for the purpose of collecting plasmatrons efficiency statistics under environmental overpressure conditions, it was decided to raise pressure in the MR to 1 gage atm, there was no arc disruption during two minutes.

At 12:54, it was decided to rise pressure in the MR to 1,5 gage atm.

At 12:56:11, the arc was extinguished spontaneously, the experiment was stopped. Total arc burning period was 2 hours 33 minutes 52 seconds. Changes for plasmatrons running parameters,

such as voltage, current, power, argon and nitrogen pressure, as well as the outer electrode nozzle temperature are graphically represented in Figure A2.2.24. Changes of cooling water flow rate and temperature of the plasmatrons and burden heating device during the experiment are included Figure A2.2.25. The gas pressure change in facility pressure vessel is in Figure A2.2.26. Change of temperature of gas released from the melt, vessel wall temperature and the temperature of the burden itself as well as the facility pressure vessel temperature during the experiment is included in Figures A2.2.27, A2.2.28, A2.2.29 and A2.2.30. In Figure A2.2.31 variation of argon and nitrogen flow rate supplied to inter-electrode plasmatrons space during the tests is demonstrated.

After completion of the test the graphite nozzles of the outer and internal electrodes and burden in the burden heating vessel were examined. In the result of the examination and required measurement there was detected as follows:

- a) length of the cylindrical part of the outer electrode graphite nozzle was reduced by 22÷31 mm, maximum length of the remaining part was equal to 38 mm. Total length of the remaining nozzle - 133 mm (before the test total nozzle length was 155 mm). The view of the outer electrode graphite nozzle after the tests is given in Figure A2.2.32;
- b) diameter of the cylindrical part of the internal electrode graphite nozzle was increased in the region of arc burning from 50 mm to 52 mm.
- c) internal surface of the outer electrode composite graphite nozzle bottom was covered with black substance, possibly that was traces of melt penetrated into the nozzle. The nozzle bottom had no burnout and traces of interaction with melt. Appearance of the internal surface of the nozzle bottom is seen in Figure A2.2.33;
- d) upper part of the outer graphite nozzle had also no visible damages. Appearance of the outer surface of the nozzle top is seen in Figure A2.2.34.

Appearance of the outer electrode nozzle and the melt after cutting the experimental device vessel is represented in Figure A2.2.35. Due to interaction with the melt the outer electrode nozzle was ruptured. In order to keep the melt location in the device the latter was filled with sulfur (blue arrows in Figure A2.2.35).

2.2.5.2 Table A2.2.4 includes averaged voltage, current, plasmatrons power, water heating in the cooling paths, heat losses with cooling water, outer electrode nozzle temperature, obtained during the plasmatrons "A" run, and also includes the temperature in different points of the burden heating vessel.

2.2.5.3 Table A2.2.5 includes averaged voltage, current and plasmatrons power, subject to percentage of argon and nitrogen in inter-electrode space.

According to the data represented in Table A2.2.5 it is seen that electrical plasmatrons parameters were changed during the experiment subject to percentage of gases in the mix. Nitrogen percentage in gas mixture supplied to the inter-electrode space, did not exceed ~70 %.



Table A2.2.4 – Parameter values resulted from the plasmatrons "A" running

Parameter	Value
Time of the plasmatrons run, h : min : s.	2 : 33 : 52
Averaged voltage of the electric arc, V	58,8
Averaged current of the electric arc, A	311,7
Averaged plasmatrons power, kW	18,2
Maximum heating of water in the plasmatrons cooling path, °C	11,3
Heat losses with plasmatrons cooling water, %	16,0
Maximum water heating in the water cooling jacket of the experimental cell, °C	3,74
Heat losses with cooling water of the burden heating device, %	54,8
Maximum temperature of the outer electrode nozzle, °C (c.p. CLT.01)	656
Maximum temperature of gas released from the burden (melt), °C	
- c.p. TCJ4	500
- c.p. TCJ5	584
- c.p. TCJ6	553
Maximum temperature of vessel wall, °C	
- at a distance of 131 mm from the vessel bottom, c.p. L.T.31	756
- at a distance of 91 mm from the vessel bottom, c.p. MDT.44	877
- at a distance of 61 mm from the vessel bottom, c.p. MDT.02	743
- at a distance of 31 mm from the vessel bottom, c.p. MDT.22	471
- on the vessel bottom, c.p. MDT.24	203
Maximum temperature of melt, °C	
- at a distance of 50 mm from the vessel bottom, c.p. MDT.04	2089*
- at a distance of 75 mm from the vessel bottom, c.p. MDT.14	2096*
- at a distance of 100 mm from the vessel bottom, c.p. MDT.34	2561
- at a distance of 125 mm from the vessel bottom, c.p. MDT.103	1975
Distance from the lower end of the internal electrode nozzle to the outer electrode nozzle bottom, mm	
- before the test	30
- after the test (minor distance)	52
Mass of the internal electrode graphite nozzle, kg:	
- before the test	0,3086
- after the test	0,215

Note: \* - indicated temperature at the moment of thermocouple failure.

Table A2.2.5 – Plasmatrons parameters depending on percentage of gas in inter-electrode space

Parameter	Value		
Averaged voltage of the electric arc, V	33,7	59,1	57,8
Averaged current of the electric arc, A	383	309	316
Averaged plasmatrons power, kW	12,9	18,2	18,2
Averaged percentage of argon in inter-electrode space, %	100	30	65
Averaged percentage of nitrogen in inter-electrode space, %	0	70	35

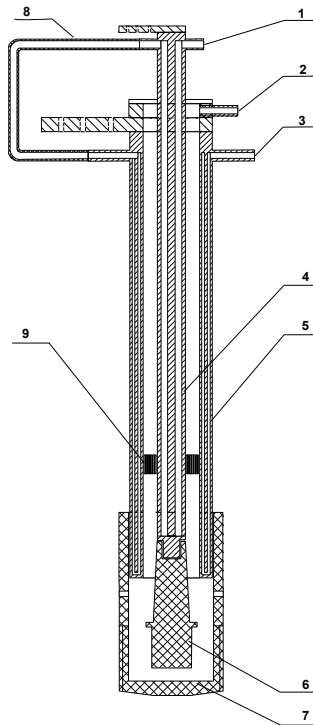
## 2.2.6 Conclusions on testing results

2.2.6.1 As a consequence of the ~154-minute experiment performed the burden melt was produced but the burden was not molten completely. Maximum burden temperature registered by the thermocouples was equal to 2561 °C. The plasmatrons energy release was ~167 MJ.

2.2.6.2 Within the experiment performance, ~36,6 % of consumable part of the internal electrode nozzle was used. Graphite burning out rate was 0,608 g/min.

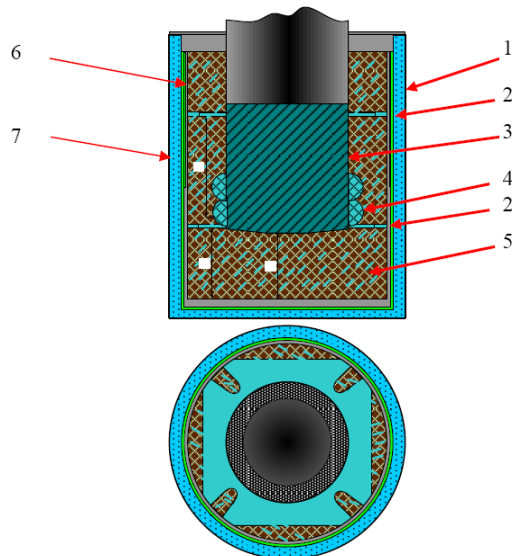
2.2.6.3 In the course of the experiment the protective coating was ruptured on the most surface of the outer electrode graphite nozzle. That resulted in through destruction of the plasmatrons outer electrode nozzle wall.

2.2.6.4 Results analysis shows that it's possible to reach steady-state combustion of the arc at preset plasmatrons power ~18 kW, supplying gases mixture of 35 % nitrogen and 65 % argon to the plasmatrons inter-electrode space.



1 – cooling water release; 2 – argon (nitrogen) supply to the inter-electrode space; 3 – cooling water supply; 4 – internal electrode; 5 – outer electrode; 6 – cylindrical graphite nozzle of the internal electrode; 7 – composite graphite nozzle of the outer electrode; 8 – rubber hose; 9 – center sleeve.

Figure A2.2.20 - Scheme of plasmatrons assembly



1 – glass fiber cloth; 2 – center rings; 3 – nozzle coated; 4 – zirconium ring; 5 – burden ( $\text{UO}_2$  (pellets)  $\text{ZrO}_2$  (powder) + Zr (grains)); 6 – vessel; 7 – experimental cell.

Figure A2.2.21 - Scheme of burden loading



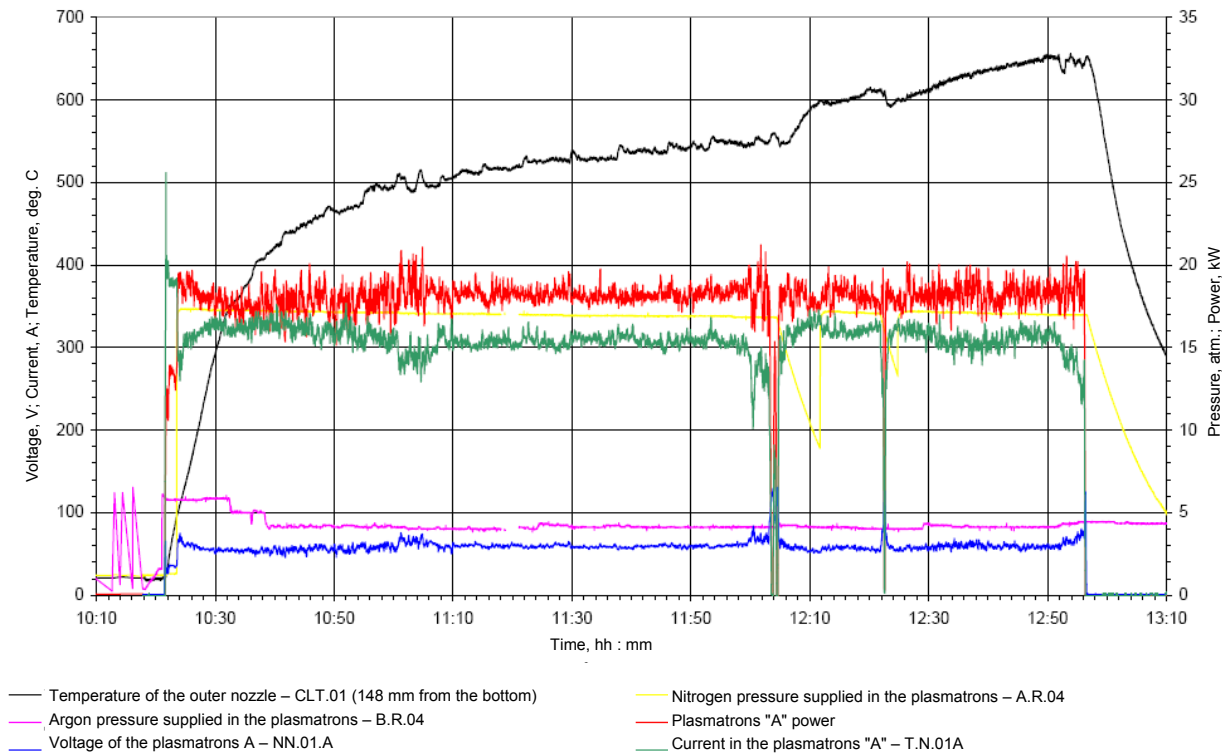


Figure A2.2.24 - Plasmatrone parameters change

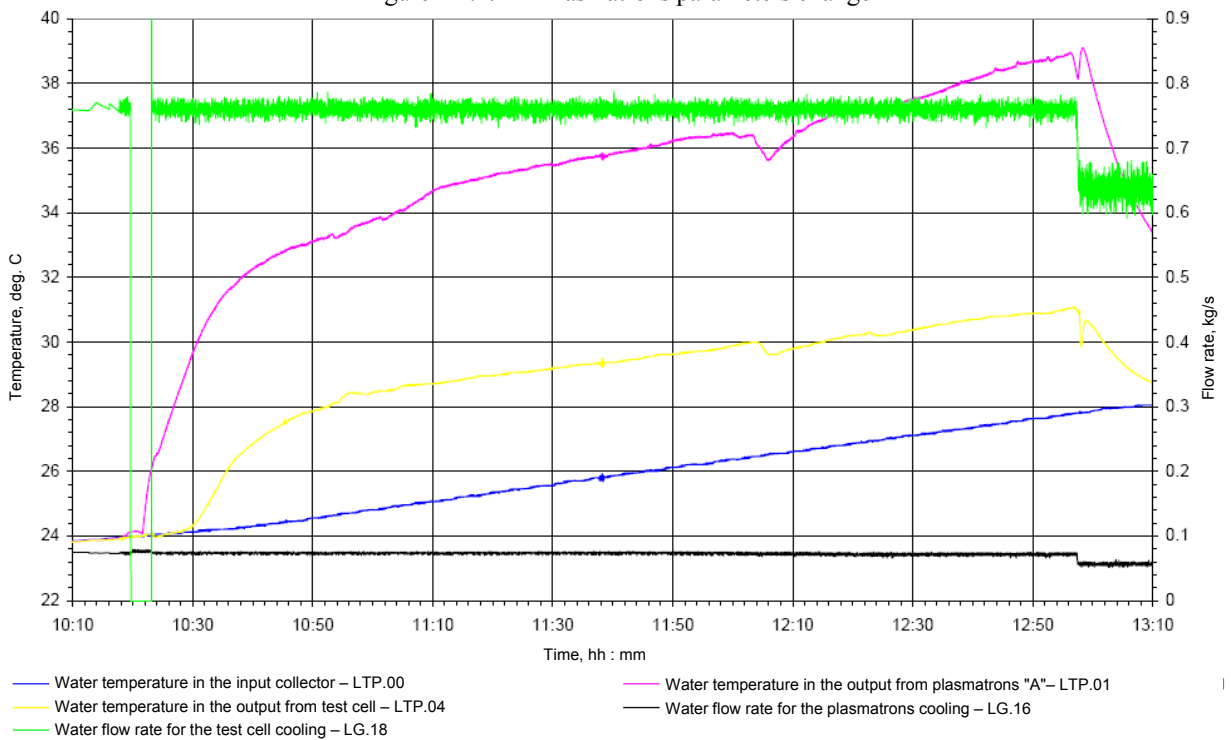


Figure A2.2.25 - Change of parameters of water cooling experimental cell and plasmatrone

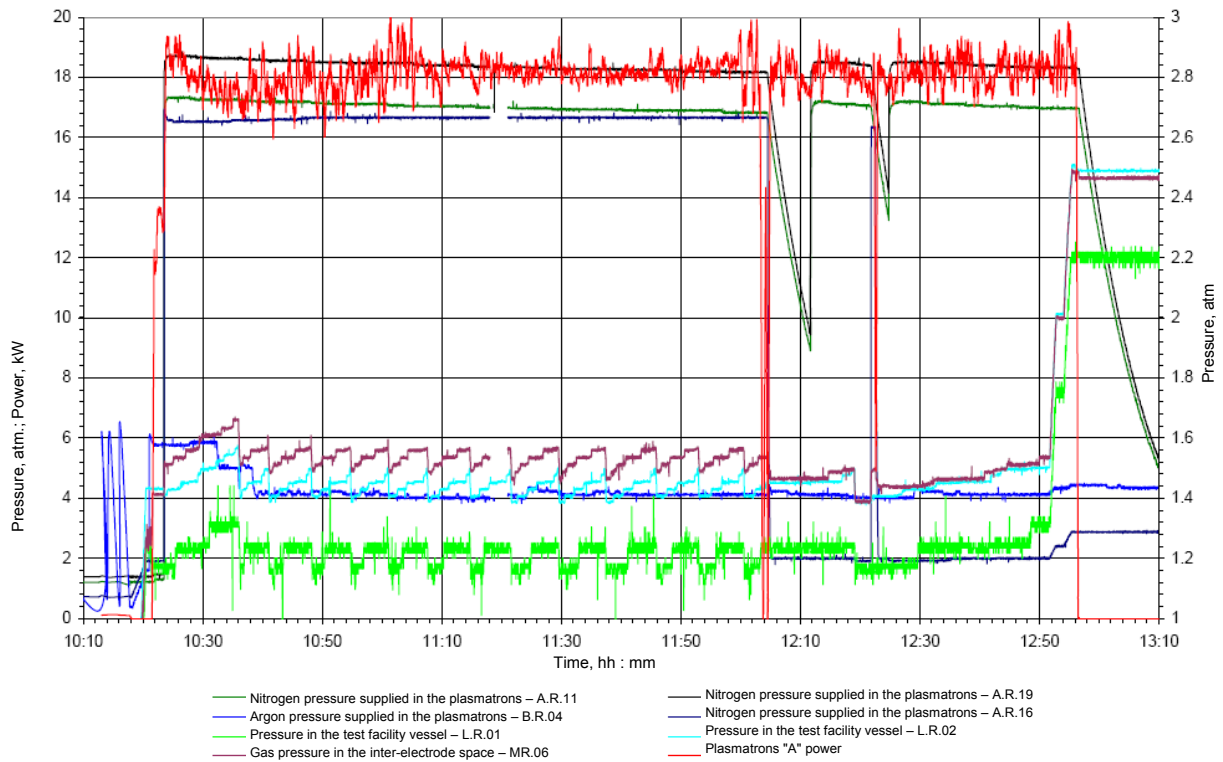


Figure A2.2.26 - Change of medium pressure in the facility pressure vessel and in the inter-electrode space of the plasmatrons

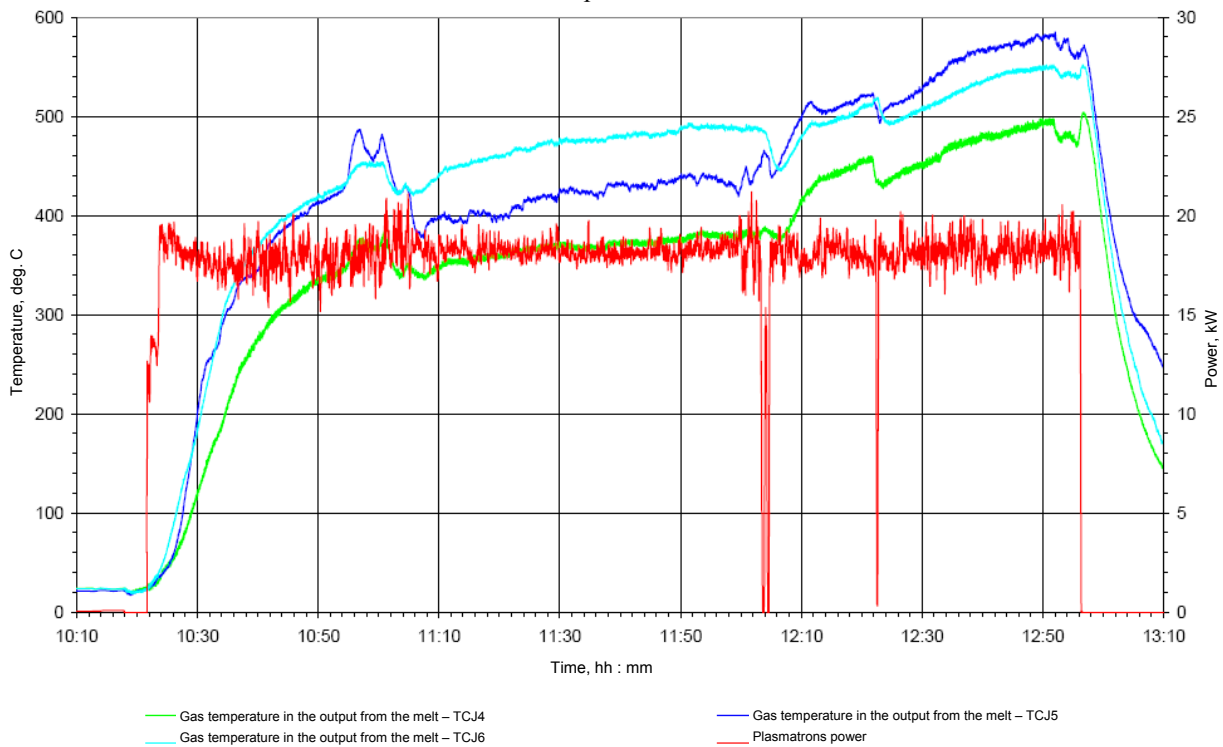


Figure A2.2.27 - Change of temperature of gas at the burden heating vessel outlet



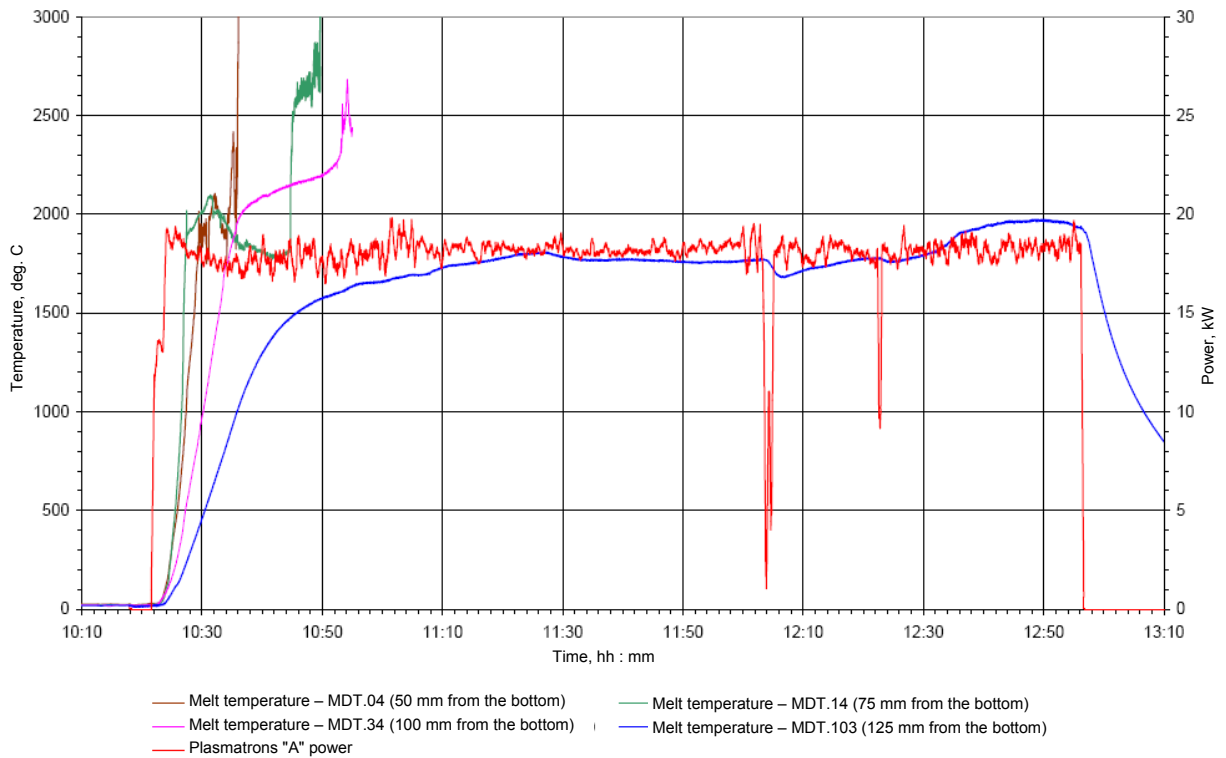


Figure A2.2.28 - Change of melt temperature in the experimental cell

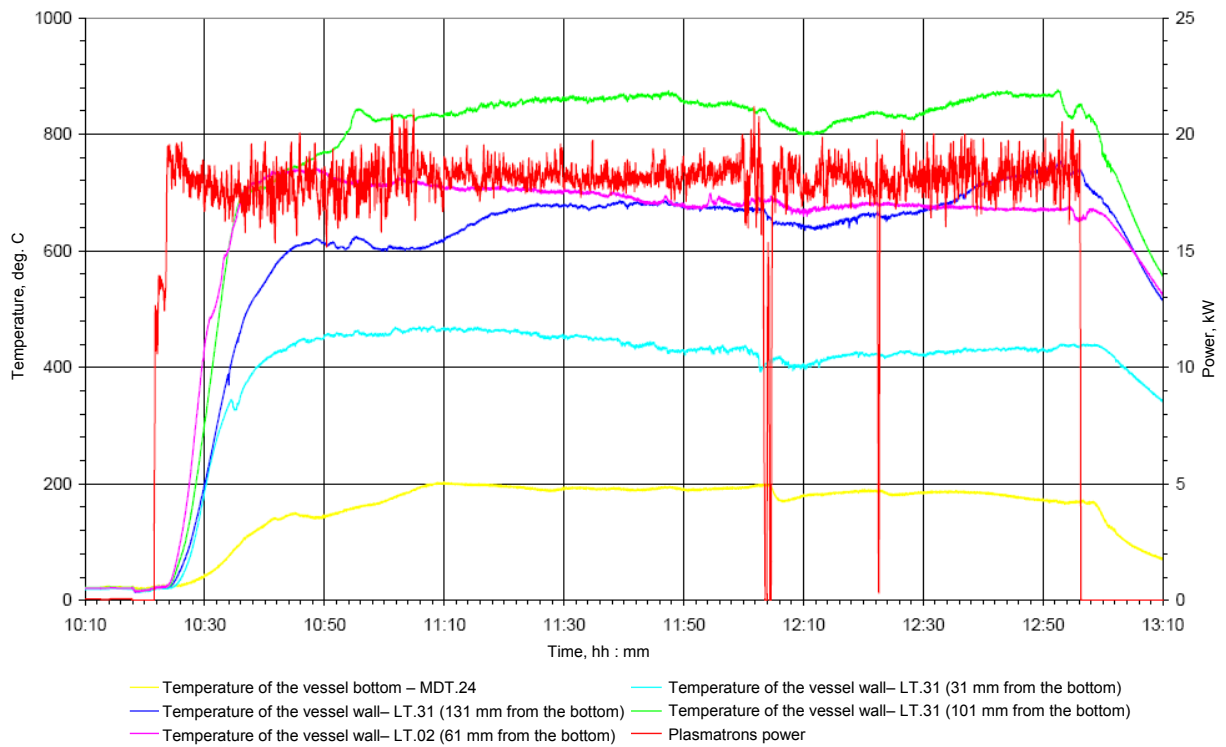


Figure A2.2.29 - Change of vessel material temperature

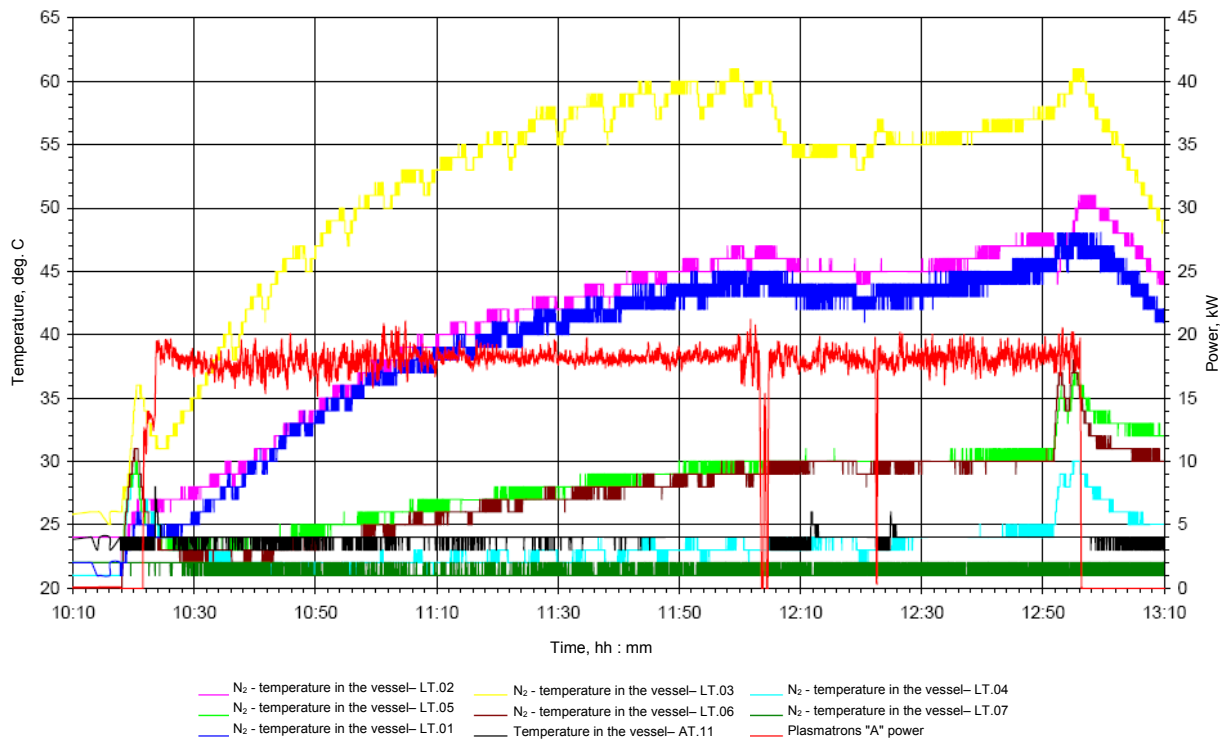


Figure A2.2.30 - Change of medium temperature in the "LAVA-B" pressure vessel

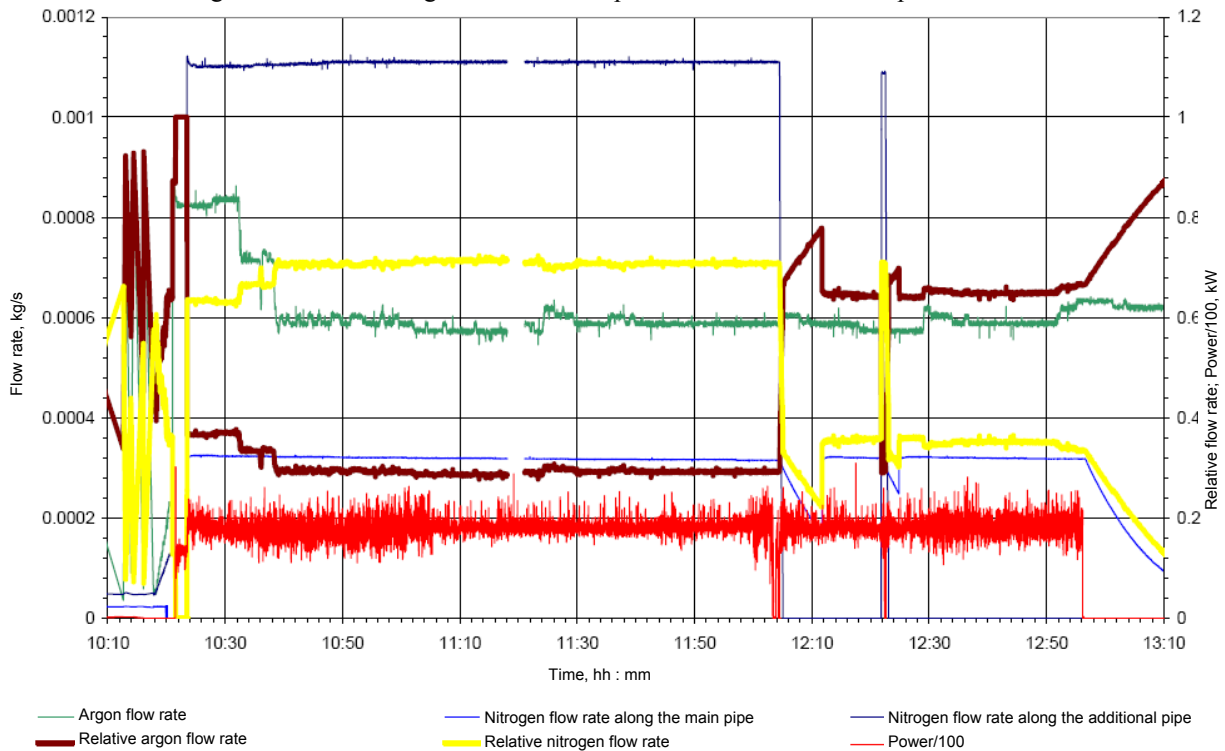
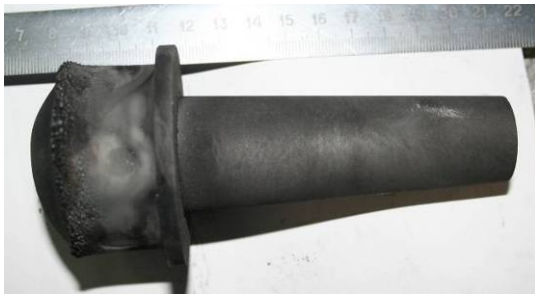


Figure A2.2.31 - Change of gas flow rate in the plasmatrons inter-electrode space



a) Side view



b) bottom view

Figure A2.2.32 - Graphite nozzle of the internal electrode after the test.



Figure A2.2.33 - Internal surface of the composite graphite outer electrode nozzle bottom and burden in the vessel after removal of a burden part



Figure A2.2.34 - Outer surface of the composite graphite outer electrode nozzle top after the test



Blue arrows – sulfur, red arrows – melt; green arrows – points of through damage of nozzles

Figure A2.2.35 - Appearance of the vessel, composite graphite nozzle bottom of the outer electrode and caked burden after cutting of the vessel with burden

### 2.1.7 Post-test research

The experimental cell was dismantled according to the scheme used in the previous tests. After removal of easily painted burden fragments the bucket with residual conglomerate and outer plasmatrons nozzle was filled with sulfur and cut vertically in a diametrical direction.

From the cuts inspection, we may conclude as follows:

1) The lateral surface of the nozzle was greatly corroded with the melt. The most significant erosion of the lateral nozzle surface is seen in the lower plasmatrons part in the form of zone of penetration belt corrosion of graphite. The lower part of the plasmatrons nozzle was less corroded. Graphite/melt interaction products were concentrated in the surface layer of melt crust and has distinctive boundary with the remaining melt part.

2) The degree of thermal influence on burden material is comparable to the previous tests. The

burden went through melting and conversions incompletely. A part of the simulator material in the vicinity of the nozzle was molten and solidified, having formed a crust of the solidified melt around the nozzle. The solidified melt material has generally no contact with the plasmatrons nozzle. Such a case is founded in the upper and lower sections of the experimental cell. The melt crust has a representative layer structure that corresponds to different phases of melt components interaction at different extent of thermal and temperature effect of the plasmatrons nozzle. The internal layer is tawny and in complete adequacy with the molten burden components. Then a darker layer of the melt crust is located with partially dissolved fragments of uranium dioxide pellets. The next conditional material layer consists of relatively whole uranium dioxide pellets immersed in the matrix of light material in the breaks of which we see metal impurities. This layer adequates to the impregnation stage of powder uranium dioxide with molten metal zirconium of the burden and their eutectic interaction. The last material layer contains uranium dioxide pellets, dense caked material of zirconium dioxide and non-fused fragments of the burden metal zirconium. This layer adequates to the cake stage of burden material, when melting point of the most fusible components is not reached.

3) Under the nozzle a melt ingot was produced with cross-section height about 10 mm. The ingot is cup-shaped. There is a fine dark-grey layer, admittedly is a product of decomposition of carbide melt components with water, on the ingot surface. Ingot structure as a whole adequates to ingots structure in Tests TOP-6, TOP-4, TOP-1.

#### *Phase analysis*

To define phase structure of the melt produced in the experiment, the melt solidified on the plasmatrons parts, protective coating and materials from different experimental cell areas were sampled. The phase composition was studied by the method of the X-ray phase analysis on powder samples. A group of melt fragments were used for producing of sections for metallographic investigation. Samples designation, sampling points are included in Figure A2.2.36.



Figure A2.2.36 - Sampling points for investigation

The phase analysis was performed with the methods of X-ray diffractometry of polycrystals on powder samples prepared from the material sampled for investigation. X-ray was carried out on the diffractometer DRON-3 with Bragg-Brentano focus in copper  $K\alpha$  emission. The resulted diffractograms were analyzed as per the method of qualitative phase analysis using the crystallographic data library and special methods for identification of phases, variable composition.

The resulted phase analysis is included in Table A2.2.6. The lattice period data  $a_0$  of oxide and oxycarbide phases and their approximate components composition are tabled below. Phases

sequence in the table columns corresponds to reduction of their volume content in the samples. Sequence of elements spacing in formulation of variable content phases corresponds also to their relative atoms concentration.

Table A2.2.6 - The results of qualitative analysis of phase samples content

Sample	Sample shape and sampling point	Basic phase	Other phases
S1	Melt fragment near the nozzle in the upper assembly part	(Zr,U)(C,O,N) (0,476 nm); UC <sub>2</sub>	(Zr,U)(C,O,N)(0,468÷0,471 nm); (U,Zr)(C,O,N) (0,489–0,483 nm)
S2	Material fragments in the vicinity of the lateral wall erosion area	(Zr,U)(C,O,N) (0,474 nm); UC <sub>2</sub>	(U,Zr)(C,O,N) (0,489–0,483 nm)
S3	Fragments of porous gold- yellow material	U <sub>0,85</sub> Zr <sub>0,15</sub> O <sub>2</sub> (0,542 nm); Zr (O,N,C) ( 0,463 nm)	(Zr,U) (C,O,N) ( 0,464÷0,472 nm)
S4.1	Fragment of dark-grey melt	U <sub>0,4</sub> Zr <sub>0,6</sub> O <sub>2</sub> (0,53 nm);	UO <sub>2</sub> ; α- Zr(O); UO <sub>2</sub> ÷U <sub>0,4</sub> Zr <sub>0,6</sub> O <sub>2</sub> (0,547÷0,530 nm); (Zr,U) (C,O,N) ( 0,464÷0,472 nm)
S4.2	Fragment of light-grey melt	α- Zr(O)	U <sub>0,4</sub> Zr <sub>0,6</sub> O <sub>2</sub> (0,53 nm); UO <sub>2</sub> ÷U <sub>0,4</sub> Zr <sub>0,6</sub> O <sub>2</sub> (0,547÷0,53 nm);
S5.1.1	Homogeneous dark-grey melt in the vicinity of the lateral wall erosion area	(Zr,U)(C,O,N) (0,474 nm); UC <sub>2</sub>	(Zr,)(O,C,N)(0,467) nm);
S5.1.2	Homogeneous dark-grey melt near the lateral wall erosion area	(Zr,U)(C,O,N)(0,468) nm); U <sub>0,85</sub> Zr <sub>0,15</sub> O <sub>2</sub> (0,543 nm);	(Zr,U)(C,O,N) (0,474 nm); UC <sub>2</sub>
S5.2	Fragment of melt away from the lateral wall erosion area	UC <sub>2</sub> ; (Zr,U)(C,O,N) (0,476 nm); U <sub>0,9</sub> Zr <sub>0,1</sub> O <sub>2</sub> (0,545 nm)	(Zr,U) (C,O,N) (0,465;0,469 nm); UO <sub>2</sub>
S5.3	Fragment of melt more away from the lateral wall erosion area	U <sub>0,9</sub> Zr <sub>0,1</sub> O <sub>2</sub> ÷U <sub>0,6</sub> Zr <sub>0,4</sub> O <sub>2</sub> (0,544÷0,535 nm)	Zr(O,C)(0,465 nm); a-Zr(O)
S6.1	Upper ingot layer	a-Zr(O); UO <sub>2</sub> ; U <sub>0,2</sub> Zr <sub>0,8</sub> O <sub>2</sub> (0,522 nm)	Zr(O,C)(0,465 nm); U <sub>0,9</sub> Zr <sub>0,1</sub> O <sub>2</sub> (0,545 nm)
S6.2	Uranium dioxide pellets dissolution layer	UO <sub>2</sub> ; U <sub>0,85</sub> Zr <sub>0,15</sub> O <sub>2</sub> (0,543 nm)	a-Zr(O); U <sub>0,2</sub> Zr <sub>0,8</sub> O <sub>2</sub> (0,52 nm)
S6.3	Impregnation layer of powder zirconium dioxide with molten metal zirconium	a-Zr(O); U <sub>0,2</sub> Zr <sub>0,8</sub> O <sub>2</sub> (0,523 nm)	U <sub>0,85</sub> Zr <sub>0,15</sub> O <sub>2</sub> (0,543 nm); ZrO <sub>2</sub> <sup>mkl</sup> ; Zr(O,C)(0,465 nm)
S7	Fragment on the periphery of the lateral wall erosion area	U <sub>0,7</sub> Zr <sub>0,3</sub> O <sub>2</sub> ÷U <sub>0,4</sub> Zr <sub>0,6</sub> O <sub>2</sub> (0,538÷0,528 nm);	Zr(O,C)(0,467 nm); a-Zr(O)
S8	Fragment of melt on the ingot under the nozzle	U <sub>0,9</sub> Zr <sub>0,1</sub> O <sub>2</sub> (0,545 nm); (U,Zr)(C,O,N) (0,487 nm)	UC <sub>2</sub> ; (U,Zr)(C,O,N) (0,483 nm); (Zr,U)(C,O,N) (0,470 nm); Zr(O,C)(0,466 nm)

According to the X-ray phase analysis, the main components of phase composition of the solidified melt samples are oxide phases of variable composition (U,Zr)O<sub>2</sub> with FCC – uranium dioxide lattice, carbide phases of variable composition with FCC zirconium carbide lattice, the general formula of which may be represented in the form of (Zr,U)(C,O) and uranium dicarbide. Uranium dicarbide and oxycarbides with high contents of uranium being in the samples in the vicinity of nozzle erosion areas, are products of oxide burden components/graphite nozzle interaction.

Oxide solutions (U,Zr)O<sub>2</sub> are characteristic of the assembly material samples where partial or full melting of components is taken place. The common feature of this material is its melting without contact with nozzle graphite and carbide melt due to emission and thermal conductivity.



Metal zirconium ( $\alpha$ -Zr(O)) is present considerably only in the external samples regions (samples S4.2, S5.2) and in the basic melt ingot under the nozzle (samples S6. (2-5)). As a rule, presence of this phase shows low-level of melt carburizing before its solidification. On the contrary, presence of the variable content phase Zr(U)(C,O) with FCC - lattice of zirconium carbide indicates increased concentration of carbon in the melt. Particularly, presence of these phases is characteristic of the solidified melt material located in the vicinity of erosion damage of the external electrode nozzle surface. In most cases, propagation of carbon specified according to this character, is limited with the layer in the solidified melt structure where uranium dioxide pellets were dissolved.

In this sense, it should be noted that the melt under the nozzle has low-level carburization that is identified by the test of large content of phase  $\alpha$ -Zr(O). In consideration of a large scope of erosion damage of the nozzle it should be expected melt crystallization in more carbidization condition. The reasons of so low carbonization of the melt under the nozzle may be both the volume of metal zirconium placed in the course of loading near the nozzle walls, and the fact that carbonized melt produced in a great number during oxide melt/graphite nozzle interaction did not mostly penetrate in the melt area under the nozzle. A large amount of the carbide melt filled the space in the nozzle walls erosion areas (samples S1, S2, S5.1.1, S5.2), and on the ingot under the nozzle.

All phases specified by the method of X-ray phase analysis are identified on the investigated microstructures of ingot material under the nozzle. The ingot material infrastructure consists of the phase  $U_xZr_{1-x}O_2$  of grey color, light cellular phase emissions Zr(O,C) of gold yellow color and (often surrounding the latter) emissions of yellow-white metal phase  $\alpha$ -Zr(O), the existence of which is mainly found in the lower ingot. Micro-hardness data (by Vickers) of these structural components are 20 GPa, 8 GPa and 3,5 GPa respectively.

Microstructure of the material near maximum erosion of the lateral nozzle side is close to that observed in the upper ingot regions under the nozzle. However, here main structural components are oxide  $U_xZr_{1-x}O_2$  and oxycarbide Zr(O,C) phases, but their content and correlation are different in different regions and these regions have distinctive boundaries. Thus, in the melt regions located from the side of graphite erosion zone, the light cellular phase is perceptibly larger, and mainly golden yellow and pink colors is a sign of possible presence of dissolved nitrogen in its composition. There is essential difference of microstructure and phase composition in the regions of carbide melt, where microstructures typical for carbides ZrC, (U,Zr)(C,O),  $UC_2$  are observed. Regions of oxide and carbonized melt have, as a rule, a distinctive boundary. The boundary is often the fragments of initial zirconium carbide coating and that favors their chemical resistance to both melt types.

#### 2.2.8 Conclusion on phase analysis

The phase content of the samples is characterized with preferential presence of high temperature burden components interaction products in the course of heating.

The cause of the coating zone damage and graphite erosion in the lower nozzle part is considered as before a local overheating of the nozzle area located opposite narrow zone of arch burning. The origin of coating damage may be thermal stresses in heating or coating overheating. Further growth of the coating damage was taken place due to penetration of the carbonized melt in discontinuity flaws and hollow spaces under the melt. Both chemical dissolving of zirconium carbide in carbide melt and its mechanical detachment play an important role in these processes.

As a consequence of apparent absence of melt/plasmatrons nozzle contact, the mechanism of melt supply to the zone of erosion damage of coating and graphite is not clear completely so far. One of the options may be gradual bottom-up fusing of the melt along the assembly and its draining along the nozzle walls due to wetting.

The products of carbonization are mainly located near the erosion damage zones and upper ingot layers. Such location favors the assumption that graphite erosion leaked at the last stages

of heating and occurred mainly as far as material supply along the nozzle walls in the course of heating of the upper burden parts contacting with the nozzle.

2.2.9 Studying of a material microstructure of an ingot near to area of lateral surface erosion of a graphite nozzle of an external electrode.

Conditionally it is possible to divide a material of the sample observed on the micro-section, on oxide and carbide ones. Areas of oxide material (areas 11-18 in Figure A2.2.37) have a golden shade and are located in an ingot with external from graphite of its site. Carbide material (areas 1, 3, 4, 7-10, 19 in Figure A2.2.37) has grey color and settles down in an ingot from graphite and a thin layer on a graphite surface.

In the bottom part of the micro-section between oxide and carbide materials fragments of a coating from zirconium carbide (area 20 in Figure A2.2.37) are visible. In other cases between oxide and carbide ingot material exist more or less smooth transitive areas (areas 2, 5 in drawing Figure A2.2.37).

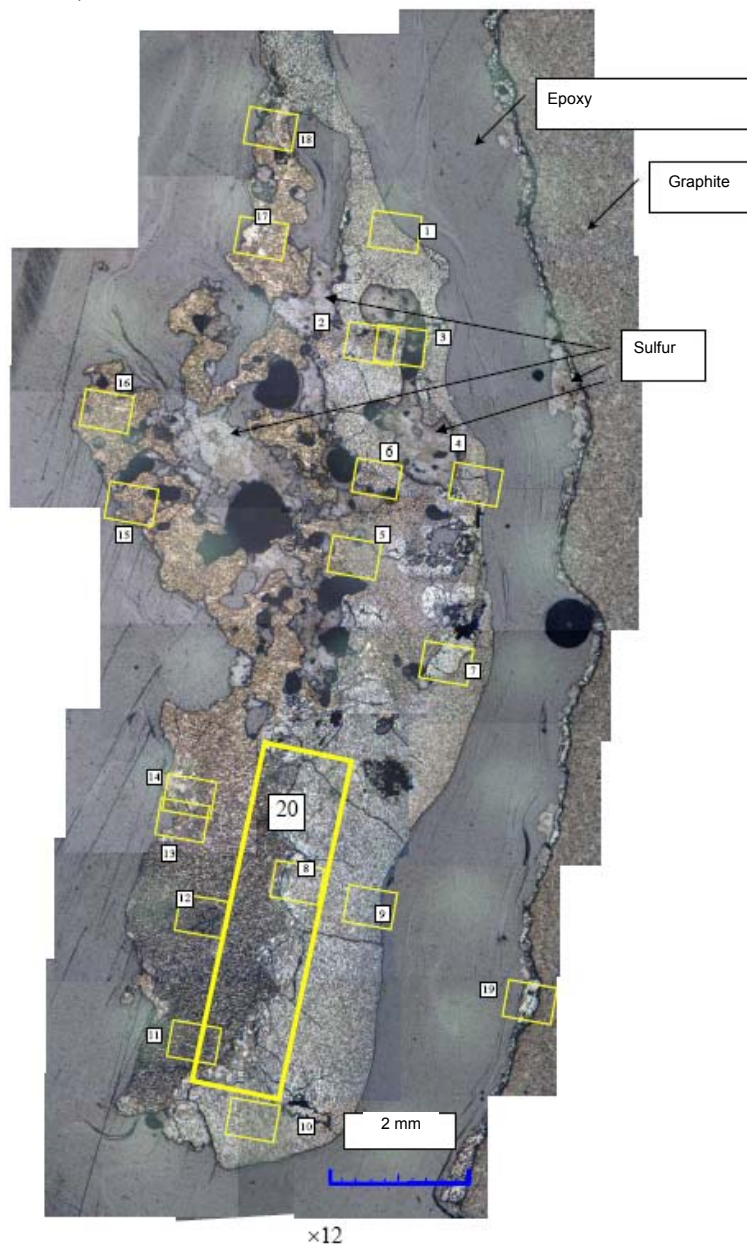


Figure A2.2.37 – Areas of microstructure research in ingot material

Photos of the microstructures observed on a micro-section surface are presented in Figure A2.2.38.



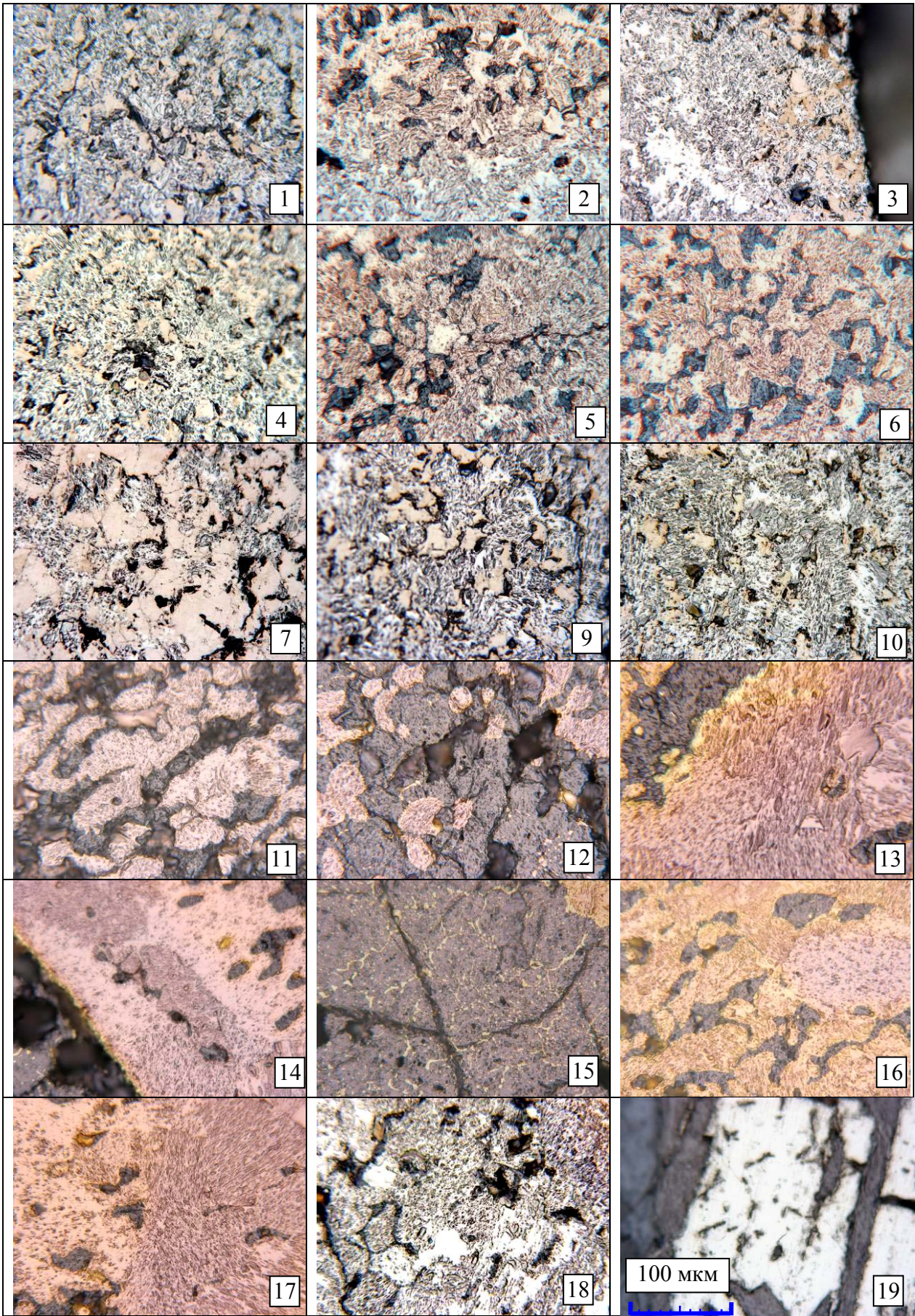



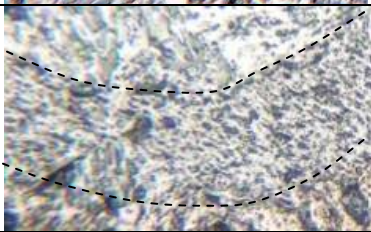


Figure A2.2.38 – Photos of microstructure on the surface of the micro-section



Microstructures of the carbide material of the melt (areas 1, 3, 4, 7-10, 19 in Figure A2.2.38) contain three basic structural components. It is a monotonous light making, lamellar light or grey component and monolithic light allocation of a beige shade. Presumably, being guided on given the phase analysis of samples of carbide material (samples S1, S2, S5.1.1, S5.2), and also on results of the micro-hardness measurement of these components (Table A2.2.7), light beige allocation are the precipitations of the uranium dicarbide  $UC_2$ , a monotonous light component represents solid solutions  $(U,Zr)(C,O,N)$  with structural type of uranium monocarbide and with its high maintenance, and lamellar allocation correspond to phases  $(Zr,U)(C,O,N)$  on the basis of zirconium carbide with a some quantity of the dissolved uranium carbide.

Table A2.2.7 - Characteristics of a microstructure of a carbide material

Structure component	View ( $\times 240$ )	Micro-hardness	Phase
Light beige allocation		$9,2\pm 0,5$ GPa	$UC_2$
Monotonous light one		$14\pm 2$ GPa	$(U, Zr)(C,O,N)$
Lamellar light or grey ones		$22\pm 2$ GPa	$(Zr, U)(C,O,N)$
In the field of a coating		$25\pm 1$ GPa	ZrC

The zirconium carbide coating has also the mixed microstructure. It is possible hardly to distinguish on a microstructure in contact zones of carbide melt with a coating. The basic difference is micro-hardness of a material of a coating and a little smaller sizes of the structural non-uniformities.

The microstructure of material in areas of oxide melt has the own basic features. Generally a material microstructure biphasic, consisting of the localized components of dark grey color and the light component changing a shade from colorless to pink and yellow (Figure A2.2.39). Change of shades of color of a light phase is the most good traced on border of their neighborhood (Figure A2.2.40). Also change of shades of a dark phase a little is less confidently fixed. The greatest quantity on an ingot of a light phase there is in the bottom part pinkish, and in the top part golden shades. The measured values of micro-hardness by Vickers make  $18\pm 2$  GPa,  $18\pm 3$  GPa,  $22\pm 2$  GPa for a light phase of golden, pink shades and colorless, accordingly.

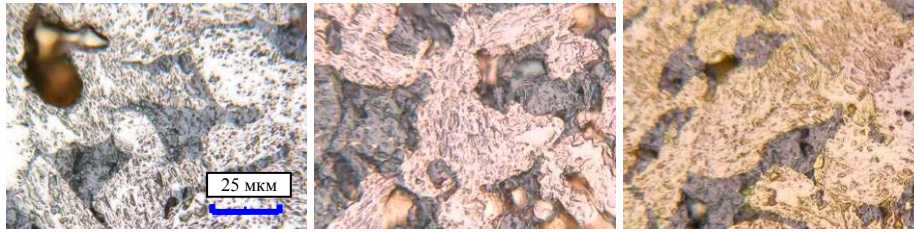


Figure A2.2.39 – Microstructure of the main part of the oxide melt ( $\times 360$ )

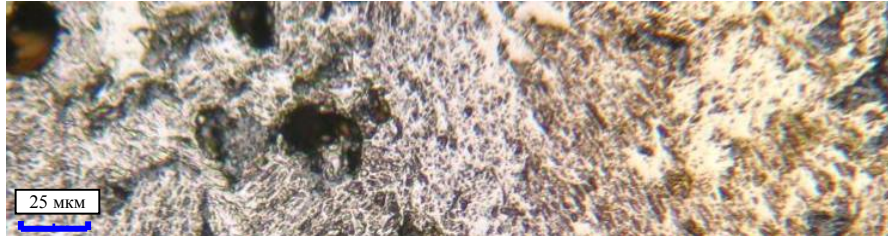


Figure A2.2.40 - Color shade change of a light phase in transitive zone between oxide and carbide melts ( $\times 360$ ) Dark making structure corresponds to a solid solution  $(U,Zr)O_2$ , on the basis of FCC- lattice of uranium dioxide. Then, resulting from phase analysis of samples S6.1 and S5.1.2 where this microstructure is observed, there corresponds to a light component a phase of variable structure  $(Zr,U) (O,C,N)$  with FCC - lattice of zirconium carbide. Presence of all elements entering into the phase formula quite reasonable also can be defining for development of this or that color shade. By experience of the previous experiments, presence of golden color of a surface of a coating connected, as a rule, with formation on a coating surface of a thin film of oxycarbide or nitro- oxycarbide of zirconium, and, naturally, has not been connected with presence of uranium atoms.

It was not possible to establish reliably the influence of a parity of oxygen, carbon and nitrogen on a color shade of this phase till now. Probably, the strongest golden coloring of a coating occurs at presence of nitrogen contained atmosphere, and the raised maintenance of carbon eliminates the coloring. Last assumption well proves to be true by consideration of change of coloring of a coating from contact with the oxide melt. It is characteristic also, that on borders of the local precipitations of a light phase of a pink shade of thin ( $\sim 2\div 5$  a micron) interface has a golden shade. Fine dispersed precipitations as well of a light phase in massive formations dark area have golden shade (area 15 in Figure A2.2.38). In this sense consideration of the massive precipitations in the light phase on ingot borders (area 13, 14, 17 Figures A2.2.38 and A2.2.41) became interesting. Generally, the golden shade of a light phase corresponds to the external border of an ingot most contacting to atmosphere and (or) with massive formations of a dark phase. Micro-hardness of a material of a light phase in large precipitations make  $21,9\pm 1,3$  GPa and  $19\pm 2$  GPa for a light phase of pink and golden shades accordingly.

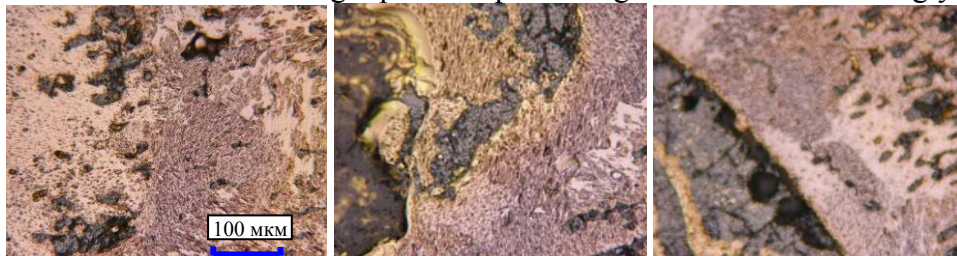


Figure A2.2.41 - Microstructure of material in a zone of massive congestions of a light phase ( $\times 180$ )

Some uncertainty of an identification result of observable phases is brought by that under the description of some authors, with a yellowish shade and lamellar structure the phase of a solid solution  $(Zr,U)O_2$  with FCT - lattice of zirconium dioxide looks light also. If in the main material of an ingot the phase structure is defined reliably, and it can compare specific structural composition in local areas on the edges of an ingot where, basically, and massive



congestions of a light phase are observed, it is difficult to guarantee phase structure. The micro-section area containing a coating fragment (area 20 in Figure A2.2.42) was exposed to separate consideration. In this area oxide and carbide melts are divided by a coating material. The coat layer is allocated on the increased image of this area structurally against both oxide and carbide melts, that shows on its structural integrity and stability to influence of both types of the melts. Appreciable infringements of a coating are visible in the areas of a coating which were settling down in deepening of a screw on a graphite nozzle. Considerable is a thickening of structurally different layer in the bottom part of a coating fragment. The last one can testify as to heterogeneity of a thickness of a coating just after its application, and its changes in experiment process.

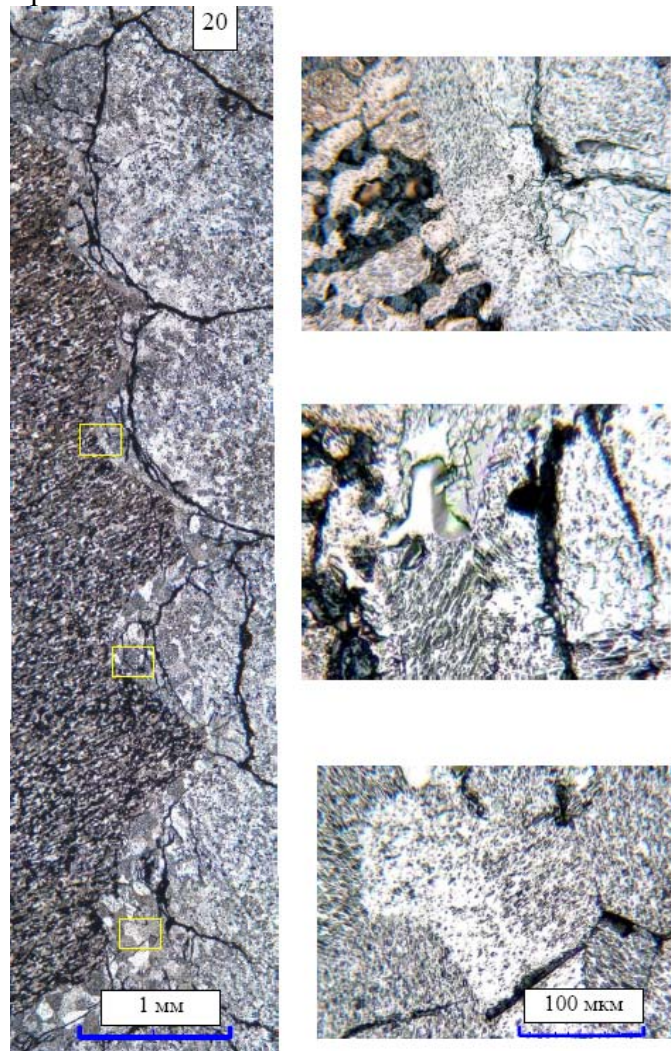


Figure A2.2.42 – Micro-section area contains the coating fragment

2.2.10 Studying of a material microstructure of an ingot under graphite nozzle of an external electrode

*The short characteristic of a micro-section material*

It is possible to display (Figure A2.2.43) two large areas of a homogeneous material.



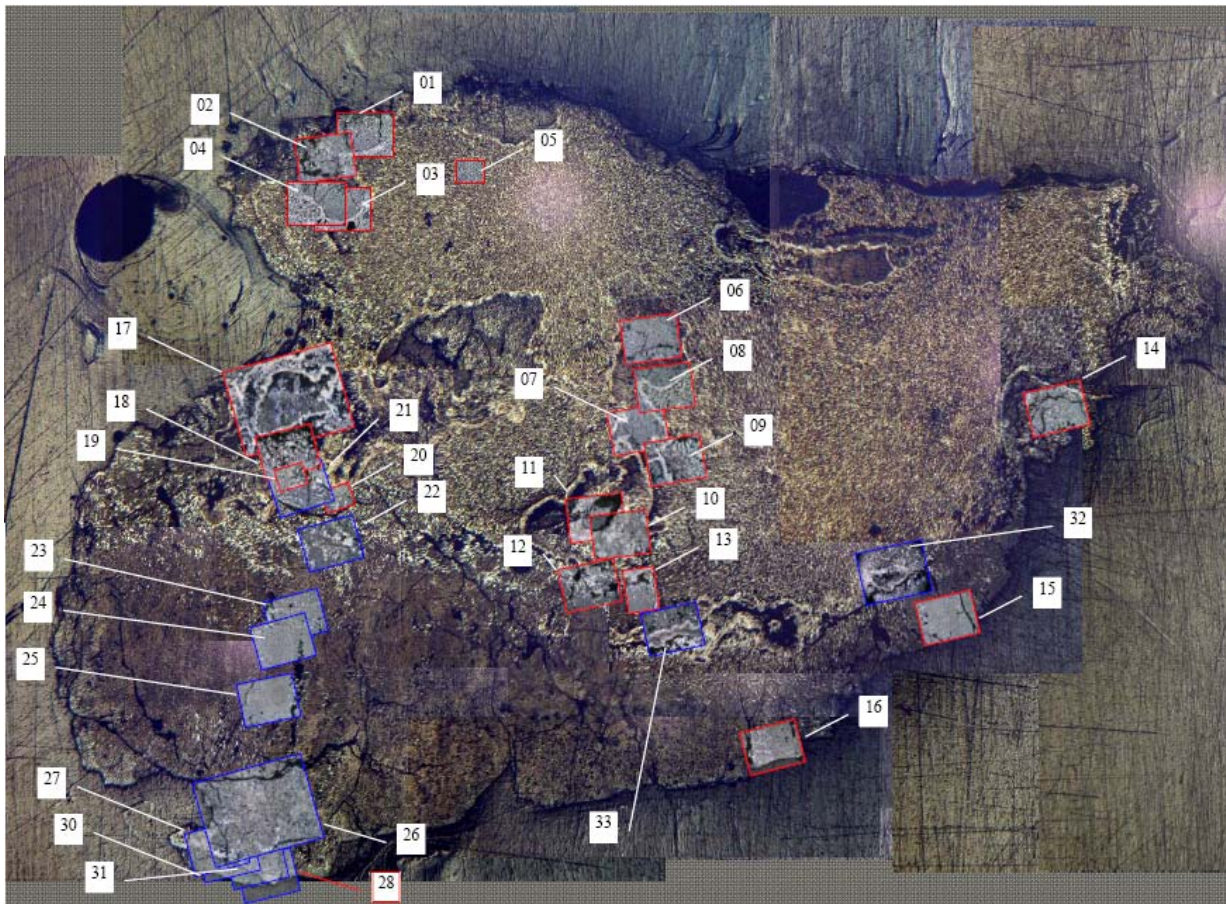


Figure A2.2.43 – Ingot section under the outer nozzle of plasmatrons

The first area occupies the top part of the cross-section, has granular structure and looks lighter and has a reddish shade. The large localized inclusions in the basic material of this area having structure distinct from the main material and, as a rule, separated from it sharp light border. Characteristic microstructures of a material of the top area of the cross-section are presented in Figure A2.2.44.

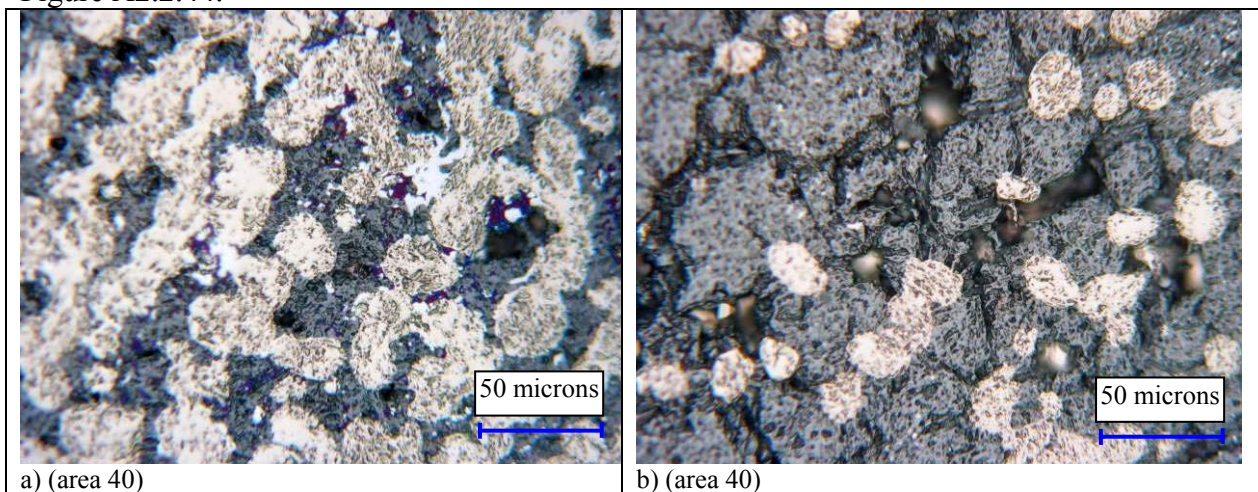


Figure A2.2.44 – Micro-structure of material in the top part of ingot under the nozzle: a) – in the top area (area 5 in Figure A2.2.43); b) – in the bottom area (area 9 in Figure A2.2.43)

It is possible to assign three basic structural components in a microstructure of this material:

- folded allocation of a light phase with golden or pinkish the shades, having the roundish form and the characteristic cross-section sizes about 20 microns;
- the dark folded matrix material of grey color filling space between allocations of a light phase;



- monolithic allocation white, presumably, the metal phase, located in the form of small impregnations in a grey phase, or on borders between light and dark basic structural components. Often, sites of these allocations, or adjoining to them allocations of one more metal phase are covered by the oxide film giving to them sharp color coloring of dark blue, violet or red tones.

Solid solution  $(U,Zr)O_2$ , on the basis of FCC - lattices of dioxide of uranium corresponds to the dark making structure. Then, proceeding from results of the phase analysis of samples S6.1 where such microstructure is observed, to a light component with folded structure there corresponds a phase of variable structure  $(Zr,U)(O,C,N)$  with FCC - lattice of zirconium carbide, and monolithic allocation a metal phase - a phase metal  $\alpha$  - zirconium, stabilized by oxygen  $\alpha$ -Zr(O). Results of the phase analysis specify also in possible presence of metal  $\alpha$ -U. In this case formation of oxide films can quite occur on a allocation surface of metal uranium. Second more dark area with a brownish shade, occupies the bottom part cross-section and has more monolithic structure consisting of large monolithic blocks divided by macro-cracks. Characteristic microstructures of a material of the bottom area cross-section are presented in Figure A2.2.45.

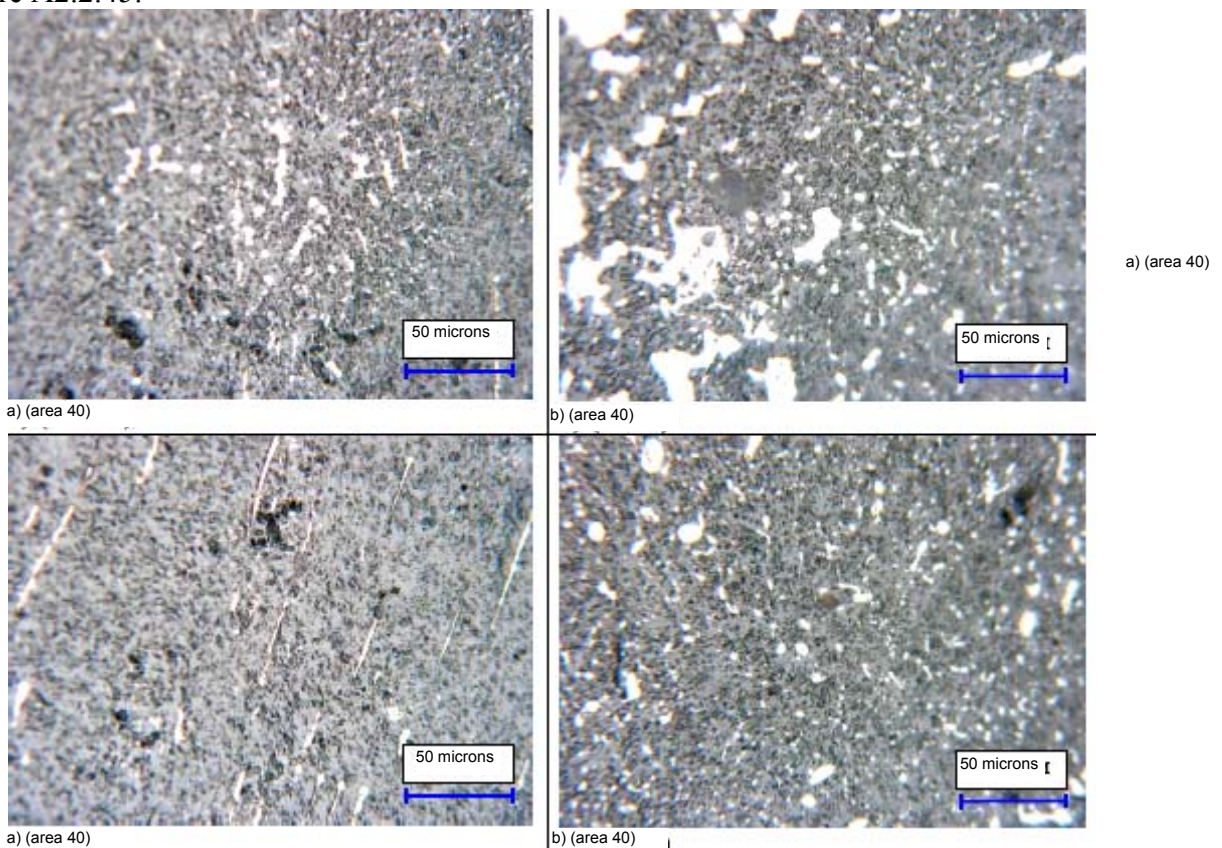


Figure A2.2.45 - Micro-structure of material in the top part of ingot under the nozzle: a) – in the top part (area 5 in Figure A2.2.43), b) – in the bottom part (area 9 in Figure A2.2.43)

It is possible to allocate three basic structural components in a microstructure of this material:

- a dark folded matrix material of grey color;
- monolithic allocation white, presumably, the metal phase, located in the form of small impregnations in a grey phase.

Dark making structure there corresponds a solid solution  $(U,Zr)O_2$ , on the basis of FCC - lattices of uranium dioxide, and monolithic segregations of metal phase - a phase of metal  $\alpha$ -zirconium, stabilized by oxygen  $\alpha$ -Zr(O).

At the bottom part of the cross-section there is a fragment not melted pellet of uranium dioxide, surrounded with solidified melt, different from the structure of the basic material of the bottom area of an ingot. The basic difference of a material around of the pellet of uranium dioxide is

solidity of its structure (absence of folders). It is possible to allocate in Figure A2.2.46 the areas of a monolithic dark phase, outwardly almost a distinguishable from a material of pellet, and the areas of more light material having eutectics structure. The areas containing eutectics have yellowish coloring. Presumably, areas of more light material can correspond to a solid solution  $(Zr,U)O_2$  with the high maintenance of zirconium dioxide, found out in phase composition of the sample from this area (sample S6.2).

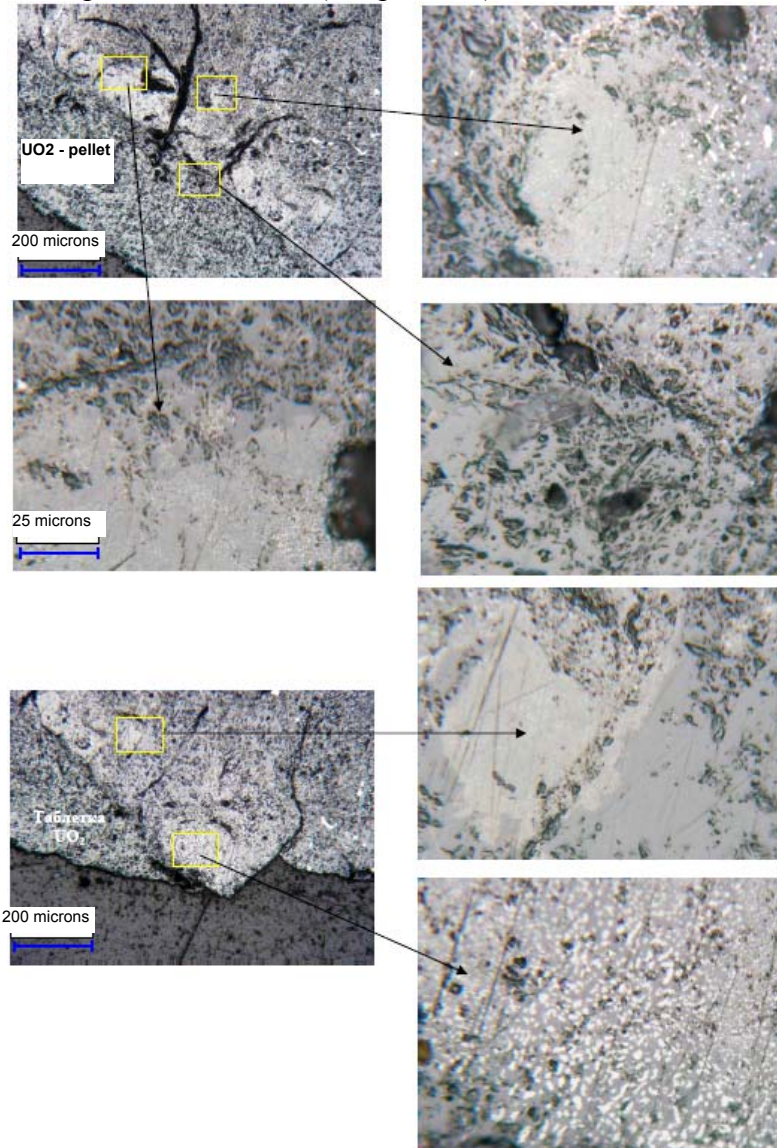


Figure A2.2.46 – Microstructures on the boundary of the melt and non-melted pellet of uranium dioxide  
 Between the basic areas exists more or less strongly pronounced zone of a transitive material where peculiar structural components of the basic types of the melts co-exist in common. It is not possible to spend the assure border between them.  
 In the top part of an ingot as it was specified earlier, in the basic material of this area there are the large localized inclusions having structure distinct from the basic material, and, as a rule, separated from it with accurate light border. Microstructures of material in these inclusions are different (Figure A2.2.47). Their general feature is absence of a color shade of light making oxycarbide component of a microstructure and presence of the sharp border separating them from the basic material of an ingot. These factors show the raised maintenance of carbon in these local formations.



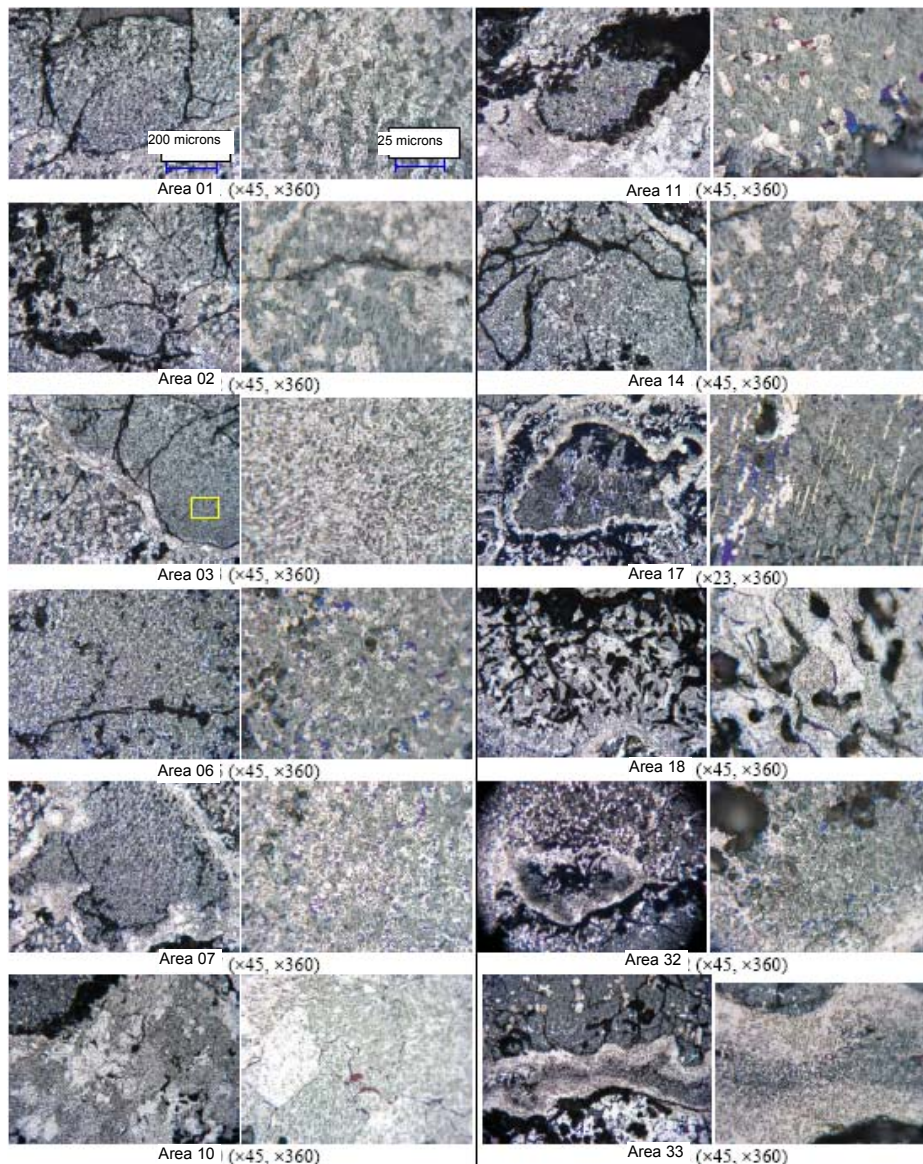


Figure A2.2.47 – Microstructures of inclusions material in the main material of the top part of ingot

### 2.2.11 Conclusion

The phase composition of samples is characterized by the primary maintenance of products of high-temperature interaction of loading components among themselves in the course of heating. It is necessary to consider as the reason of damage zone of a coating and graphite erosion in the bottom area of a nozzle still local overheat of this area of the nozzle located opposite to a narrow zone of arc burning. Thermal stress at heating or a coating overheat could become an original cause of infringement of a coating. The further growth of coating destruction followed from the penetration of carbided melt in discontinuity flaws and emptiness under it. The important role in these processes plays both chemical dissolution of zirconium carbide in carbide melt and its mechanical separation.

In connection with visible absence of contact of the melt with a plasmatrons nozzle, the movement of the melt in a zone of erosive damage of a coating and graphite is not clear while. One of variants can be gradual infusion of the burden from below upwards on assemblage and its running off on walls of a nozzle due to wetting.

Carbiding products are located mainly near to zones of erosive damages and the top layer of an ingot. Such their arrangement allows to assume that graphite erosion proceeded up to last stages of heating and occurred basically in process of material coming on walls of a nozzle in the course of warming up of the top layers of the loading contacting to a nozzle.



### 3 Research after large-scale calibrating tests performed within 2<sup>nd</sup> year

#### 3.1 Research after TOP-4 test

Dismantling of experimental cell has been done after experiment performance.

It was found out during dismantling (Figure A2.3.1), that full melting of the loaded materials has not occurred. The material in the top part of assemblage, as well as in the previous experiments, has appeared not melted and has been removed from assemblage. Further not fused centering zirconium ring and a part of a friable burden material have been removed. Graphite nozzle with melted off and caked with not melted a loading material remained in a metal vessel after removal of the top part of material. The remained conglomerate was not taken out freely from the metal container. In this connection, it has been decided to make the cutting of experimental cell without removal of a nozzle with the material attached to it from the metal container.

Experimental cell has been cut by an abrasive disk in diametrical section. Assemblage has been filled in with molten sulfurs for material fixing before cell cutting.

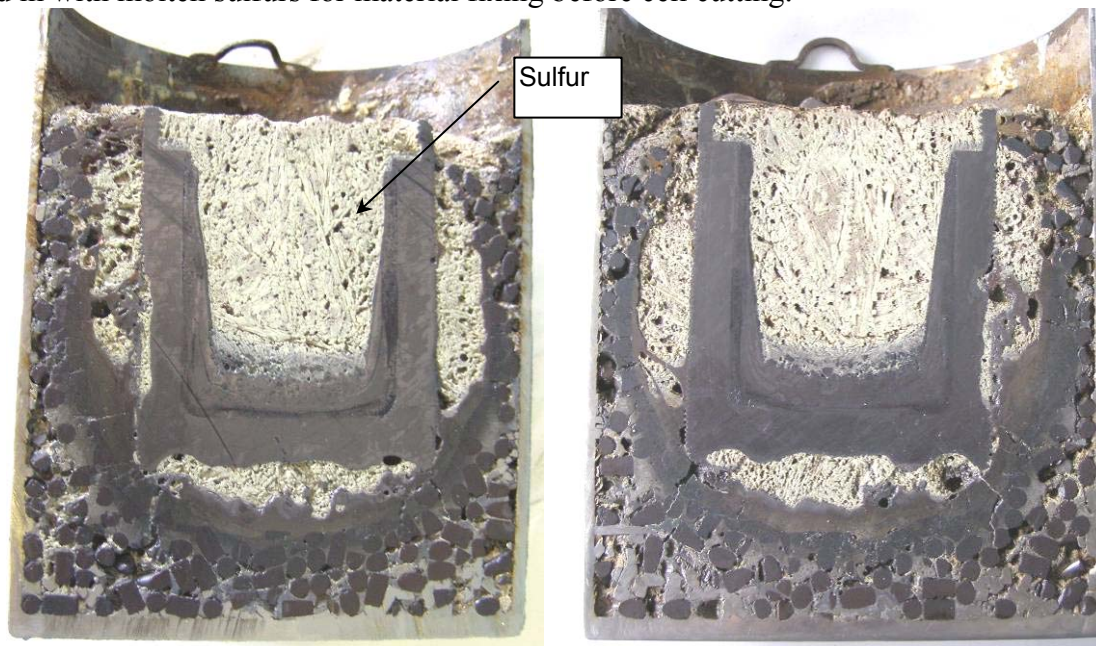


Figure A2.3.1 – Appearance of cutting plane of the experimental cell after TOP-4 test

It is possible to draw the following conclusions by results of observation of a cut of assemblage:

- 1) The part of a loading material near to a tip was melted and solidified having formed a crust of solidified melt around a nozzle. The solidified melt material generally, has no contact to a plasmatrons nozzle. Outside of a crust fragments of uranium dioxide pellets surrounded with melt or caked powder of zirconium dioxide are observed. Such picture is traced on all section of assemblage.
- 2) The lateral surface of a nozzle from one of the parties practically has not exposed to erosion by the melt. The nozzle surface in these areas is covered by a crust of a material of golden color. On the other site of a nozzle in the bottom part considerable erosive damages of graphite walls are visible. Depth of erosive damages here makes nearby 3 ... 5 mm. The coating in this area is completely destroyed, and there are at vicinities the solidified products of interaction of graphite with the melt (Figure A2.3.2).

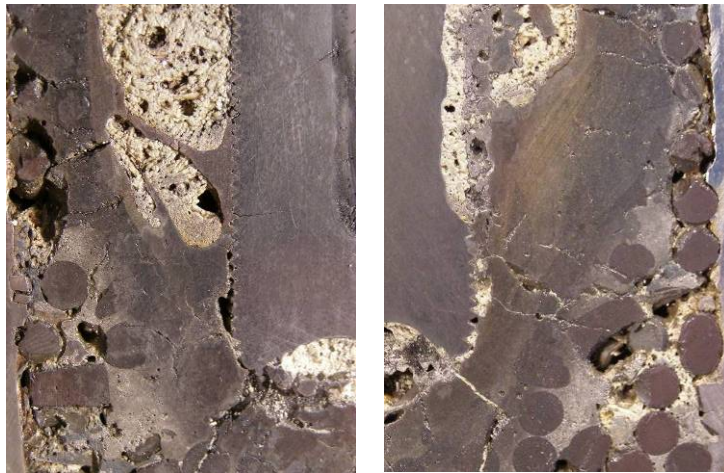


Figure A2.3.2 – State of the lateral surfaces of an electrode nozzle

The bottom part of a plasmatrons nozzle also has exposed to considerable erosion from the site of the prototypic corium melt. Between eroded surface of a nozzle and a surface of the melt the simulator the cavity was formed. Interaction products of the melt with graphite are concentrated in a crust layer of the melt and have the sharp border with other part of the melt (Figure A2.3.3).

The melt crust on all section of assemblage has the characteristic layered structure corresponding to various stages of interaction of corium components at various degree of thermal and temperature influence of a plasmatrons nozzle. The inside layer has brown color and corresponds to completely melting of loading components. Darker layer of a melt crust with partially dissolved fragments of uranium dioxide pellets further settles down. This layer corresponds to a stage of dissolution of a material of uranium dioxide pellets on border with liquid melt. The following conditional layer of a material consists of rather whole pellets of uranium dioxide, dipped in a matrix from a light material in which breaks metal inclusions are visible. This layer corresponds to process of impregnation of dioxide zirconium powder by the molten metal zirconium of loading and them eutectics interaction. Last layer of a material contains uranium dioxide pellets, dense caked material of zirconium dioxide and not melted off fragments of metal zirconium. This layer corresponds to a stage of sintering of burden materials when the melting temperature of its most low-melt components is not reached yet.

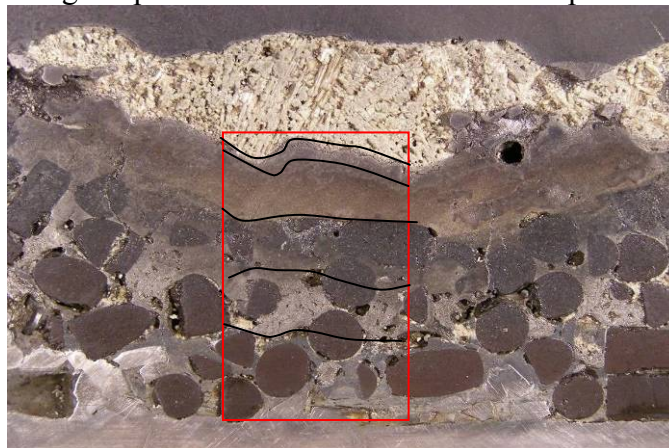


Figure A2.3.3 - State of the frontal surface of an electrode nozzle

For definition of phase composition of a melt material, obtained in this experiment, the melt samples, solidified on plasmatrons details, samples of a coating of a samples material from various areas of assemblage have been selected. Research of phase composition was performed by a method of the X-ray phase analysis on powder samples. Micro-sections for metallographic analysis have been prepared from a number of melt fragments. A designation of samples, places of their selection are presented in Table A2.3.1 and in Figure A2.3.4.



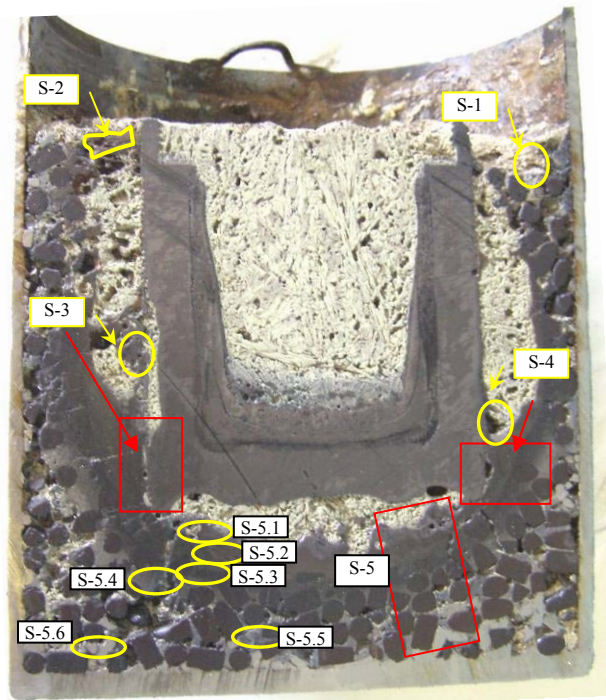


Figure A2.3.4 – Places of melt sampling

Table A2.3.1 – Samples for analysis

Sample	Shape of sample and place of selection	Micro-section	Phase analysis
S1	Fragment of light caked material in the top part of assemblage	-	+
S2	Melt fragment a golden shade near to a nozzle in the top part of assemblage	-	+
S3	Fragments of a material near to a zone of nozzle lateral wall erosion	+	+
S4	Material fragments of close not damaged lateral wall in the bottom part of a nozzle	+	+
S5.1	Top layer (carbide one)	+	+
S5.2	Layer of homogeneous melt		+
S5.3	Layer of uranium dioxide pellets dissolution		+
S5.4	Layer of impregnation of zirconium dioxide powder by molten metal zirconium		+
S5.5	Caked dark material of zirconium dioxide		+
S5.6	Caked light material of zirconium dioxide		+
S6	Melted off pellet of uranium dioxide	+	+

The phase analysis was performed with the methods of X-ray diffractometry of polycrystals on powder samples prepared from the material sampled for investigation. X-ray was carried out on the diffractometer DRON-3 with Bragg-Brentano focus in copper  $K\alpha$  emission. The resulted diffractograms were analyzed as per the method of qualitative phase analysis using the crystallographic data library and special methods for identification of phases, variable composition.

The basic components of phase composition of the majority of samples of solidified melt by results of the X-ray phase analysis are solid solutions of type  $(U,Zr)O_2$  with FCC - lattice of uranium dioxide and a phase of the variable composition which general formula like  $Zr(U)(C,O,N)$ .

Results of an estimation of oxide phase compositions are reflected in Table A2.3.2 near to values of the lattice period. Measured values of the lattice periods  $a_0$  oxide and oxycarbide phases and their approximate componential composition are resulted in the Table A2.3.2. The sequence of phases in Table cells corresponds to reduction of their volume maintenance in samples.

Table A2.3.2 The results of qualitative analysis of phase samples content

Sample	Main phases	Other phases	Shape and place of sample
S1	UO <sub>2</sub> ; U <sub>0.75</sub> Zr <sub>0.25</sub> O <sub>2</sub> (0,539 nm);	U <sub>0.6</sub> Zr <sub>0.4</sub> O <sub>2</sub> (0,534 nm); ZrO <sub>2</sub> <sup>tetr</sup> ; Zr(N,O,C) (0,459 nm);	Material of flowed pellet in the top part of assemblage
S2	Zr(C,O)(0,466 nm) ZrO <sub>2</sub> <sup>tetr</sup>	ZrO <sub>2</sub> <sup>monocl</sup> ; U <sub>0.4</sub> Zr <sub>0.6</sub> O <sub>2</sub> (0,527 nm); UO <sub>2</sub>	Melt fragment a golden shade near to a nozzle in the top part of cell
S3	UO <sub>2</sub> ; (U,Zr)(O,C,N) (0,492±0,474 nm);	UC <sub>2</sub> ; Zr (C,O,N) ( 0,469; 0,466 nm); U <sub>0.6</sub> Zr <sub>0.4</sub> O <sub>2</sub> (0,534 nm)	Material fragments near to a zone of lateral wall erosion
S4	Zr(C,O)(0,466 nm) ZrO <sub>2</sub> <sup>tetr</sup>	ZrO <sub>2</sub> <sup>monocl</sup> ; U <sub>0.4</sub> Zr <sub>0.6</sub> O <sub>2</sub> (0,527 nm); UO <sub>2</sub>	Material fragments of close not damaged lateral wall in the bottom part of a nozzle
S5.1	U(Zr)(C,O,N) (0,489–0,481 nm);	U <sub>0.8</sub> Zr <sub>0.2</sub> O <sub>2</sub> (0,542 nm); UO <sub>2</sub> ; Zr (C,O,N) ( 0,466; 0,463 nm);	Ingot fragments from the bottom part of the cell
S5.2	U <sub>0.8</sub> Zr <sub>0.2</sub> O <sub>2</sub> (0,542 nm); α-Zr(O)	UO <sub>2</sub> ; U <sub>0.4</sub> Zr <sub>0.6</sub> O <sub>2</sub> (0,527 nm); Zr(O,C)(0,464 nm)	
S5.3	UO <sub>2</sub> ; U <sub>0.9</sub> Zr <sub>0.2</sub> O <sub>2</sub> ÷ U <sub>0.4</sub> Zr <sub>0.6</sub> O <sub>2</sub> (0,542 ÷ 0,527 nm)	α-Zr(O); Zr(O,C)(0,464 nm)	
S5.4	α-Zr(O);	U <sub>0.4</sub> Zr <sub>0.6</sub> O <sub>2</sub> (0,527 nm); ZrO <sub>2</sub> <sup>MKL</sup> ; U <sub>0.8</sub> Zr <sub>0.2</sub> O <sub>2</sub> (0,542 nm);	
S5.5	α-Zr(O); ZrO <sub>2</sub> <sup>monocl</sup>	Sulfur	
S5.6	ZrO <sub>2</sub> <sup>monocl</sup>	Sulfur	

As it was marked above, the basic phases characteristic for assemblage areas where there was a melting of loaded material during experiment are ceramic oxide phase type (U,Zr)O<sub>2</sub> with FCC - lattice of uranium dioxide and conditional oxycarbide phase (Zr<sub>x</sub>U<sub>1-x</sub>)(O, C, N)<sub>1-y</sub> with FCC - lattice of zirconium carbide.

In a material of ingot layers the structure of oxide phases varies from phases of initial uranium and zirconium dioxides to solid solutions with approximate composition U<sub>~0.6</sub>Zr<sub>~0.4</sub>O<sub>2</sub>. The similar dispersion of compositions of a solid solution corresponds to various degree of completeness of interaction processes of burden components as of removal from a plasmatron nozzle. The most homogeneous composition of a solid solution is found in sample S-5.2 from the top part of an ingot under a nozzle. In a layer corresponding to sample S-5.3 phase composition is presented basically by uranium dioxide and solid solutions of replacement (U,Zr)O<sub>2</sub> with the high maintenance of uranium atoms. The basic phase in layer S-5.4 is the phase of metal zirconium α-Zr(O) with the high maintenance of the oxygen caused by interaction of molten metal zirconium with zirconium dioxide powder. The phase composition of material samples from layers S-5.5 and S-5.6 is practically identical and corresponds to initial phase composition of loading.

Metal zirconium (α-Zr(O)) presents at significant amounts in all layers on of the melted material (samples S5.2-S5.6), except for internal carbide layer, where crystallization of free zirconium has occurred to formation of oxycarbide phases (Zr<sub>x</sub>U<sub>1-x</sub>)(O,C,N)<sub>1-y</sub>. This circumstance is feature of phase composition of experiment products in carbon contained environment and can serve as criterion of an estimation of degree of melt carbonization in the course of experiment., It is possible to specify following this criterion in the concentrated maintenance of carbon in carbide layer of solidified melt under a nozzle and its small penetration into following layers.

Uranium bicarbide and oxycarbides with the high maintenance of the uranium, present in samples near to zones of erosive damage of a nozzle are interaction products of oxide burden components with graphite of nozzle (samples S-3, S-5.1). Attracts attention the fact of almost full absence of uranium bicarbide in carbonized layer of an ingot material under a nozzle. The

basic phase here is solid solution  $U(Zr)(O,C,N)$  with FCC - lattice and the high maintenance of atoms of uranium. The similar phase composition of products testifies about not to full degree of melt carbonization that can be a consequence of effect of ablation mechanisms of melt substance from an interaction zone due to gases formation. Formation uranium bicarbide is characteristic for areas near to plasmatrons where ablation of products of primary carbonization of the melt has for whatever reasons appeared inconvenient.

The basic phases in a crust material on undamaged electrode walls are phases characteristic for a layer 5.2 of ingot and the zirconium carbide which is a material of a coating.

### Conclusions

The phase composition of samples corresponds to various degree of completeness of interaction processes of loading components under the influence of high-temperature heating. Interaction products are located on levels according to the intensity of heating decreasing to peripheral areas of assemblage. Carbide phases are localized near the zones of erosive damage of a nozzle, and their distribution to other part of the melt is not considerable.

### 3.2 Researches after TOP-5 test

In experiment TOP-5, as well as in the previous experiments of a series of TOP was tested plasmatrons in contact with loading of prototype corium (C-30). The coating from zirconium carbide has been put on a graphite nozzle of plasmatrons in order to avoid interaction of graphite with a corium. The experiment purposes were obtaining the melt of prototypic corium and check of protective properties of a coating from zirconium carbide in contact with the melt. In the report the description of state of experimental cell after experiment and results of the phase analysis of coating fragments, solidified melt of prototypic corium and products of their interaction is resulted.

It was found during dismantling of the experimental cell that full melting of corium components has not occurred (Figure A2.3.5). The material part in the top of assemblage, as well as in the previous experiments has appeared not melted.

Fragments of the centering zirconium ring and a part of friable burden material have been easily removed from assemblage. The remained conglomerate did not manage to be taken out freely from the metal container. It has been decided in this connection to make the cutting of experimental assemblage not taking a nozzle with an ingot from the metal container.



Figure A2.3.5 – Non melted part of loading in the top of the experimental cell  
Experimental cell has been cut by an abrasive disk in diametrical section, for material fixing before cutting the assemblage has been filled in with molten sulfurs (Figure A2.3.6).





Figure A2.3.6 – Section plane of the experimental cell after test

The melted part of loading has hardened around of nozzle having formed a crust. The solidified melt material generally, has no contact to a plasmatrons nozzle. On total section of assemblage outside of a melt crust fragments of uranium dioxide pellets surrounded by the melt or caked powder of zirconium dioxide are observed.

The lateral surface of a nozzle from different directions has exposed to erosion by the melt. Depth of erosive damages has made 3÷10 mm. The coating was completely destroyed.

The crust of the melt on a lateral surface of a nozzle has the layered structure corresponding to different stages of interaction of corium components among themselves at various degree of thermal influence. The inside layer has brown color and corresponds to completely melted of burden components. Darker layer of a crust with partially dissolved fragments of uranium dioxide pellets further settles down. The following conditional layer of a material consists of rather integral pellets of uranium dioxide dipped in a matrix from a light material in which breaks metal inclusions are visible. This layer corresponds to process of impregnation of zirconium dioxide powder by the molten metal zirconium and their eutectics interaction. Last layer of a material contains pellets of uranium dioxide dense caked with a material of zirconium dioxide and not melted off fragments of metal zirconium. This layer corresponds to a stage of sintering of burden materials when the melting temperature of its most low-melt components is not reached yet.

The structure of ingot layers in the bottom part of assemblage has essential feature. Here the main part of an observable layer of the solidified melt up to border with area of dissolution of pellets of uranium dioxide is made by interaction products of the melt with graphite. Transitive area, as a rule, is narrow.

For definition of phase structure of a ingot material obtained in this experiment, samples of the melt hardened on plasmatrons details, samples of a coating and samples of a material from various areas of assemblage have been selected. Research of phase composition was done by a method of the X-ray phase analysis on powder samples. From a number of ingot fragments have been prepared micro-sections for metallographic researches. A designation of samples, places of their selection are presented in Table A2.3.3 and in Figure A2.3.7.

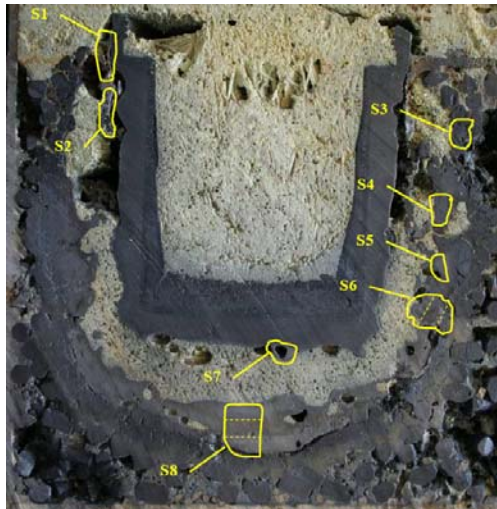


Figure A2.3.7 – Areas for ingot sampling

The phase analysis was performed with the methods of X-ray diffractometry of polycrystals on powder samples prepared from the material sampled for investigation. X-ray was carried out on the diffractometer DRON-3 with Bragg-Brentano focus in copper  $K\alpha$  emission. The resulted diffractograms were analyzed as per the method of qualitative phase analysis using the crystallographic data library and special methods for identification of phases, variable composition.

Table A2.3.3 – Results of qualitative phase analysis

Sample	Main phases	Other phases	Shape and place of sample
S1	Zr(O,C)(0,463 nm); U <sub>0,2</sub> Zr <sub>0,8</sub> O <sub>2</sub> (0,525 nm);	UO <sub>2</sub> ; (U,Zr)(O,C,N) (0,492÷0,474 nm); Zr (C,O,N) ( 0,469; 0,466 nm);	Ingot fragment a golden shade near to a nozzle in the top of cell
S2	U(Zr)(C,O,N) (0,489–0,481 nm);	UC <sub>2</sub> ; (Zr,U)(O,C,N) (0,468÷0,471 nm); UO <sub>2</sub> ÷U <sub>0,6</sub> Zr <sub>0,4</sub> O <sub>2</sub> (0,534 nm);	Material fragments near to a zone of erosion of a lateral wall of nozzle
S3	UO <sub>2</sub> ; $\alpha$ -Zr(O)	ZrO <sub>2</sub> <sup>mcl</sup> ; U <sub>0,75</sub> Zr <sub>0,25</sub> O <sub>2</sub> (0,539 nm)	Material fragments near to a wall of a steel vessel
S4	U <sub>0,75</sub> Zr <sub>0,25</sub> O <sub>2</sub> (0,539 nm) Zr(C,O)(0,468 nm)	UO <sub>2</sub> ; U <sub>0,6</sub> Zr <sub>0,4</sub> O <sub>2</sub> (0,535 nm)	Fragment of homogeneous melt dark brown color
S-5	UO <sub>2</sub> ÷U <sub>0,85</sub> Zr <sub>0,15</sub> O <sub>2</sub> (0,544 nm) Zr(C,O)(0,469 nm)	(U,Zr)(O,C,N) (0,48÷0,47 nm); U <sub>0,6</sub> Zr <sub>0,4</sub> O <sub>2</sub> (0,535 nm)	Fragment of homogeneous melt dark brown color
S6.1	U(Zr)(C,O,N) (0,489–0,481 nm);	UC <sub>2</sub> ; U <sub>0,8</sub> Zr <sub>0,2</sub> O <sub>2</sub> (0,542 nm); UO <sub>2</sub> ; Zr (C,O,N) ( 0,47 nm);	Layer of an ingot at a lateral near to a nozzle surface
S6.2	UO <sub>2</sub> ÷U <sub>0,6</sub> Zr <sub>0,4</sub> O <sub>2</sub> (0,535 nm)	(U,Zr)(O,C,N) (0,48÷0,47 nm); Zr (C,O,N) ( 0,467 nm)	Middle of an ingot at a lateral surface
S6.3	U <sub>0,6</sub> Zr <sub>0,4</sub> O <sub>2</sub> (0,535 nm); U <sub>0,3</sub> Zr <sub>0,7</sub> O <sub>2</sub> (0,526 nm);	U(Zr)(C,O,N) (0,495–0,475 nm); Zr(O,C)(0,467 nm)	Outer layer of an ingot at a lateral surface
S7	C, UC <sub>2</sub>	(U,Zr)(C,O,N) (0,495÷0,475 nm)	Melt drop on the nozzle
S8.1	(U,Zr)(C,O,N) (0,476÷0,480 nm); UC <sub>2</sub>	U(Zr)(C,O,N) (0,480–0,475 nm);	Upper layer of an ingot under nozzle
S8.2	UC <sub>2</sub> ; (U,Zr)(C,O,N) (0,476÷0,480 nm)	UC	Middle layer of an ingot under nozzle
S8.3	UC <sub>2</sub> ; (U,Zr)(C,O,N) (0,478÷0,484 nm)	UC; Zr(O,C)(0,466 nm)	Bottom layer of an ingot under nozzle on the boundary with dissolution zone

Also in the Table rough compositions of oxide and oxycarbide phases are reflected, the measured values of the lattice period  $a_0$  and their approximate compositional composition are resulted. The sequence of phases in Table cells corresponds to reduction of their volume maintenance in samples.

The basic components of phase structure of the majority of samples of solidified melt by results of the X-ray phase analysis, are oxides  $(U,Zr)O_2$  with FCC - lattice of uranium dioxide, carbide phases of the variable compositions, which general formula is approximately:  $Zr(U)(C,O,N)$  and bicarbide of uranium.

The main phases, characteristic for an ingot areas where there was a burden material melted during experiment, are ceramic oxide type phase  $(U,Zr)O_2$  with FCC - lattice of uranium dioxide and conditional oxycarbide phase  $(Zr_xU_{1-x})(O,C,N)_{1-y}$  with FCC - lattice of zirconium carbide.

The main feature of phase compositions of a material of this experiment is the maintenance of carbonization products of burden components. Uranium bicarbide and oxycarbides with the high maintenance of the uranium present in samples near to zones of erosive damage of a nozzle are interaction products of oxide components of corium with graphite of nozzle (samples S2, S6.1, S7, S8. (1-3)). It should be noted the considerable maintenance of uranium bicarbide in carbonized layer of an ingot material under a nozzle. The basic phase here is solid solution  $U(Zr)(O,C,N)$  with FCC - lattice and the high maintenance of uranium atoms. The similar phase compositions of products show the almost full degree of the melt carbonization.

Metal zirconium ( $\alpha$ -Zr(O)) presents in significant amounts only in external areas of assemblage (sample S3).

Oxide solid solutions  $(U,Zr)O_2$  are characteristic for samples of a material from the top of assemblage and after distribution border of a carbide melt to peripheral areas of assemblage. The general feature of this material is its melting without contact to graphite of a nozzle and carbide melt due to radiation heat exchange.

### *Conclusions*

The phase composition of samples is characterized by the high maintenance of carbonization products of the burden components at its contact interaction with graphite of a nozzle. Considerable carbonization degree of the melt and degree of erosion of graphite says that the melt contacted to graphite long time.

Main components of the majority of samples of the solidified melt are oxide phases type  $(U,Zr)O_2$  with FCC - lattice of uranium dioxide, carbide phases of the variable composition, which general formula may be present as  $Zr(U)(C,O,N)$  and uranium bicarbide.

## 4 Calculation support of experiments

### 4.1 Calculation of temperature fields of RPV model with the plasmatrons heater

#### 4.1.1 Statement of problem

Based upon the technical assignment "Thermal calculation of the experimental section for simulating decay heat in the corium pool at the corium melt retention in the reactor pressure vessel" - No. 114/K-1265 of 06.04.2009, and the memo "About thermal calculation" - No.115/K-1265 of 07.04.2009, the assessment of temperature fields of the lower head model with the plasmatrons heater in its loading with corium components C-32 free of preliminary melting of the burden loaded is required.

*Major calculation objective:*

- assessment of the lower head temperature field and the corium loaded;
- assessment of the period of the plasmatrons heater coming to the steady-state heating condition;
- assessment of a share of liquid fraction in the corium melt at steady-state heating condition;
- assessment of optimal cooling water flow rate in the outer cooling jacket of RPV model.

*Initial data:*

Corium mass, kg	60,0
Corium composition C-32:	
- mass of uranium dioxide (UO <sub>2</sub> ), kg	45,6;
- mass of zirconium dioxide (ZrO <sub>2</sub> ), kg	5,4;
- mass of zirconium (Zr), kg	15;
Power of a plasmatrons, kW	18;
Number of plasmatrons, pieces	5;
Duration of heating, h	2,5;
Zirconium melting heat, kJ/kg	210;
Heat of uranium dioxide dissolution in zirconium melt, kJ/kg	260;
Corium porosity	0,4;
Flow rate of water cooling the lower head model, kg/s	0,1÷1;
Percentage of plasmatrons power removed with the plasmatrons cooling water	0,2.

Thermo-physical properties of corium C-32 with zero porosity are represented in the diagram, Figure A2.4.1 [1].

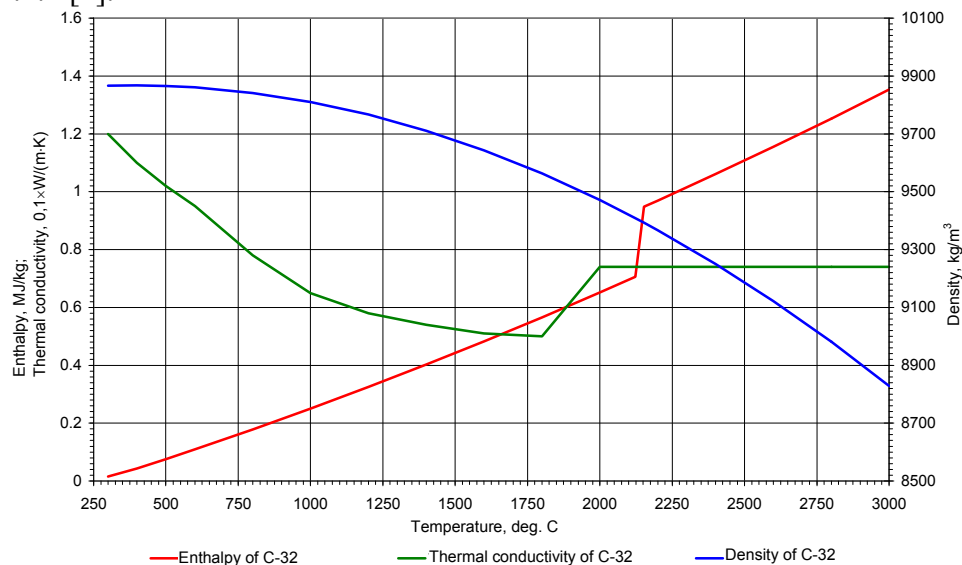


Figure A2.4.1 – Thermo-physical properties of corium C-32 with zero porosity

Diagram of the reactor lower head model with basic dimensions is depicted in Figure A2.4.2.

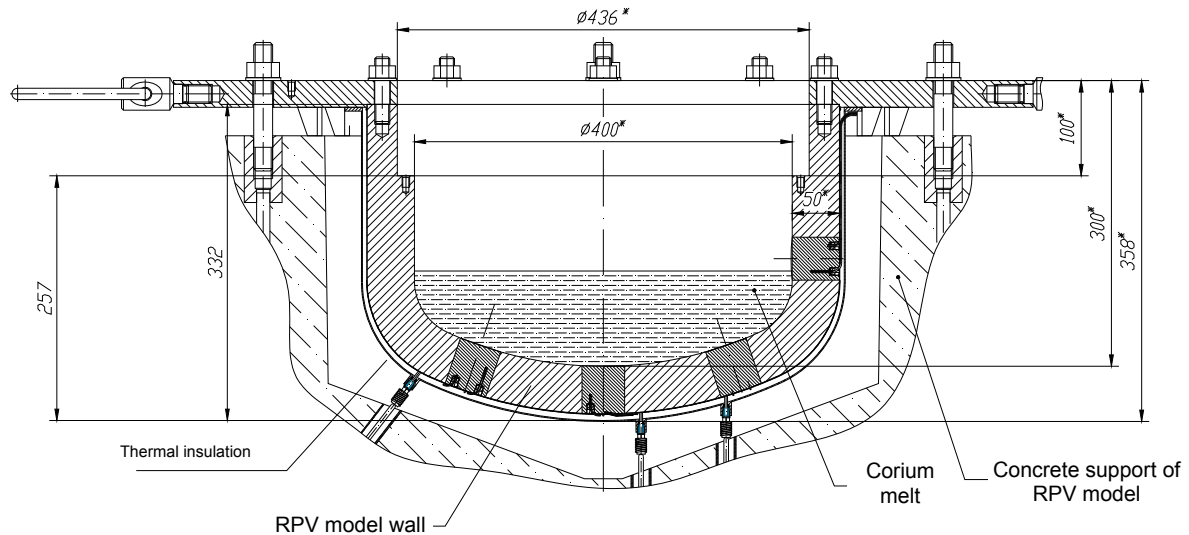


Figure A2.4.2 – Diagram of the reactor lower head model

Diagram of the reactor lower head model with plasmatrons is depicted in Figure A2.4.3.

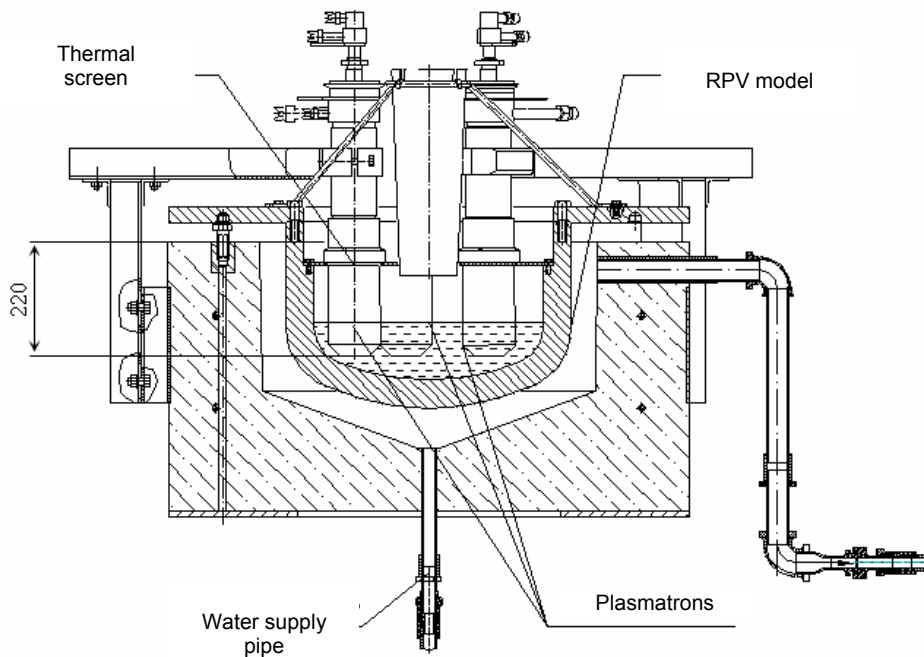


Figure A2.4.3 – Diagram of the reactor lower head model with plasmatrons

The diagram of graphite plasmatrons nozzles with basic dimensions is shown in Figure A2.4.4. The plasmatrons part of 220 mm height immersed in the lower head model is used in calculating temperature field of the experimental section (see Fig. A2.4.3). In calculation it was assumed that water cools surface of the outer nozzle – see blue lines in Figure A2.4.4. Red lines are the surface through which the energy emitted in the plasmatrons is transmitted to the graphite nozzle and further to the burden surrounding plasmatrons. The 62 mm surface height is limited with the corium-immersion depth of the external nozzle



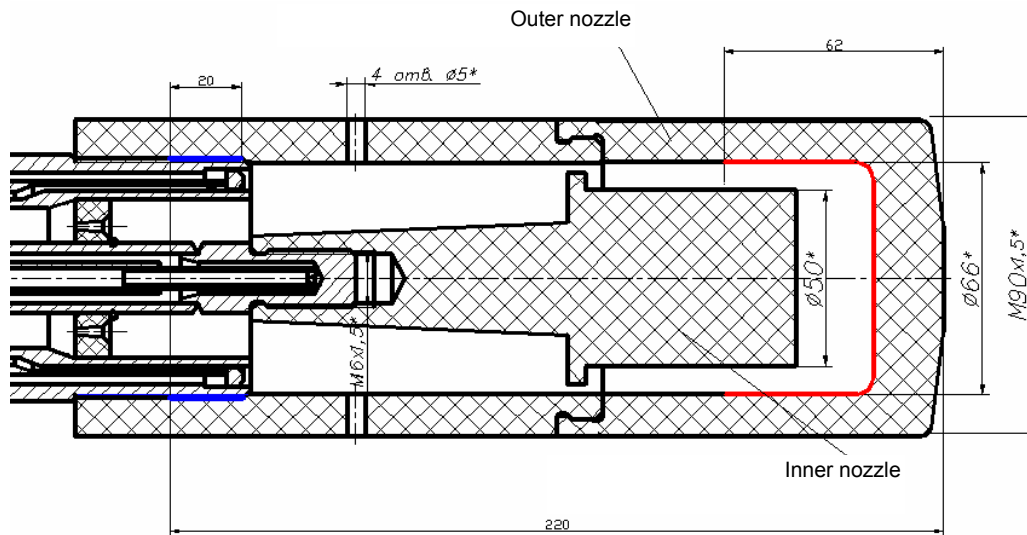


Figure A2.4.4 – Diagram of the lower plasmatrons part

#### 4.1.2 Calculation of temperature fields of the lower head model with a plasmatrons heater

Corium C-32 is a loose material. In this connection, the correction of thermal conductivity and corium density is applied.

The density of corium is found from the formula [2]

$$\rho(T) = \left( \rho_{UO_2}(T) \times \frac{M_{UO_2}}{M} + \rho_{ZrO_2}(T) \times \frac{M_{ZrO_2}}{M} + \rho_{Zr}(T) \times \frac{M_{Zr}}{M} \right) \times (1 - \mu), \quad (1)$$

where  $\rho_{UO_2}(T)$  - density of uranium dioxide at temperature T, kg/m<sup>3</sup>;

$\rho_{ZrO_2}(T)$  - density of zirconium dioxide at temperature T, kg/m<sup>3</sup>;

$\rho_{Zr}(T)$  - zirconium density at temperature T, kg/m<sup>3</sup>;

$M_{UO_2}$  - mass of uranium dioxide, kg;

$M_{ZrO_2}$  - mass of zirconium dioxide, kg;

$M_{Zr}$  - mass of zirconium, kg;

$M$  - corium mass, kg;

$\mu$  - corium porosity.

Corium thermal conductivity is found from the formula:

$$\lambda(T) = \left( \lambda_{UO_2}(T) \times \frac{M_{UO_2}}{M} + \lambda_{ZrO_2}(T) \times \frac{M_{ZrO_2}}{M} + \lambda_{Zr}(T) \times \frac{M_{Zr}}{M} \right) \times (1 - \mu), \quad (2)$$

where  $\lambda_{UO_2}(T)$  - thermal conductivity of UO<sub>2</sub> at temperature T, W/(m·K);

$\lambda_{ZrO_2}(T)$  - thermal conductivity of ZrO<sub>2</sub> at temperature T, W/(m·K);

$\lambda_{Zr}(T)$  - thermal conductivity of Zr at temperature T, W/(m·K).

If zirconium melting point is below 2123 K, corium porosity equals to 0,4, if zirconium melting point is over, porosity is assumed zero.

In calculation the heat flux density is assigned on the internal surface of the graphite plasmatrons nozzle and is determined by the formula:

$$q = \frac{N}{\pi \times d \times (l - \Delta) + 0,25 \times \pi \times d^2} = \frac{18000}{3,1415 \times 0,066 \times (0,062 - 0,02) + 0,25 \times 3,1415 \times 0,066^2} = 1,484 \cdot 10^6 \text{ W/m}^2, \quad (3)$$

where  $N$  – power released with plasmatrons, W;

$d$  – internal diameter of the external nozzle, m;

$l$  – immersion depth of the external plasmatrons nozzle in the corium melt, m;

$\Delta$  – thickness of the external nozzle basis, m.

Water heat removal is performed from the external surface of the lower head model insulation as well as from the surface marked with blue lines in Figure A2.4.4.

Heat-transfer coefficients are determined by the method represented below.

Hydraulic diameter of the channel cooling the lower head model is found from the formula:

$$d_{r.m.d} = 4 \times \frac{F}{P} = 4 \times \frac{0,25 \times \pi \times (d_2^2 - d_1^2)}{\pi \times (d_2 + d_1)} = \frac{d_2^2 - d_1^2}{d_2 + d_1} = d_2 - d_1 = 0,59 - 0,51 = 0,08 \text{ m}, \quad (4)$$

where  $F$  – open flow area of the channel, m<sup>2</sup>;

$P$  – wetted perimeter, m;

$d_2$  – internal diameter of the concrete basis, m;

$d_1$  – external diameter of the lower head model housing, m.

Reynolds number is found from the equation:

$$Re = G \times \frac{d_{z.m.d}}{F \times \mu} = 0,1 \times \frac{0,08}{0,069 \times 0,000653} = 177, \quad (5)$$

where  $G$  – flow rate of water cooling the lower head model, kg/s;

$\mu$  – dynamic viscosity coefficient, at temperature 40 °C  $\mu = 0,000653 \text{ n}\cdot\text{s}/\text{m}^2$  [1].

Mode of water flow cooling the lower head model, is streamline since the Reynolds number is below 3000. In this case Nusselt number is calculated from the formula:

$$Nu = 1,4 \times \left( Re \times \frac{d_{z.m.d}}{L} \right)^{0,4} \times Pr^{0,33} = 1,4 \times \left( 177 \times \frac{0,08}{0,33} \right)^{0,4} \times 4,35^{0,33} = 10,2, \quad (6)$$

where  $L$  – defining dimension, since the lower head model is cooled in longitudinal direction then lower head model height,  $L = 0,33 \text{ m}$ , was selected as a defining dimension;

$Pr$  – Prandtl number, at water temperature 40 °C  $Pr = 4,35$  [1].

Heat-transfer coefficient from the lower head model to the cooling water is found from the equation:

$$\alpha = Nu \times \frac{\lambda}{d_{z.m.d}} = 10,2 \times \frac{0,627}{0,08} = 80,2 \text{ Wt}/(\text{m}^2 \times \text{K}), \quad (7)$$

where  $\lambda$  – water thermal conductivity, at temperature 40 °C  $\lambda = 0,627 \text{ Wt}/(\text{m} \times \text{K})$ .

Dependence of heat-transfer coefficient from the outer plasmatrons nozzle to the cooling water on the temperature of cooling nozzle surface is determined by the equation:

$$\alpha(T) = \frac{k \times N}{F \times (T - T_{\text{Bodbi}})}, \quad (8)$$

where  $k$  – proportion of plasmatrons power removed with plasmatrons cooling water,  $k = 0,2$ ;

$F$  – heat transfer area,  $F = 0,004147 \text{ m}^2$ ;

$T$  – temperature of cooling plasmatrons surface, K;

$T_{\text{Water}}$  – cooling water temperature,  $T_{\text{Water}} = 300 \text{ K}$ .

The posted task of unsteady heat calculation has been solved using the program ANSYS [3]. Figure A2.4.5 demonstrates the temperature field and check points of temperature in longitudinal section of the model in 2 hours and 30 minutes after heating start. Red arrows show the surfaces involved in convective heat transfer. Emission heat transfer is occurred between corium surface, nozzles and internal wall of the lower head model. Emissivity factor of the said surfaces is assumed as equal to 0,6. The model ignores availability of the heat shield.

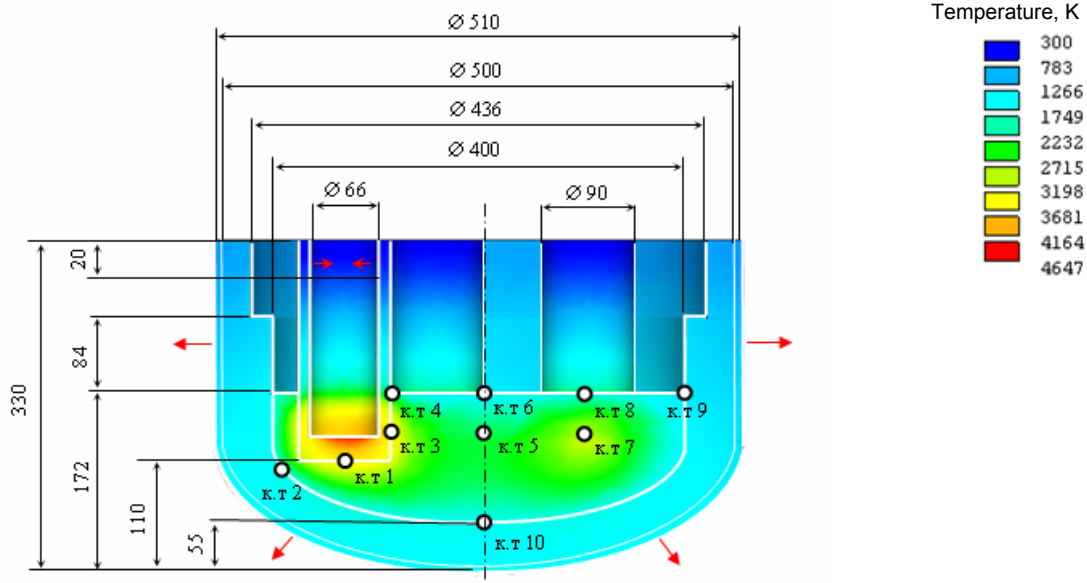


Figure A2.4.5 – Temperature field in longitudinal section of the model in 2,5 hours after heating start  
 Figure A2.4.6 illustrates corium temperature field in the most high-heat longitudinal section that goes through checkpoint 3 at a distance of 130 mm from the calculation model bottom.

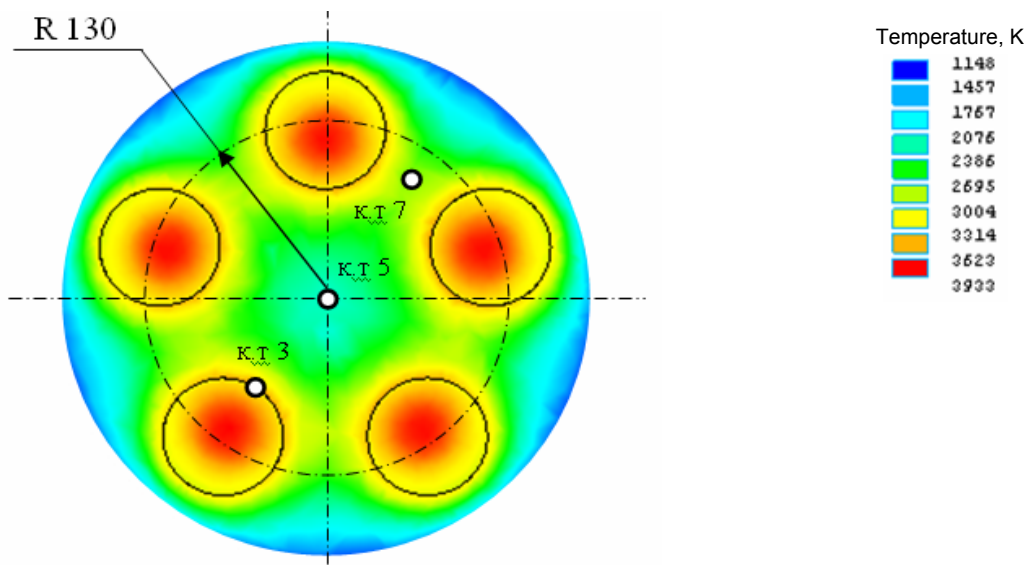


Figure A2.4.6 – Corium temperature field in 2 hours and 30 minutes after heating start. Section goes through checkpoint 3. Top view

Figure A2.4.7 shows the diagram of corium temperature dependence on time in different checkpoints. In this case, water flow rate in the outer lower head model cooling jacket is equal to 0,1 kg/s.

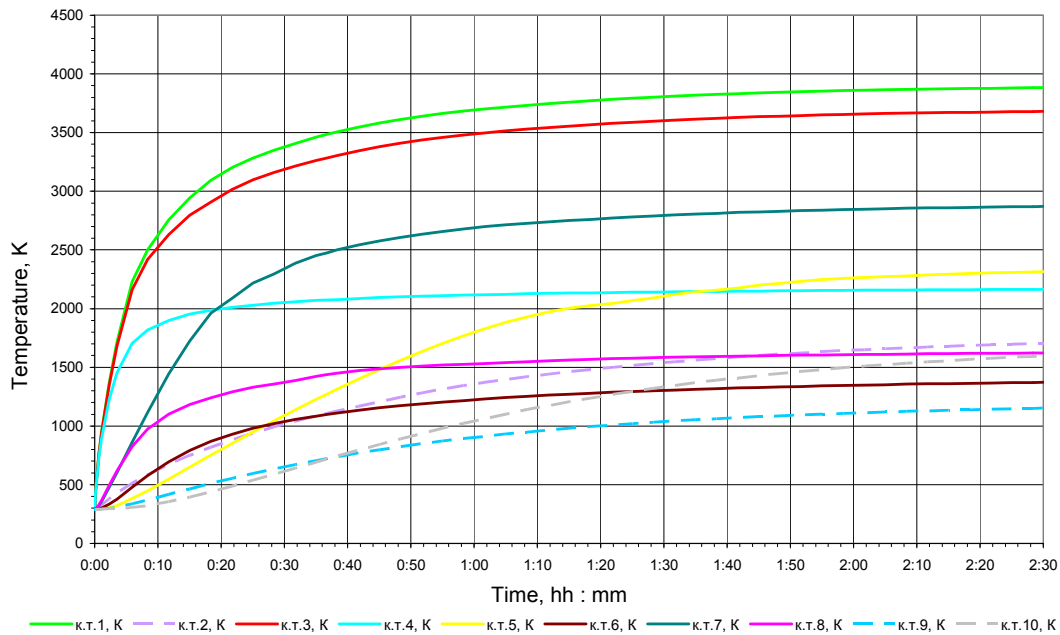


Figure A2.4.7 – Dependence of corium temperature on heating time

Within the time range from 2 hours to 2,5 hours the checkpoints temperature changes less than 50%, consequently, the time of coming to heat-exchange steady-state condition is ~ 2 hours.

In the experiment completion, in 2 hours and 30 minutes after heating start, the temperature 21% of corium C-32 volume will exceed melting point that is equal to 2773 K; temperature of 41% of corium volume will below 2123 K, temperature of 38% of corium volume is in the range from 2123 to 2773 K.

The resulted calculation in 2,5 hours after heating start at different flow rates of water cooling the lower head model housing is included in Table A2.4.1.

Table A2.4.1 – Resulted calculation of temperature in the checkpoints

Water flow rate, kg/s	Heat-transfer coefficient, W/(m <sup>2</sup> ·K)	Temperature, K									
		ch.p.1	ch.p.2	ch.p.3	ch.p.4	ch.p.5	ch.p.6	ch.p.7	ch.p.8	ch.p.9	ch.p.10
0,1	80	3883	1704	3680	2164	2314	1371	2870	1622	1152	1597
0,3	125	3820	1485	3632	2144	2257	1306	2818	1582	987	1348
0,5	152	3794	1406	3611	2139	2231	1287	2797	1570	928	1252
1,0	202	3755	1307	3583	2132	2196	1267	2773	1558	856	1129

From the data included in Table 1 we see that when cooling water rate is 0,1 kg/s the maximum temperature of the lower head model housing in c.p. 2 will exceed the melting point of steel - 1680 K, and will be equal to ~ 1704 K. When the lower head model cooling water rate is 0,3 kg/s the maximum temperature of the lower head model housing in c.p. 2 wouldn't exceed ~ 1485 K. On increasing cooling water rate up to 0,5 kg/s the calculated temperature of the lower head model reduces insufficiently, consequently, the water rate 0,3 kg/s is optimal for cooling reactor lower head model.

Tables A2.4.2 and A2.4.3 give calculated portions of liquid fraction in the corium in 1 hour and 2,5 hours after heating start in dependence of flow rate of water cooling the lower head model.

Table A2.4.2 – Resulted calculation of the corium state in the lower head model in 1 hour after heating start

Water flow rate, kg/s	Corium state			
	Solid fraction, %		Liquid fraction, %	
	Temperature below 2123 K		2123 K < T < 2773 K	T > 2773 K
0,1	57		32	11
0,3	58		31	11
0,5	60		30	10
1,0	61		29	10



Table A2.4.3 – Resulted calculation of the corium state in the lower head model in 2,5 hours after heating start

Water flow rate, kg/s	Corium state		
	Solid fraction, %		Liquid fraction, %
	Temperature below 2123 K	2123 K < T < 2773 K	T > 2773 K
0,1	41	38	21
0,3	45	37	18
0,5	48	36	16
1,0	51	35	14

From the calculation results it is seen that with increase in cooling water rate the liquid fraction portion in the corium reduces insufficiently. At optimal rate of water cooling the lower head model housing, 0,3 kg/s the liquid fraction portion in the corium, in an hour after the experiment start, will be ~ 42 %. At the completion stage of the test at the specified rate of water the liquid fraction portion in the corium will be ~ 55 %.

### Conclusions

Several alternative calculations of the lower head temperature field and loaded corium C-32 have been carried out and the following results have been reached:

1. the period for coming to the heating steady-state condition was equaled to ~2 hours;
2. optimal flow rate of the cooling water in the outer lower head model cooling jacket was equal to 0,3 kg/s;
3. calculated portion of the liquid fraction in the corium at heating steady-state condition and cooling water rate 0,3 kg/s will be near 55% at the experiment end;
4. at optimal cooling water rate 0,3 kg/s in the outer lower head model cooling jacket the maximum temperature of the lower head model housing wall wouldn't exceed ~1485 K. Maximum corium temperature between plasmatrons will reach ~2820 K. In the geometric center of the model the maximum corium temperature will be ~2260 K.

### References to item 4.1

- 1 V.S. Chirkin, Thermophysical properties of nuclear energy technology materials, reference book, Atomizdat, Moscow, - 1968. – 484 p.
- 2 Mikheev M.A., Mikheeva I.M. Heat-transfer Principles, Moscow, "Energiya", - 1977. – 320 p.
- 3 Release 10.0 - Documentation for ANSYS.

## 4.2 Calculation of hydraulic parameters of system of a departing gases drainage from the electro-melting furnace of "LAVA-B" Facility

Before discharging gases mixture released from the electric melting furnace to the atmosphere, they should be cooled to avoid thermal rupture of the gas discharge system construction elements. Thereto, the shell-and-tube heat exchanger was designed. The heat exchanger is a component of the "LAVA-B" facility equipment and is installed on the top cover of the electric melting furnace (EMF) [1].

Pre-cooling of the gases mixture is carried out in water-cooled pipe branch along which gas is supplied to the shell-and-tube heat exchanger and which is practically a heat exchanger of a type similar to annular tube. The water-cooled pipe branch is made of two stainless steel tubes of the following dimensions: outer tube –  $\varnothing 65 \times 8.5$  mm; internal tube –  $\varnothing 42 \times 5$  mm. In addition, to reduce temperature of the internal tube, a graphite insert with  $\varnothing 32 \times 3$  mm is put in it. The active pipe branch length is 250 mm, including the part placed in the furnace top cover. The pipe branch diagram is represented in Figure A2.4.8.

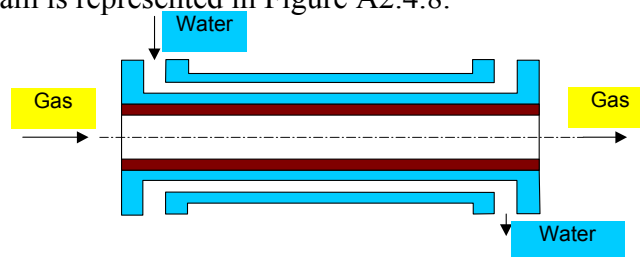
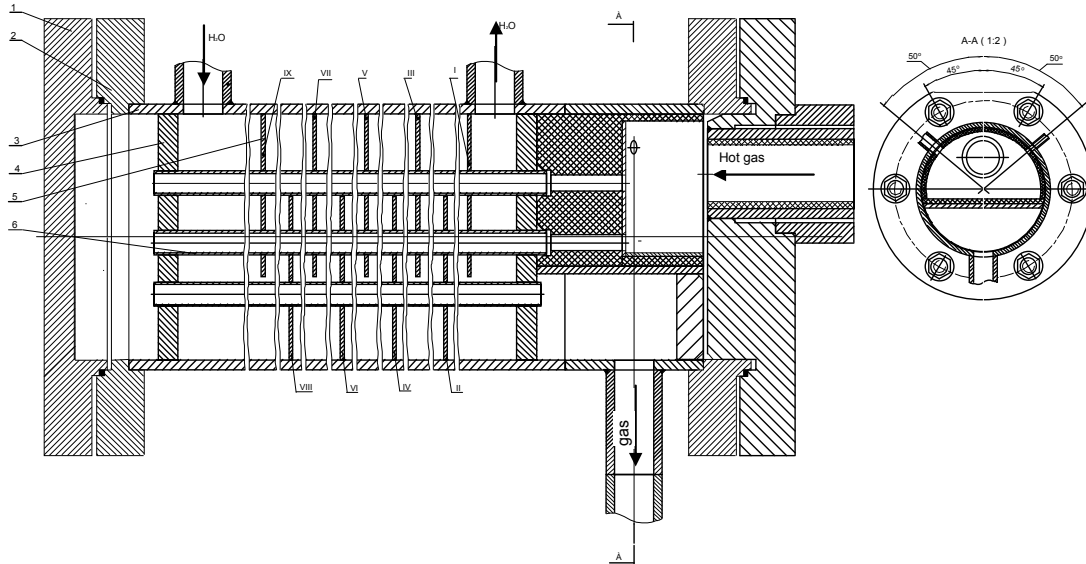


Figure A2.4.8 - Water-cooled gas pipe branch

The general cooling of gases is performed in the shell-and-tube heat exchanger consisting of flanges, two pipe plates, 9 partitions, housing with external diameter 140 mm, thickness 5 mm and length 628 mm, 29 tubes with outer diameter 12 mm, thickness 1mm and length 600 mm. Hot gas passes through 20 tubes with  $\text{Ø}12 \times 1$  mm in forward direction and through 9 tubes with  $\text{Ø}12 \times 1$  mm in backward direction. Water goes through the tube space thereby cooling the tubes from the outside. Gas temperature in the shell-and-tube heat exchanger reduces from  $\sim 2500^\circ\text{C}$  to  $\sim 500^\circ\text{C}$ . The diagram of the shell-and-tube heat exchanger is represented in Figure A2.4.9.



1 - cover; 2 - flange; 3 - housing; 4 - tube plate; 5 - partitions (Roman numeral – partition number, they are in all – 9); 6 – heat exchange tubes.

Figure A2.4.9 – Design of the shell-and-tube heat exchanger

#### 4.2.1 Statement of Problem

Pressure losses in the gas path of the system for discharging gases released from the "LAVA-B" facility EMF should be defined.

#### 4.2.2 Initial data

The heat exchanger (HE) designed for gas cooling provides with the following technical characteristics [1]:

- gas flow rate, kg/s - to 0.012;
- inlet gas temperature,  $^\circ\text{C}$  - 2500;
- outlet gas temperature,  $^\circ\text{C}$  - 500;
- gas pressure at the HE inlet, MPa - to 4.0.

Basic components of the gas mixture are: hydrogen, carbon oxide, carbon dioxide, nitrogen, argon, water vapor. Hot gas, taken for the performance of thermo-hydraulic calculation, as per the averaged data represented in "The test log of experimental items in the "ANGARA" test facility. No.7, inv. No. 2653" is a gas mixture of the following composition, in volume %:

- hydrogen ( $\text{H}_2$ ) - 20 %;
- nitrogen ( $\text{N}_2$ ) - 50 %;
- carbon dioxide ( $\text{CO}_2$ ) - 30 %.

From the heat exchanger the gas mixture is discharged to the atmosphere through the discharge tube. Geometrical parameters of the discharge tube are included in Table A2.4.4.

Table A2.4.4 – Geometrical parameters of the discharge tube

Area number	Flow area diameter, m	Length, m	Number of bends	Number of valves
1	0.020	1	0	1
2	0.032	6	4	0

### 4.2.3 Hydraulic Calculation of the Gas Path

Pressure loss in the gas discharge system is defined by the following formula:

$$\Delta P = \Delta P_{20} + \Delta P_9 + \Delta P_{\text{gaspipe}} + \Delta P_{\text{disch}} = 629 + 4745 + 6096 + 26330 = 0.038 \text{ MPa,}$$

where  $\Delta P_{20}$  – loss of gas pressure after passing in forward direction through 20 heat exchange tubes, Pa;

$\Delta P_9$  – loss of gas pressure after passing through 9 heat exchange tubes in backward direction, Pa;

$\Delta P_{\text{gaspipe}}$  – loss of gas mixture pressure in water-cooled gas pipeline – pipe branch, Pa;

$\Delta P_{\text{disch}}$  – loss of gas mixture pressure in discharge pipeline, Pa.

Gas pressure loss [2] after passing in forward direction:

$$\Delta P_{20} = \xi_{20} \times \frac{\left(\frac{G_g}{20}\right)^2}{2 \times \rho_g \times S_{mp}^2} = 4.8 \times \frac{\left(\frac{0.012}{20}\right)^2}{2 \times 0.222 \times (7.85 \times 10^{-5})^2} = 629 \text{ Pa,}$$

where  $\xi_{20}$  – hydraulic resistance coefficient from 20 pipes of forward direction;

$G_g$  – gas flow rate,  $G_g = 0.012$  kg/s;

$\rho_g$  – gas density, kg/s<sup>2</sup>;

$S_{mp}$  – flow area of the heat exchange tube,  $S_{mp} = 7.85 \times 10^{-5}$  m<sup>2</sup>.

Gas pressure loss after passing in backward direction:

$$\Delta P_9 = \xi_9 \times \frac{\left(\frac{G_g}{9}\right)^2}{2 \times \rho_g \times S_{mp}^2} = 4.3 \times \frac{\left(\frac{0.012}{9}\right)^2}{2 \times 0.222 \times (7.85 \times 10^{-5})^2} = 4745 \text{ Pa,}$$

where  $\xi_9$  – hydraulic resistance coefficient of one of 9 heat exchange tubes of backward direction.

Hydraulic resistance coefficient of one of 20 tubes of forward direction:

$$\xi_{20} = \xi_{in} + \xi_{fr20} + \xi_{out} = 0.5 + 3.3 + 1 = 4.8,$$

$\xi_{fr20}$  – friction resistance coefficient of heat exchange tube if forward direction.

Friction resistance coefficient of heat exchange tube  $\xi_{fr20}$  is defined in line with the formula:

$$\xi_{fr20} = \lambda_{20} \times \frac{L}{d_0} = 0.055 \times \frac{0.6}{0.01} = 3.3,$$

where  $L$  – length of heat exchange tube,  $L = 0.6$  m;

$d_0$  – diameter of heat exchange tube flow area,  $d_0 = 0.01$  m;

$\lambda_{20}$  – Darcy coefficient.

In order to calculate the Darcy coefficient the value of Reynolds' number should be defined:

$$\text{Re}_{20} = \frac{\frac{G_g}{20} \times d_0}{S_{mp} \times \mu_g} = \frac{\frac{0.012}{20} \times 0.01}{7.85 \times 10^{-5} \times 5.9 \times 10^{-5}} = 1294,$$

where  $\mu_g$  – coefficient of gas dynamic viscosity.

The coefficient of dynamic viscosity of the given gas mixture is determined by the following formula:

$$\mu_g = 1.86859 \times 10^{-5} + 2.68858 \times 10^{-8} \times T_{sr} = 1.86859 \times 10^{-5} + 2.68858 \times 10^{-8} \times 1500 = 5.9 \times 10^{-5} \text{ Pa}\cdot\text{s;}$$

where  $T_{sr}$  – gas averaged temperature,  $T_{sr} = 1500$  °C.

In the case if  $10 < \frac{\text{Re} \times \Delta}{d} < 500$  (transition region of rough tubes) Darcy coefficient is defined by the Altshul formula:

$$\lambda_{20} = 0.11 \times \left( \frac{\Delta}{d_0} + \frac{68}{\text{Re}_{20}} \right)^{0.25} = 0.11 \times \left( \frac{0.0001}{0.01} + \frac{68}{1294} \right)^{0.25} = 0.055.$$

Hydraulic resistance coefficient of the heat exchange tube of backward direction is defined in the line with the above algorithm and is  $\xi_9 = 4.3$ .

Gas mixture density:

$$\rho_e = \frac{P}{R \times T} = \frac{0.119 \times 10^6}{301.7 \times 1773} = 0.222 \text{ kg/s}^3,$$

where P – gas mixture pressure in the first approximation P = 0.119 MPa;

T – averaged temperature of gas mixture, T = 1773 K (1500 °C);

R – gas constant of gas mixture.

Define mass fraction of gas mixture. Mass fraction of hydrogen:

$$H_m = \frac{H \times \rho_H}{H \times \rho_H + N \times \rho_N + CO_2 \times \rho_{CO_2}} = \frac{0.2 \times 0.016}{0.2 \times 0.016 + 0.5 \times 0.226 + 0.3 \times 0.355} = 0.015.$$

Mass fraction of nitrogen:

$$N_m = \frac{N \times \rho_N}{H \times \rho_H + N \times \rho_N + CO_2 \times \rho_{CO_2}} = \frac{0.5 \times 0.226}{0.2 \times 0.016 + 0.5 \times 0.226 + 0.3 \times 0.355} = 0.507.$$

Mass fraction of carbon dioxide:

$$CO_m = \frac{CO_2 \times \rho_{CO_2}}{H \times \rho_H + N \times \rho_N + CO_2 \times \rho_{CO_2}} = \frac{0.3 \times 0.355}{0.2 \times 0.016 + 0.5 \times 0.226 + 0.3 \times 0.355} = 0.478,$$

where H – hydrogen volume fraction, H = 0.2;

N – nitrogen volume fraction, N = 0.5;

CO<sub>2</sub> – volume fraction of CO<sub>2</sub>, CO<sub>2</sub> = 0.3;

$\rho_H$  – hydrogen density at averaged temperature 1773 °K  $\rho_H = 0.016 \text{ kg/s}^3$ ;

$\rho_N$  – nitrogen density at averaged temperature 1773 °K  $\rho_N = 0.226 \text{ kg/s}^3$ ;

$\rho_{CO_2}$  – carbon dioxide density at averaged temperature 1773 °K  $\rho_{CO_2} = 0.355 \text{ kg/s}^3$ .

Gas constant of gas mixture is defined as follows:

$$R = H_m \times \frac{R_0}{M_H} + N_m \times \frac{R_0}{M_N} + CO_m \times \frac{R_0}{M_{CO_2}} = 0.015 \times \frac{8314}{2} + 0.507 \times \frac{8314}{28} + 0.478 \times \frac{8314}{44} = 301.7,$$

where R<sub>0</sub> – universal gas constant, R<sub>0</sub> = 8314 J/(mol·K);

M<sub>H</sub> – hydrogen molecular weight, M<sub>H</sub> = 2;

M<sub>N</sub> – nitrogen molecular weight, M<sub>N</sub> = 28;

M<sub>CO<sub>2</sub></sub> – molecular weight of CO<sub>2</sub>, M<sub>CO<sub>2</sub></sub> = 44.

Losses of gas mixture pressure in the gas pipeline – pipe branch is defined in the line with the above algorithm and is ~ 0.0061 MPa. Gas mixture pressure loss in the discharge pipeline is ~ 0.026 MPa.

### Conclusion

Losses of gas mixture pressure in the discharge system of the released gas would not exceed 0.04 MPa.

### Literature to item 4.2

1. “LAVA B@ Test Facility. Explanatory note AK.65000.00.934 PZ.
2. A.D.Altshul. Hydraulics and aerodynamics. M.: Stroiizdat (1987).

### 4.3 Calculation thermal hydraulics of the corium melt in RPV model

Calculations have been executed with a uniform thermal insulation of an external surface of RPV model. Temperature field in the melt and a corium crust near to coaxial plasmatrons is shown in Figure A2.4.10, and distribution of a heat flux on an internal surface of RPV model is resulted in Figure A2.4.11.



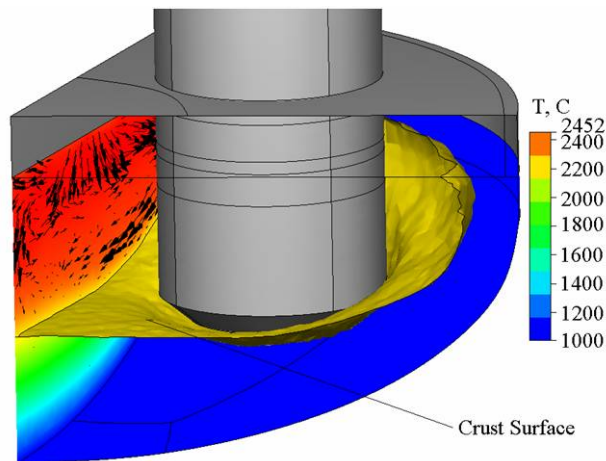


Figure A2.4.10 – Temperature field in the melt and in the bottom crust of corium

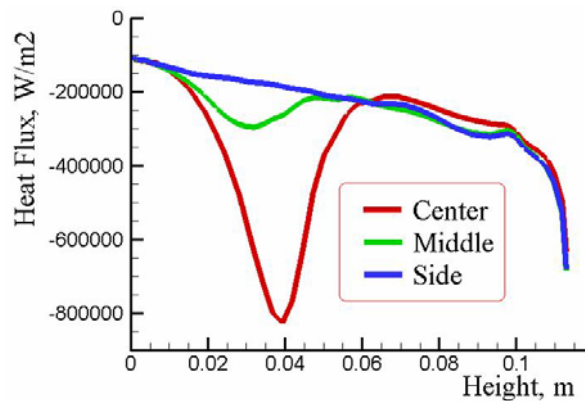


Figure A2.4.11 – Distribution of the heat flux along the inner surface of the RPV model

Apparently from Figure A2.3.11, the maximum of a heat flux is observed in a plane of an axis of an electrode near to an arc zone of the plasmatrons.

Heat conductivity of a corium crust  $5 \text{ W}/(\text{m}\cdot\text{K})$  is specified by results of large-scale calibration experiments TOP.

*Thermo-stressed state of RPV model (1/10) ( $T_{max} \approx 1000 \text{ }^\circ\text{C}$ )*

In Figure A2.4.12 the temperature field in a wall of RPV model is shown provided that the maximum temperature of an internal surface of model makes nearby  $1000 \text{ }^\circ\text{C}$ . Thus fields of deformation of a RPV model wall will look like, shown in Figure A2.4.13.

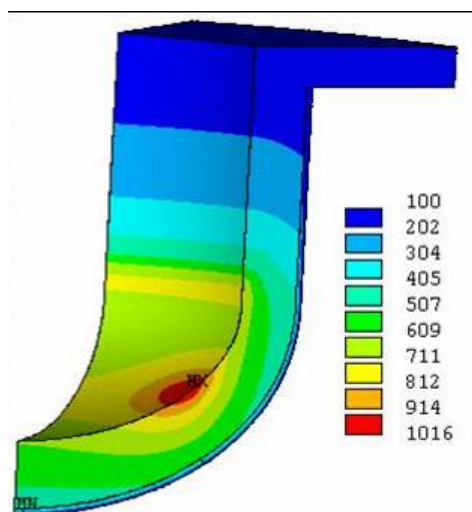


Figure A2.4.12 – Temperature field in a RPV model wall at the maximum temperature  $1000 \text{ }^\circ\text{C}$

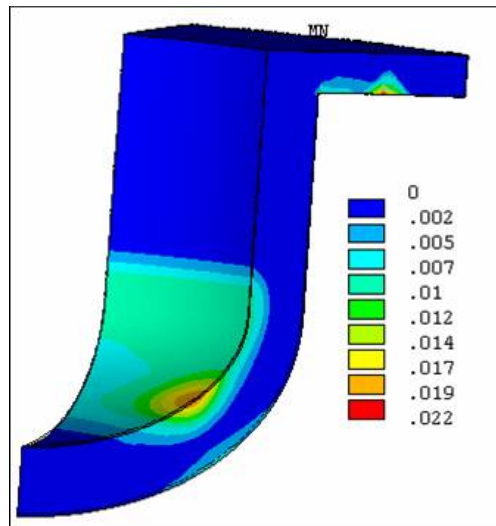


Figure A2.4.13 – Field of deformations in a RPV model wall at the maximum temperature 1000 °C

It was accepted for calculations that the thickness of a thermal insulation makes 5 mm, heat conductivity of a thermal insulation 1.8 W/(m·K), the relation of heat conductivity to a thickness of a thermal insulation make  $\lambda/\delta=360$  W/(m<sup>2</sup>·K). Thus the maximum deformations of a wall of RPV model will make about 2 %.

*Thermo-stressed state of RPV model (1/10) ( $T_{max} \approx 1200$  °C)*

It was accepted for calculations that the thickness of a thermal insulation makes 5 mm, heat conductivity of a thermal insulation 1.2 W/(m·K), the relation of heat conductivity to a thickness of a thermal insulation makes  $\lambda/\delta=240$  W/(m<sup>2</sup>·K). Thus the maximum deformations of a wall of RPV model will exceed critical values for a case steel.

Temperature field in a wall of RPV model is shown in Figure A2.4.14 provided that the maximum temperature of an internal surface of model makes nearby 1200 °C.

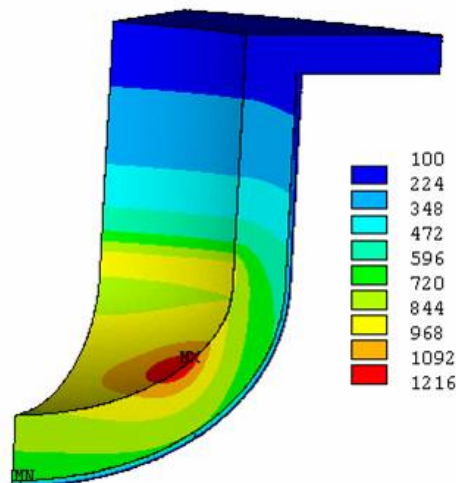


Figure A2.4.14 – Temperature field in the wall of RPV model at maximum temperature 1200 °C

*Comments*

- Calculations are executed with a uniform thermal insulation of an external surface of RPV model;
- Non-uniform thermal insulation, basically, can provide more uniform distribution of temperature on an internal surface;
- Absence of direct water cooling of an external surface of RPV model because of its thermal insulation (absence of a cold steel layer) worsens strength of model. The small increase in temperature of a steel over admissible value can lead to model destruction.

## **5 Complex works on test and adjustment of the device for imitation of decay heat on the basis of five plasmatrons**

### **5.1 Life testing of the modified plasmatrons and welding units VD306C1 of group "D" of the melt heating system**

5.1.1 Subject of study – The melt heating system in the RPV model of "LAVA-B" facility.

5.1.2 The objective and goals of the tests:

5.1.2.1 The objective of the tests was the characterization of the melt heating system and steady-state arcing conditions of the modified plasmatrons, drawing No. AKK.21086.01.000 CB.

5.1.2.2 The goals of the tests were:

- life testing of transformers VD306C1 of group "D" for feeding plasmatrons at running plasmatrons current 250 A with supplying nitrogen to the plasmatrons inter-electrode space;
- definition of running current of transformers VD306C1 using the thyristor rectifier on running more than 30 minutes for which temperature of transformer secondary winding does not exceed 90 °C;
- definition of running current of transformers VD 306C1 using the diode rectifier on running more than 30 minutes for which temperature of transformer secondary winding does not exceed 90 °C.

5.1.3 General conditions

5.1.3.1 The melt heating system in the reactor lower head model (drawing No. DKIG.681.613.001.CB) is designed for simulating heat decay in the melt located in the lower head model. The lower head model with the plasmatrons installed was located in the "LAVA-B" facility pressure vessel.

5.1.3.2 The experiments were carried out in compliance with the program and procedure "Testing of the melt heating system with modified plasmatrons" reg. No.240-02/142 of 05.11.2008 and according to the decision on repairing work on the welding units VD306C1 of the melt heating system in the reactor lower head model, reg. No. D-761 of 01.12.2008.

5.1.4 Tests conditions

5.1.4.1 The experimental work on the melt heating system in the reactor lower head model was performed in the "ANGARA" thermo-technical test facility.

5.1.4.2 Magnetic medium recording and data display were performed by means of the "ANGARA" test facility data acquisition system (DAS).

5.1.4.3 The test facility automatic control systems (ACS) were managed manually.

5.1.4.4 Nominal parameters of the melt heating system in the reactor vessel lower head model are as follows:

- maximum value of the plasmatrons working current, A – to 310;
- plasmatrons volts, V – to 70;
- open circuit volts on the plasmatrons, V – to 140;
- water flow rate through the plasmatrons cooling path, kg/s – to 0,08;
- consumption of argon supplied to inter-electrode space, kg/s – 0,0005;
- consumption of nitrogen supplied to inter-electrode space, kg/s – 0,0005;
- flow rate of gas mixture supplied to inter-electrode space, kg/s – 0,001.

5.1.4.5 The work was done using the modified plasmatrons "A" installed on the reactor lower head model and welding units VD306C1 of group "D". The modified plasmatrons design is illustrated in Figure A2.5.1 (in contrast to the plasmatrons of previous construction the length of the working part of the outer electrode reduced by 170 mm, and the internal - by 210 mm).

5.1.4.6 Plasmatrons voltage was measured by the standard normalizing converter 73G-IV10 (c.p. NN.04D).

5.1.4.7 Plasmatrons current strength was measured by the standard normalizing converter 73G-IV100M (ch.p. TH.04D).

5.1.4.8 Working medium and facility elements temperature was measured by the standard thermocouples of the "LAVA-B" test facility.

5.1.4.9 Working medium pressure was measured with the standard pressure gauges DDM.

5.1.4.10 Working parameters were measured with the certified instruments.

5.1.4.11 On the graphite nozzle of the plasmatrons outer electrode there were installed three thermocouples: c. p. TCJ.04 at a distance 110 mm from the nozzle end, c.p. MDT.04 at a distance 70 mm from the nozzle end and c.p. MDT.103 at a distance 50 mm from the nozzle end.

5.1.4.12 Electric arc ignition was performed with supply of argon to the inter-electrode space with its further change for nitrogen or for mixture of argon and nitrogen gases.

5.1.4.13 The former-used graphite nozzles were installed on the electrodes. The nozzle made of graphite R4340 was installed on the internal electrode. The two-part graphite nozzle – the upper part was made of graphite ARV-1, and the bottom part was made of graphite GE, was installed on the outer electrode.

5.1.4.14 Before the first start-up of the plasmatrons the distance from the internal electrode nozzle end to the outer electrode nozzle bottom was equal to 30 mm.

5.1.4.15 The needle with effective open area  $6,467 \times 10^{-8} \text{ m}^2$  was installed in the reservoir of gas supply to the plasmatrons inter-electrode space. In preparation of gas mixture supply to the plasmatrons inter-electrode space, the needle in the reservoir was changed for a separator, in the nitrogen supply path the needle with effective open area  $5,667 \times 10^{-8} \text{ m}^2$  was installed, and in the argon supply path the nozzle with critical cross-section diameter  $d_{cr} = 0,7 \text{ mm}$  was installed.

5.1.4.16 The thyristor rectifier was installed on transformer No. 8. The diode rectifier was installed on transformer No. 7.

5.1.4.17 Resistance thermometers (RT) were installed on the transformers' secondary winding of the transformer: on VD #7 – c.p. MTR.33; on VD #8 – c.p. MTR.44. Over the transformers' primary winding of the transformer there were installed resistance thermometers as follows: on VD #7 – c.p. MTR.11; on VD # 8 – c.p. MTR.22.

5.1.4.18 The transformer electric circuit was modified as follows – VD ventilators are switched on immediately on pushing the button "Plasma process" on the control board (CB) of the console.

#### 51.5 Scope of activity accomplished

5.1.5.1 The test sequence is stated in the "functional program" (inv. No.D 698 of 18.11.2008).

5.1.5.2 From 06.01.2009 up to 03.02.2009, eleven tests with plasmatrons start-up and using transformer VD306C1 of group "D" as a power-supply source were carried out.

5.1.5.3 On 09.01.2009, the plasmatrons start-up was attempted. After the oscillator actuation, it was observed pressure drop of free running from 129 to 66 V, at that there was no arc ignition. As a result of examination it was appeared that two diodes in the transformer VD #7 were failed.

At 12:55, after replacement of the diode rectifier into the thyristor one in the transformer VD #7, the life testing of the modified plasmatrons on current  $\sim 250 \text{ A}$  was started. The electric arc was initiated at the first push. In 6 minutes after changing of argon for nitrogen in the inter-electrode space, the arc was extinguished spontaneously. During the test, after replacement of argon for nitrogen in the inter-electrode space, the arc was extinguished six times. Every time the start-up of the plasmatrons was performed from the CB of the console. At 13:55, it was decided not to change argon for nitrogen in the inter-electrode space and continue the life testing with argon. Total arc ignition period in the plasmatrons was 1 hour 29 minutes and 29 seconds. Physical parameters resulted from the modified plasmatrons running are included in Table A2.5.1.

5.1.5.4 To test of whether the cause of spontaneous arc quenching on supplying nitrogen to the inter-electrode space in the test of 09.01.2009 was under-voltage rate, the test start-up of the



plasmatoms with supplying argon to the inter-electrode space and its change for nitrogen was carried out on 12.01.2009. The welding units were operated with thyristor rectifiers and were adjusted at operating current 270 A. On plasmatoms starting-up the electric arc was initiated. In 10 minutes and 58 seconds after the start-up, there was planned outage of the arc in the plasmatoms. The assumption that the cause of arc quenching in the test conducted on the 9<sup>th</sup> of January was under-voltage rate that was not sufficient for the arc support was confirmed. Physical parameters resulted from the plasmatoms running are included in Table A2.5.1.

Table A2.5.1 – Parameters values of the modified plasmatoms

Parameter	Parameters value	
Data of test performance	09.01.09	12.01.09
Time of plasmatoms operation, hh : mm : ss	1 : 29 : 29	10 : 58
Average voltage of electrical arc, V	53,0	59,8
Average current of electrical arc, A	228,0	267,5
Average power of plasmatoms, kW	12,0	15,9
Maximum warming-up of water in a cooling path of plasmatoms, °C	6,3	6,3
Heat losses with the cooling water of plasmatoms, %	18,7	11,4
Maximum temperature of a nozzle of an external electrode, °C		
- On distance of 50 mm from a nozzle end face, c.p. MDT.103	1233	1213
- On distance of 70 mm from a nozzle end face, c.p. MDT.04	813	813
- On distance of 110 mm from a nozzle end face, c.p. THJ.04	622	665
Maximum temperature of windings of transformers, deg. C		
- Primary winding of the transformer VD306C1 #7, c.p. MTP.11	28,1	16,3
- Primary winding of the transformer VD306C1 # 8, c.p. MTP.22	28,3	16,1
- Secondary winding of the transformer VD306C1 #7, c.p. MTP.33	100,6	45,5
- Secondary winding of the transformer VD306C1 #8, c.p. MTP.44	86,6	39,3
Distance from the bottom end face of a nozzle of an internal electrode to the nozzle bottom of an external electrode, mm		
- before test	30	30
- after test (minimum distance)	30	30

5.1.5.5 On 20.01.2009, seven tests were carried out. The internal electrode nozzle and the outer electrode nozzle bottom newly-manufactured from graphite APV were installed on the electrodes. Before the test the distance from the internal electrode nozzle end to the outer electrode nozzle bottom was equal to 25 mm. The transformers were equipped with thyristor rectifiers. Before the tests the welding units were adjusted at operating current ~280 A. In all tests the argon/nitrogen mixture with proportion 85 % Ar + 15% N<sub>2</sub> was supplied to the plasmatoms inter-electrode space. Tests 1, 5, 6 and 7 were carried out on two transformers VD306C1 #7, 8. The 2<sup>nd</sup> test was performed on the transformer VD306C1 #7; Tests 3 and 4 – on transformer VD306C1 #8.

5.1.5.6 During the first test the electric arc in the plasmatoms was initiated at a one push. In 20 minutes 23 seconds the arc in the plasmatoms was switched off due to reaching temperature 92,6 °C of the transformer secondary winding VD306C1 #7.

During the test the secondary winding of the transformers #7 and #8 were heated up to 92,6 °C and 69,63 °C, respectively. The assumption that such difference in RT readings c.p. MTR.33 and MTR.44 was caused by different rates of operating current of the transformers #7 and #8. With the view of the assumption justification, Tests 2-4 were performed.

5.1.5.7 During the second test which was conducted with the use of the transformer #7, the electric arc was initiated at a one push (argon was supplied to the inter-electrode space). In 2 minutes 51 seconds there was planned outage of the arc in the plasmatoms.

5.1.5.8 During the third test which was conducted with the use of the transformer #8, the electric arc was initiated at a one push (argon was supplied to the inter-electrode space). In 3 minutes 30 seconds there was planned outage of the arc in the plasmatoms. It was noted that the arc running current rate when using transformer #8 was higher than using the transformer #7. Therefore the plasmatoms operating parameters obtained with the use of the transformer #7 were taken as reference value for adjusting running parameters of the plasmatoms with the use

of the transformer #8. To reduce operating current in the transformer secondary winding VD306C1 #8, the transformer primary winding was upward displaced in relation to the transformer construction elements, at that the secondary winding position was not changed.

5.1.5.9 In the fourth test which was performed with the use of the transformer #8, the electric arc was initiated at a one push at 10 hours 22 minutes and 17 seconds (argon was supplied to the inter-electrode space). In 2 minutes 41 seconds after the start-up the arc was spontaneously quenched. In the course of the test the electric arc was spontaneously quenched three times: in 3 minutes 59 seconds, in 4 minutes 35 seconds and in 8 minutes 6 seconds after the test start. Every time the plasmatrons was started up from the CB console. At 10:32 the planned outage of the arc in the plasmatrons was done by the operator. Total running time of the plasmatrons was 4 minutes 47 seconds. Due to unsteady combustion of the electric arc in the plasmatrons it was decided to stop further reduction of the transformer operating current.

5.1.5.10 As a check of the secondary winding heat of the transformers #7 and № 8, after their adjusting at, approximately, equal individual operating current, Test 5 was conducted. In Test 5 the electric arc in the plasmatrons was initiated at a one push (argon/nitrogen mixture was supplied to the inter-electrode space). In 45 minutes 24 seconds the electric arc in the plasmatrons was switched off as the argon available was used up.

Tests #2 – 5 demonstrated that difference in RT readings installed in c.p. MTR.33 and c.p. MTR.44, was conditioned sooner with the feature of each RT position on the transformer secondary winding than with value of the current passing through one transformer.

5.1.5.11 Before Test 6 the adjustment of the transformers running current VD306C1 #7 and #8 was reduced, for that the transformers primary windings were upward displaced by 6 mm in relation to the construction elements.

In Test 6 the electric arc was initiated at a one push. In 38 minutes 35 seconds after the start-up the electric arc in the plasmatrons was switched off due to reaching temperature 92 °C of the secondary winding of the transformer VD306C1 #7.

5.1.5.12 Preceding Test 7 the operating current of the transformers VD306C1 No. 7 and No. 8 was readjusted thereto the transformers primary winding were raised upward on 4 mm.

On conducting Test 7 the electric arc was initiated at a one push. In 3 minutes 48 seconds after starting the operating current of the transformers VD306C1 #7 and #8 was reduced. In 45 minutes 11 seconds after starting up the planned switching off of the electric arc in the plasmatrons was executed.

Physical parameters resulted from the plasmatrons running during the seven experiments of January 20 are included in Table A2.5.2.

Table A2.5.2 – Parameters values of the modified plasmatrons

Parameter	Parameters value						
	1	2	3	4	5	6	7
Test number	1	2	3	4	5	6	7
Time of plasmatrons operation, mm : ss	20:23	2:51	3:30	4:47	45:24	38:35	45:11
Average voltage of electrical arc, V	49,6	41,4	32,7	29,1	43,7	41,8	42,3
Average current of electrical arc, A	280	190	240	214	256	245	231
Average power of plasmatrons, kW	13,8	7,9	7,8	6,2	11,2	10,2	9,8
Maximum warming-up of water in a cooling path of plasmatrons, °C	6,2	2,3	---	---	7,2	6,8	7,0
Heat losses with the cooling water of plasmatrons, %	11,4	6,2	---	---	17,0	17,5	19,2
Maximum temperature of a nozzle of an external electrode, °C							
- c.p. MDT.103 (50 mm from a nozzle end face)	949	300	416	329	1008	945	965
- c.p. MDT.04 (70 mm from a nozzle end face)	659	237	301	339	715	660	694
- c.p. THJ.04 (110 mm from a nozzle end face)	456	145	216	347	479	442	453
Maximum temperature of transformers windings, °C							
- c.p. MTP.11 (Primary winding of VD306C1 #7)	20,2	10,3	7,6	7,0	18,1	27,9	23,2
- c.p. MTP.22 (Primary winding of VD306C1 #8)	18,2	9,6	9,7	9,8	16,4	26,9	21,8
- c.p. MTP.33 (Secondary winding of VD306C1 #7)	92,6	24,8	12,1	13,0	89,9	92,2	76,5
- c.p. MTP.44 (Secondary winding of VD306C1 #8)	69,3	14,2	23,1	27,2	68,7	72,2	54,4

5.1.5.13 On 28.01.2009, the test with plasmatrions was carried out. The objective of the test was to define running parameters of the welding units when temperature of the transformers secondary winding would not exceed 90 °C. The test was performed using the thyristor rectifiers. Preceding the experiment, the running parameters adjustment of the transformers VD306C1 #7 and #8 was increased. Gases mixture composed of 30 % nitrogen and 70 % argon was supplied to the plasmatrions inter-electrode space. In the experiment the electric arc was initiated at a one push. During the test, for the purpose of the preset operating current support, the operating current adjustment of the transformers VD306C1 #7 and #8 was corrected twice. In 2 hours 2 minutes 11 seconds after starting up the planned switching off of the electric arc in the plasmatrions was executed. Physical parameters resulted from the plasmatrions running are included in Table A2.5.3.

Table A2.5.3 – Parameters values of the modified plasmatrions

Parameter	Parameters value	
Data of test performance	28.01.09	3.02.09
Time of plasmatrions operation, hh : mm : ss	2 : 02 : 11	1 : 51 : 11
Average voltage of electrical arc, V	56,0	52,3
Average current of electrical arc, A	233	250
Average power of plasmatrions, kW	13,0	13,0
Maximum warming-up of water in a cooling path of plasmatrions, deg. C	11,7	7,7
Heat losses with the cooling water of plasmatrions, %	17,2	15,7
Maximum temperature of a nozzle of an external electrode, deg. C		
- On distance of 50 mm from a nozzle end face, c.p. MDT.103	1292	1175
- On distance of 70 mm from a nozzle end face, c.p. MDT.04	825	806
- On distance of 110 mm from a nozzle end face, c.p THJ.04	559	559
Maximum temperature of windings of transformers, deg. C		
- Primary winding of the transformer VD306C1 #7, c.p. MTP.11	17,4	29,7
- Primary winding of the transformer VD306C1 # 8, c.p. MTP.22	19,4	33,2
- Secondary winding of the transformer VD306C1 #7, c.p. MTP.33	78,6	105,5
- Secondary winding of the transformer VD306C1 #8, c.p. MTP.44	57,4	93,6
Distance from the bottom end face of a nozzle of an internal electrode to the nozzle bottom of an external electrode, mm		
- before test	25	25
- after test (minimum distance)	26	25
Mass of graphite nozzle of inner electrode, kg:		
- before test	0,3046	0,297
- after test	0,297	0,292
Mass of bottom part of graphite nozzle of outer electrode, kg:		
- before test	0,5799	0,5261
- after test	0,5261	0,4952

5.1.5.14 On 03.02.2009, the test with plasmatrions was carried out. The objective of the test was to define running parameters of the welding units when temperature of the transformers secondary winding would not exceed 90 °C. Before the experiment start the thyristor rectifiers were changed for the standard diode rectifiers in the welding units. Gases mixture composed of 30 % nitrogen and 70 % argon was supplied to the plasmatrions inter-electrode space. In the experiment the electric arc was initiated at a one push. At constant relative position of primary and secondary windings of the transformers the replacement of thyristor rectifiers for standard diode ones resulted in the arc running current rise from 240 to 300 A. It was decided to reduce the adjustment of the rectifiers running current to 240 A.

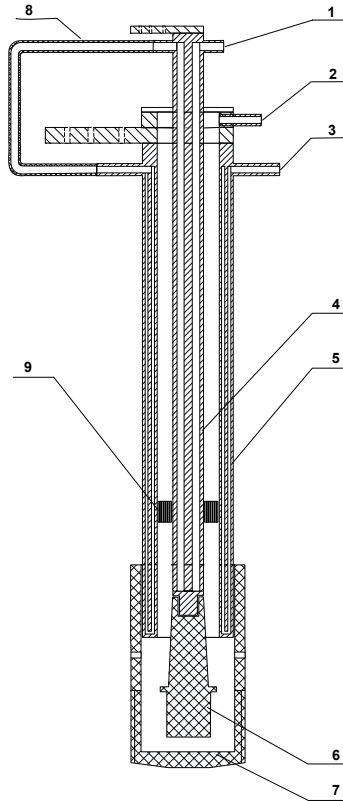
After 90 minutes of the plasmatrions run additional tests were conducted:

- the operability of the plasmatrions at the given transformers VD setup with supplying nitrogen to the inter-electrode space was tested;
- medium pressure in the MR (~1,3 gage atm) where arc quenching was occurred in supplying gas mixture composed of 30 % nitrogen and 70 % argon to the inter-electrode space, was defined.

It was shown that in supplying nitrogen instead of nitrogen/argon gases mixture to the inter-electrode space the plasmatrons power increased by  $\sim 1$  kW, but arcing nature became less steady.

In 1 hour 51 minutes 11 seconds after the plasmatrons startup the routine arc disconnection in the plasmatrons was carried out. Physical parameters resulted from the plasmatrons running are included in Table A2.5.3.

5.1.5.15 From these tests the parameter variation curves were plotted (see also Figures A2.5.2...A2.5.19).



1 – cooling water release; 2 – gas supply to the inter-electrode space; 3 – cooling water supply; 4 – internal electrode; 5 – outer electrode; 6 – cylindrical graphite nozzle of the internal electrode; 7 – composite graphite nozzle of the outer electrode; 8 – rubber hose; 9 – center sleeve.

Figure A2.5.1 – Scheme of plasmatrons assembly

### 5.1.6 Conclusion

5.1.6.1 On supplying nitrogen to the inter-electrode space it was not succeeded in steady operating of the plasmatrons at running current 230 A. When increasing the current up to 270 A, spontaneous arc extinction in the course of the plasmatrons operation was not found, but the temperature of the transformers secondary winding exceeded  $100^{\circ}\text{C}$ .

5.1.6.2 At the same position of the transformers primary and secondary winding of the welding units of group “D” the replacement of the customized thyristor rectifiers for standard diode ones resulted in the arc current rise by  $\sim 60$  A.

5.1.6.3 The plasmatrons running regimes were selected, where the temperature of the transformers secondary winding of the VD306C1 did not exceed  $90^{\circ}\text{C}$ :

- when operating with thyristor rectifiers (with supply of gases mixture composed of nitrogen and argon to the inter-electrode space of the plasmatrons) the running arc current was  $\sim 240$  A, and plasmatrons power  $\sim 13$  kW;

- when operating with diode rectifiers (with supply of gases mixture composed of nitrogen and argon to the inter-electrode space of the plasmatrons) the running arc current was  $\sim 240$  A, and plasmatrons power  $\sim 12$  kW.



5.1.6.4 The steady running of the plasmatrons using gases mixture composed of 30 % nitrogen and 70 % argon is possible before gas pressure in the MR ~1,3 gage atm. In further pressure rise in the MR the plasmatrons arc extinction will take place.

5.1.6.5 Change of argon/nitrogen mixture supplied to the inter-electrode space for pure nitrogen, at the same welding units setting, results in plasmatrons power increase by ~1 kW, but arcing nature becomes unsteady and arc extinction in the plasmatrons is possible.

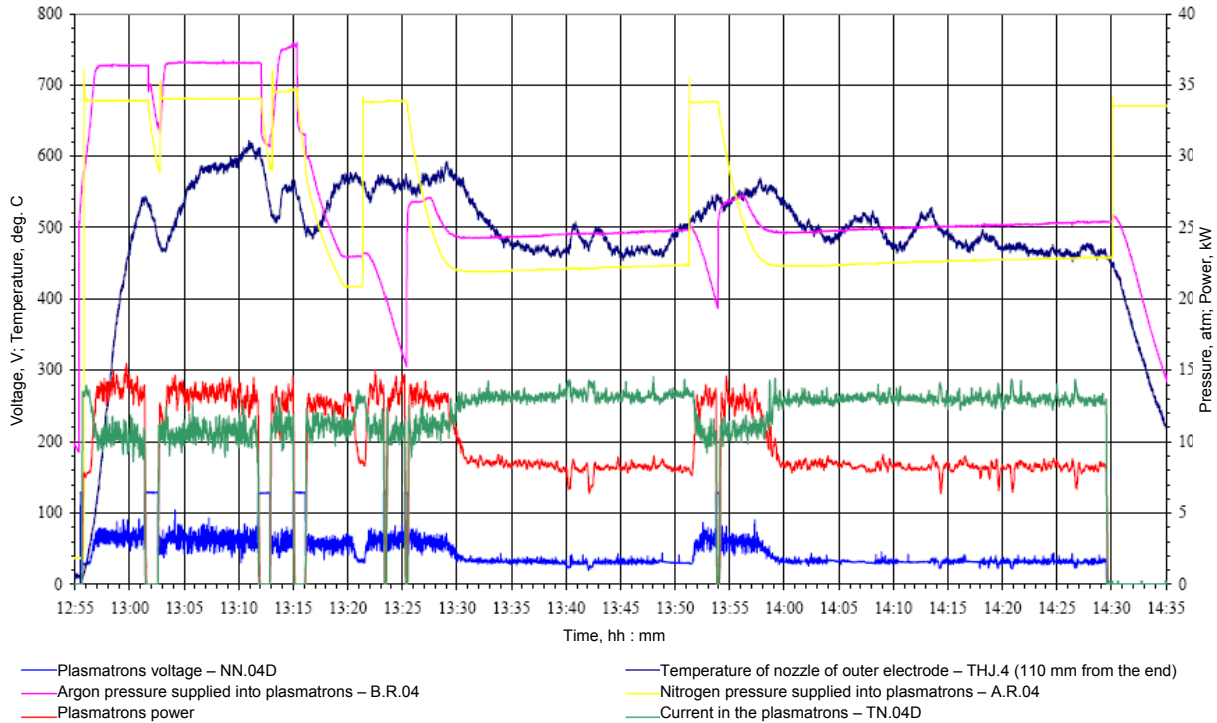


Figure A2.5.2 – Change of plasmatrons parameters in the course of test at 09.01.2009

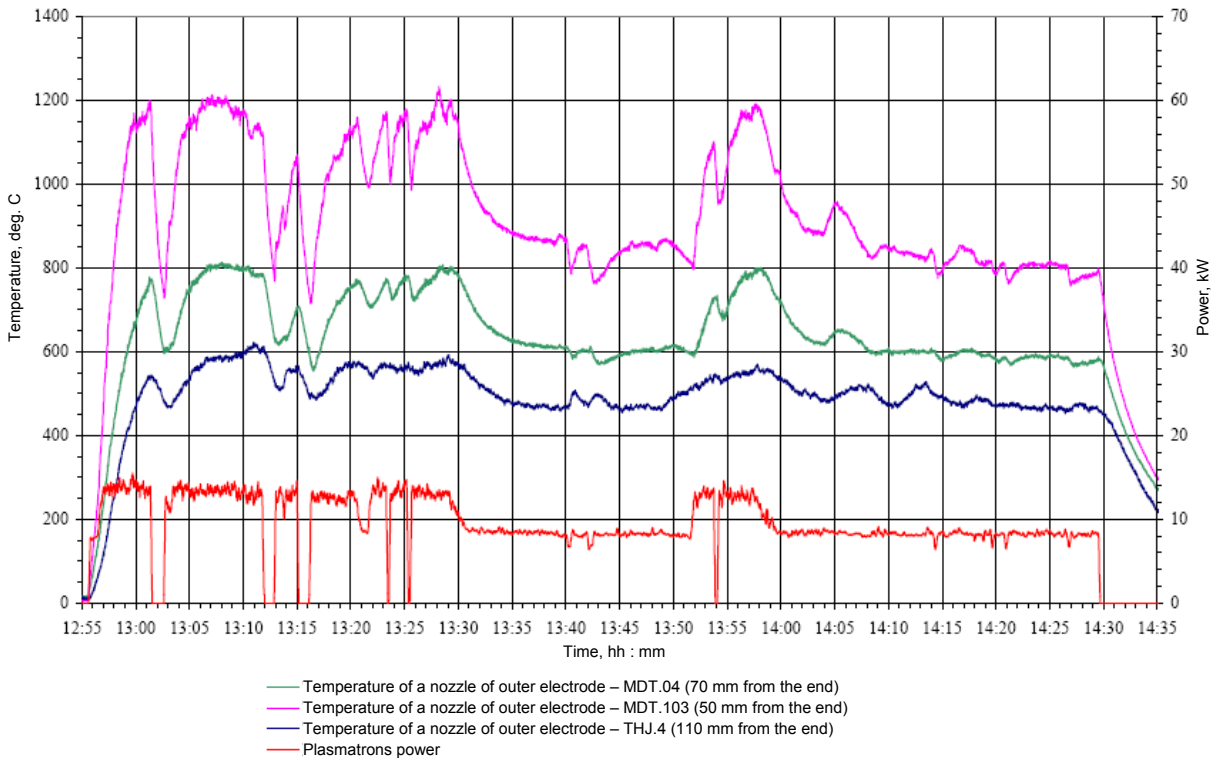


Figure A2.5.3 – Change of a nozzle temperature of outer electrode in the course of test at 09.01.2009

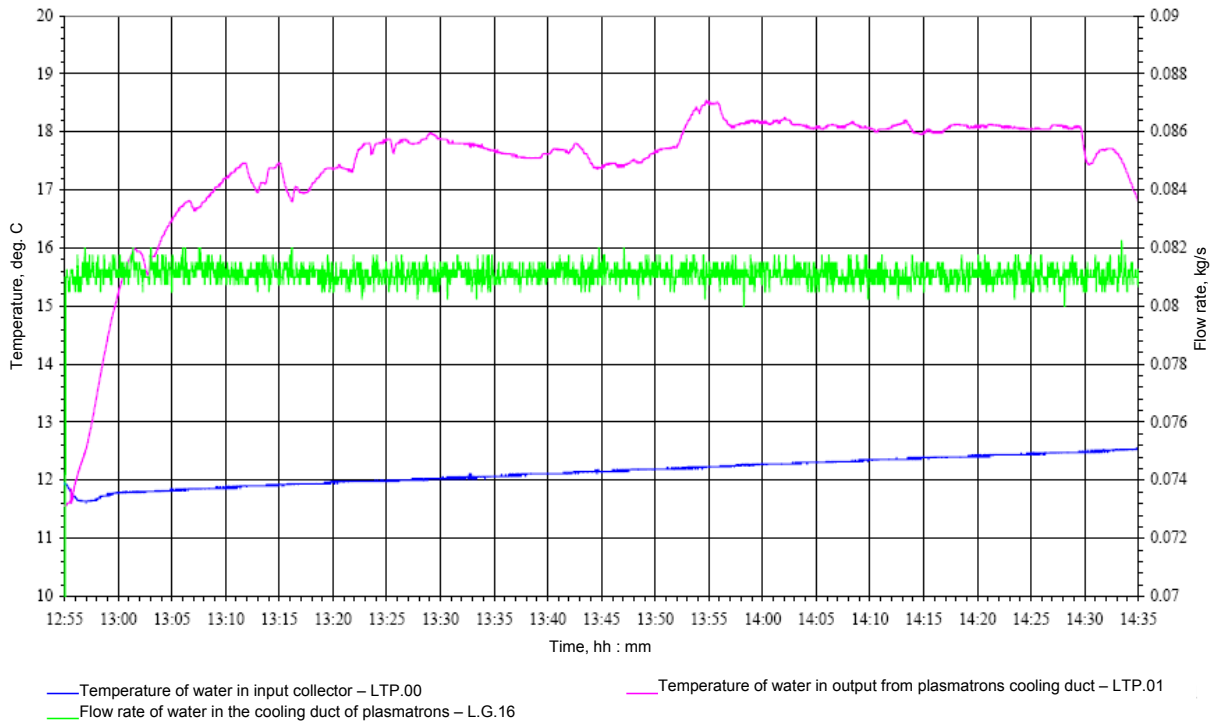


Figure A2.5.4 – Change of water parameters for plasmatrons cooling in the course of test at 09.01.2009

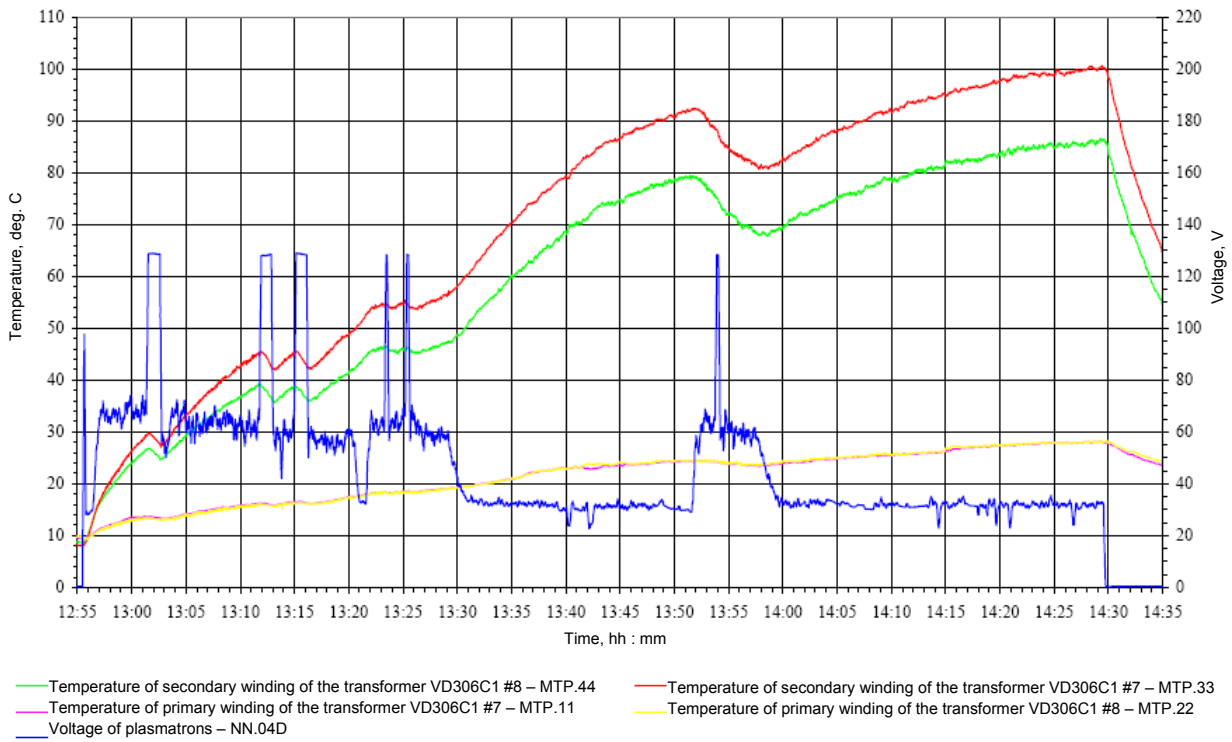


Figure A2.5.5 – Change of temperature of the transformers windings in the course of test at 09.01.2009

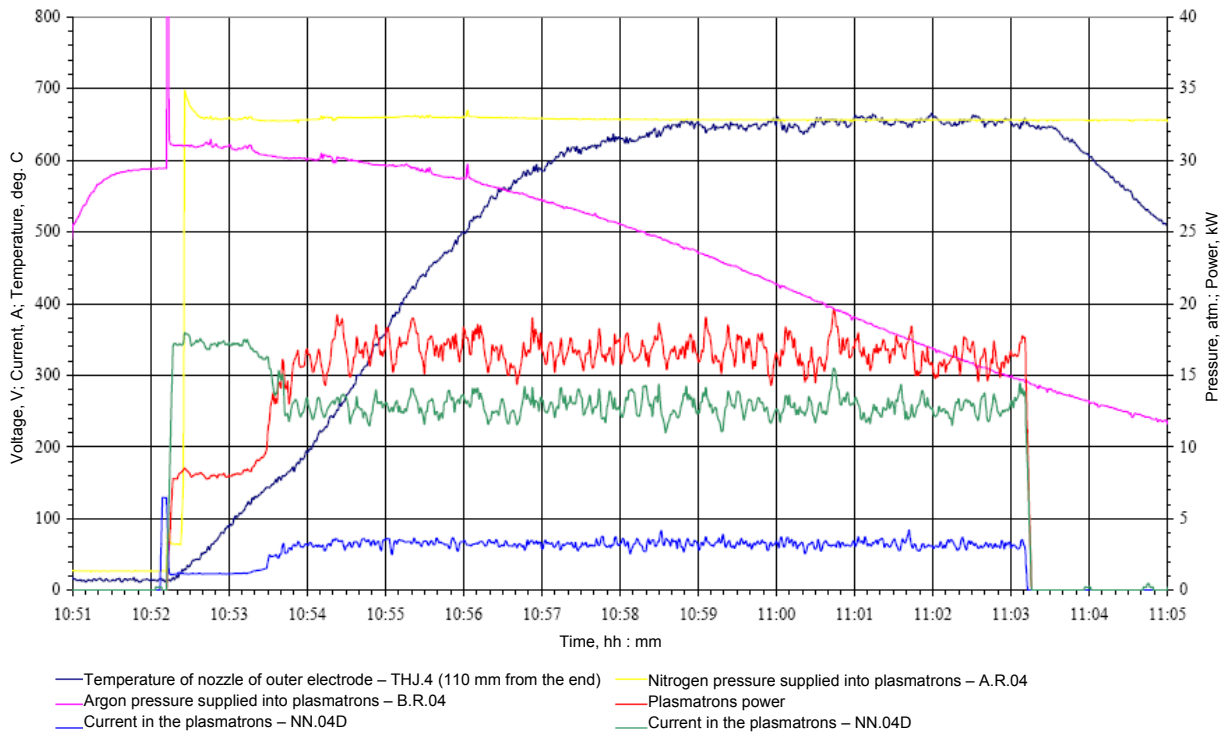


Figure A2.5.6 – Change of plasmatrone parameters in the course of test at 12.01.2009

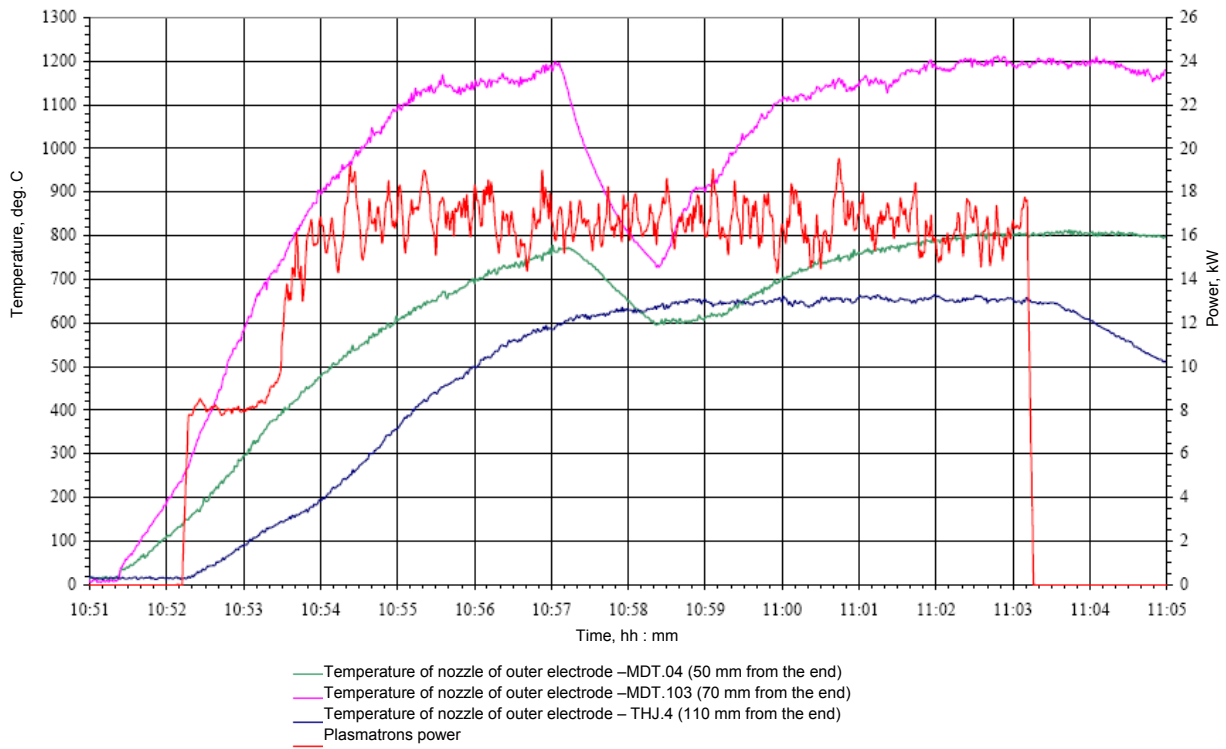
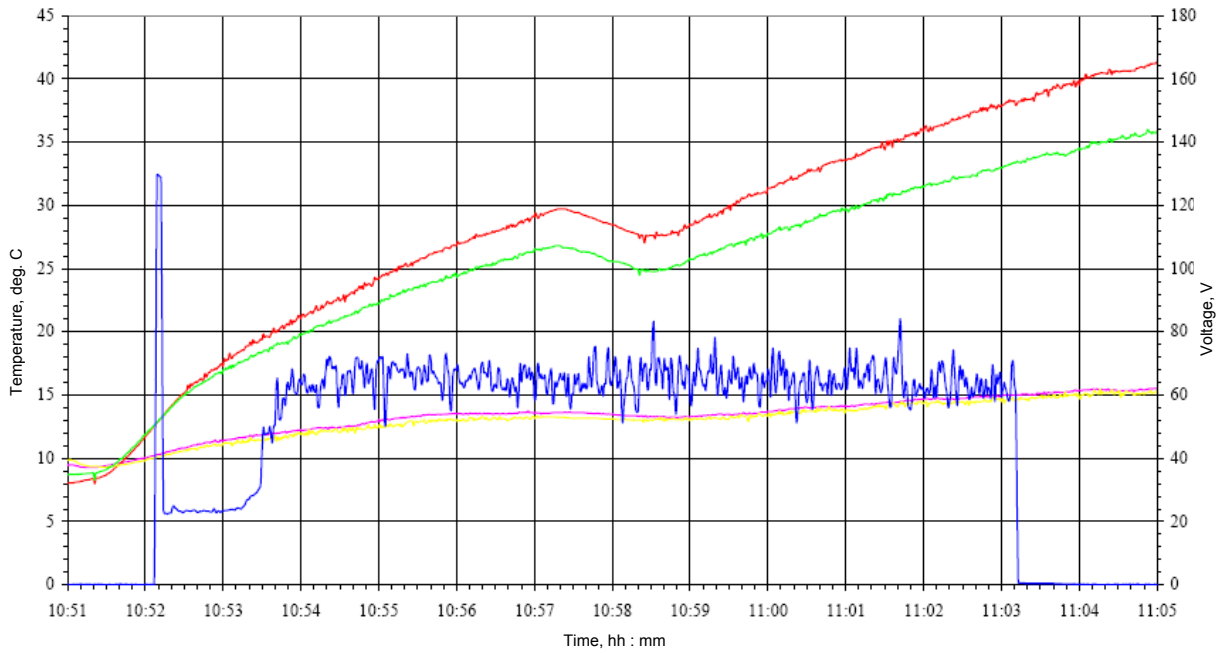
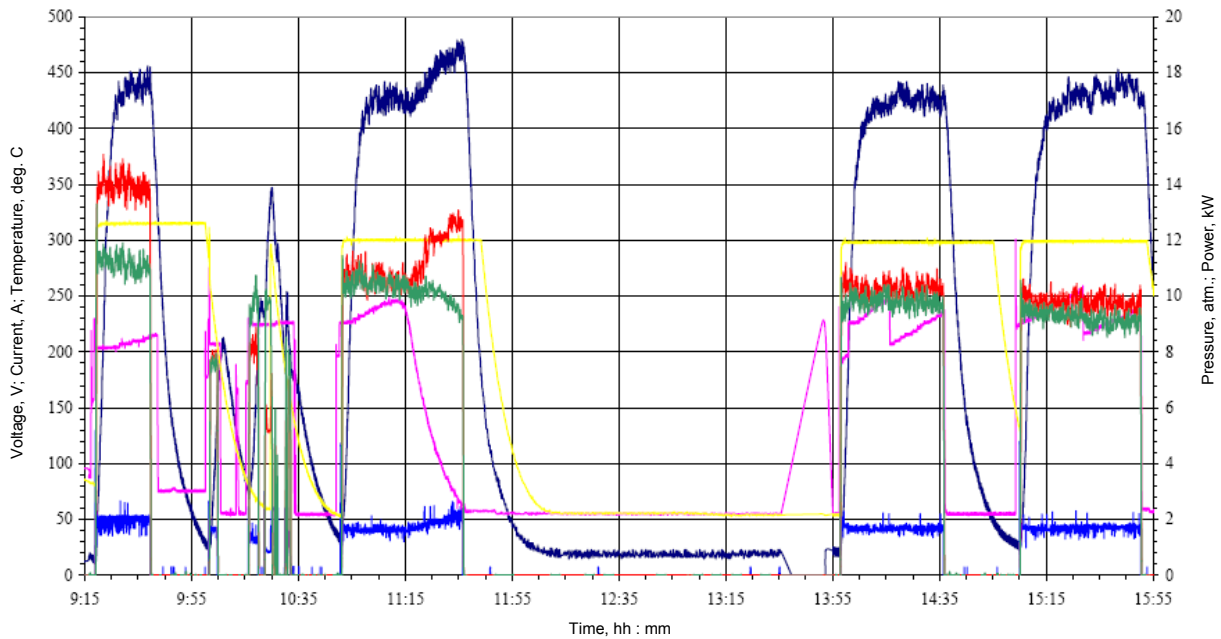


Figure A2.5.7 – Change of temperature of a outer electrode nozzle in the course of test at 12.01.2009



— Temperature of primary winding of VD306C1 #7 -MTP.11  
— Temperature of primary winding of VD306C1 #8 -MTP.22  
— Plasmatrons voltage - NN.04D  
— Temperature of secondary winding of VD306C1 #7 -MTP.33  
— Temperature of secondary winding of VD306C1 #8 -MTP.44

Figure A2.5.8 – Change of temperature of transformers windings in the course of test at 12.01.2009



— Temperature of nozzle of outer electrode - THJ.4 (110 mm from the end)  
— Argon pressure supplied in a plasmatrons - BR.04  
— Plasmatrons power  
— Plasmatrons voltage - NN.04D  
— Nitrogen pressure supplied in a plasmatrons - AR.11  
— Current of plasmatrons - TN.04D

Figure A2.5.9 – Change of plasmatrons parameters in the course of test at 20.01.2009



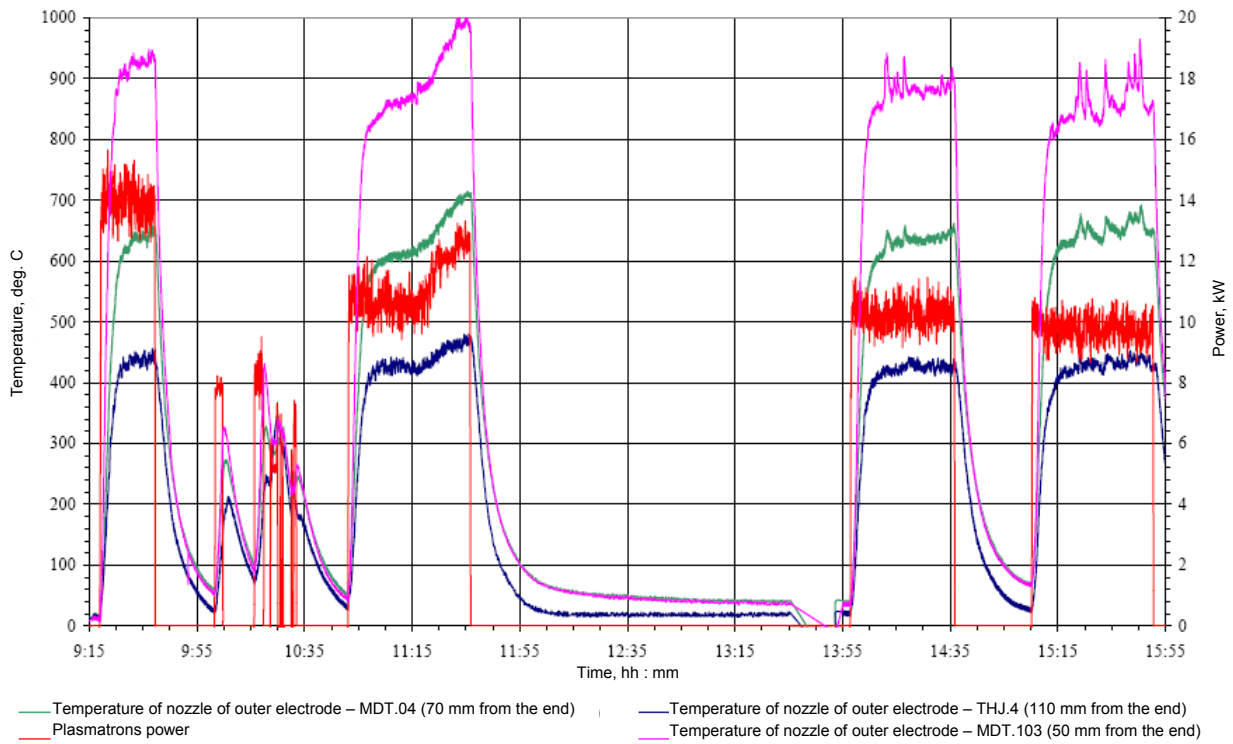


Figure A2.5.10 – Change of temperature of the outer electrode nozzle in the course of test at 20.01.2009

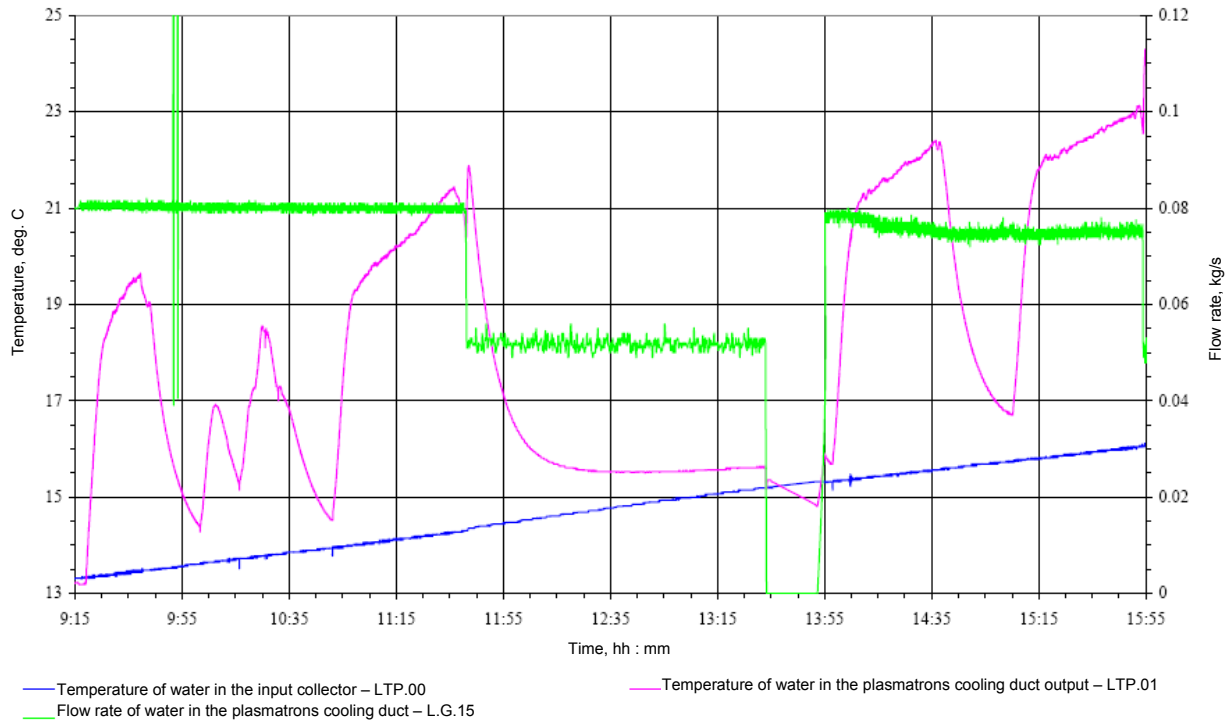


Figure A2.5.11 – Change of water parameters for plasmatrons cooling in the course of test at 20.01.2009

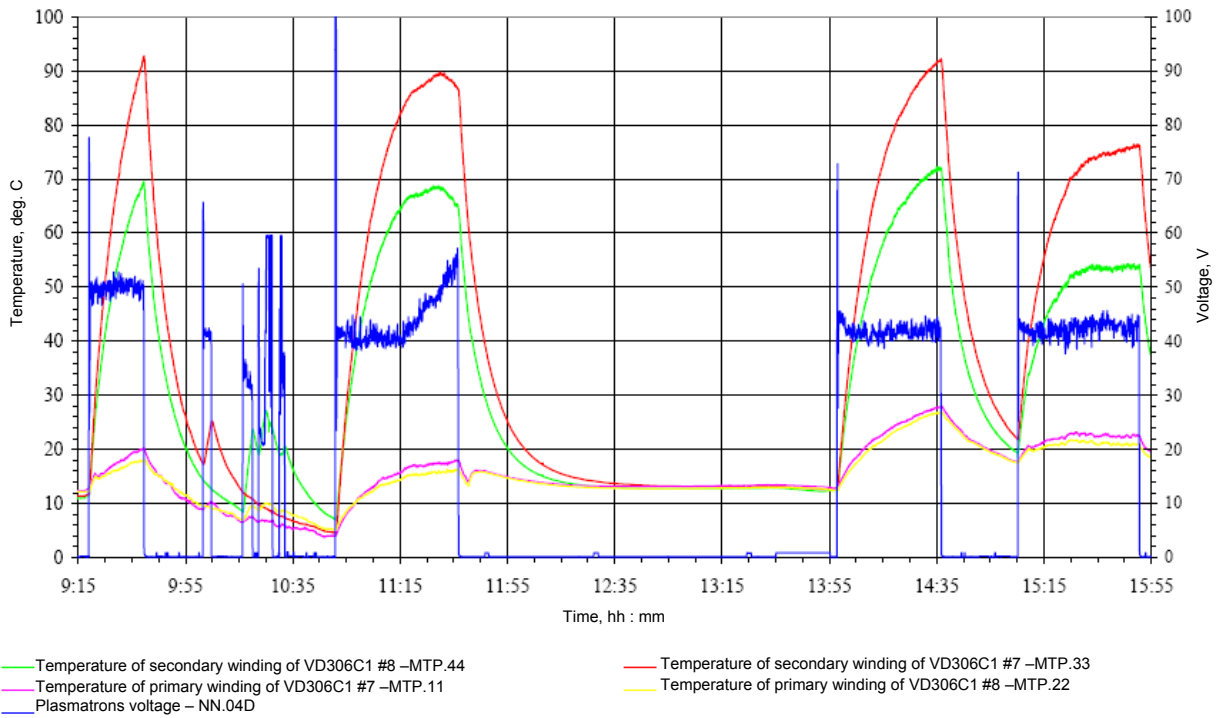


Figure A2.5.12 – Change of temperature of transformers windings in the course of test at 20.01.2009

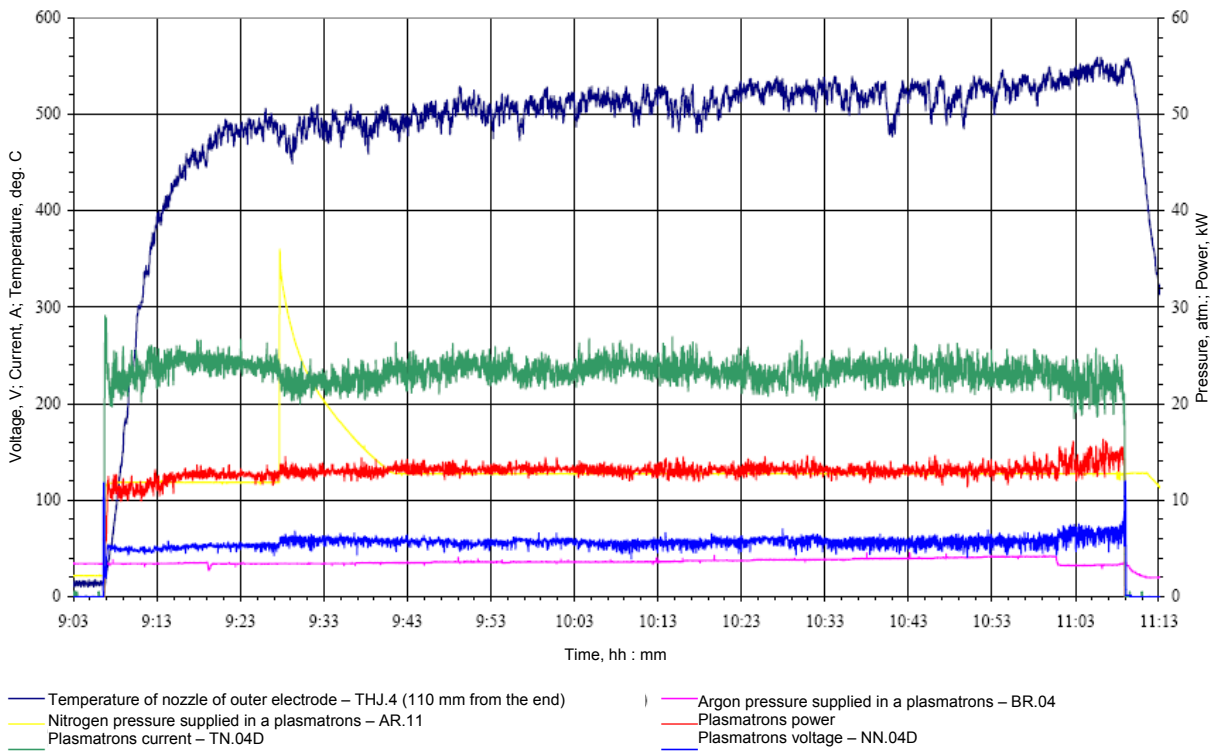


Figure A2.5.13 – Change of plasmatrons parameters in the course of test at 28.01.2009

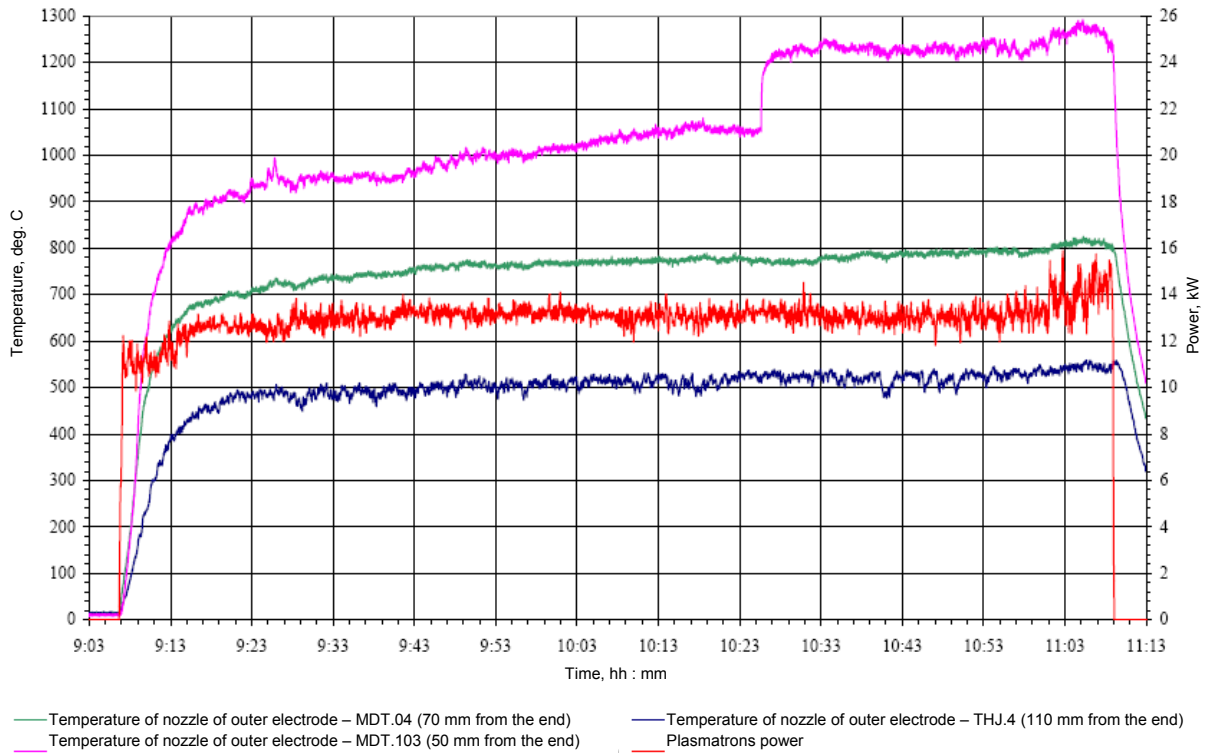


Figure A2.5.14 – Change of temperature of the outer electrode nozzle in the course of test at 28.01.2009

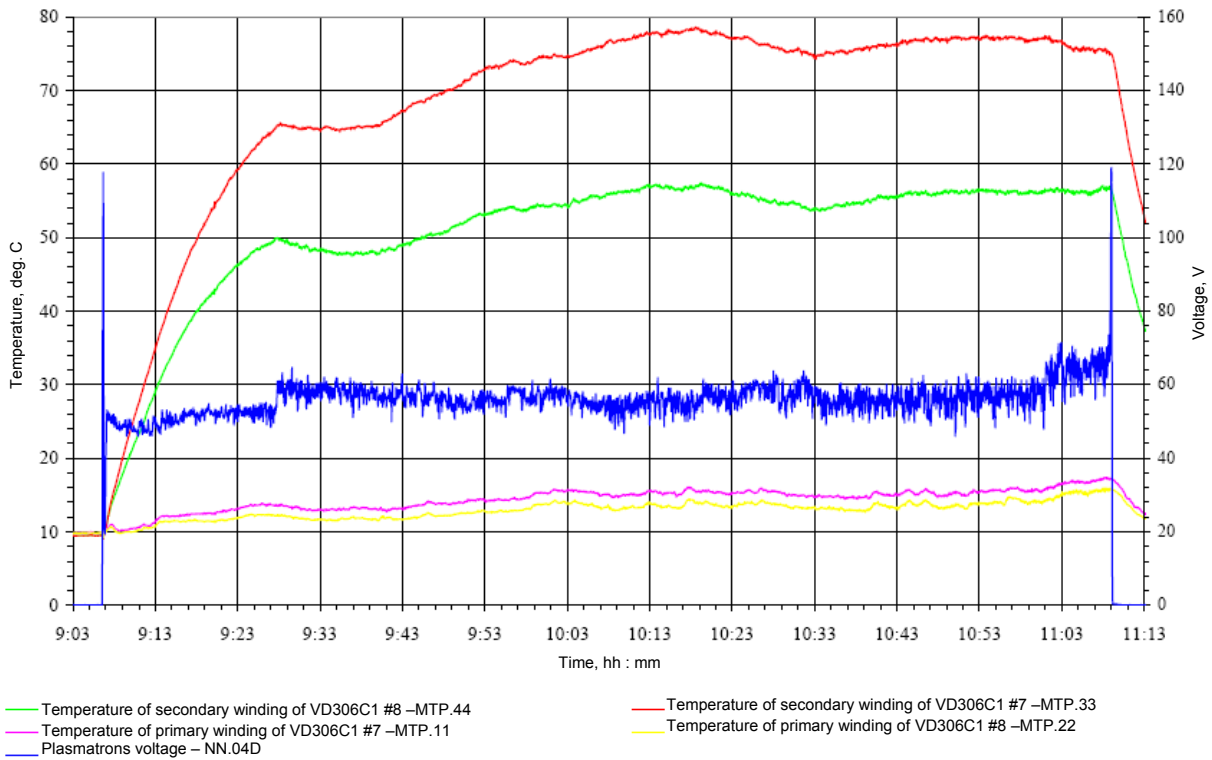


Figure A2.5.15 – Change of temperature of transformers windings in the course of test at 28.01.2009

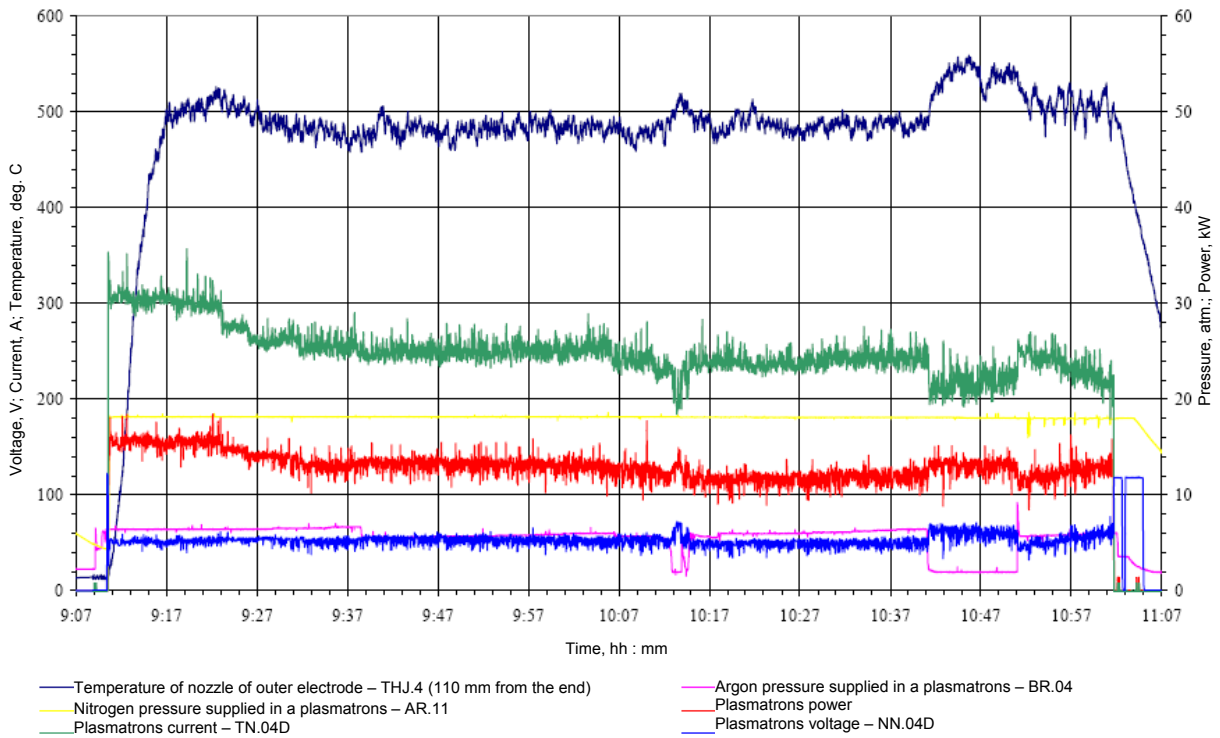


Figure A2.5.16 – Change of plasmatron parameters in the course of test at 03.02.2009

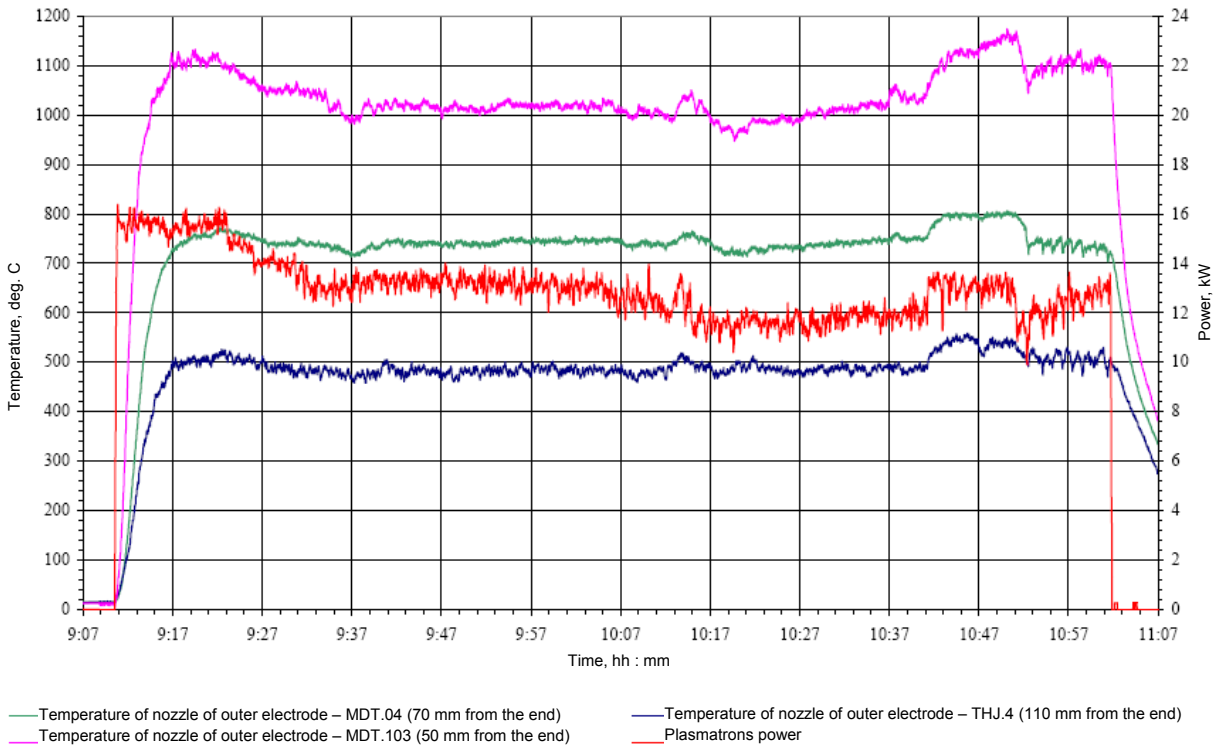


Figure A2.5.17 – Change of temperature of the outer electrode nozzle in the course of test at 03.02.2009



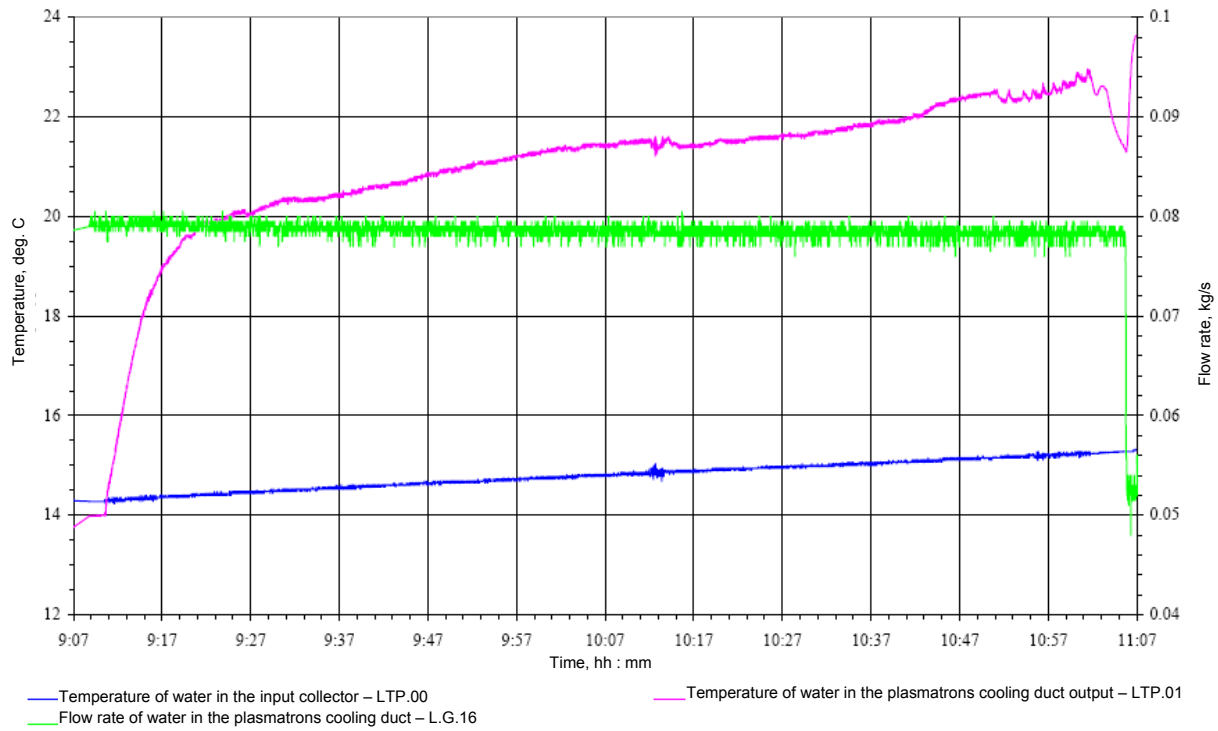


Figure A2.5.18 – Change of water parameters for plasmatrons cooling in the course of test at 03.02.2009

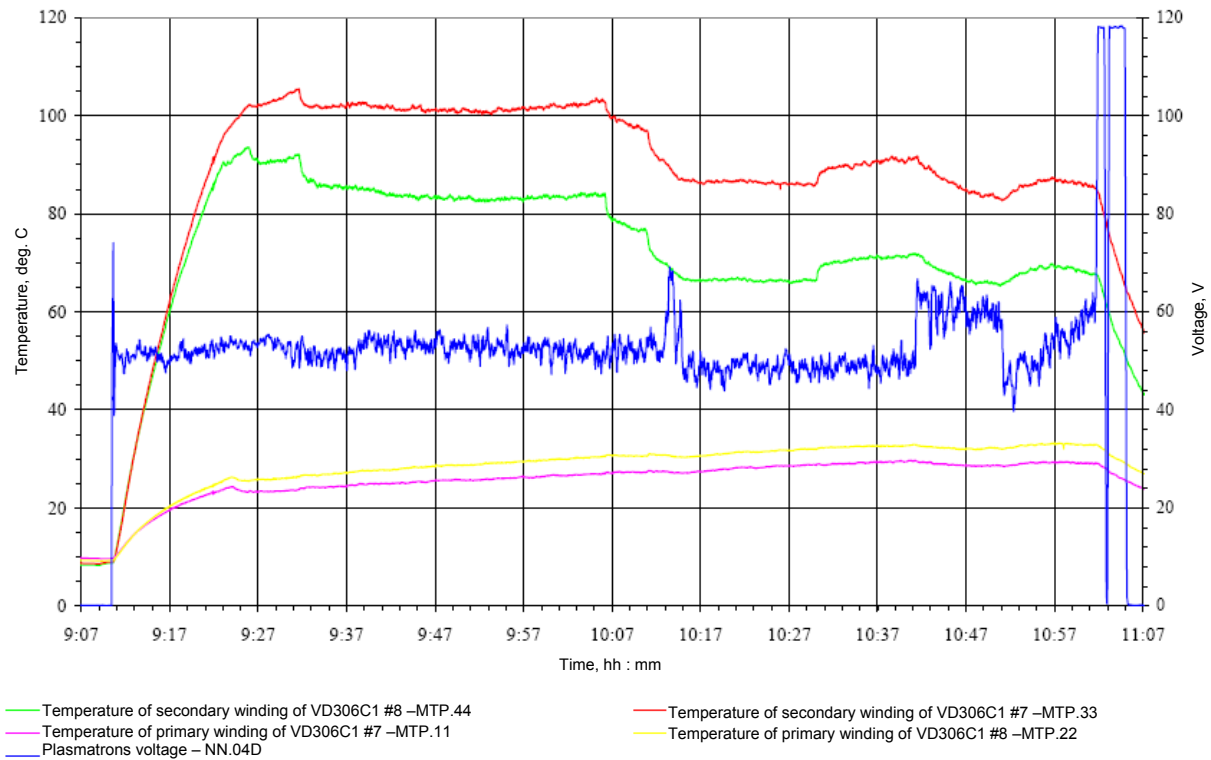


Figure A2.5.19 – Change of temperature of transformers windings in the course of test at 03.02.2009

## 5.2 Testing of a modified plasmatrons and VD306C1 transformers of group "D" and "E" of system of melt heating

5.2.1 Subject of study – the melt heating system in the RPV model of "LAVA-B" facility.

5.2.2 Objective of the test:

- testing of the modified plasmatrons;
- testing of transformers VD306C1 of groups "D" and "E" operability;
- life testing of transformers VD306C1 of group "E".

### 5.2.3 General conditions

5.2.3.1 The melt heating system in the reactor lower head model (drawing № ДКИЖ.681.613.001.СБ) is designed for simulating heat decay in the melt located in the lower head model. The lower head model with the plasmatrons installed was located in the "LAVA-B" pressure vessel.

5.2.3.2 The tests were carried out in the thermo-technical test facility "ANGARA".

5.2.3.3 The experiments were carried out in compliance with the program and procedure "Testing of the melt heating system with modified plasmatrons" reg. No. 240-02/142 of 5.11.2008 and according to the decision on off-line pre-commissioning (OLPC) of the melt heating system in the reactor lower head model, reg. No. D697 of 18.11.2008.

### 5.2.4 Tests conditions

5.2.4.1 Experimental work on the melt heating system in the reactor lower head model was performed in building 10 of the "ANGARA" thermo-technical test facility.

5.2.4.2 Magnetic medium recording and data display were performed by means of the "ANGARA" test facility data acquisition system (DAS).

5.2.4.3 The test facility automatic control systems (ACS) were managed manually.

5.2.4.4 Nominal parameters of the melt heating system in the reactor vessel lower head model are as follows:

- maximum value of the plasmatrons working current, A – to 315;
- plasmatrons volts, V – to 70;
- open circuit volts on the plasmatrons, V – to 140;
- water flow rate through the plasmatrons cooling path, kg/s – to 0,08;
- consumption of argon supplied to inter-electrode space, kg/s – 0,0005;
- consumption of nitrogen supplied to inter-electrode space, kg/s – 0,0005.

5.2.4.5 The work was done using the modified plasmatrons "A" installed on the reactor lower head model and transformers VD306E of group "A" and transformers VD306C1 of groups "D" and "E". The modified plasmatrons construction is illustrated in Figure A2.5.1. The length of the working part of the outer electrode of the modified plasmatrons was reduced from 377 mm to 207 mm. The length of the working part of the internal electrode of the modified plasmatrons was reduced respectively from 660 mm to 450 mm.

5.2.4.6 Plasmatrons voltage was measured by the standard normalizing converter 73G-IV10 (c.p. NN.01A, NN.04D, NN.05E).

5.2.4.7 Plasmatrons current strength was measured by the standard normalizing converter 73G-IV100M (c.p. TH.01A, TH.04D, TH.05E).

5.2.4.8 Working medium and facility elements temperature was measured by the standard thermocouples of the "LAVA-B" test facility.

5.2.4.9 Working medium pressure was measured with the standard pressure gauges DDM.

5.2.4.10 Working parameters were measured with the certified instruments.

5.2.4.11 To supply gas to the inter-electrode space, the needle with effective open area  $6,566 \times 10^{-8} \text{ m}^2$  was installed in the supply path.

5.2.4.12 On the graphite nozzle of the plasmatrons outer electrode there were installed three thermocouples: c.p. CLT.01 at a distance 110 mm from the nozzle end, c.p. MDT.04 at a distance 70 mm from the nozzle end and c.p. MDT.103 at a distance 50 mm from the nozzle end.

5.2.4.13 Electric arc ignition was performed with supply of argon to the inter-electrode space with its further change for nitrogen.

5.2.4.14 The former-used graphite nozzles were installed on the electrodes. The nozzle made of graphite R4340 was installed on the internal electrode, and on the outer electrode – the nozzle made of graphite ARV-1.

5.2.4.15 Before the first start-up of the plasmatrons the distance from the internal electrode nozzle end to the outer electrode nozzle bottom was equal to 30 mm. In further plasmatrons

startups the distance between the nozzles was not corrected.

#### 5.2.5 Scope of activity accomplished

5.2.5.1 The test sequence is stated in the "functional program" (inv. No. D 698 of 18.11.2008).

5.2.5.2 From 13.11.2008 up to 20.11.2008, five tests with plasmatrons start-up and using transformers VD306E of group "A" and transformers VD306C1 of groups "D" and "E" as a power-supply source were performed.

5.2.5.3 On 13.11.2008, the plasmatrons start-up was attempted using transformer VD306E of group "A" as a power-supply source. On plasmatrons starting up the electric arc was struck. After plasmatrons coming to the steady-state condition the routine disconnection of the arc was taken place. The arcing period in the plasmatrons was 7 minutes 36 seconds. The implemented physical parameters resulted from the plasmatrons running are included in Table A2.5.4.

Table A2.5.4 – Parameters values of modified plasmatrons

Parameter	Parameter value
Time of plasmatrons operation, mm : ss	07 : 36
Average voltage of electrical arc, V	57,5
Average current of electrical arc, A	325
Average power of plasmatrons, kW	18,7
Maximum temperature of a nozzle of an external electrode, deg. C	
- On distance of 50 mm from a nozzle end face, c.p. MDT.103	-
- On distance of 70 mm from a nozzle end face, c.p. MDT.04	1112
- On distance of 110 mm from a nozzle end face, c.p. CLT.01	626

5.2.5.4 On 18.11.2008, after the plasmatrons power transfer from transformers of group "A" to group "D" and then to the transformers of group "E", there were conducted two plasmatrons startups. In the experiments the electric arc was initiated at first oscillator response. After coming to the steady state condition the routine disconnection of the plasmatrons arc was carried out. The plasmatrons run time on the transformers of group "D" was 9 minutes 10 seconds, and on transformers of group "E" – 7 minutes 49 seconds. The implemented physical parameters resulted from the plasmatrons running are included in Table A2.5.5.

Table A2.5.5 – Parameters values of modified plasmatrons

Parameter	Parameter value	
	Group "D"	Group "E"
Time of plasmatrons operation, mm : ss	09 : 10	07 : 49
Average voltage of electrical arc, V	55,3	54,3
Average current of electrical arc, A	217,6	214,1
Average power of plasmatrons, kW	12,0	11,6
Maximum temperature of a nozzle of an external electrode, deg. C		
- On distance of 50 mm from a nozzle end face, c.p. MDT.103	1346	1372
- On distance of 70 mm from a nozzle end face, c.p. MDT.04	996	958
- On distance of 110 mm from a nozzle end face, c.p. CLT.01	687	685

5.2.5.5 On 19.11.2008, the start-up of the plasmatrons using the units VD306C1 of group "E" as a power-supply source was conducted. The outer electrode end was covered with thermo insulation material – three-layer graphite felt of ~6 – 8 mm thickness. The thermo-insulation height was ~90 mm. On the plasmatrons starting the electric arc was struck at a one push. In 5 minutes 14 seconds after the startup the routine arc disconnection was carried out. In the course of the plasmatrons start-up the standard normalizing converter 73G-IV10 was failed and further pressure registration was performed by means of the indicating gage from the control board (CB). The implemented physical parameters resulted from the plasmatrons running are included in Table A2.5.6.

Table A2.5.6 – Parameters values of modified plasmatrons

Parameter	Parameter value
Time of plasmatrons operation, mm : ss	05 : 14
Average voltage of electrical arc, V	65 <sup>*)</sup>
Average current of electrical arc, A	213,9
Average power of plasmatrons, kW	13,9 <sup>**)</sup>
Maximum temperature of a nozzle of an external electrode, deg. C	
- On distance of 50 mm from a nozzle end face, c.p. MDT.103	1938
- On distance of 70 mm from a nozzle end face, c.p. MDT.04	1195
- On distance of 110 mm from a nozzle end face, c.p. CLT.01	858

Note: <sup>\*)</sup> – averaged value according to the indicating gage in the CB.

<sup>\*\*)</sup> – on calculating plasmatrons power, the arc voltage was taken from the CB indicating gage readings.

5.2.5.6 On 20.11.2008, the start-up of the plasmatrons using the units VD306C1 of group "E" as a power-supply source was conducted. On plasmatrons starting up the arc was struck. In the course of the test the electric arc was spontaneously extinguished three times: in 4, 16 and 34 minutes after the experiment start. Every time the plasmatrons startup was conducted from CB console, moreover the interruption of plasmatrons operation did not exceed 20 seconds. At 15:40 the electrical system operator reported that the heating of the welding units of group "E" was in exceed of allowable norm. The experiment was stopped. Total plasmatrons running time was 1 hour 26 minutes 53 seconds. The implemented physical parameters resulted from the plasmatrons running are included in Table A2.5.7.

Table A2.5.7 – Parameters values of modified plasmatrons obtained at 20.11.2008

Parameter	Parameters value
Time of plasmatrons operation, hh : mm : ss	1 : 26 : 53
Average voltage of electrical arc, V	62,7
Average current of electrical arc, A	316,7
Average power of plasmatrons, kW	19,9
Maximum warming-up of water in a cooling path of plasmatrons, deg. C	13,0
Heat losses with the cooling water of plasmatrons, %	16,6
Maximum temperature of a nozzle of an external electrode, deg. C	
- On distance of 50 mm from a nozzle end face, c.p. MDT.103	1482
- On distance of 70 mm from a nozzle end face, c.p. MDT.04	1046
- On distance of 110 mm from a nozzle end face, c.p. CLT.01	603
Distance from the bottom end face of a nozzle of an internal electrode to the nozzle bottom of an external electrode, mm	
- before test	30
- after test (minimum distance)	33
Mass of graphite nozzle of an inner electrode, kg:	
- before test	0,275
- after test	0,260

After completion of the test the internal and outer electrodes nozzles were examined. In the result of the examination there were detected as follows:

- the surface of the internal electrode nozzle was burned out non-uniformly, total length of the nozzle was reduced by 3 mm;
- practically overall working surface of the cylindrical graphite nozzle of the internal electrode was covered with a light-grey film;
- arc effect marks are available on the internal surface of the outer electrode composite nozzle bottom.

From the examination and measurement of the transformer winding resistance of the units "E" there were detected as follows:

- no apparent failures on the transformer windings;
- the transformer winding resistance meets with the passport data. The winding insulation failures were not found;
- the diode bridges of both welding units were failed: one diode was failed in unit #9, and three – in unit #10.

5.2.5.7 From these tests the parameter variation curves were plotted (see also Figures A2.5.20...A2.5.36).

5.2.5.8 Figures A2.5.37... A2.5.39 represent the photos of the internal and outer electrode nozzles after a group of tests.

## 5.2.6 Conclusion

5.2.6.1 The modified plasmatrone has been tested. In the test the averaged plasmatrone power was 18,7 kW (supply from the units of group "A").

5.2.6.2 The operability test of the units VD306C1 of group "D" and "E" was conducted.

5.2.6.3 In life testing of the units VD306C1 of group "E" the averaged power of the modified plasmatrone was 19,9 kW. Rate of the internal electrode nozzle material burn out was ~0,17 gram per minute.

5.2.6.4 In order to continue the tests the diode bridges of the units VD306C1 of group "E" should be restored as well as the thermocouples on the secondary coils in the region of diode bridges of the welding units transformers should be installed for monitoring temperature.

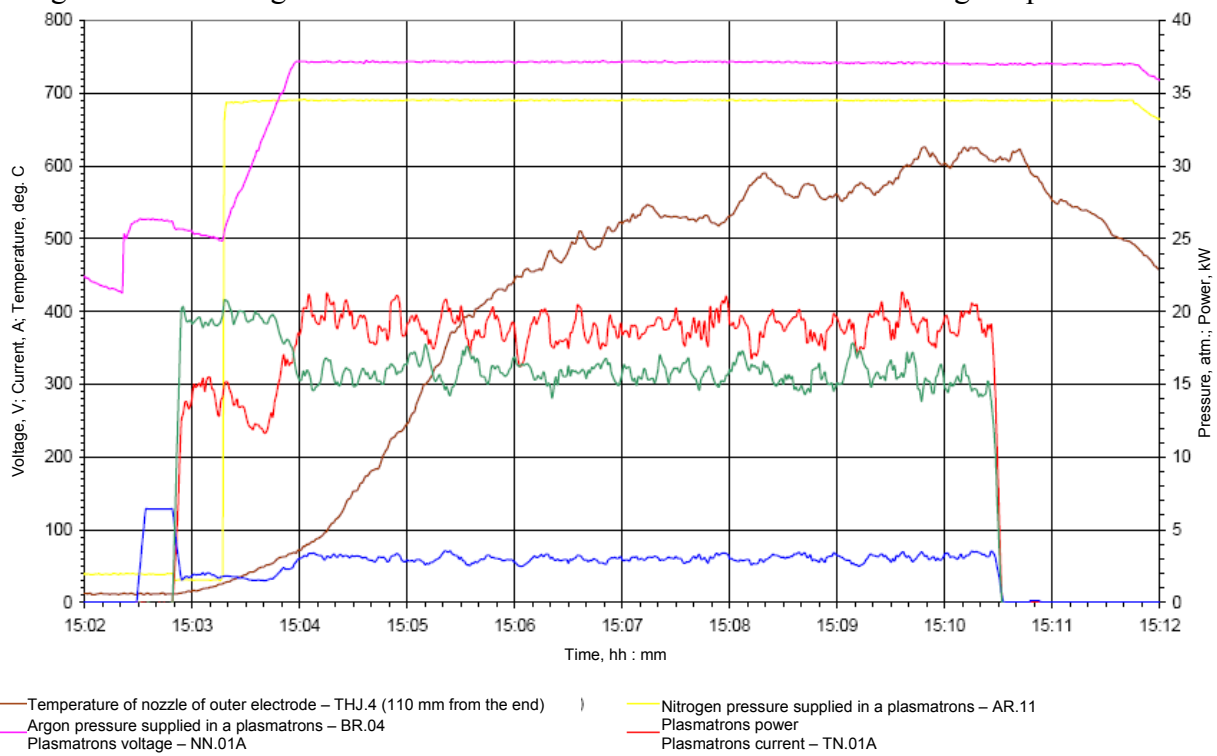
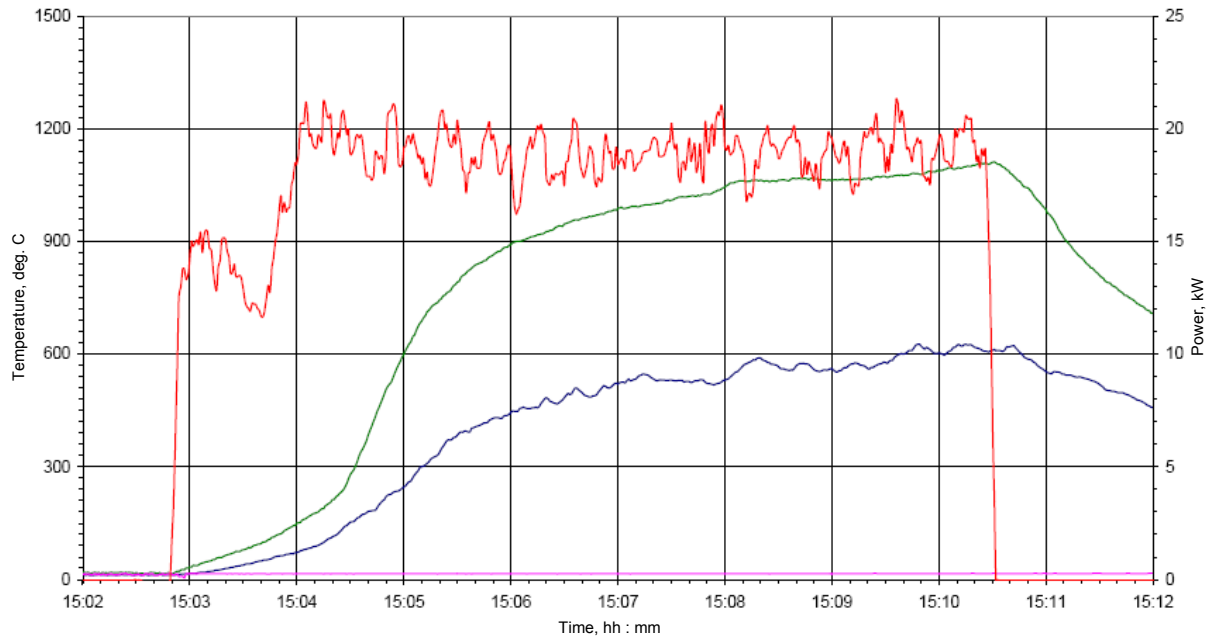


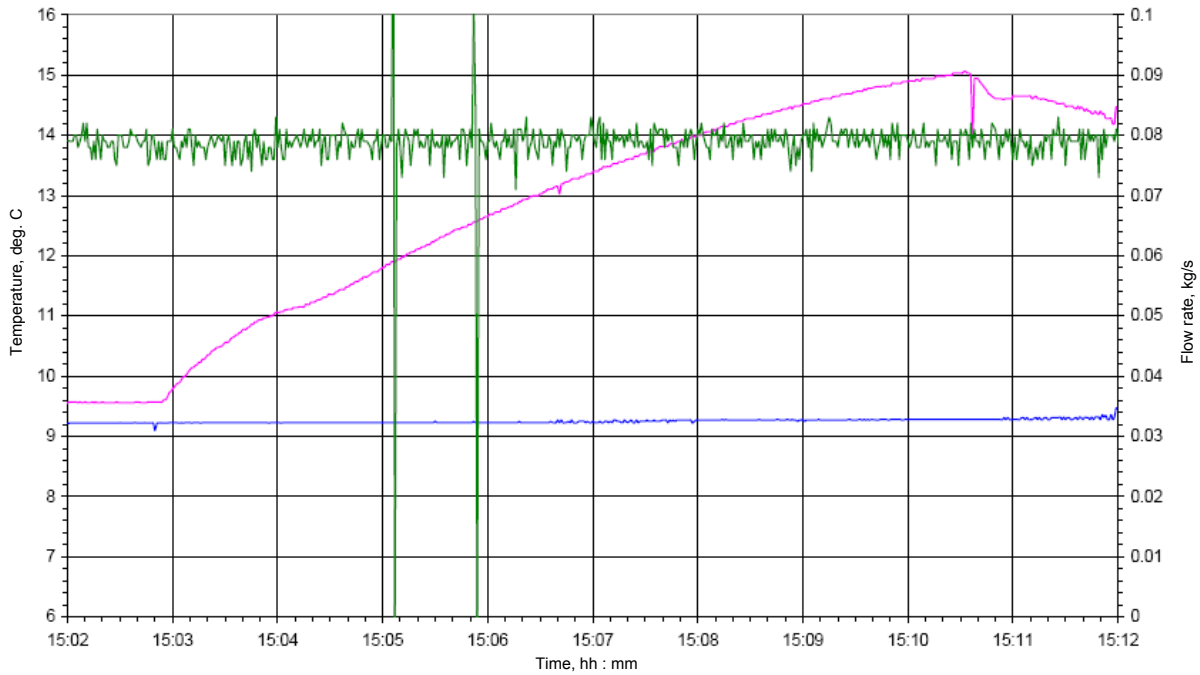
Figure A2.5.20 – Change of plasmatrone parameters (13.11.2008). Plasmatrone electric power supply from transformers of "A" group





— Temperature of nozzle of outer electrode – CLT.01 (110 mm from the end) — Temperature of nozzle of outer electrode – MDT.04 (70 mm from the end)  
 — Temperature of nozzle of outer electrode – MDT.103 (50 mm from the end) — Plasmatrons power

Figure A2.5.21 – Change of temperature of graphite nozzle of outer electrode (13.11.2008)



— Temperature of water in the input collector – LTP.00 — Temperature of water in the plasmatrons cooling duct output – LTP.01  
 — Flow rate of water in the plasmatrons cooling duct – L.G.16

Figure A2.5.22 – Change of water parameters for plasmatrons cooling (13.11.2008)

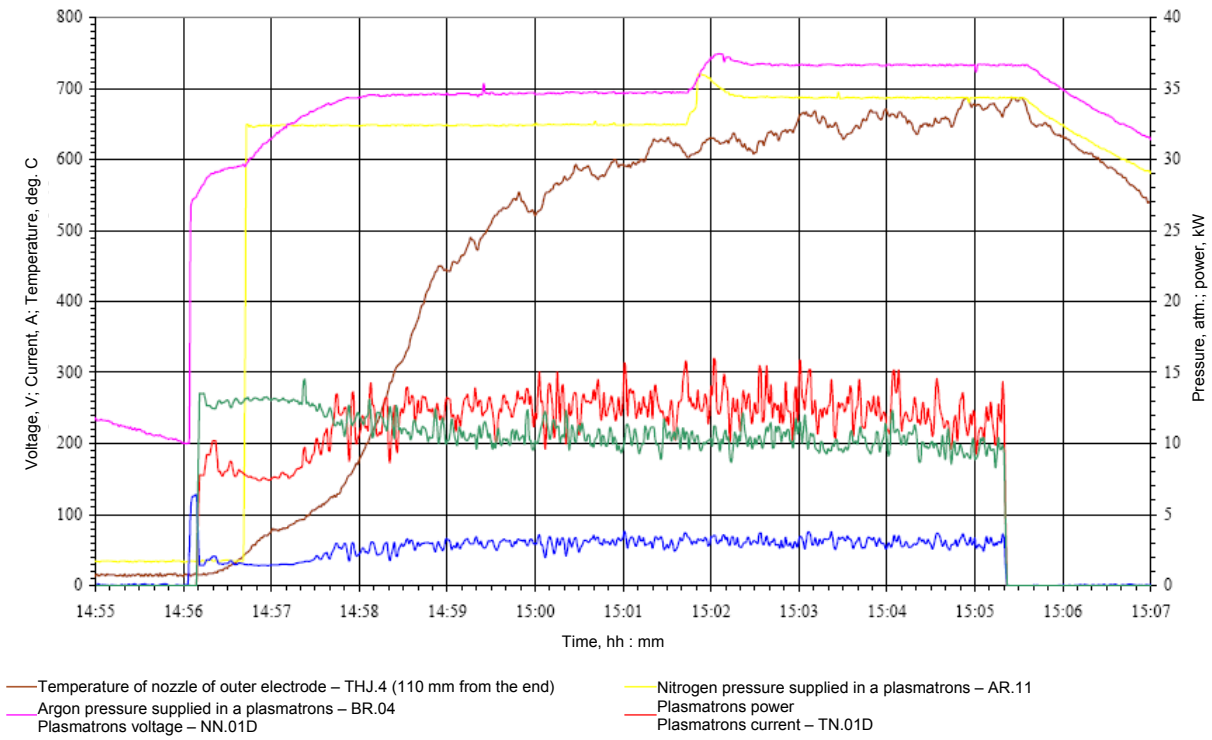


Figure A2.5.23 – Change of plasmatrons parameters (18.11.2008). Plasmatrons electric power supply from transformers of "D" group

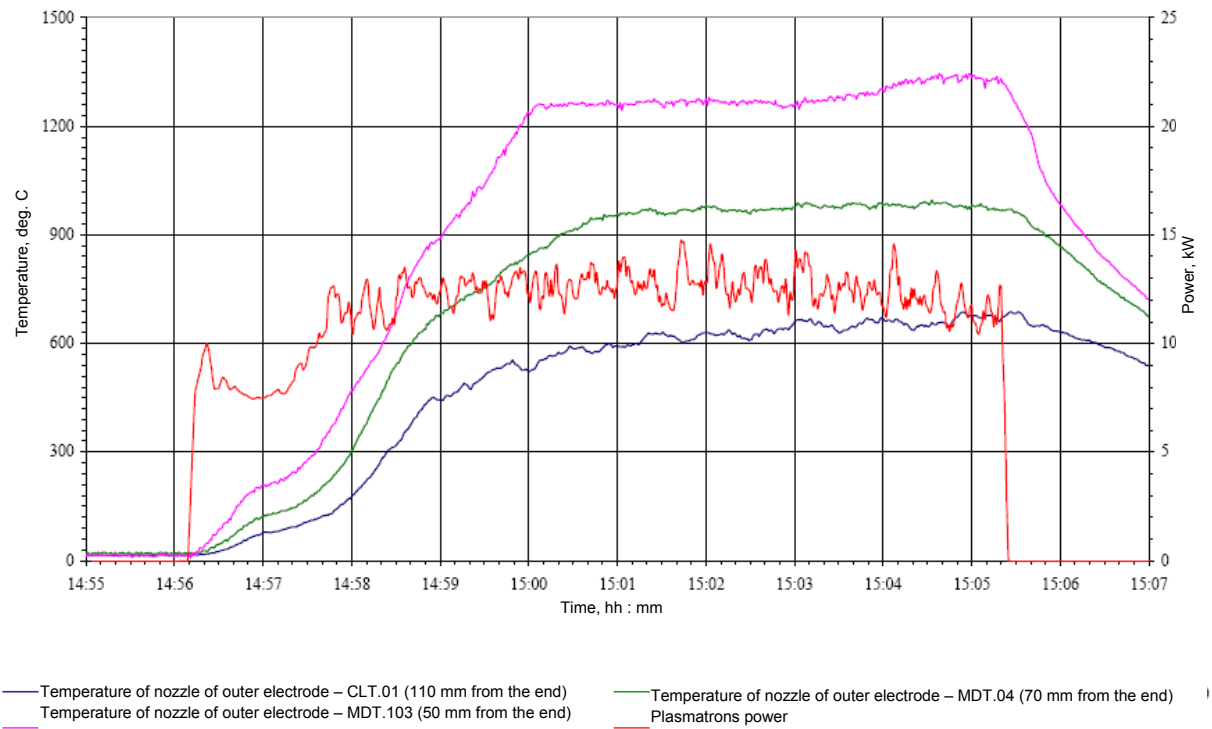


Figure A2.5.24 – Change of temperature of graphite nozzle of outer electrode (18.11.2008) Plasmatrons electric power supply from transformers of "D" group

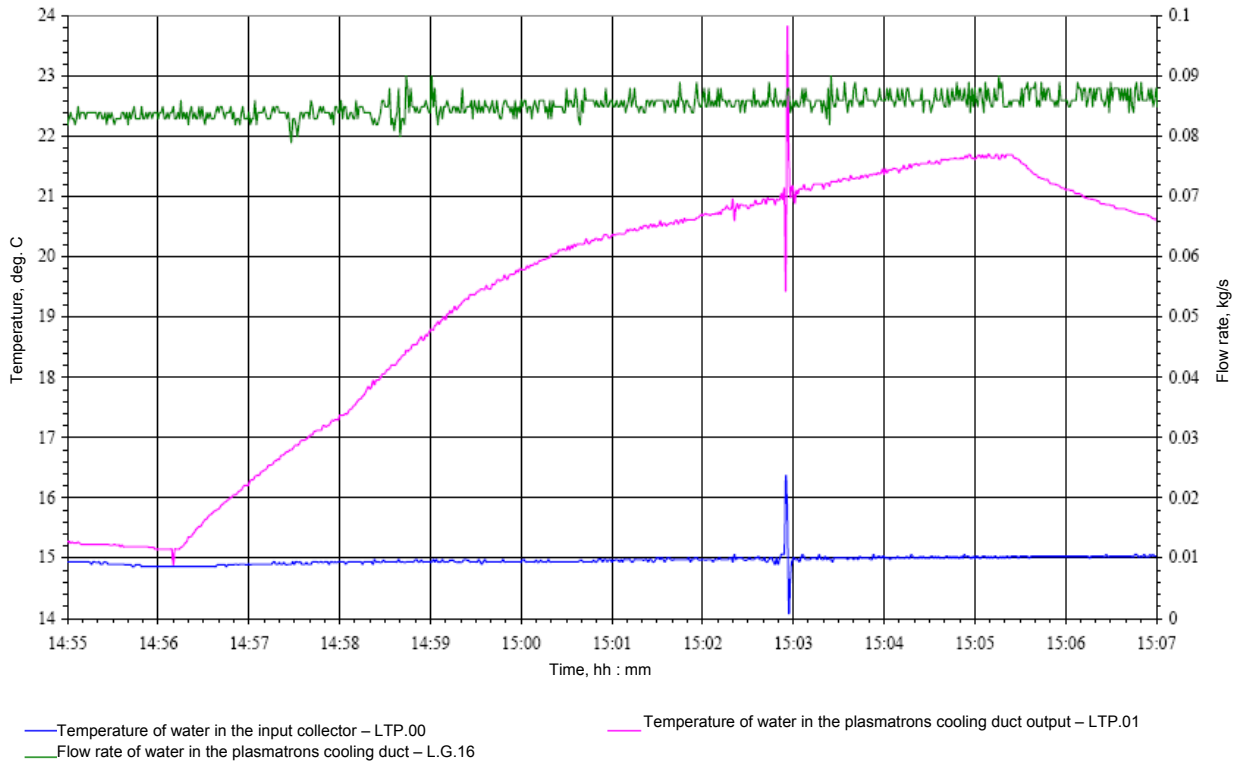


Figure A2.5.25 – Change of water parameters for plasmatrons cooling (18.11.2008). Plasmatrons electric power supply from transformers of "D" group

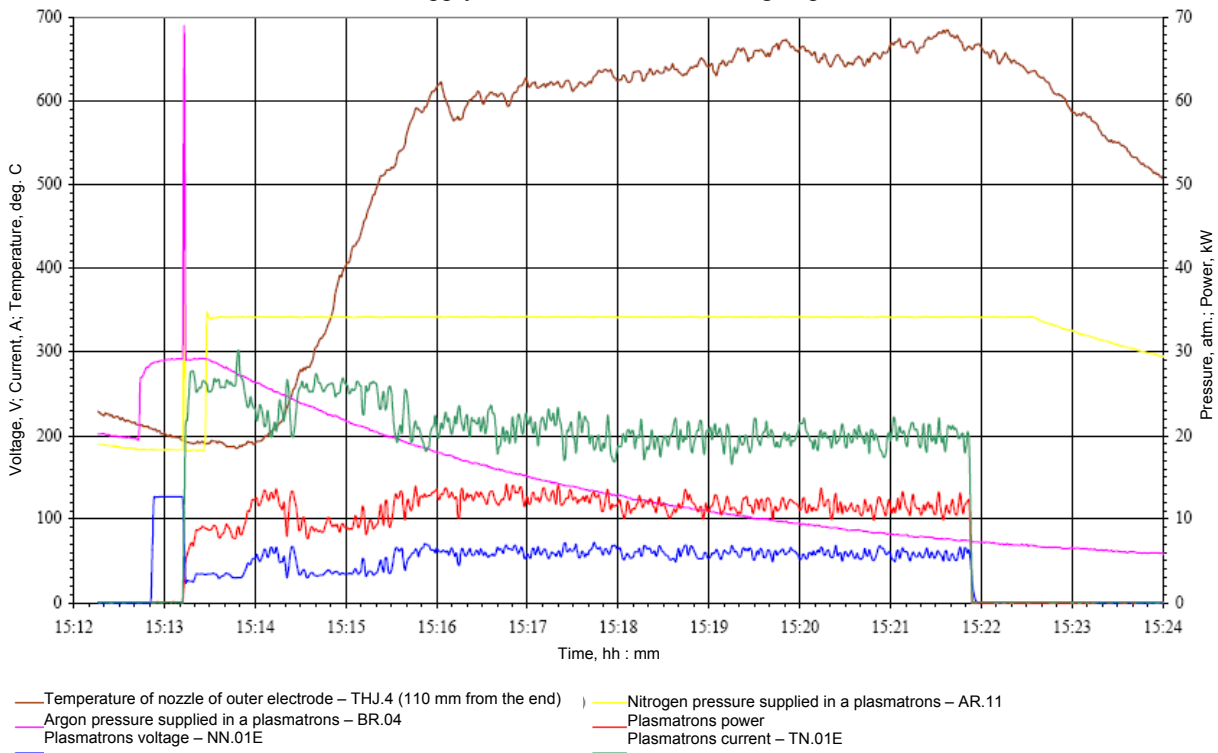
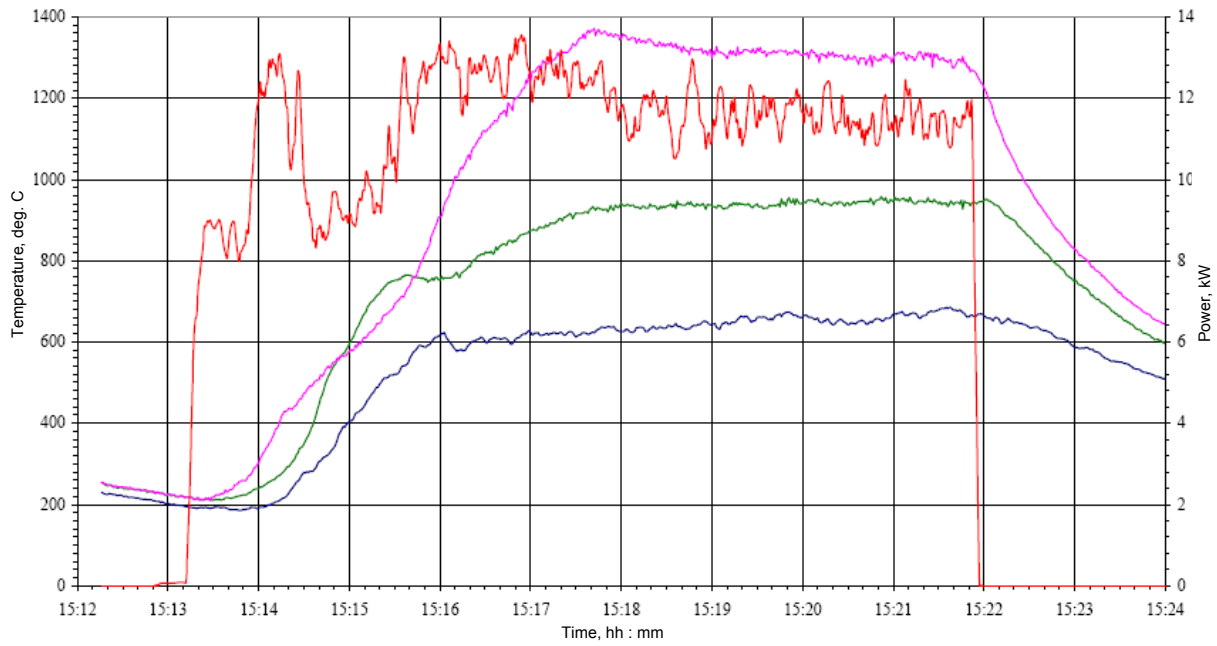
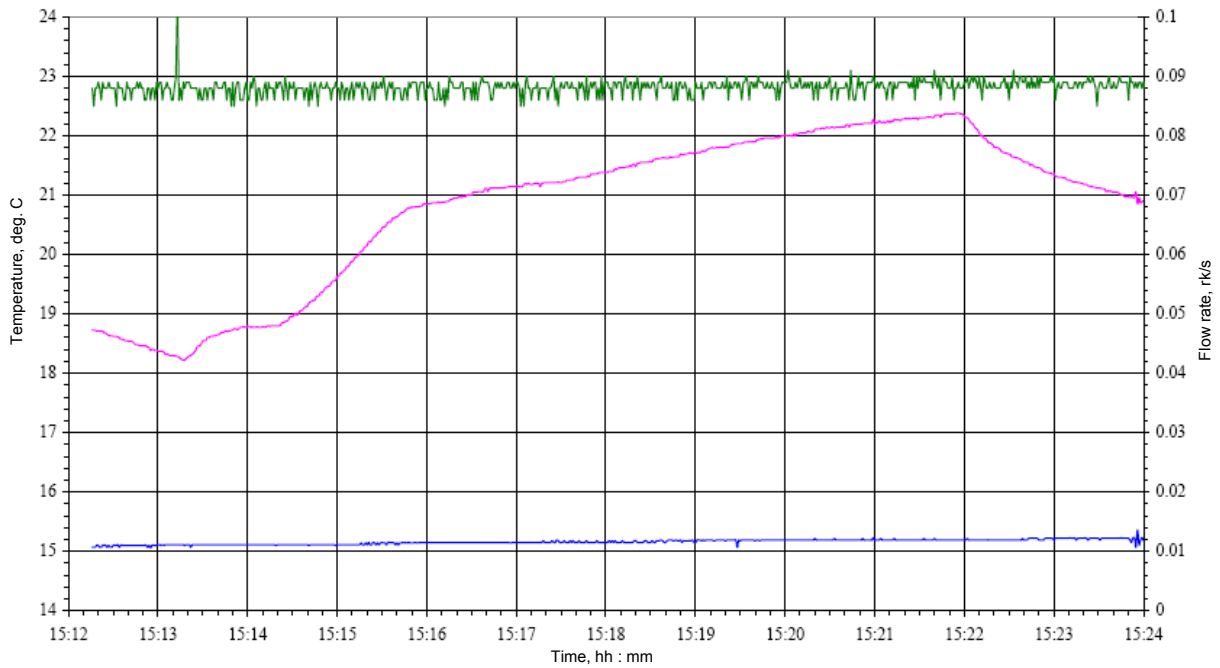


Figure A2.5.26 – Change of plasmatrons parameters (18.11.2008). Plasmatrons electric power supply from transformers of "E" group



— Temperature of nozzle of outer electrode – CLT.01 (110 mm from the end) — Temperature of nozzle of outer electrode – MDT.04 (70 mm from the end)  
 — Temperature of nozzle of outer electrode – MDT.103 (50 mm from the end) — Plasmatrons power

Figure A2.5.27 – Change of temperature of graphite nozzle of outer electrode (18.11.2008). Plasmatrons electric power supply from transformers of "E" group



— Temperature of water in the input collector – LTP.00 — Temperature of water in the plasmatrons cooling duct output – LTP.01  
 — Flow rate of water in the plasmatrons cooling duct – L.G.16

Figure A2.5.28 – Change of water parameters for plasmatrons cooling (18.11.2008). Plasmatrons electric power supply from transformers of "E" group

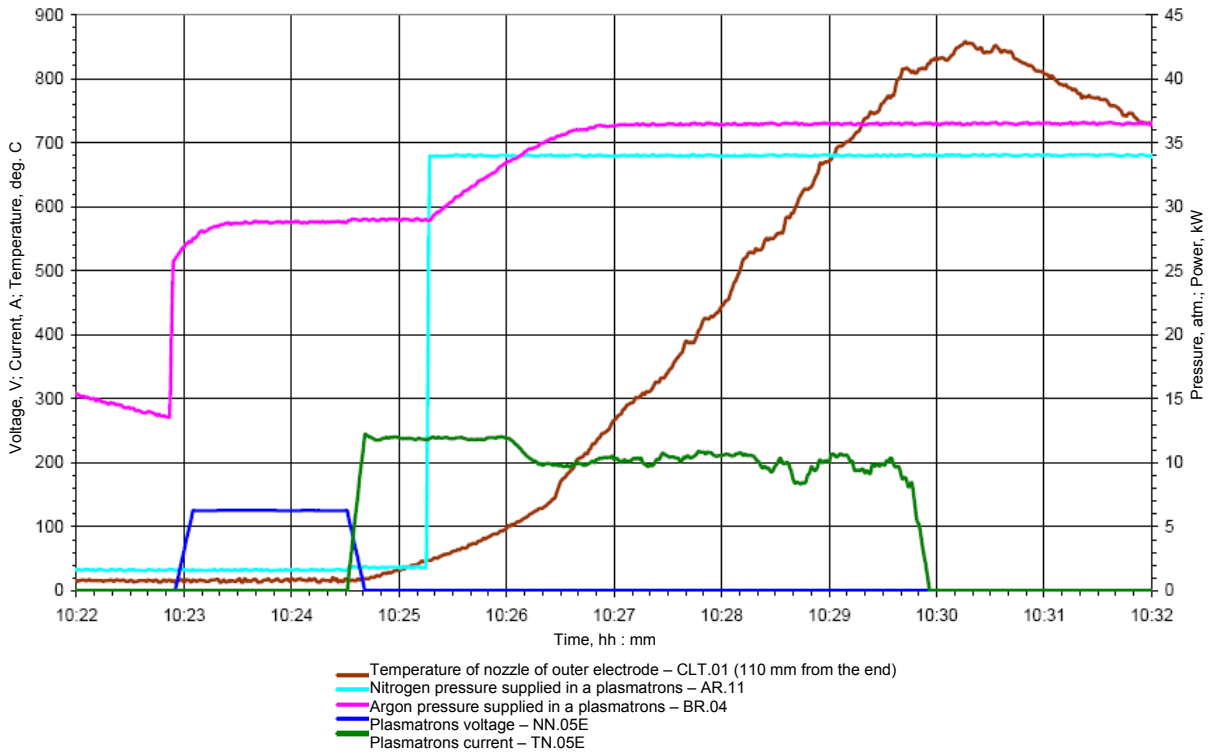


Figure A2.5.29 – Change of plasmatrons parameters (19.11.2008). Plasmatrons electric power supply from transformers of "E" group. Thermal insulation is installed on the surface of a nozzle of outer electrode

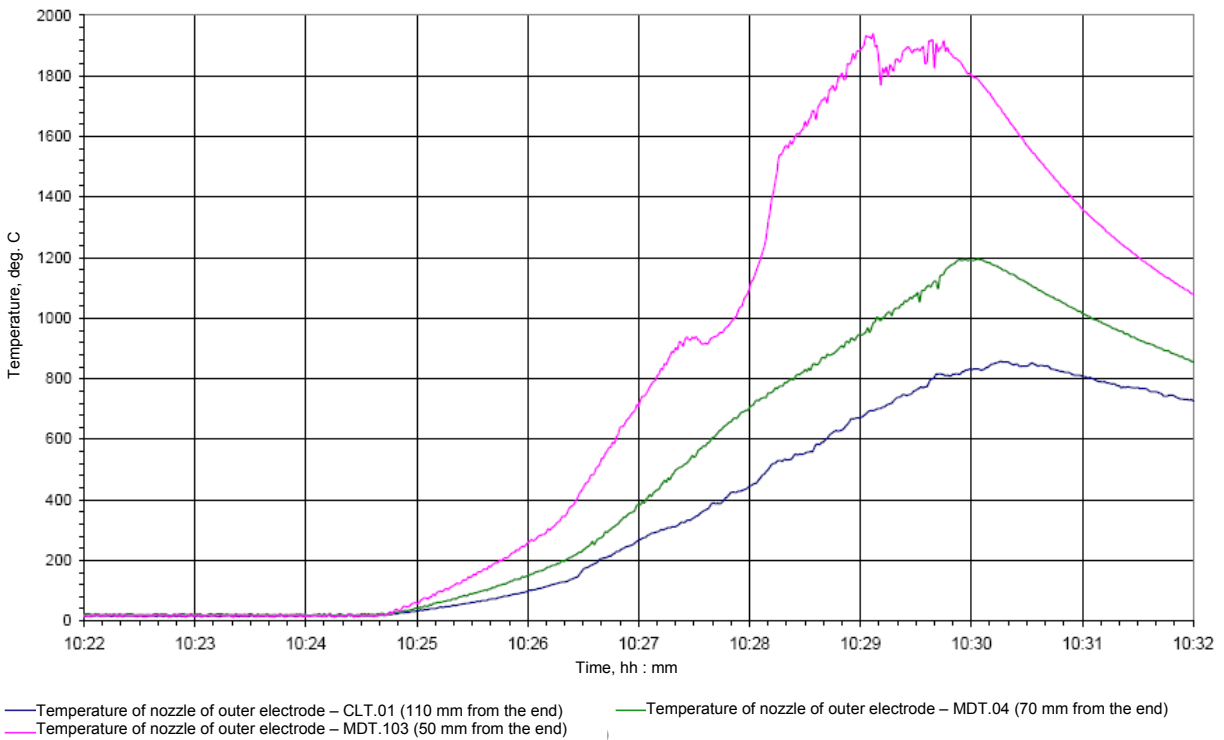


Figure A2.5.30 – Change of temperature of graphite nozzle of outer electrode (19.11.2008)



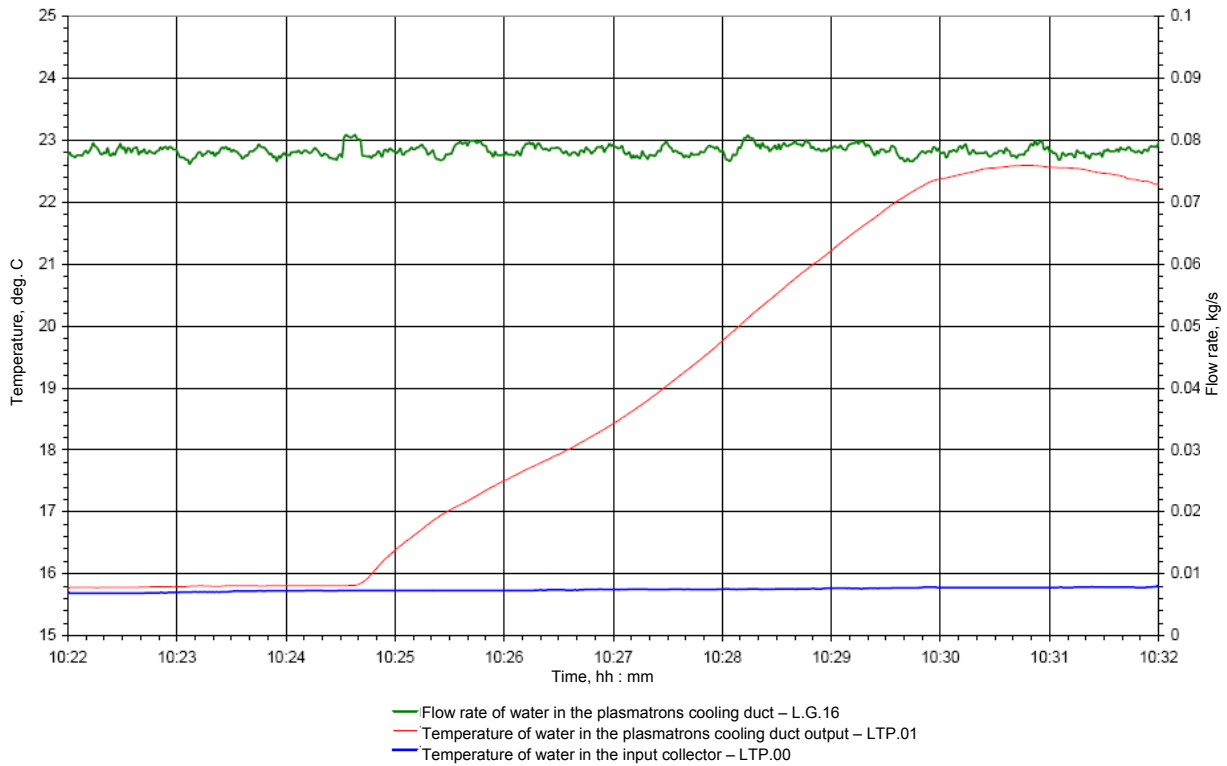


Figure A2.5.31 – Change of water parameters for plasmatrons cooling (19.11.2008)

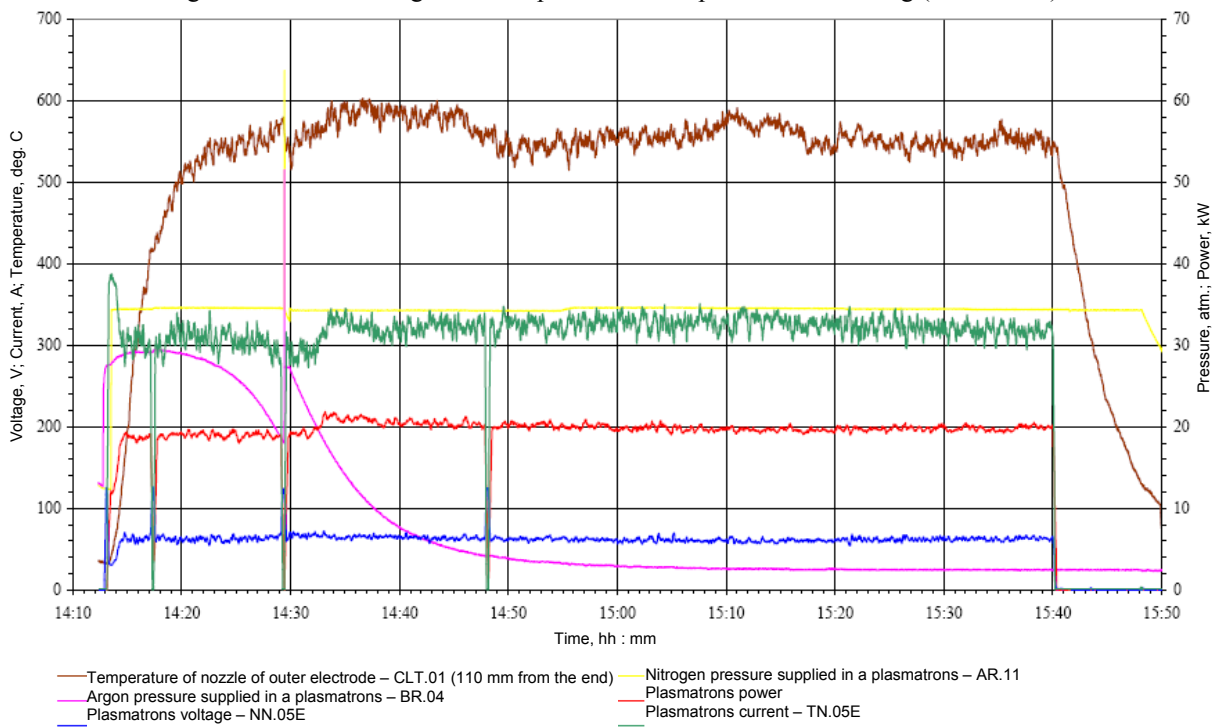


Figure A2.5.32 – Change of plasmatrons parameters (20.11.2008). Plasmatrons electric power supply from transformers of "E" group. Life-time testing.

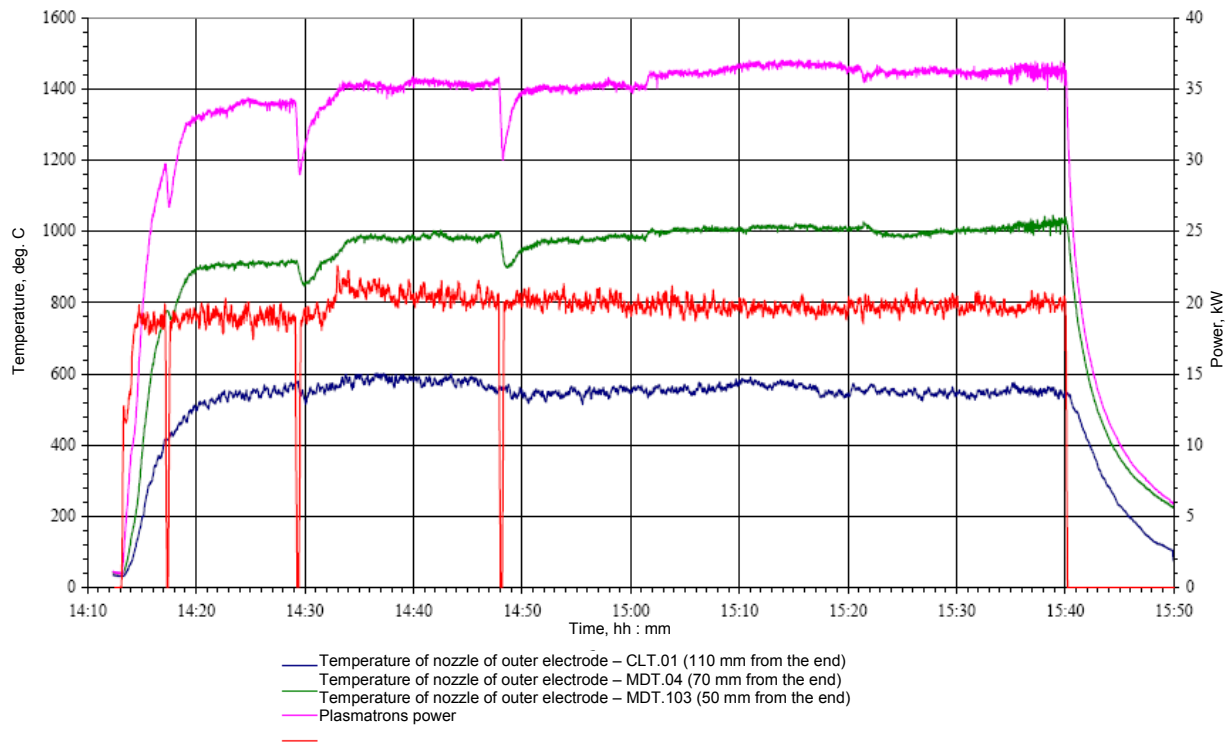


Figure A2.5.33 – Change of temperature of graphite nozzle of outer electrode (20.11.2008). Life-time testing.

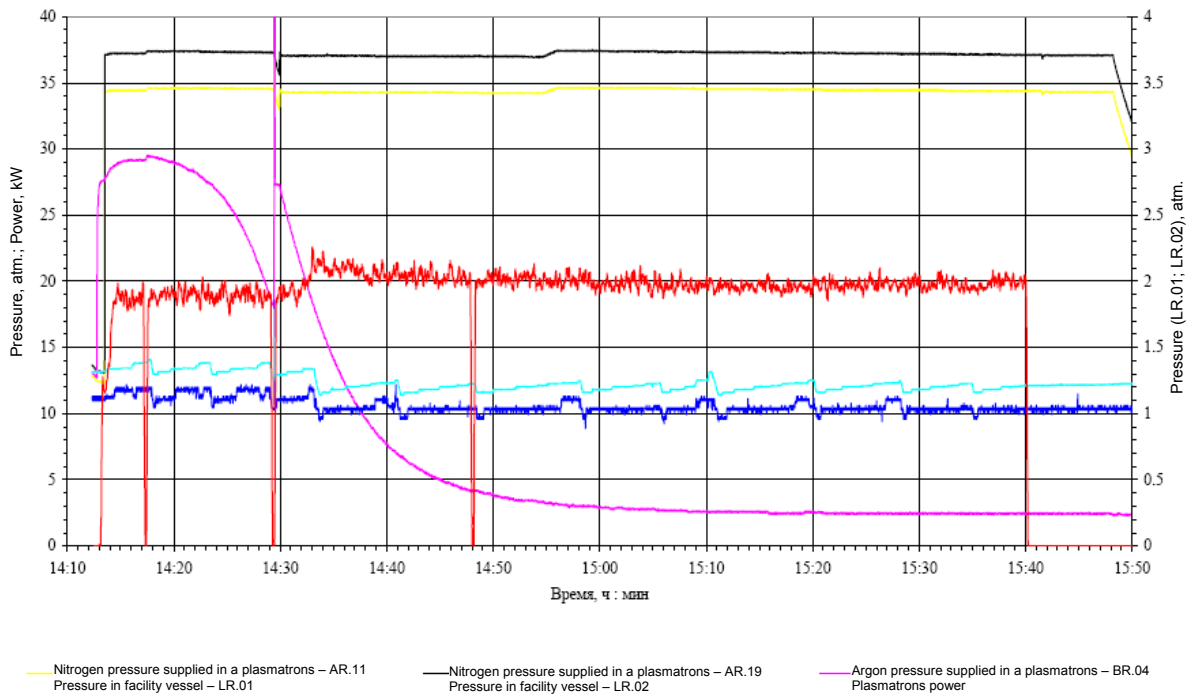


Figure A2.5.34 – Change of a medium pressure in the test facility "LAVA-B" vessel (20.11.2008). Life-time testing

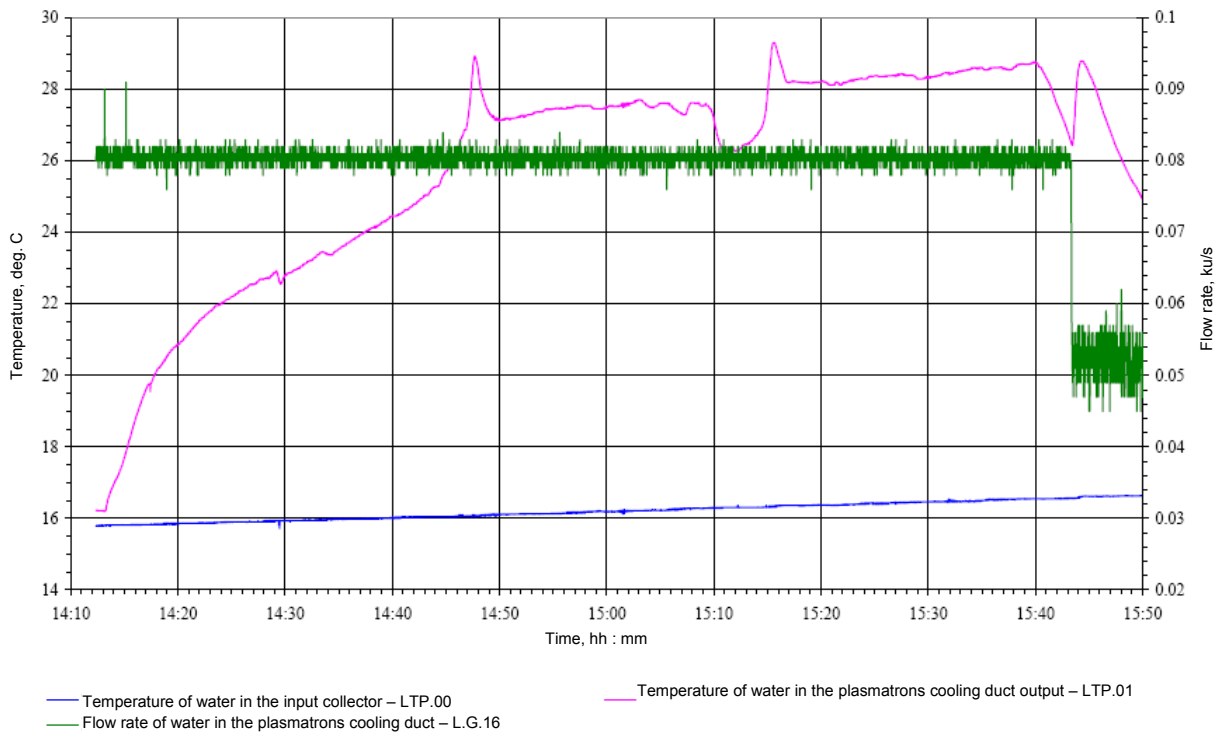


Figure A2.5.35 – Change of water parameters for plasmatrons cooling (20.11. 2008). Life-time testing.

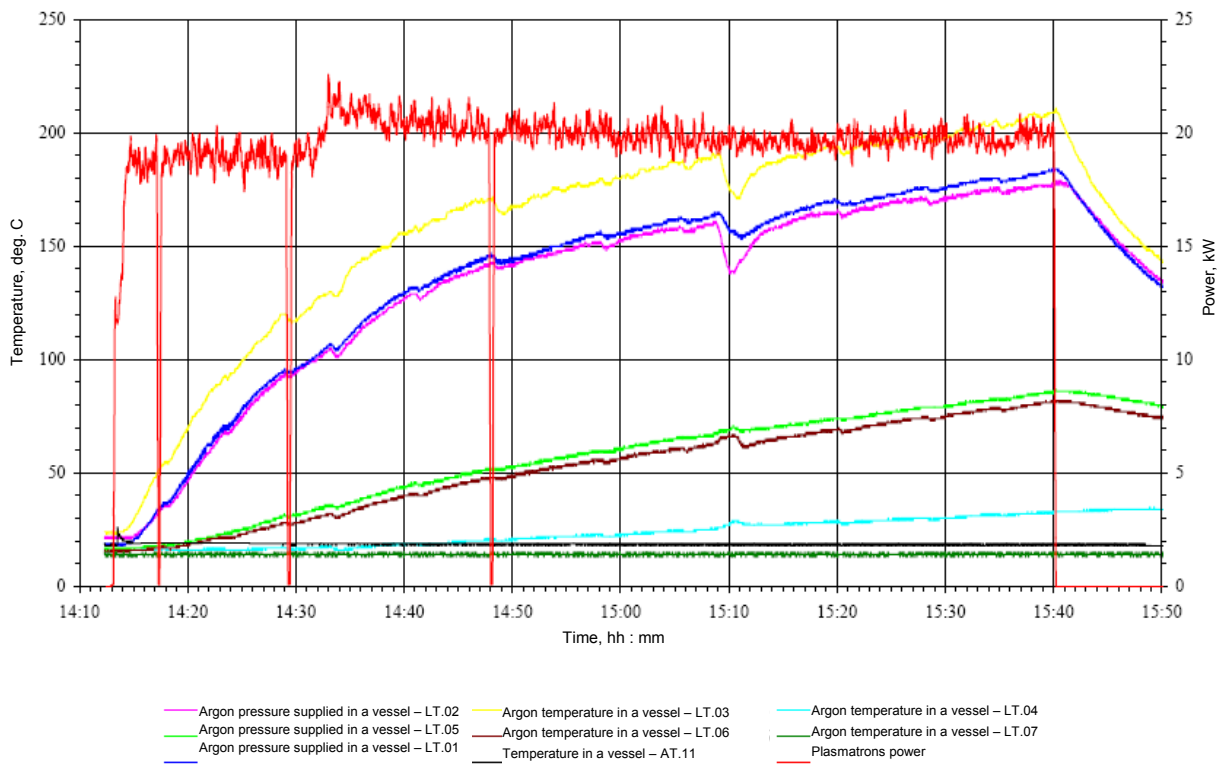


Figure A2.5.36 – Change of a medium pressure in the test facility "LAVA-B" vessel (20.11.2008). Life-time testing.



Figure A2.5.37 – Appearance of a nozzle of inner electrode after test (20.11.2008)



Figure A2.5.38 – State of outer surface of the nozzle of outer electrode after test (20.11.2008)

Figure A2.5.39 – State of inner surface of the nozzle of outer electrode after test (20.11.2008)

### 5.3 Testing of the modified plasmatrons cooling paths of the melt heating system in the reactor pressure vessel model

In compliance with the program and procedure "Testing of the melt heating system with modified plasmatrons" reg. No.240-02/142 of 05.11.2008 the plasmatrons cooling paths testing was carried out for the purpose of defining their hydraulic characteristics.

The diagram of water delivery in the course of the plasmatrons cooling paths and water-cooled cable testing is represented in Figures A2.5.40, A2.5.41. Reduced factor of hydraulic resistance  $t$  was defined on the following formula:

$$t = (2 \times \rho \times 98066,5 \times \Delta P) / G^2,$$

where  $\rho$  – water density at 20°C was equal to  $\rho = 998 \text{ kg/m}^3$ ;

$G$  – water flow rate defined by the volumetric-weight method, kg/s;

$\Delta P$  – difference of water pressure along the plasmatrons cooling path, kgs/cm<sup>2</sup>.

For calculation of the reduced hydraulic resistance factor of the plasmatrons cooling path with the delivery and discharge pipelines the pressure difference  $\Delta P_1$  was taken as equal to reading difference of the standard pressure gages MO-1 and MO-4. For calculation of the reduced hydraulic resistance factor of the plasmatrons cooling path the pressure difference  $\Delta P_2$  was taken as equal to reading difference of the standard pressure gages MO-2 and MO-3.

5.3.1 The first was flushing of the plasmatrons "E" cooling path. A 20-liter graduated barrel was used as a volumetric tank. From the first flushing results it was decided to repeat flushing of the plasmatrons "E" cooling path with replacement of the flow gauge L.G.16 aperture from diameter  $\varnothing 9,4 \text{ mm}$  for aperture  $\varnothing 6,9 \text{ mm}$  and change of the pressure gages measured pressure in points MO-3 and MO-4 (see Figure A2.5.40).

In the course of the second flushing of the plasmatrons "E" cooling path, at pressure 14 abs atm, water run from the connector of the drain section of the plasmatrons cooling path. The

limiting expected pressure of water supply – equaled to 16 abs atm, was not reached, therefore it was decided to conduct the third flushing of the plasmatrions "E" cooling path with replacement of the hose of the path drain section and volumetric tank of less size.

The results from the third flushing of the plasmatrions "E" cooling path were recognized satisfactory.

5.3.2 During the flushing of the plasmatrions "A" cooling path there were replaced as follows:

- pressure gage in point MO-1;
- pressure gage in point MO -2;
- pressure gage in point MO -3;
- pressure gage in point MO -4.

The flushing program was run in full. The flushing results were recognized satisfactory.

5.3.3 The results from the third flushing of the plasmatrions "B" cooling path were recognized satisfactory.

5.3.4 The flushing of the plasmatrions "D" cooling path was carried out, the results were recognized unsatisfactory due to high resistance coefficient of the pipeline supplying water to the plasmatrions cooling path.

5.3.5 The flushing of the plasmatrions "C" cooling path was carried out. The flushing program was run in full. The flushing results were recognized satisfactory.

5.3.6 The cooling path flushing of the negative water cooling cable was carried out, the results were recognized satisfactory.

5.3.7 The flushing of all plasmatrions cooling paths and water-cooled cables was conducted. Prior to flushing the plasmatrions "D" and "E" cooling paths were disassembled, examined and master nozzles were compared, the delivery cooling paths were rearranged after valve D 2.20. The given flushing was carried out for definition of the supply pipeline effect on the coefficient of the cooling path hydraulic resistance. According to the given flushing there were no deviations, therefore the delivery cooling paths of the plasmatrions "D" and "E" after valve D 2.20 were returned to their position and the flushing of all cooling paths was repeated. The flushing results were recognized satisfactory.

5.3.8 The flushing of the plasmatrions "D" cooling path was repeated, the results were recognized satisfactory, but the limiting expected water supply pressure was not reached due to overpressure 10 gage atm at the plasmatrions inlet.

The resulted flushing data of the plasmatrions cooling paths and water-cooled cable are included in Tables A2.5.8...A2.5.16.

5.3.9 From the flushing the diagrams of the flow rate variation depending on pressure difference are plotted and represented in Figures A2.5.42...A2.5.47. Pressure difference in the diagrams is the difference between pressure in the delivery section of the cooling path (pressure gage MO-1) and water pressure in the discharge section of the cooling path (pressure gage MO-4).

5.3.10 The coefficients of approximating dependence of water flow rate  $G$  through the plasmatrions cooling paths and water-cooled cable on pressure difference  $\Delta P$  at MO-1 inlet and MO-4 outlet from the plasmatrions cooling paths and water-cooled cable were defined respectively:

- for plasmatrions "A"  $G = 0,0802 \times \Delta P^{1/2} + 0,0022$ ;
- for plasmatrions "B"  $G = 0,0707 \times \Delta P^{1/2} + 0,0035$ ;
- for plasmatrions "C"  $G = 0,0663 \times \Delta P^{1/2} - 0,0047$ ;
- for plasmatrions "D"  $G = 0,0698 \times \Delta P^{1/2} + 0,0044$ ;
- for plasmatrions "E"  $G = 0,0797 \times \Delta P^{1/2} - 0,0075$ ;
- for water-cooled cable  $G = 0,1182 \times \Delta P^{1/2} + 0,0241$ .

Figures A2.5.48...A2.5.54 illustrate variation of reduced hydraulic resistance coefficients of the plasmatrions and water-cooled cable depending on water flow rate.



5.3.11 The coefficients of approximating dependence of reduced hydraulic resistance coefficient of full cooling path with delivery and discharge sections  $t$  and the section including the plasmatrons itself, water-cooled cable  $t_p$  on cooling water flow rate  $G$  were defined.

for the plasmatrons "A" cooling path:

$$t = 2,0164 \times 10^{-10} \times G^{-0,0690}; \quad t_p = 1,3685 \times 10^{-10} \times G^{-0,1969};$$

for the plasmatrons "B" cooling path:

$$t = 2,8679 \times 10^{-10} \times G^{-0,0621}; \quad t_p = 1,7608 \times 10^{-10} \times G^{-0,2074};$$

for the plasmatrons "C" cooling path:

$$t = 1,5660 \times 10^{-10} \times G^{-0,4176}; \quad t_p = 2,8351 \times 10^{-10} \times G^{-0,0470};$$

for the plasmatrons "D" cooling path:

$$t = 2,5507 \times 10^{-10} \times G^{-0,2122}; \quad t_p = 1,2356 \times 10^{-10} \times G^{-0,3675};$$

for the plasmatrons "E" cooling path:

$$t = 1,0299 \times 10^{-10} \times G^{-0,4806}; \quad t_p = 0,8660 \times 10^{-10} \times G^{-0,4143};$$

for water-cooled cable:

$$t = 0,9752 \times 10^{-10} \times G^{-0,3577}; \quad t_k = 0,2745 \times 10^{-10} \times G^{-0,5321}.$$

Averaged values of the reduced hydraulic resistance coefficients of the plasmatrons and water-cooled cable are:

plasmatrons "A" (15.04.09)	$t_{A \text{ av.p.}} = 2,41 \times 10^{-10} \text{ m}^{-4};$
plasmatrons "B" (22.04.09)	$t_{B \text{ av.p.}} = 3,26 \times 10^{-10} \text{ m}^{-4};$
plasmatrons "C" (27.04.09)	$t_{C \text{ av.p.}} = 3,40 \times 10^{-10} \text{ m}^{-4};$
plasmatrons "D" (05.05.09)	$t_{D \text{ av.p.}} = 3,69 \times 10^{-10} \text{ m}^{-4};$
plasmatrons "E" (13.04.09)	$t_{E \text{ av.p.}} = 2,82 \times 10^{-10} \text{ m}^{-4};$
water-cooled cable (05.05.09)	$t_{K \text{ av.p.}} = 0,85 \times 10^{-10} \text{ m}^{-4}$

Averaged values of the reduced hydraulic resistance coefficients of the plasmatrons and water-cooled cable with delivery and discharge pipelines are:

plasmatrone "A"	$t_{A \text{ av.}} = 2,47 \times 10^{-10} \text{ m}^{-4};$
plasmatrone "B"	$t_{B \text{ av.}} = 3,48 \times 10^{-10} \text{ m}^{-4};$
plasmatrone "C"	$t_{C \text{ av.}} = 5,70 \times 10^{-10} \text{ m}^{-4};$
plasmatrone "D"	$t_{D \text{ av.}} = 4,78 \times 10^{-10} \text{ m}^{-4};$
plasmatrone "E"	$t_{E \text{ av.}} = 4,16 \times 10^{-10} \text{ m}^{-4};$
water-cooled cable	$t_{K \text{ av.}} = 2,06 \times 10^{-10} \text{ m}^{-4}$

5.3.12 Figures A2.5.55...A2.5.60 illustrate variation of water flow rate and pressure at the inlet/outlet of the plasmatrons cooling paths and water-cooled cable on time. The data was obtained in the course of all cooling paths flushing.

When water pressure at the cooling path inlet is 13,5 abs atm the water flow rate through the plasmatrons cooling paths varies from 0,07 to 0,08 kg/s and through the electric cable cooling path equals to 0,18 kg/s.

### 5.3.13 Conclusion

As a consequence of the activity accomplished the system for water cooling of plasmatrons and delivery electric cables has been prepared for testing.

When water pressure at the cooling system inlet (at the feed pump outlet) was equal to 13,5 abs atm the cooling system parameters are:

- water pressure at the plasmatrons cooling path inlet, in compliance with pressure gages readings, varies from 8,7 to 9,6 abs atm;
- water pressure at the plasmatrons cooling path outlet, in compliance with pressure gages readings, varies from 7,6 to 8,3 abs atm;
- maximum water differential pressure in the plasmatrons cooling paths is equal to 1,2 abs atm;
- minimum water differential pressure in the plasmatrons cooling paths is equal to 0,9 abs atm;
- averaged water differential pressure in the plasmatrons cooling paths is equal to ~1,1 abs atm;
- averaged water flow rate in the plasmatrons cooling paths varies from 0,069 to 0,080 kg/s;

- water pressure at the electric cable cooling path inlet is 10,2 abs atm;
- water pressure at the electric cable cooling path outlet is 6,9 abs atm;
- average water flow rate in the electric cable cooling path is 0,18 kg/s;
- water pressure at the cooling system discharge is 1,9 abs atm.

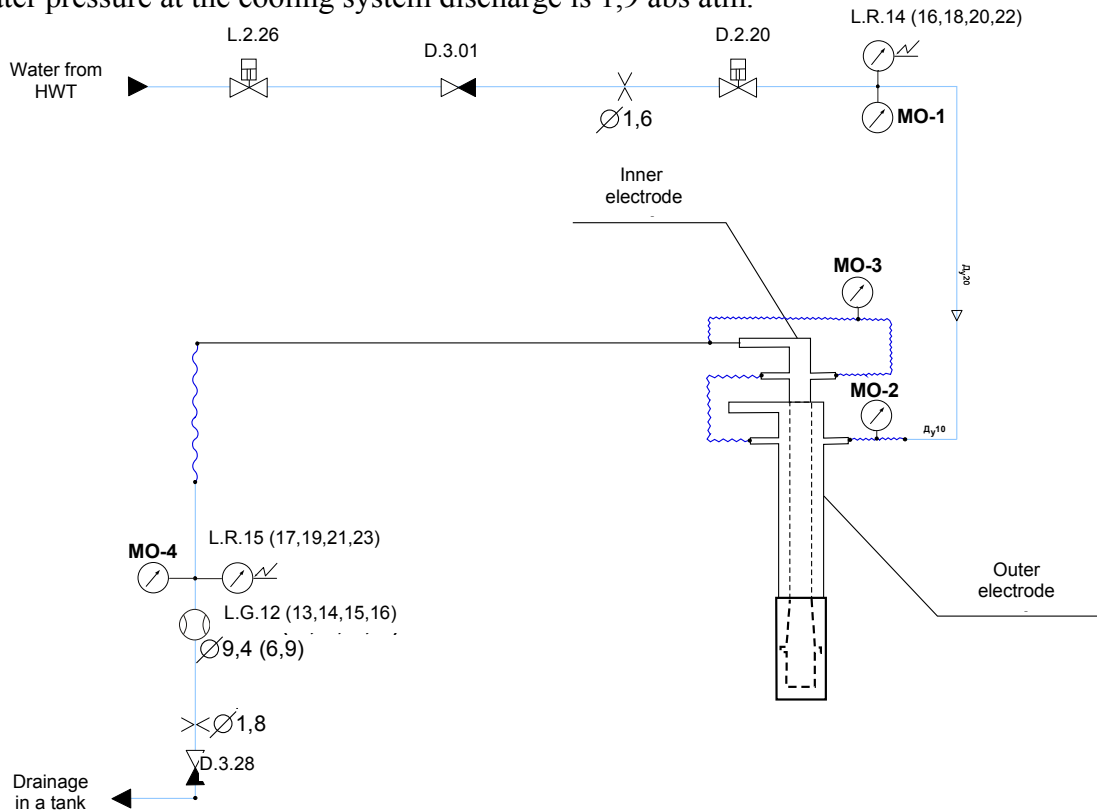


Figure A2.5.40 – Scheme of water flow testing of the plasmatrons cooling paths

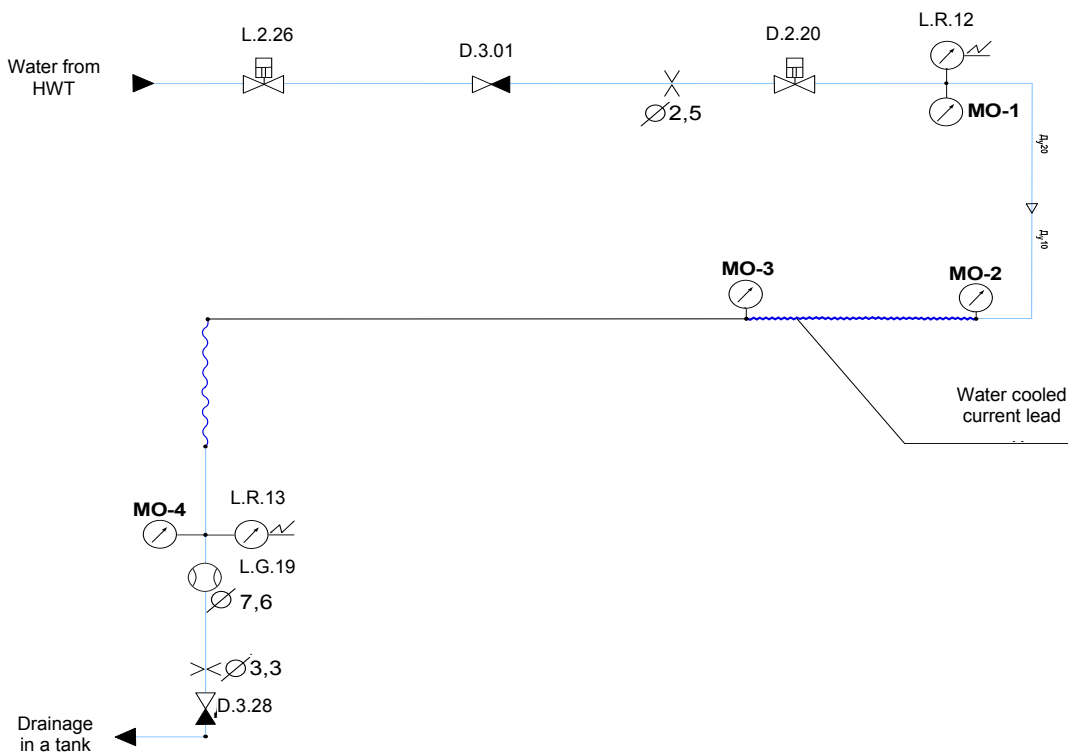


Figure A2.5.41 – Scheme of water flow testing of the water cooling cable

Table A2.5.8 – Results of flushing of plasmatrons "E" cooling path

Parameter	Parameter value									
	1	2	3	4	5	6	7	8	9	10
Number of mode	1	2	3	4	5	6	7	8	9	10
Pressurization in a HTW-3 (c.p. L.R.09), atm.	3,1	5,0	7,27	9,17	11,33	13,11	12,22	9,86	8,07	6,25
Water pressure in the input path P <sub>1</sub> (MO-1), atm.	1,88	2,76	4,52	5,56	6,6	7,4	6,92	5,64	4,76	3,72
Water pressure in the input into electrode (MO-2), atm.	1,85	2,75	4,55	5,55	6,63	7,98	6,9	5,65	4,75	3,7
Water pressure in the output from electrode (MO-3), atm.	1,72	2,53	4,12	5,02	5,9	6,79	6,22	5,02	4,27	3,34
Water pressure in the drainage path P <sub>4</sub> (MO-4), atm.	1,72	2,5	4,0	4,84	5,74	6,46	5,92	4,84	4,12	3,22
Duration of water supply τ, s	418	247	169	152	134	124	129	158	165	206
Mass of supplied water M, kg	10	10	10	10	10	10	10	10	10	10
Measured water flow rate G <sub>p</sub> , kg/s	0,024	0,041	0,059	0,066	0,075	0,081	0,078	0,063	0,061	0,049
Water pressure P <sub>1d</sub> in the input path (L.R.22), atm	1,2	2,17	3,76	4,82	5,81	6,67	6,11	4,87	3,98	2,94
Water pressure P <sub>4d</sub> in the output path (c.p. L.R.23), atm	1,05	1,79	3,14	3,99	4,82	5,48	5,08	3,98	3,27	2,4
Water flow rate through electrodes G (L.G.16), kg/s	0,036	0,045	0,062	0,069	0,074	0,082	0,078	0,078	0,075	0,063
Difference of flow rates G - G <sub>p</sub> , kg/s	0,012	0,005	0,003	0,003	-0,001	0,001	0,001	0,015	0,014	0,011
Relation (G - G <sub>p</sub> )/G <sub>p</sub> , %	50,48	11,15	4,78	4,88	-0,84	1,68	0,62	23,24	23,75	29,78
Difference of pressures P <sub>1d</sub> - P <sub>1</sub> , atm.	0,32	0,41	0,24	0,26	0,21	0,27	0,19	0,23	0,22	0,22
Relation (P <sub>1d</sub> - P <sub>1</sub> )/P <sub>1</sub> , %	17,02	14,86	5,31	4,68	3,18	3,65	2,75	4,08	4,62	5,91
Difference of pressures P <sub>4d</sub> - P <sub>4</sub> , atm.	0,33	-0,71	0,14	0,15	0,08	0,02	0,16	0,14	0,15	0,18
Relation (P <sub>4d</sub> - P <sub>4</sub> )/P <sub>4</sub> , %	19,19	-28,40	3,50	3,10	1,39	0,31	2,70	2,89	3,64	5,59
Reduced factor of hydraulic resistance of plasmatrons τ <sub>r</sub> × 10 <sup>-10</sup> , m <sup>-4</sup>	4,45	2,63	2,40	2,39	2,56	3,58	2,22	3,08	2,56	2,99
Reduced factor of hydraulic resistance of plasmatrons with pipelines τ × 10 <sup>-10</sup> , m <sup>-4</sup>	5,47	3,11	2,91	3,26	3,02	2,83	3,26	3,91	3,41	4,15
Relation (τ <sub>r</sub> - τ <sub>av,r</sub> )/τ <sub>av,r</sub> , % (τ <sub>av,r</sub> = 2,87 × 10 <sup>-10</sup> m <sup>-4</sup> )	54,70	-8,59	-16,36	-16,60	-10,97	24,62	-22,93	7,12	-10,99	4,05
Relation (τ - τ <sub>av</sub> )/τ <sub>av</sub> , % (τ <sub>av</sub> = 3,46 × 10 <sup>-10</sup> m <sup>-4</sup> )	58,01	-10,35	-16,06	-5,98	-12,72	-18,31	-5,95	12,88	-1,52	19,92

Table A2.5.9 – Results of second flushing of plasmatrons "E" cooling path

Parameter	Parameter value												
	1	2	3	4	5	6	7	8	9	10	11	12	13
Number of mode	1	2	3	4	5	6	7	8	9	10	11	12	13
Pressurization in a HTW-3 (c.p. L.R.09), atm.	2,53	3,94	6,15	8,0	9,98	12,01	13,9	12,97	11,02	9,17	7,26	5,24	3,07
Water pressure in the input path P <sub>1</sub> (MO-1), atm.	1,2	1,92	3,04	4,45	5,38	6,3	7,36	6,88	5,84	4,8	3,79	2,64	1,2
Water pressure in the input into electrode (MO-2), atm.	1,22	1,93	3,07	4,45	5,4	6,33	7,45	6,88	5,78	4,78	3,82	2,65	1,2
Water pressure in the output from electrode (MO-3), atm.	1,08	1,7	2,7	3,97	4,8	5,62	6,57	6,14	5,12	4,2	3,34	2,34	1,01
Water pressure in the drainage path P <sub>4</sub> (MO-4), atm.	1,08	1,63	2,58	3,72	4,52	5,3	6,21	5,8	4,8	3,92	3,12	2,18	0,98
Duration of water supply τ, s	378,9	246,1	182,6	143	138	124	123,2	127,6	137,8	152,2	177,8	195,8	276,4
Mass of supplied water M, kg	10	10	10	10	10	10	10	10	10	10	10	10	10
Measured water flow rate G <sub>p</sub> , kg/s	0,026	0,041	0,055	0,069	0,072	0,081	0,081	0,078	0,073	0,066	0,056	0,051	0,036
Water pressure P <sub>1d</sub> in the input path (L.R.22), atm	2,49	3,17	4,48	5,69	6,62	7,51	4,91	7,92	6,97	6,0	5,03	3,93	2,49
Water pressure P <sub>4d</sub> in the output path (c.p. L.R.23), atm	2,29	2,83	3,9	4,89	5,69	6,42	4,32	6,76	5,97	5,14	4,33	3,41	2,22
Water flow rate through electrodes G (L.G.16), kg/s	0,026	0,037	0,051	0,061	0,068	0,075	0,054	0,077	0,072	0,065	0,058	0,049	0,033
Difference of flow rates G - G <sub>p</sub> , kg/s	-0,0004	-0,003	0,003	0,009	0,004	0,006	-0,03	0,001	0,001	-0,0003	0,002	0,002	0,003
Relation (G - G <sub>p</sub> )/G <sub>p</sub> , %	-1,58	-8,3	-6,07	-12,5	-5,64	-7,01	-33,5	-1,79	-0,94	-0,58	3,67	-3,96	-8,35
Difference of pressures P <sub>1d</sub> - P <sub>1</sub> , atm.	0,29	0,25	0,44	0,25	0,23	0,20	-3,45	0,04	0,13	0,20	0,24	0,29	0,29
Relation (P <sub>1d</sub> - P <sub>1</sub> )/P <sub>1</sub> , %	13,11	8,59	10,87	4,53	3,68	2,77	-41,3	0,49	1,92	3,50	4,99	8,00	13,03
Difference of pressures P <sub>4d</sub> - P <sub>4</sub> , atm.	0,21	0,20	0,32	0,18	0,18	0,12	-2,89	-0,04	0,17	0,22	0,21	0,23	0,24
Relation (P <sub>4d</sub> - P <sub>4</sub> )/P <sub>4</sub> , %	10,13	7,78	8,97	3,77	3,17	1,83	-40,1	-0,59	2,86	4,50	4,98	7,18	12,21
Reduced factor of hydraulic resistance of plasmatrons τ <sub>r</sub> × 10 <sup>-10</sup> , m <sup>-4</sup>	3,82	2,73	2,41	1,91	2,24	2,14	2,61	2,36	2,45	2,63	2,97	2,33	2,87
Reduced factor of hydraulic resistance of plasmatrons with pipelines τ × 10 <sup>-10</sup> , m <sup>-4</sup>	3,37	3,46	3,0	2,91	3,22	3,02	3,42	3,44	3,87	3,99	4,16	3,45	3,29
Relation (τ <sub>r</sub> - τ <sub>av,r</sub> )/τ <sub>av,r</sub> , % (τ <sub>av,r</sub> = 2,53 × 10 <sup>-10</sup> m <sup>-4</sup> )	51,08	7,79	-4,54	-24,4	-11,6	-15,5	3,12	-6,77	-3,17	3,96	17,42	-8,04	13,50
Relation (τ - τ <sub>av</sub> )/τ <sub>av</sub> , % (τ <sub>av</sub> = 3,37 × 10 <sup>-10</sup> m <sup>-4</sup> )	0,04	2,69	-10,9	-13,6	-4,45	-10,4	1,36	2,11	14,68	18,38	23,37	2,41	-2,39

Table A2.5.10 – Results of third flushing of plasmatrons "E" cooling path

Parameter	Parameter value														
	1	2	3	4	5	6	7	8	9	10	11	12	13	14	15
Number of mode															
Pressurization in a HTW-3 (c.p. L.R.09), atm.	3,15	5,24	7,05	9,08	10,88	13	15,07	17,28	16,28	14,23	12,20	10,21	8,3	6,27	4,22
Water pressure in the input path P <sub>1</sub> (MO-1), atm.	1,80	2,84	4,20	5,24	6,36	7,40	8,68	10,04	9,40	8,12	6,89	5,88	4,92	3,64	2,28
Water pressure in the input into electrode (MO-2), atm.	1,8	2,9	4,22	5,28	6,2	7,43	8,65	10,0	9,4	8,13	6,88	5,96	4,95	3,67	2,26
Water pressure in the output from electrode (MO-3), atm.	1,64	2,62	3,8	4,78	5,56	6,72	7,86	9,06	8,46	7,30	6,20	5,26	4,40	3,36	2,06
Water pressure in the drainage path P <sub>4</sub> (MO-4), atm.	1,44	2,56	3,60	4,32	5,28	6,40	7,48	8,64	8,12	7,0	5,88	5,08	4,20	3,20	2,04
Duration of water supply τ, s	373,2	244,6	182,0	161,4	142,2	131,6	123,8	115,2	117,4	126,8	137,4	150,4	169,2	202,6	290,8
Mass of supplied water M, kg	10	10	10	10	10	10	10	10	10	10	10	10	10	10	10
Measured water flow rate G <sub>p</sub> , kg/s	0,027	0,041	0,055	0,062	0,070	0,076	0,081	0,087	0,085	0,079	0,073	0,066	0,059	0,049	0,034
Water pressure P <sub>1d</sub> in the input path (L.R.22), atm	2,1	3,17	4,43	5,51	6,37	7,61	8,83	10,15	9,6	8,32	7,15	6,18	5,2	3,99	2,59
Water pressure P <sub>4d</sub> in the output path (c.p. L.R.23), atm	1,9	2,79	3,8	4,71	5,47	6,51	7,57	8,72	8,22	7,07	6,10	5,29	4,45	3,44	2,30
Water flow rate through electrodes G (L.G.16), kg/s	0,026	0,041	0,053	0,061	0,069	0,075	0,082	0,087	0,085	0,078	0,072	0,066	0,059	0,049	0,033
Difference of flow rates G - G <sub>p</sub> , kg/s	-0,001	0,0001	-0,002	-0,0001	-0,0013	-0,0001	0,0012	0,0002	-0,0002	-0,0009	-0,0008	-0,0005	-0,0001	-0,0004	-0,001
Relation (G - G <sub>p</sub> )/G <sub>p</sub> , %	-2,97	0,29	-3,54	-1,55	-1,88	-1,30	1,52	0,22	-0,21	-1,1	-1,1	-0,74	-0,17	-0,73	-4,04
Difference of pressures P <sub>1d</sub> - P <sub>1</sub> , atm.	0,30	0,33	0,23	0,27	0,01	0,21	0,15	0,11	0,20	0,20	0,26	0,30	0,28	0,35	0,31
Relation (P <sub>1d</sub> - P <sub>1</sub> )/P <sub>1</sub> , %	16,67	11,62	5,48	5,15	0,16	2,84	1,73	1,10	2,13	2,46	3,80	5,10	5,69	9,62	13,60
Difference of pressures P <sub>4d</sub> - P <sub>4</sub> , atm.	0,46	0,23	0,20	0,39	0,19	0,11	0,09	0,08	0,10	0,07	0,22	0,21	0,25	0,24	0,26
Relation (P <sub>4d</sub> - P <sub>4</sub> )/P <sub>4</sub> , %	31,94	8,98	5,56	9,03	3,60	1,72	1,20	0,93	1,23	1,00	3,74	4,13	5,95	7,50	12,75
Reduced factor of hydraulic resistance of plasmatrons t <sub>r</sub> × 10 <sup>-10</sup> , m <sup>-4</sup>	4,36	3,28	2,72	2,55	2,53	2,41	2,37	2,44	2,55	2,61	2,51	3,10	3,08	2,49	3,31
Reduced factor of hydraulic resistance of plasmatrons with pipelines t × 10 <sup>-10</sup> , m <sup>-4</sup>	9,81	3,28	3,89	4,69	4,27	3,39	3,60	3,64	3,45	3,52	3,72	3,54	4,03	3,54	3,97
Relation (t <sub>r</sub> - t <sub>av,r</sub> )/t <sub>av,r</sub> , % (t <sub>av,r</sub> = 2,82 × 10 <sup>-10</sup> m <sup>-4</sup> )	54,65	16,25	-3,46	-9,61	-10,20	-14,67	-15,97	-13,43	-10,10	-7,40	-10,91	-9,88	-9,27	-11,69	17,37
Relation (t - t <sub>av</sub> )/t <sub>av</sub> , % (t <sub>av</sub> = 4,16 × 10 <sup>-10</sup> m <sup>-4</sup> )	136,1	-21,13	-6,43	12,83	2,82	-18,46	-13,41	-12,53	-16,94	-15,22	-10,41	-14,80	-2,96	-14,97	-4,45

Table A2.5.11 – Results of flushing of plasmatrons "A" cooling path

Parameter	Parameter value														
	1	2	3	4	5	6	7	8	9	10	11	12	13	14	15
Number of mode															
Pressurization in a HTW-3 (c.p. L.R.09), atm.	3,35	5,24	7,38	9,19	11,11	13,05	15,19	17,32	16,19	14,22	12,20	10,21	8,27	6,25	4,11
Water pressure in the input path P <sub>1</sub> (MO-1) atm.	1,85	2,71	4,01	5,08	6,31	7,64	8,76	10,36	9,64	8,44	7,08	5,80	4,52	3,34	2,20
Water pressure in the input into electrode (MO-2), atm.	1,86	2,72	2,86	3,56	4,31	5,12	5,84	6,80	6,37	5,60	4,76	3,98	3,20	2,45	1,72
Water pressure in the output from electrode (MO-3), atm.	1,75	2,49	1,66	1,92	2,19	2,50	2,76	3,11	2,95	2,66	2,36	2,07	1,78	1,50	1,26
Water pressure in the drainage path P <sub>4</sub> (MO-4), atm.	1,76	2,48	3,70	4,72	5,80	6,98	8,00	9,36	8,72	7,64	6,44	5,30	4,16	3,06	2,03
Duration of water supply τ, s	377,2	246,2	190,6	167	149,6	135,6	126,8	116,8	121,5	129,2	142,2	157,4	178	209,2	306,8
Mass of supplied water M, kg	10	10	10	10	10	10	10	10	10	10	10	10	10	10	10
Measured water flow rate G <sub>p</sub> , kg/s	0,027	0,041	0,052	0,059	0,067	0,074	0,079	0,086	0,082	0,077	0,07	0,064	0,056	0,048	0,033
Water pressure P <sub>1d</sub> in the input path (L.R.22), atm	2,22	3,12	4,42	5,60	6,80	8,13	9,37	10,87	10,17	8,96	7,58	6,37	5,05	3,74	2,58
Water pressure P <sub>4d</sub> in the output path (c.p. L.R.23), atm	1,97	2,80	3,88	4,94	6,03	7,17	8,45	9,69	9,11	7,94	6,68	5,57	4,42	3,24	2,29
Water flow rate through electrodes G (L.G.16), kg/s	0,023	0,03	0,045	0,052	0,059	0,065	0,07	0,076	0,073	0,068	0,062	0,056	0,049	0,041	0,026
Difference of flow rates G - G <sub>p</sub> , kg/s	-0,004	-0,011	-0,007	-0,008	-0,008	-0,009	-0,009	-0,0096	-0,0093	-0,0094	-0,008	-0,0075	-0,0072	-0,0068	-0,0066
Relation (G - G <sub>p</sub> )/G <sub>p</sub> , %	-13,244	-26,14	-14,23	-13,16	-11,736	-11,86	-11,24	-11,232	-11,305	-12,144	-11,836	-11,856	-12,78	-14,228	-20,232
Difference of pressures P <sub>1d</sub> - P <sub>1</sub> , atm.	0,37	0,41	0,41	0,52	0,49	0,49	0,61	0,51	0,53	0,52	0,50	0,57	0,53	0,40	0,38
Relation (P <sub>1d</sub> - P <sub>1</sub> )/P <sub>1</sub> , %	20,13	15,04	10,28	10,24	7,73	6,41	6,96	4,92	5,50	6,16	7,06	9,83	11,73	12,11	17,27
Difference of pressures P <sub>4d</sub> - P <sub>4</sub> , atm.	0,21	0,32	0,18	0,22	0,23	0,19	0,45	0,33	0,39	0,30	0,24	0,27	0,26	0,18	0,26
Relation (P <sub>4d</sub> - P <sub>4</sub> )/P <sub>4</sub> , %	11,93	12,90	4,86	4,66	3,97	2,72	5,62	3,53	4,47	3,93	3,73	5,09	6,25	5,88	12,92
Reduced factor of hydraulic resistance of plasmatrons t <sub>r</sub> × 10 <sup>-10</sup> , m <sup>-4</sup>	3,008	2,753	2,276	2,271	2,313	2,188	2,216	2,222	2,312	2,353	2,343	2,405	2,481	2,604	2,358
Reduced factor of hydraulic resistance of plasmatrons with pipelines t × 10 <sup>-10</sup> , m <sup>-4</sup>	2,451	2,753	2,190	1,965	2,243	2,375	2,392	2,670	2,658	2,614	2,533	2,425	2,233	2,364	3,169
Relation (t <sub>r</sub> - t <sub>av,r</sub> )/t <sub>av,r</sub> , % (t <sub>av,r</sub> = 2,41 × 10 <sup>-10</sup> m <sup>-4</sup> )	24,973	14,370	-5,454	-5,643	-3,895	-9,078	-7,943	-7,688	-3,952	-2,253	-2,643	-0,060	3,074	8,204	-2,013
Relation (t - t <sub>av</sub> )/t <sub>av</sub> , % (t <sub>av</sub> = 2,47 × 10 <sup>-10</sup> m <sup>-4</sup> )	-0,739	11,485	-11,295	-20,405	-9,158	-3,791	-3,126	8,153	7,670	5,869	2,596	-1,795	-9,574	-4,240	28,349

Table A2.5.12 – Results of flushing of plasmatrons "B" cooling path

Parameter	Parameter value														
	1	2	3	4	5	6	7	8	9	10	11	12	13	14	15
Number of mode															
Pressurization in a HTW-3 (c.p. L.R.09), atm.	3,04	5,30	7,00	9,14	11,02	13,05	15,05	17,08	16,00	14,12	12,20	10,21	8,12	6,01	4,20
Water pressure in the input path P <sub>1</sub> (MO-1), atm.	1,56	2,38	3,56	4,76	6,12	7,48	8,76	10,12	9,32	8,20	6,84	5,72	4,28	3,00	1,96
Water pressure in the input into electrode (MO-2), atm.	1,56	2,36	3,56	4,76	6,04	7,32	8,60	9,96	9,24	8,04	6,84	5,72	4,28	3,00	1,96
Water pressure in the output from electrode (MO-3), atm.	1,48	2,14	3,18	4,28	5,48	6,60	7,77	9,05	8,28	7,24	6,12	5,06	3,77	2,65	1,80
Water pressure in the drainage path P <sub>4</sub> (MO-4), atm.	1,48	2,14	3,20	4,30	5,12	6,68	7,84	8,92	8,28	7,28	6,16	5,12	3,80	2,68	1,80
Duration of water supply τ, s	520,4	261,8	212,0	180,4	162,0	144,8	133,6	125,8	130,8	140,0	149,8	166,2	191,0	227,6	329,0
Mass of supplied water M, kg	10	10	10	10	10	10	10	10	10	10	10	10	10	10	10
Measured water flow rate G <sub>p</sub> , kg/s	0,019	0,038	0,047	0,055	0,062	0,069	0,075	0,079	0,076	0,071	0,067	0,060	0,052	0,044	0,030
Water pressure P <sub>1d</sub> in the input path (L.R.22), atm	1,88	2,91	3,88	5,22	6,49	7,71	9,02	10,43	9,61	8,48	7,26	6,10	4,63	3,37	2,33
Water pressure P <sub>4d</sub> in the output path (c.p. L.R.23), atm	1,89	2,67	3,50	4,63	5,80	6,90	8,04	9,26	8,59	7,54	6,46	5,42	4,15	3,06	2,23
Water flow rate through electrodes G (L.G.16), kg/s	0,0	0,023	0,034	0,043	0,051	0,057	0,063	0,068	0,065	0,06	0,054	0,049	0,04	0,033	0,016
Difference of flow rates G - G <sub>p</sub> , kg/s	-0,019	-0,015	-0,013	-0,012	-0,012	-0,012	-0,012	-0,011	-0,011	-0,011	-0,013	-0,011	-0,012	-0,011	-0,014
Relation (G - G <sub>p</sub> )/G <sub>p</sub> , %	-100	-39,79	-27,92	-22,43	-17,38	-17,46	-15,83	-14,46	-14,98	-16,0	-19,11	-18,56	-23,60	-24,89	-47,36
Difference of pressures P <sub>1d</sub> - P <sub>1</sub> , atm.	0,32	0,53	0,32	0,46	0,37	0,23	0,26	0,31	0,29	0,28	0,42	0,38	0,35	0,37	0,37
Relation (P <sub>1d</sub> - P <sub>1</sub> )/P <sub>1</sub> , %	20,51	22,47	8,99	9,66	6,05	3,07	2,97	3,06	3,11	3,41	6,14	6,64	8,18	12,33	18,88
Difference of pressures P <sub>4d</sub> - P <sub>4</sub> , atm.	0,41	0,53	0,30	0,33	0,68	0,22	0,20	0,34	0,31	0,26	0,30	0,30	0,35	0,38	0,43
Relation (P <sub>4d</sub> - P <sub>4</sub> )/P <sub>4</sub> , %	27,70	24,77	9,37	7,67	13,28	3,29	2,55	3,81	3,74	3,57	4,87	5,86	9,21	14,18	23,89
Reduced factor of hydraulic resistance of plasmatrons τ × 10 <sup>-10</sup> , m <sup>4</sup>	4,241	3,005	3,378	3,058	2,877	2,955	2,907	2,825	3,215	3,069	3,163	3,547	3,656	3,569	3,390
Reduced factor of hydraulic resistance of plasmatrons with pipelines t × 10 <sup>-10</sup> , m <sup>4</sup>	4,241	3,166	3,167	2,930	5,137	3,283	3,214	3,717	3,483	3,530	2,987	3,244	3,428	3,245	3,390
Relation (τ - t <sub>av,r</sub> )/t <sub>av,r</sub> , % (t <sub>av,r</sub> = 3,26 × 10 <sup>-10</sup> m <sup>4</sup> )	30,207	-7,731	3,723	-6,118	-11,674	-9,272	-10,75	-13,259	-1,291	-5,764	-2,898	8,902	12,255	9,587	4,084
Relation (τ - t <sub>av</sub> )/t <sub>av</sub> , % (t <sub>av</sub> = 3,48 × 10 <sup>-10</sup> m <sup>4</sup> )	21,951	-8,952	-8,926	-15,734	47,724	-5,584	-7,568	6,896	0,154	1,499	-14,108	-6,710	-1,434	-6,693	-2,516

Table A2.5.13 – Results of flushing of plasmatrons "D" cooling path

Parameter	Parameter value														
	1	2	3	4	5	6	7	8	9	10	11	12	13	14	15
Number of mode															
Pressurization in a HTW-3 (c.p. L.R.09), atm.	3,18	5,10	7,01	9,07	11,11	13,02	14,96	17,18	16,00	14,09	12,20	10,10	8,25	6,11	4,19
Water pressure in the input path P <sub>1</sub> (MO-1), atm.	1,64	2,22	3,02	3,80	4,78	5,72	6,78	7,88	7,32	6,36	5,34	4,49	3,42	2,62	1,82
Water pressure in the input into electrode (MO-2), atm.	1,53	2,28	3,08	3,78	4,76	5,66	6,76	7,80	7,27	6,28	5,32	4,44	3,40	2,60	1,80
Water pressure in the output from electrode (MO-3), atm.	1,48	2,06	2,76	3,40	4,28	5,06	6,07	7,00	6,49	5,64	4,76	3,96	3,00	2,36	1,64
Water pressure in the drainage path P <sub>4</sub> (MO-4), atm.	1,56	2,12	2,76	3,40	4,20	5,04	5,88	6,92	6,34	5,56	4,68	3,96	3,04	2,40	1,72
Duration of water supply τ, s	685,8	354,2	268,2	220,0	191,4	173,0	159,6	146,2	153,6	164,0	177,4	200,2	231,2	287,8	399,4
Mass of supplied water M, kg	10	10	10	10	10	10	10	10	10	10	10	10	10	10	10
Measured water flow rate G <sub>p</sub> , kg/s	0,015	0,028	0,037	0,045	0,052	0,058	0,063	0,068	0,065	0,061	0,056	0,049	0,043	0,035	0,025
Water pressure P <sub>1d</sub> in the input path (L.R.22), atm	2,0	2,65	3,49	4,23	5,24	6,19	7,34	8,75	8,00	6,94	5,90	4,78	3,86	3,12	2,23
Water pressure P <sub>4d</sub> in the output path (c.p. L.R.23), atm	1,7	2,23	2,85	3,34	4,23	5,08	5,91	7,00	6,33	5,56	4,76	3,87	3,09	2,50	1,86
Water flow rate through electrodes G (L.G.16), kg/s	0,0	0,016	0,026	0,036	0,043	0,05	0,055	0,061	0,057	0,053	0,048	0,043	0,037	0,028	0,019
Difference of flow rates G - G <sub>p</sub> , kg/s	-0,015	-0,012	-0,011	-0,009	-0,009	-0,008	-0,008	-0,007	-0,008	-0,008	-0,008	-0,007	-0,006	-0,007	-0,006
Relation (G - G <sub>p</sub> )/G <sub>p</sub> , %	-100,0	-43,33	-30,27	-20,80	-17,67	-13,50	-12,22	-10,82	-12,45	-13,08	-14,85	-13,91	-14,46	-19,42	-24,11
Difference of pressures P <sub>1d</sub> - P <sub>1</sub> , atm.	0,36	0,43	0,47	0,43	0,46	0,47	0,56	0,87	0,68	0,58	0,56	0,29	0,44	0,50	0,41
Relation (P <sub>1d</sub> - P <sub>1</sub> )/P <sub>1</sub> , %	21,95	19,58	15,72	11,32	9,72	8,22	8,32	11,04	9,29	9,12	10,57	6,51	13,00	19,27	22,80
Difference of pressures P <sub>4d</sub> - P <sub>4</sub> , atm.	0,14	0,11	0,09	-0,06	0,03	0,04	0,03	0,08	-0,01	0,00	0,08	-0,09	0,05	0,10	0,14
Relation (P <sub>4d</sub> - P <sub>4</sub> )/P <sub>4</sub> , %	8,97	5,39	3,11	-1,76	0,71	0,79	0,51	1,16	-0,16	0,00	1,71	-2,27	1,64	3,99	8,14
Reduced factor of hydraulic resistance of plasmatrons τ × 10 <sup>-10</sup> , m <sup>4</sup>	4,419	5,501	4,506	3,638	3,442	3,468	3,430	3,347	3,621	3,369	3,449	3,766	4,185	3,891	4,996
Reduced factor of hydraulic resistance of plasmatrons with pipelines t × 10 <sup>-10</sup> , m <sup>4</sup>	7,36	2,46	3,55	3,79	4,13	3,98	4,467	4,016	4,526	4,212	4,041	4,142	3,934	3,437	2,998
Relation (τ - t <sub>av,r</sub> )/t <sub>av,r</sub> , % (t <sub>av,r</sub> = 3,94 × 10 <sup>-10</sup> m <sup>4</sup> )	12,292	39,784	14,493	-7,554	-12,535	-11,869	-12,83	-14,946	-7,995	-14,379	-12,339	-4,307	6,352	-1,121	26,954
Relation (τ - t <sub>av</sub> )/t <sub>av</sub> , % (t <sub>av</sub> = 4,10 × 10 <sup>-10</sup> m <sup>4</sup> )	80,968	-39,659	-12,816	-6,884	1,489	-2,115	9,772	-1,308	11,205	3,489	-0,705	1,784	-3,333	-15,543	-26,345



Table A2.5.14 – Results of flushing of plasmatrons "C" cooling path

Parameter	Parameter value														
	1	2	3	4	5	6	7	8	9	10	11	12	13	14	15
Number of mode															
Pressurization in a HTW-3 (c.p. L.R.09), atm.	3,08	5,11	7,12	9,03	11,00	13,14	15,03	17,00	16,10	14,12	12,00	10,15	8,01	6,20	4,17
Water pressure in the input path P <sub>1</sub> (MO-1), atm.	1,62	2,60	3,56	4,82	5,96	7,40	8,60	9,88	9,16	8,04	6,84	5,56	4,28	3,21	2,09
Water pressure in the input into electrode (MO-2), atm.	1,56	2,52	3,48	4,68	5,80	7,24	8,44	9,56	9,00	7,72	6,68	5,40	4,15	3,08	1,98
Water pressure in the output from electrode (MO-3), atm.	1,48	2,36	3,16	4,20	5,24	6,52	7,48	8,60	8,12	7,00	5,99	4,84	3,75	2,82	1,93
Water pressure in the drainage path P <sub>4</sub> (MO-4), atm.	1,48	2,29	3,08	4,12	5,12	6,16	7,24	8,36	7,84	6,88	5,80	4,78	3,68	2,78	1,86
Duration of water supply τ, s	10	10	10	10	10	10	10	10	10	10	10	10	10	10	10
Mass of supplied water M, kg	642,6	310,8	225,6	194,2	176,4	154,2	143,4	132,0	137,4	148,8	158,6	173,6	203,8	251,2	384,2
Measured water flow rate G <sub>p</sub> , kg/s	0,016	0,032	0,044	0,051	0,057	0,065	0,069	0,076	0,073	0,067	0,063	0,058	0,049	0,039	0,026
Water pressure P <sub>1d</sub> in the input path (L.R.22), atm	1,75	2,76	3,83	4,92	6,22	7,5	8,65	9,85	9,29	8,22	6,97	5,79	4,46	3,42	2,3
Water pressure P <sub>4d</sub> in the output path (c.p. L.R.23), atm	1,71	2,57	3,40	4,39	5,45	6,60	7,61	8,70	8,20	7,25	6,10	5,09	3,97	3,06	2,17
Water flow rate through electrodes G (L.G.16), kg/s	0,011	0,026	0,037	0,044	0,05	0,056	0,061	0,065	0,063	0,059	0,053	0,048	0,041	0,032	0,02
Difference of flow rates G - G <sub>p</sub> , kg/s	-0,005	-0,006	-0,007	-0,007	-0,007	-0,009	-0,009	-0,011	-0,009	-0,008	-0,01	-0,009	-0,008	-0,008	-0,006
Relation (G - G <sub>p</sub> )/G <sub>p</sub> , %	-29,31	-19,19	-16,53	-14,55	-11,8	-13,65	-12,53	-14,2	-13,44	-12,21	-15,94	-16,67	-16,44	-19,62	-23,16
Difference of pressures P <sub>1d</sub> - P <sub>1</sub> , atm.	0,13	0,16	0,27	0,10	0,26	0,10	0,05	-0,03	0,13	0,18	0,13	0,23	0,18	0,21	0,21
Relation (P <sub>1d</sub> - P <sub>1</sub> )/P <sub>1</sub> , %	7,76	6,15	7,58	1,99	4,36	1,35	0,58	-0,30	1,42	2,24	1,90	4,14	4,21	6,61	10,15
Difference of pressures P <sub>4d</sub> - P <sub>4</sub> , atm.	0,23	0,28	0,32	0,27	0,33	0,44	0,37	0,34	0,36	0,37	0,30	0,31	0,29	0,28	0,31
Relation (P <sub>4d</sub> - P <sub>4</sub> )/P <sub>4</sub> , %	15,54	12,33	10,39	6,55	6,45	7,14	5,11	4,07	4,59	5,38	5,17	6,49	7,88	10,07	16,67
Reduced factor of hydraulic resistance of plasmatrons t × 10 <sup>-10</sup> , m <sup>-4</sup>	6,466	3,025	3,188	3,543	3,411	3,351	3,864	3,274	3,252	3,12	3,388	3,304	3,252	3,162	1,387
Reduced factor of hydraulic resistance of plasmatrons with pipelines t × 10 <sup>-10</sup> , m <sup>-4</sup>	11,639	5,899	4,782	5,197	5,116	5,771	5,474	5,184	4,878	5,027	5,121	4,601	4,878	5,287	6,588
Relation (t - t <sub>av,r</sub> )/t <sub>av,r</sub> , % (t <sub>av,r</sub> = 3,40 × 10 <sup>-10</sup> m <sup>-4</sup> )	90,231	-10,999	-6,214	4,244	0,345	-1,415	13,679	-3,677	-4,332	-8,199	-0,343	-2,815	-4,329	-6,977	-59,2
Relation (t - t <sub>av</sub> )/t <sub>av</sub> , % (t <sub>av</sub> = 5,70 × 10 <sup>-10</sup> m <sup>-4</sup> )	104,335	3,566	-16,051	-8,763	-10,18	1,319	-3,897	-8,998	-14,366	-11,74	-10,104	-19,222	-14,364	-7,193	15,651

Table A2.5.15 – Results of flushing of plasmatrons "D" cooling path

Parameter	Parameter value													
	1	2	3	4	5	6	7	8	9	10	11	12	13	14
Number of mode														
Pressurization in a HTW-3 (c.p. L.R.09), atm.	3,08	5,11	7,14	9,06	11,20	13,01	15,19	16,15	14,12	12,00	10,20	8,12	6,00	4,19
Water pressure in the input path P <sub>1</sub> (MO-1), atm.	1,80	2,89	4,06	5,19	6,47	7,72	9,16	9,67	8,52	7,21	6,04	4,68	3,42	2,38
Water pressure in the input into electrode (MO-2), atm.	1,80	2,86	4,01	5,16	6,38	7,67	9,16	9,58	8,44	7,08	5,94	4,68	3,40	2,31
Water pressure in the output from electrode (MO-3), atm.	1,64	2,54	3,56	4,60	5,74	6,84	8,20	8,60	7,56	6,38	5,32	4,17	3,00	2,12
Water pressure in the drainage path P <sub>4</sub> (MO-4), atm.	1,64	2,48	3,48	4,46	5,60	6,64	7,88	8,32	7,32	6,24	5,18	4,00	2,95	2,08
Duration of water supply τ, s	429,4	257,4	204,6	178,6	160	147,2	135,4	130,8	140,7	152,6	168	189	222,4	307,8
Mass of supplied water M, kg	10	10	10	10	10	10	10	10	10	10	10	10	10	10
Measured water flow rate G <sub>p</sub> , kg/s	0,0233	0,0389	0,0489	0,0559	0,0625	0,0679	0,0739	0,0765	0,0711	0,0655	0,0595	0,0529	0,0449	0,0325
Water pressure P <sub>1d</sub> in the input path (L.R.22), atm	2,20	3,26	4,46	5,71	7,23	8,76	10,08	10,79	9,40	7,93	6,60	5,11	3,86	2,74
Water pressure P <sub>4d</sub> in the output path (c.p. L.R.23), atm	1,83	2,63	3,56	4,51	5,73	6,74	7,87	8,39	7,42	6,35	5,26	4,13	3,07	2,19
Water flow rate through electrodes G (L.G.16), kg/s	0,021	0,04	0,051	0,06	0,069	0,076	0,083	0,086	0,08	0,073	0,067	0,056	0,046	0,041
Difference of flow rates G - G <sub>p</sub> , kg/s	-0,0023	0,0012	0,0021	0,004	0,0065	0,0081	0,0091	0,0095	0,0089	0,0075	0,0075	0,0031	0,001	0,0085
Relation (G - G <sub>p</sub> )/G <sub>p</sub> , %	-9,83	2,96	4,346	7,16	10,4	11,87	12,38	12,49	12,56	11,39	12,56	5,84	2,3	26,19
Difference of pressures P <sub>1d</sub> - P <sub>1</sub> , atm.	0,40	0,37	0,40	0,52	0,76	1,04	0,92	1,12	0,88	0,72	0,56	0,43	0,44	0,36
Relation (P <sub>1d</sub> - P <sub>1</sub> )/P <sub>1</sub> , %	22,22	12,88	9,96	9,98	11,71	13,47	10,4	11,56	10,33	10,02	9,27	9,19	13,00	15,32
Difference of pressures P <sub>4d</sub> - P <sub>4</sub> , atm.	0,19	0,15	0,08	0,05	0,13	0,10	-0,01	0,07	0,10	0,11	0,08	0,13	0,12	0,11
Relation (P <sub>4d</sub> - P <sub>4</sub> )/P <sub>4</sub> , %	11,59	6,05	2,30	1,12	2,32	1,51	-0,13	0,84	1,37	1,76	1,54	3,25	4,00	5,09
Reduced factor of hydraulic resistance of plasmatrons t × 10 <sup>-10</sup> , m <sup>-4</sup>	5,77	4,15	3,67	3,49	3,21	3,53	3,45	3,27	3,41	3,21	3,45	3,58	3,87	3,56
Reduced factor of hydraulic resistance of plasmatrons with pipelines t × 10 <sup>-10</sup> , m <sup>-4</sup>	5,77	5,29	4,72	4,57	4,37	4,58	4,59	4,53	4,65	4,41	4,75	4,75	4,49	5,42
Relation (t - t <sub>av,r</sub> )/t <sub>av,r</sub> , % (t <sub>av,r</sub> = 3,69 × 10 <sup>-10</sup> m <sup>-4</sup> )	56,61	12,55	-0,44	-5,17	-13,02	-4,29	-6,57	-11,36	-7,52	-12,97	-6,51	-2,91	5,03	-3,43
Relation (t - t <sub>av</sub> )/t <sub>av</sub> , % (t <sub>av</sub> = 4,78 × 10 <sup>-10</sup> m <sup>-4</sup> )	20,84	10,72	-1,24	-4,36	-8,56	-4,15	-3,88	-5,25	-2,69	-7,67	-0,58	-0,51	-5,99	13,31

Table A2.5.16 – Results of flushing of water cooling cable

Parameter	Parameter value														
Number of mode	1	2	3	4	5	6	7	8	9	10	11	12	13	14	15
Pressurization in a HTW-3 (c.p. L.R.09), atm.	3,04	5,09	7,12	9,01	11,06	13,20	15,10	17,10	16,03	14,12	12,10	10,08	8,13	6,04	4,19
Water pressure in the input path P <sub>1</sub> (MO-1), atm.	1,62	2,86	4,20	5,43	7,00	8,44	9,83	11,08	10,36	9,16	7,80	6,36	4,92	3,64	2,36
Water pressure in the input into electrode (MO-2), atm.	1,48	2,47	3,32	4,20	5,35	6,44	7,48	8,60	7,98	7,08	6,06	4,97	3,88	2,95	2,02
Water pressure in the output from electrode (MO-3), atm.	1,40	2,04	2,68	3,40	4,36	5,37	6,28	7,24	6,73	5,88	5,13	4,02	3,14	2,44	1,75
Water pressure in the drainage path P <sub>4</sub> (MO-4), atm.	1,42	2,04	2,74	3,44	4,45	5,44	6,42	7,26	6,80	5,94	5,04	4,08	3,21	2,52	1,83
Duration of water supply τ, s	283	122,8	86,2	72	63	55,6	51	47	48,6	53,40	58,20	66,00	77,20	99,40	159,20
Mass of supplied water M, kg	10	10	10	10	10	10	10	10	10	10	10	10	10	10	10
Measured water flow rate G <sub>p</sub> , kg/s	0,0353	0,0814	0,1160	0,1389	0,1587	0,1799	0,1961	0,2128	0,2058	0,1873	0,1718	0,1515	0,1295	0,1006	0,0628
Water pressure P <sub>1d</sub> in the input path (L.R.22), atm	1,85	3,14	4,34	5,54	7,02	8,42	9,94	11,02	10,50	9,32	7,90	6,46	5,04	3,81	2,55
Water pressure P <sub>4d</sub> in the output path (c.p. L.R.23), atm	1,66	2,25	2,91	3,62	4,59	5,54	6,57	7,47	6,94	6,15	5,26	4,30	3,42	2,71	2,04
Water flow rate through electrodes G (L.G.16), kg/s		0,07	0,11	0,12	0,14	0,17	0,19	0,20	0,19	0,18	0,16	0,13	0,12	0,09	0,05
Difference of flow rates G - G <sub>p</sub> , kg/s	-0,0353	-0,0084	-0,0090	-0,0179	-0,0147	-0,0149	-0,0101	-0,0098	-0,0118	-0,0093	-0,0138	-0,0185	-0,0085	-0,0066	-0,0088
Relation (G - G <sub>p</sub> )/G <sub>p</sub> , %	-100,00	-10,36	-7,77	-12,88	-9,28	-8,26	-5,14	-4,59	-5,72	-4,95	-8,04	-12,22	-6,59	-6,56	-14,03
Difference of pressures P <sub>1d</sub> - P <sub>1</sub> , atm.	0,23	0,28	0,14	0,11	0,02	-0,02	0,11	-0,06	0,14	0,16	0,10	0,10	0,12	0,17	0,19
Relation (P <sub>1d</sub> - P <sub>1</sub> )/P <sub>1</sub> , %	13,92	9,94	3,33	1,99	0,29	-0,24	1,10	-0,54	1,35	1,75	1,28	1,57	2,44	4,67	8,05
Difference of pressures P <sub>4d</sub> - P <sub>4</sub> , atm.	0,24	0,21	0,17	0,18	0,14	0,10	0,15	0,21	0,14	0,21	0,22	0,22	0,21	0,19	0,21
Relation (P <sub>4d</sub> - P <sub>4</sub> )/P <sub>4</sub> , %	16,90	10,29	6,20	5,23	3,19	1,84	2,34	2,89	2,06	3,54	4,37	5,39	6,61	7,54	11,35
Reduced factor of hydraulic resistance of plasmatrons τ × 10 <sup>-10</sup> , m <sup>-4</sup>	1,25	1,28	0,93	0,81	0,77	0,65	0,61	0,59	0,58	0,67	0,62	0,80	0,86	0,99	1,35
Reduced factor of hydraulic resistance of plasmatrons with pipelines t × 10 <sup>-10</sup> , m <sup>-4</sup>	3,20	2,41	2,12	2,02	1,98	1,82	1,74	1,65	1,65	1,80	1,83	1,94	2,00	2,17	2,62
Relation (τ - t <sub>av,τ</sub> )/t <sub>av,τ</sub> , % (t <sub>av,τ</sub> = 0,85 × 10 <sup>-10</sup> m <sup>-4</sup> )	47,48	49,95	9,46	-4,54	-9,37	-23,72	-28,15	-30,85	-32,15	-21,23	-27,64	-5,35	0,97	16,44	58,68
Relation (t - t <sub>av,t</sub> )/t <sub>av,t</sub> , % (t <sub>av,t</sub> = 2,06 × 10 <sup>-10</sup> m <sup>-4</sup> )	55,05	16,78	2,95	-2,00	-3,87	-11,99	-15,78	-19,92	-20,20	-12,86	-11,28	-5,75	-3,17	5,02	27,00

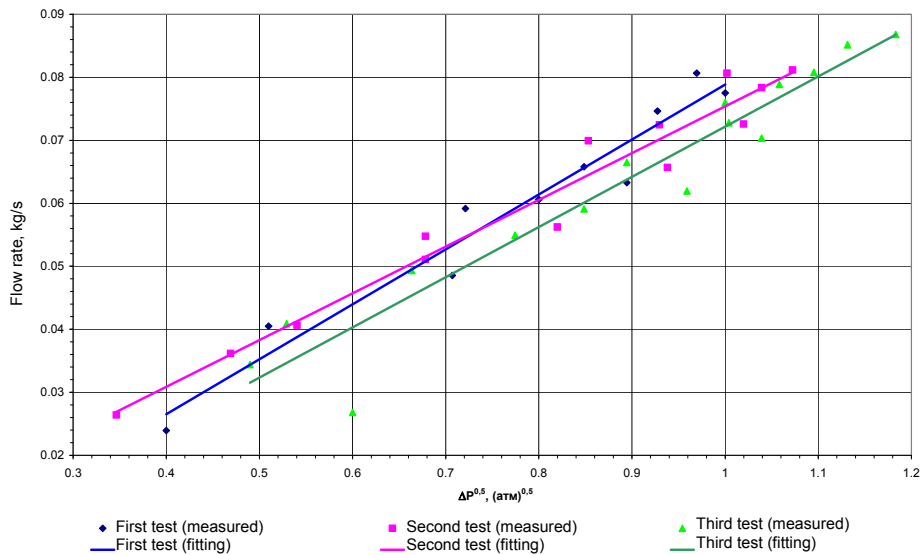


Figure A2.5.42 – Flushing of plasmatrons "E" cooling path

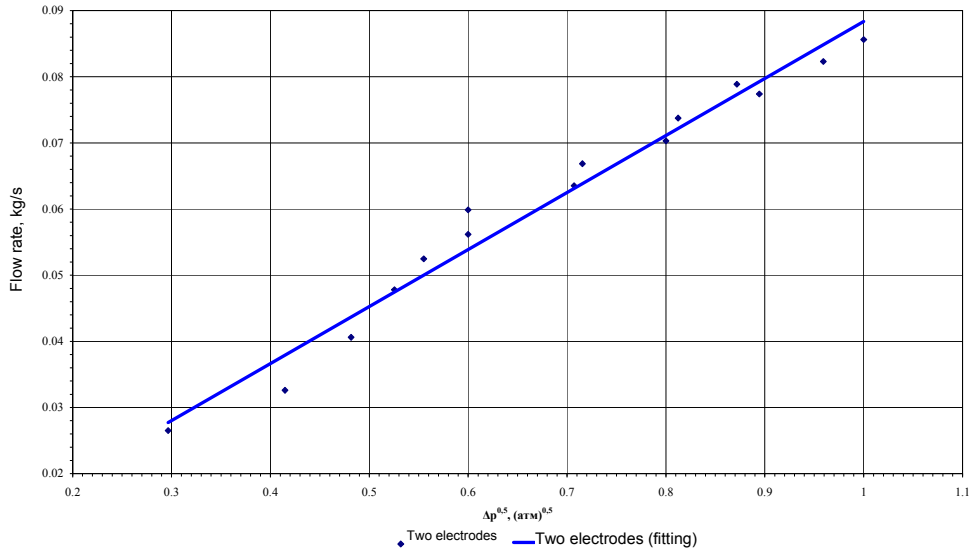


Figure A2.5.43 – Flushing of plasmatrons "A" cooling path

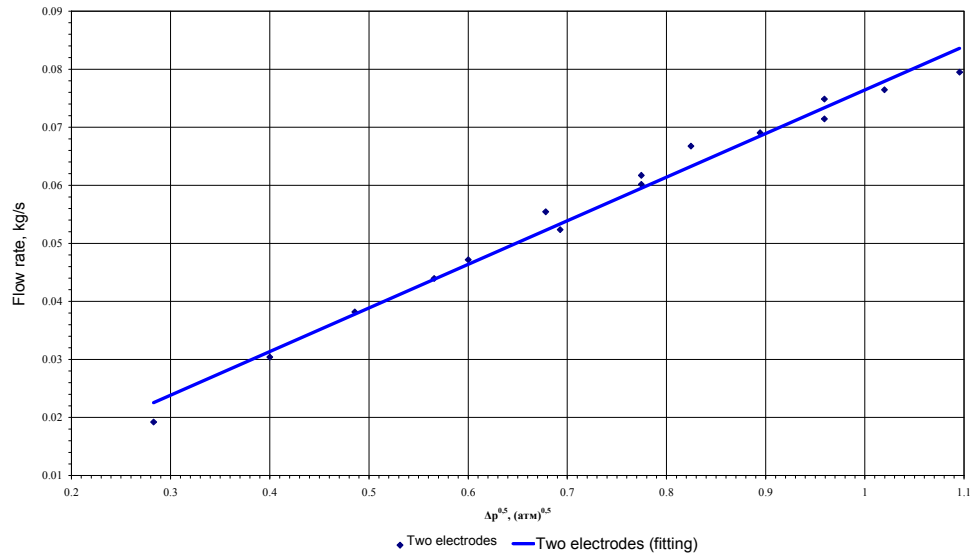


Figure A2.5.44 – Flushing of plasmatrons "B" cooling path

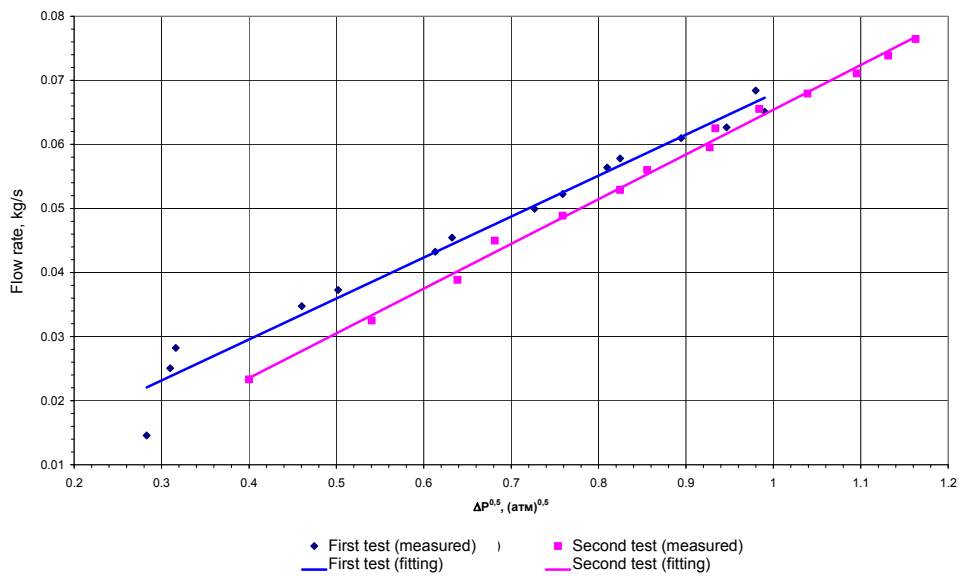


Figure A2.5.45 – Flushing of plasmatrons "D" cooling path

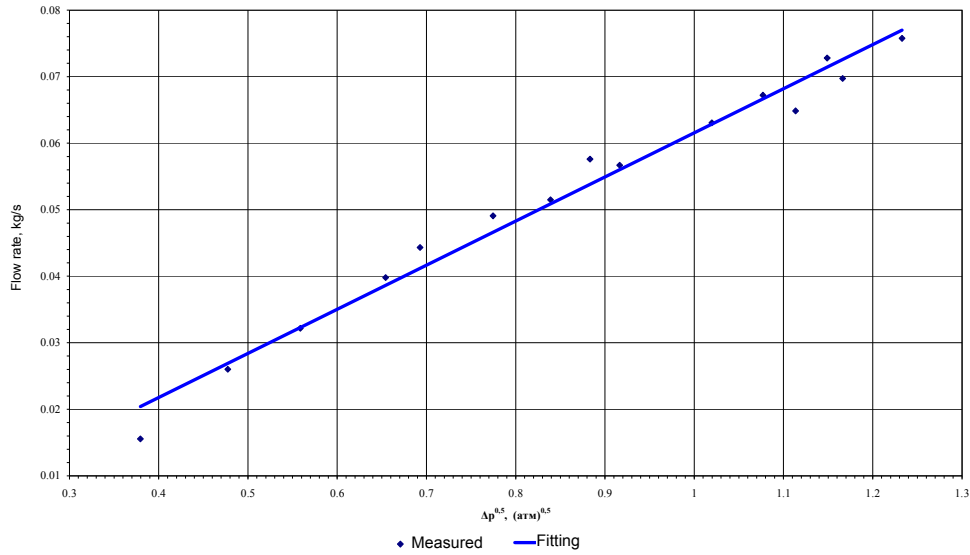


Figure A2.5.46 – Flushing of plasmatrons "C" cooling path

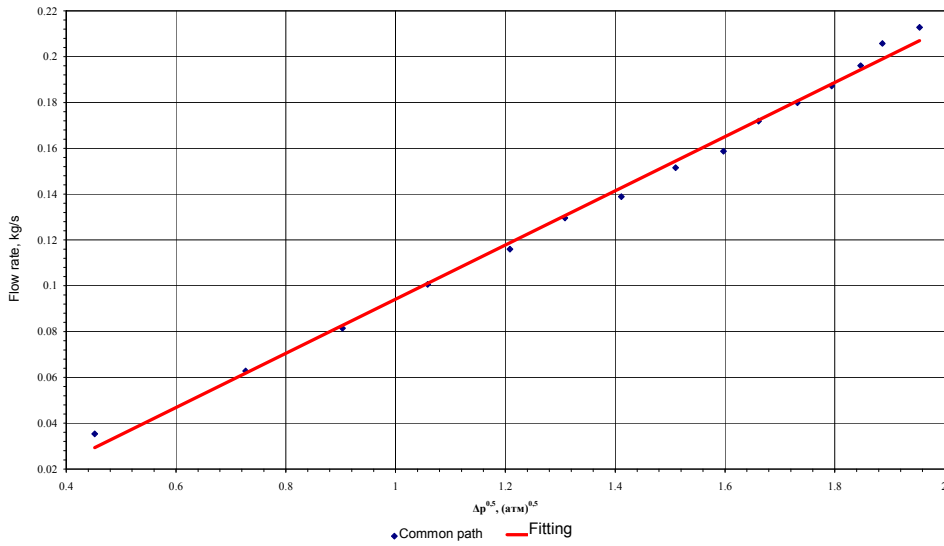


Figure A2.5.47 – Flushing of water-cooled cable

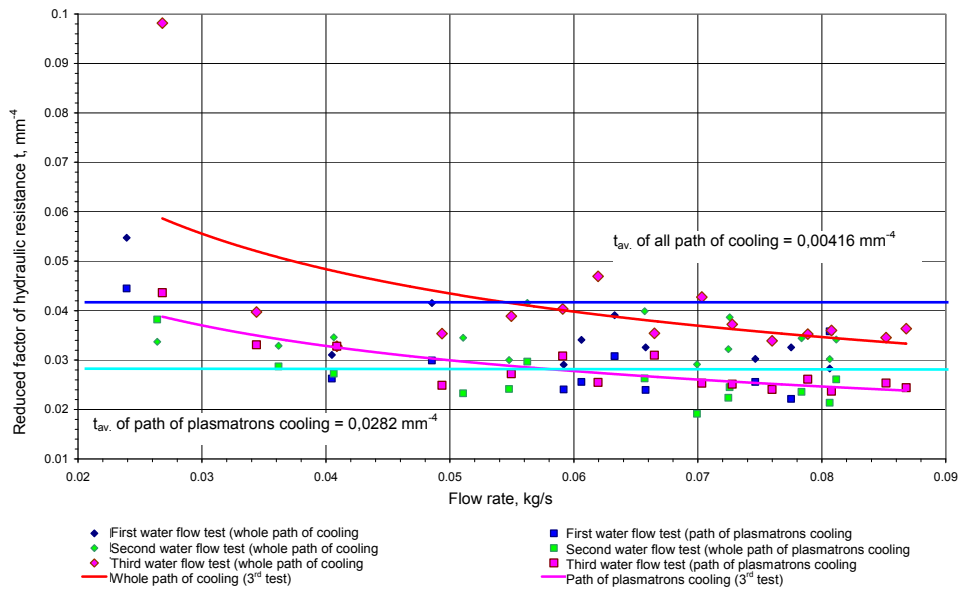


Figure A2.5.48 – Flushing of plasmatrons "E"

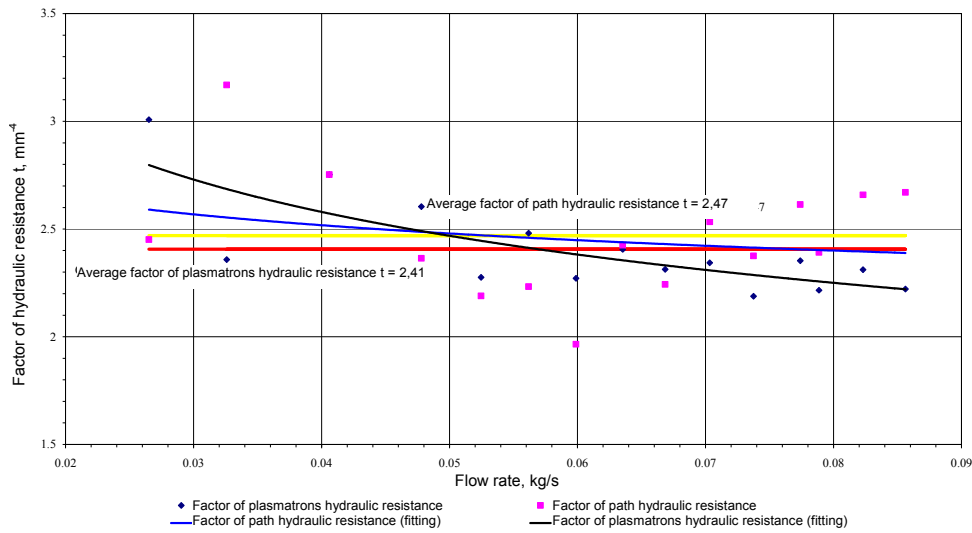


Figure A2.5.49 – Flushing of plasmatrons "A"

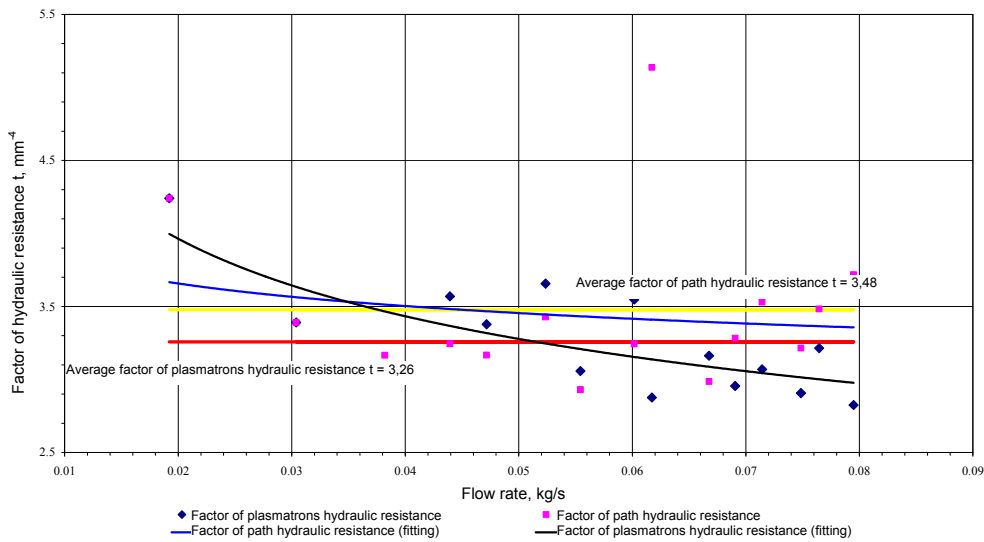


Figure A2.5.50 – Flushing of plasmatrons "B"

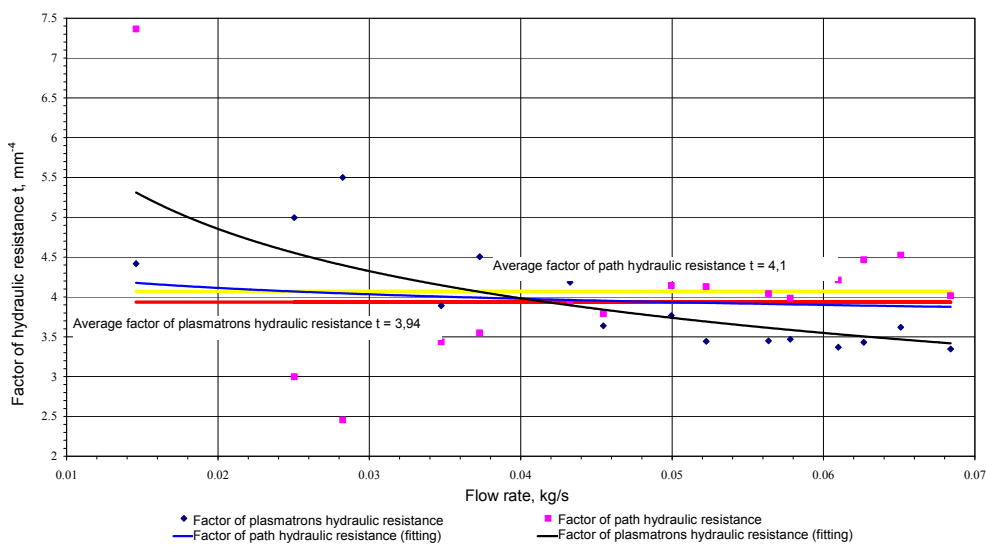


Figure A2.5.51 – Flushing of plasmatrons "D"



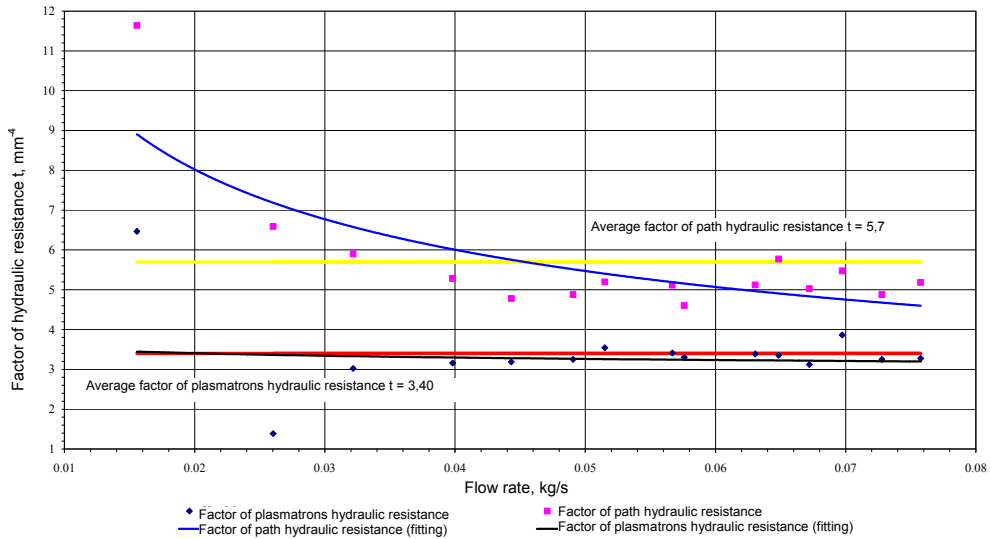


Figure A2.5.52 – Flushing of plasmatrons "C"

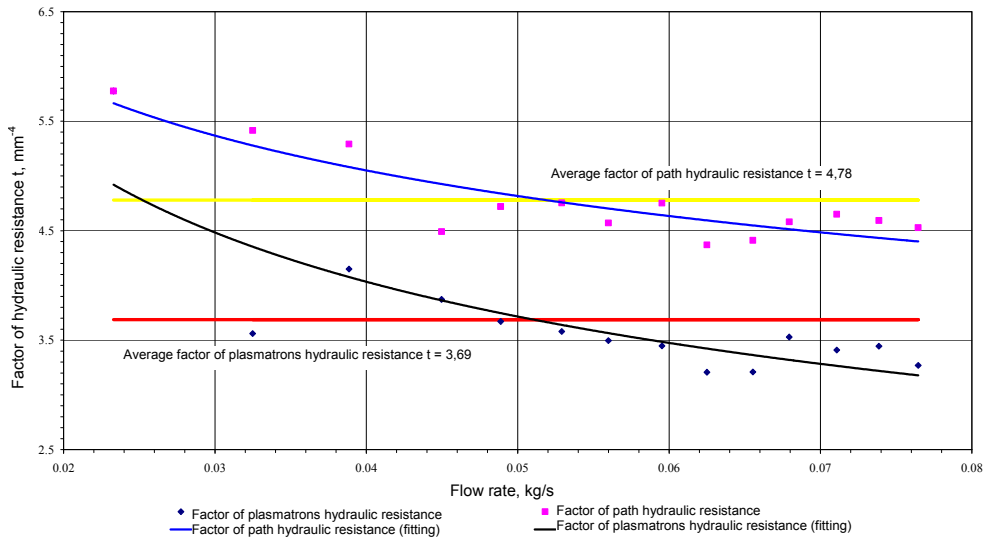


Figure A2.5.53 – Flushing of plasmatrons "D"

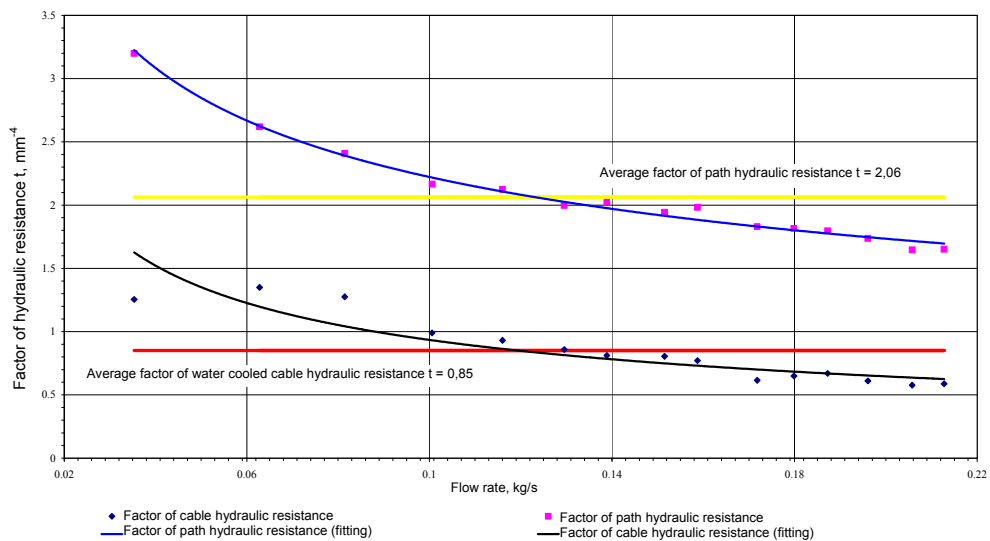


Figure A2.5.54 – Flushing of water-cooled cable

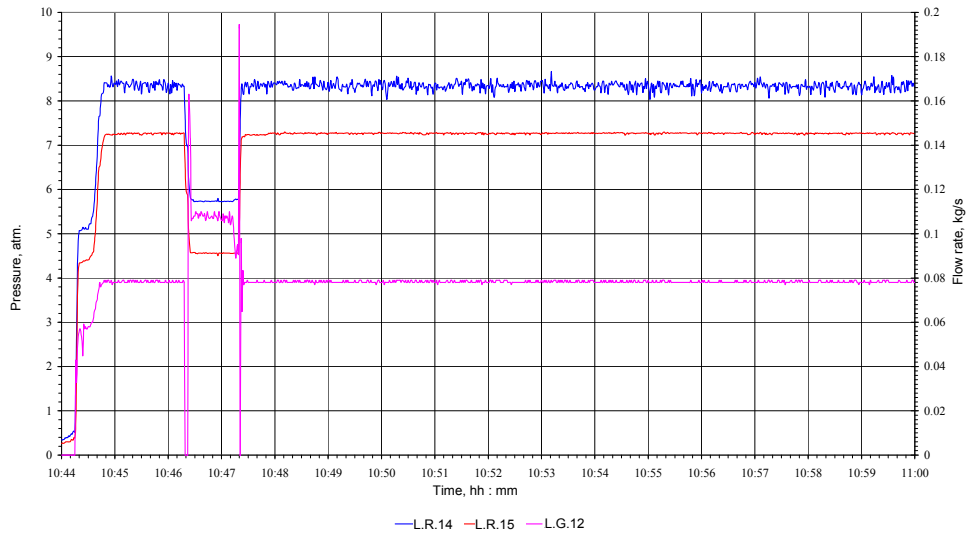


Figure A2.5.55 – Flushing of all paths of cooling. Plasmatrons "A"

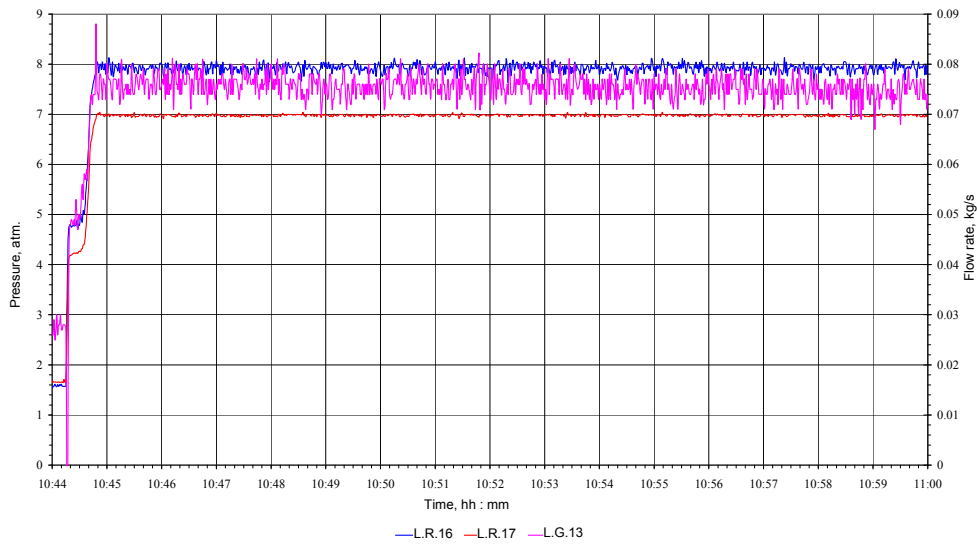


Figure A2.5.56 – Flushing of all paths of cooling. Plasmatrons "B"

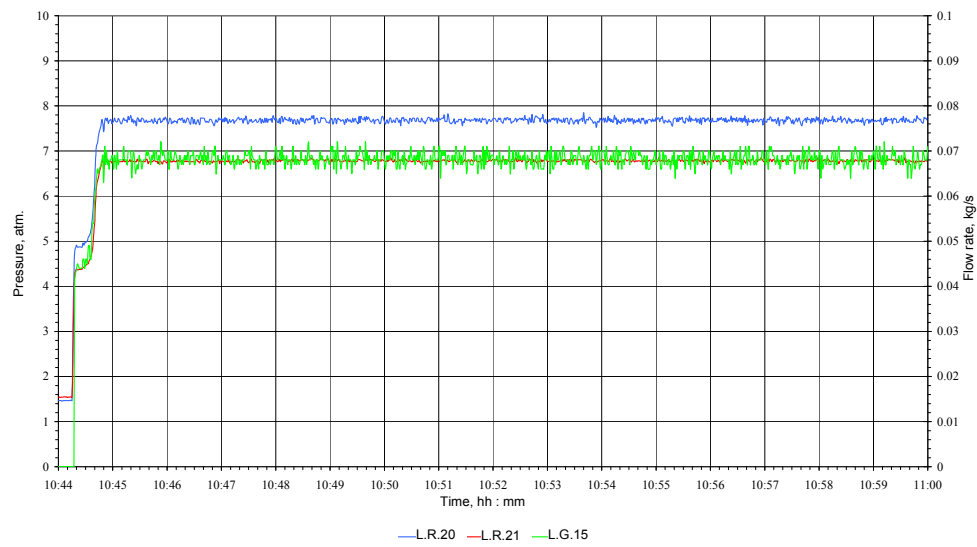


Figure A2.5.57 – Flushing of all paths of cooling. Plasmatrons "C"

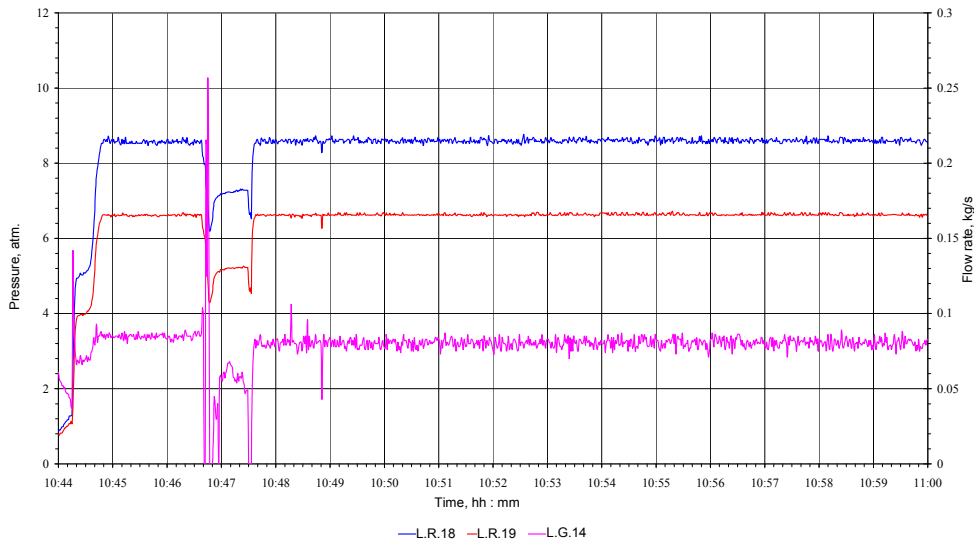


Figure A2.5.58 – Flushing of all paths of cooling. Plasmatrons "D"

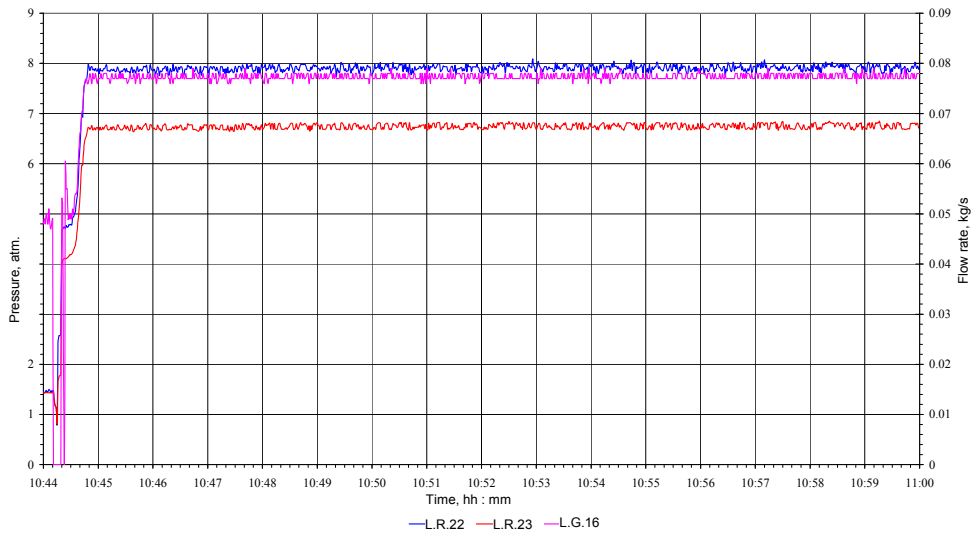


Figure A2.5.59 – Flushing of all paths of cooling. Plasmatrons "E"

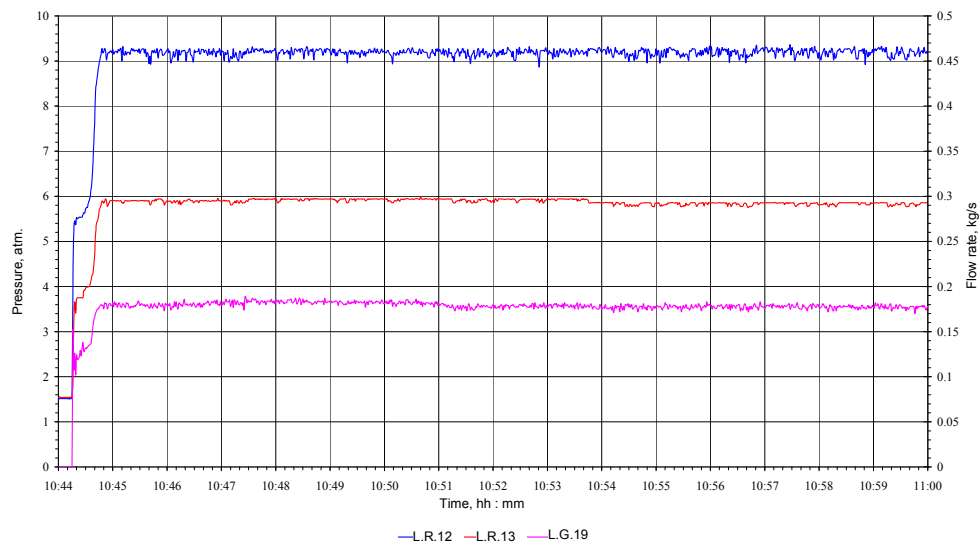


Figure A2.5.60 – Flushing of all paths of cooling. Water-cooled cable.

### 5.4 Comprehensive testing of the device for simulating corium heat decay

The comprehensive testing of the device for simulating corium heat decay on the basis of five plasmatrone was performed. At first the plasmatrone were started one at a time and then a group of plasmatrone was tested. The tests were carried out under atmospheric pressure and with open pressure vessel of the "LAVA-B" test facility. Figure A2.5.61 illustrates variation of the plasmatrone pressure and temperature of the plasmatrone "A" graphite nozzle at a distance 50 mm from the end (c.p. MDT.103) during the test.

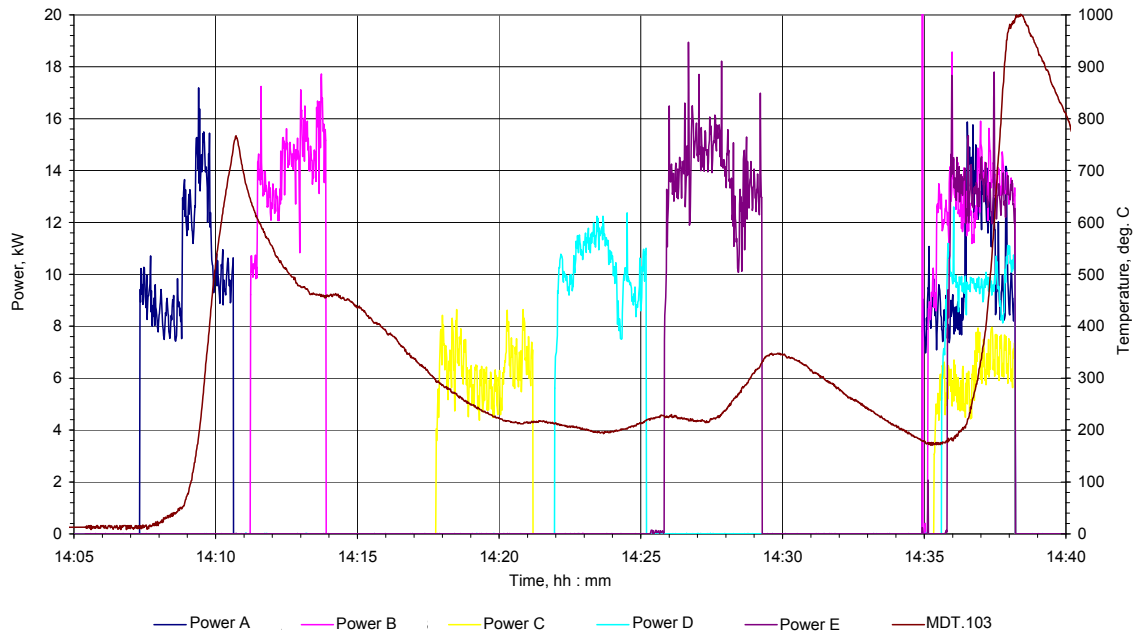


Figure A2.5.61 –Plasmatrone power and temperature of graphite nozzle of "A" plasmatrone

Figure A2.5.62 shows variation of plasmatrone power during starting of a group of five plasmatrone. The start up of five plasmatrone was performed during ~50 seconds. The interval between plasmatrone starts was less than 15 seconds. Running time of the five plasmatrone was equal to ~2,5 minutes.

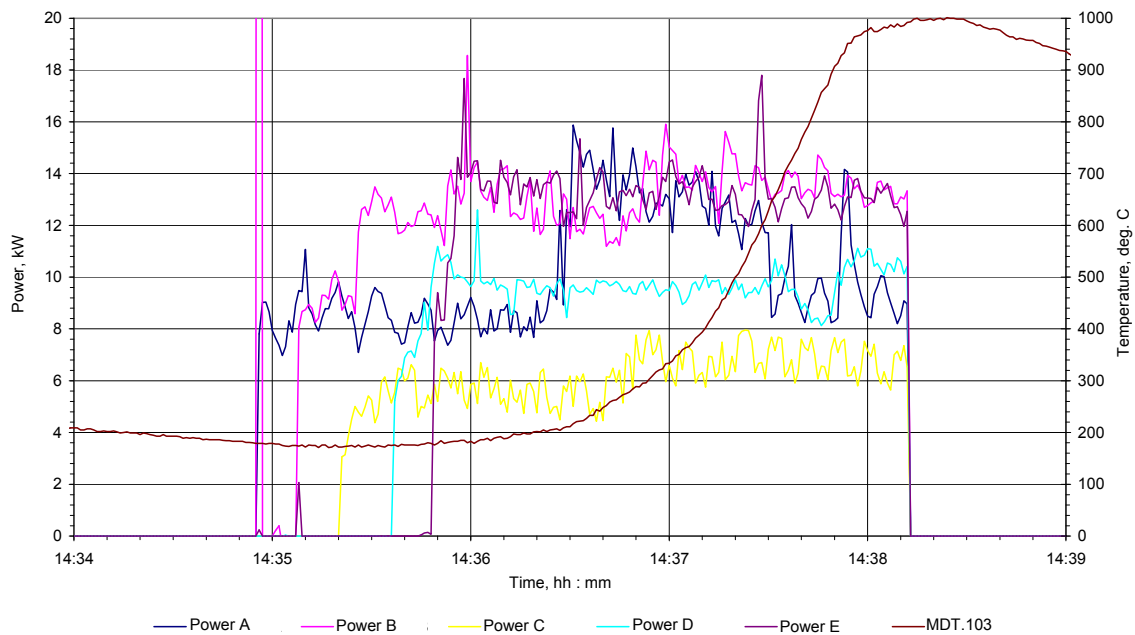


Figure A2.5.62 – Testing of group of plasmatrone

Startup of the five plasmatrone was tested with the use of argon for supplying to the inter-

electrode space. Argon pressure before the delivery nozzle of diameter 0,7 mm was equal to 5,5 abs atm. Total argon flow rate in the plasmatrons inter-electrode space was ~0,6 g/s.

Maximum plasmatrons power was as follows:

- plasmatrons "A" 16 kW;
- plasmatrons "B" 16 kW;
- plasmatrons "C" 16 kW \*);
- plasmatrons "D" 11 kW;
- plasmatrons "E" 14 kW.

\*) – In the startup the plasmatrons "C" current was not registered by the DAS although according to the indicating gages it was about 300 A. The plasmatrons "C" pressure registered by DAS was ~2 times lower than on other plasmatrons. According to the indicating gages the plasmatrons "C" pressure was the same as on other plasmatrons. Therefore, considering the above, the plasmatrons "C" power in the table increases twice.

Maximum power of a group of five plasmatrons was 73 kW.

Temperature of the plasmatrons "A" graphite nozzle at a distance 50 mm from the end reached 1000 °C at the end of the test. Temperature of the plasmatrons "A" graphite nozzle at a distance 110 mm from the end reached 635 °C at the test end.

The cooling water pressure at the forcing pump outlet was 12,9 abs atm. Water pressure at the inlet of the plasmatrons cooling path and water-cooled electric cable was equal to from 8,4 to 9,7 abs atm. Water pressure at the cooling paths outlet was from 6,7 to 7,9 abs atm. Water pressure at discharge was 1,9 abs atm.

Water flow rate for cooling plasmatrons was from 0,066 to 0,079 kg/s. Water flow rate for cooling electric cable was equal to ~0,175 kg/s. Variation of water temperature at inlet and outlet of the plasmatrons cooling paths and electric cable is given in Figure A2.5.63. Maximum heating of water in one of the cooling paths was 7,5 °C.

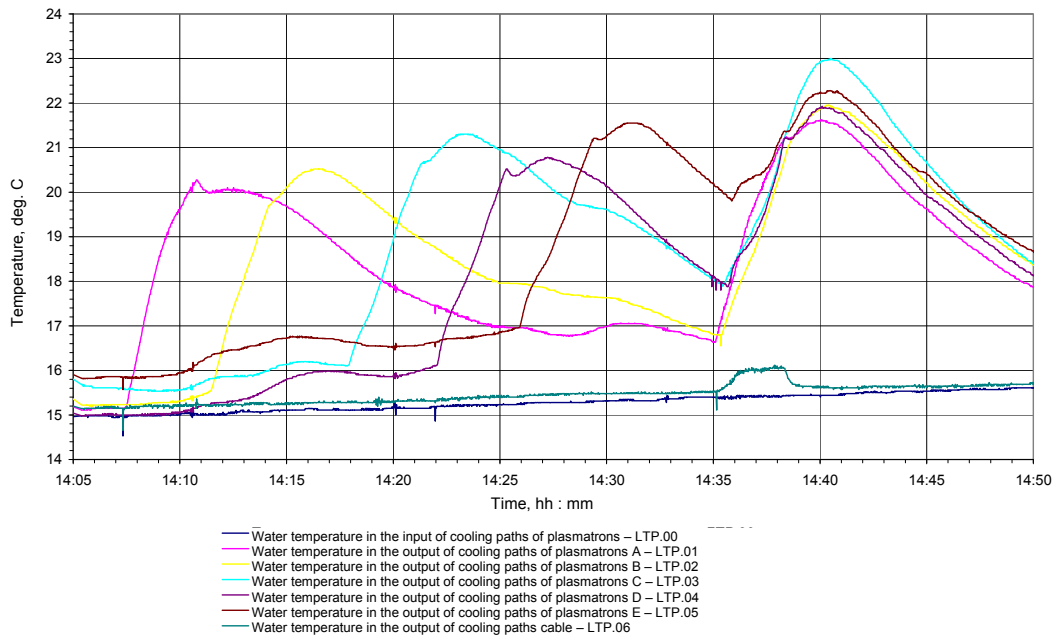


Figure A2.5.63 – Water temperature in the cooling paths

In the course of the test the vessel model bottom was covered with asbestos of thickness 3 mm. Figures A2.5.64-A2.5.67 illustrate variation of the vessel model temperature during the test.

The check points of the first thermocouple group (Figure A2.5.64) were located on the lateral surface of the vessel model in the point of plasmatrons "A" position. The second thermocouple group, seen in Figure A2.5.65, was located on the vessel model bottom in the point of the plasmatrons "A" position. The third thermocouple group, seen in Figure A2.5.66, was located at the bottom in the vessel model center. The fourth thermocouple group, modification of readings is given in Figure A2.5.67, was located at the vessel model bottom between the



plasmatrons "C" and "D".

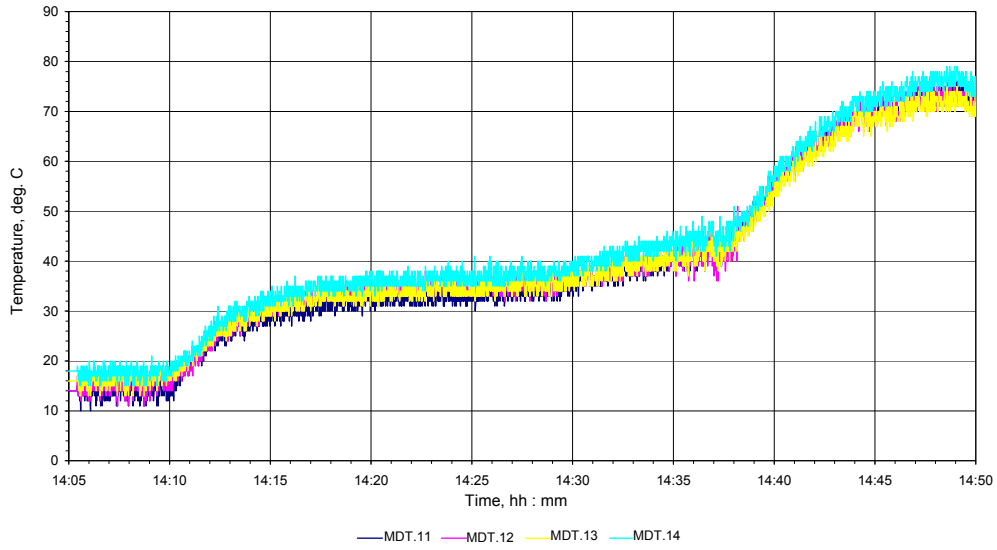


Figure A2.5.64 – Data of first group of thermocouples

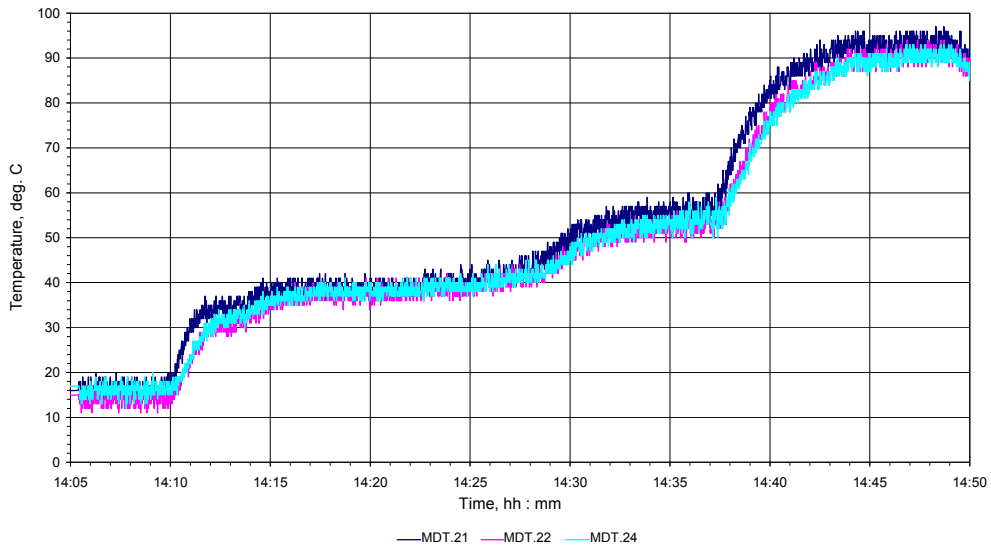


Figure A2.5.65 – Data of second group of thermocouples

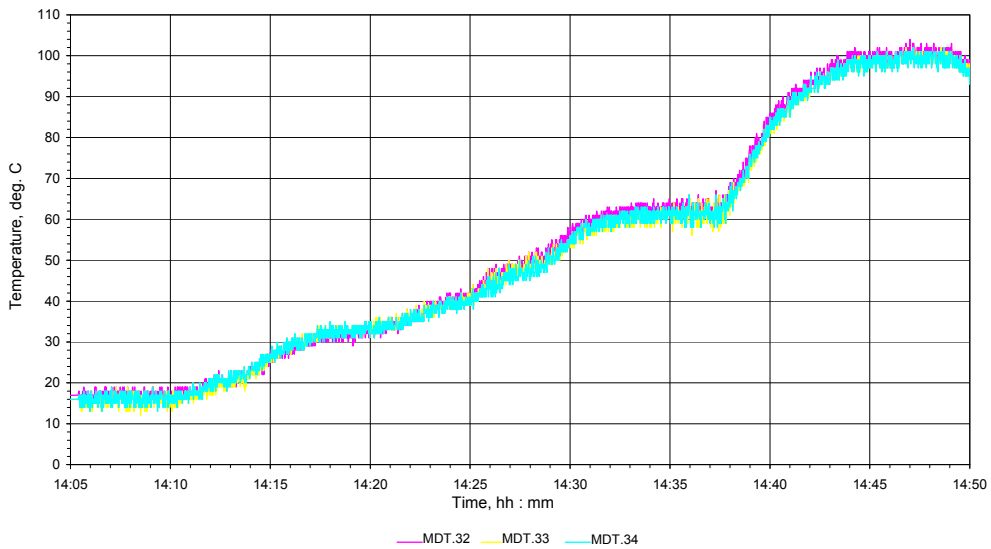


Figure A2.5.66 – Data of third group of thermocouples

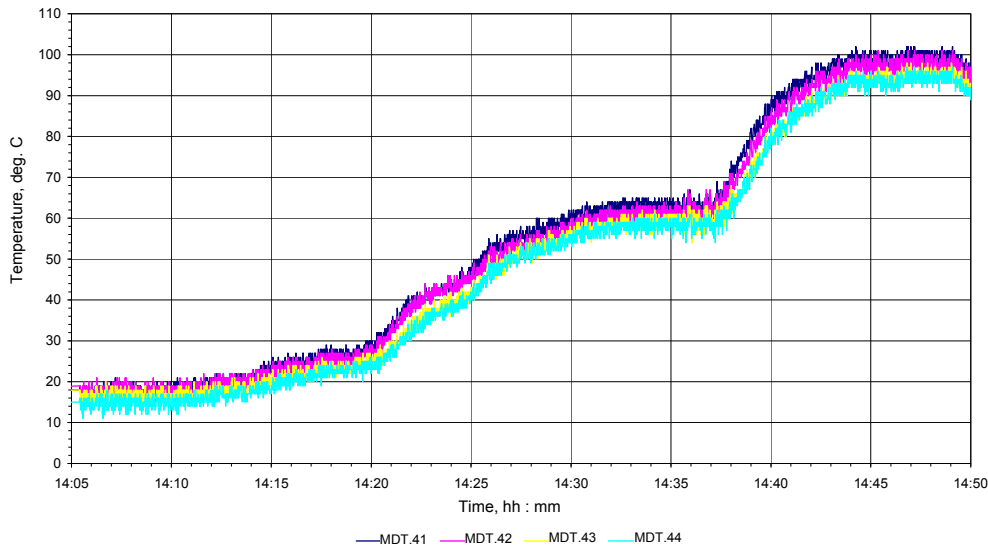


Figure A2.5.67 – Data of fourth group of thermocouples

All groups of thermocouples are shown in Figure A2.5.68 on one plot. The initial temperature of RPV model wall by indications of thermocouples was 13 ... 17 °C. It is visible in the plot that the thermocouples located at the bottom of RPV model show about identical temperature during experiment, but on a lateral surface temperature was more low on ~17 °C. Heating on a lateral surface of RPV model approximately on ~40 % lower that indirectly specifies that the place of electric arc burning in plasmatrons is in the bottom part of plasmatrons nozzles. After plasmatrons switching off at 14:38:13 the temperature of RPV model increased due to return heat exchange from hot surfaces of plasmatrons. After termination of the experiment the average temperature of a wall at the bottom of RPV model for 10 minutes has increased from 60 to 95 °C, and of lateral wall from 43 to 75 °C.

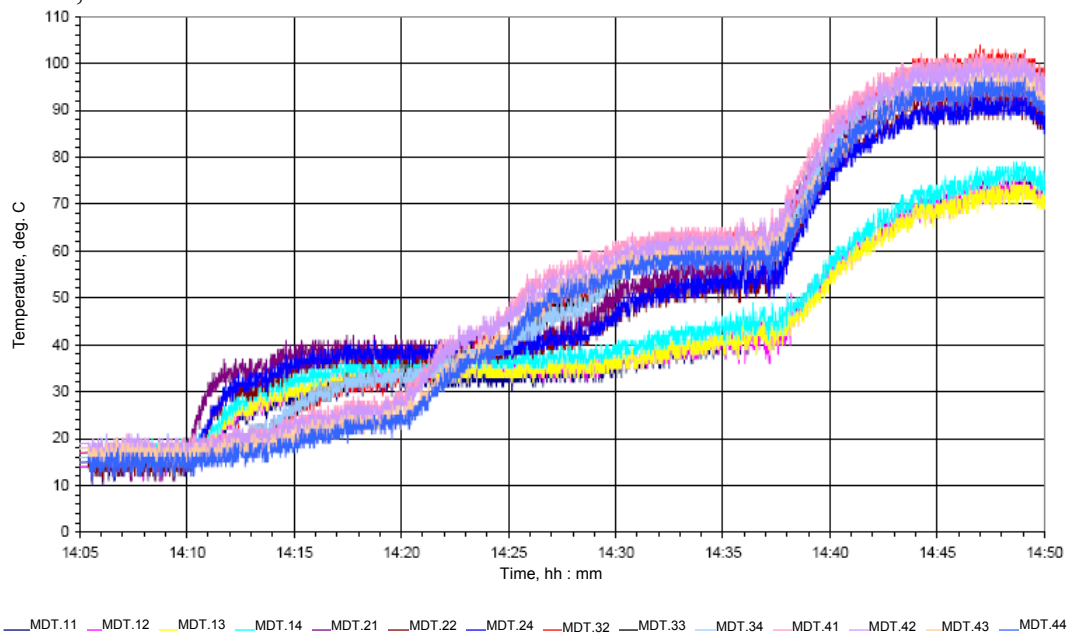


Figure A2.5.68 – Data of thermocouples measured temperature of the RPV model wall

Six experiments have been executed using group of five plasmatrons. Tests have been performed at supply in inter-electrode space of plasmatrons gases mixes of argon and nitrogen with the general flow rate ~1 g/s. The gases mix consisted from 70 - 74% of argon and 30 - 26% of nitrogen. The water flow rate on plasmatrons cooling during experiments was 0,067...0,079 kg/s.

Only 4 plasmatrons were ignited in one of experiments. Therefore experiment has been stopped, but in 1 minute have been successfully ignited all 5 plasmatrons. Duration of test of group of five plasmatrons was 30 ... 45 seconds.

The general operation time of five plasmatrons on six experiments was more than 32 minutes. Duration of one experiment was about 5 minutes.

Voltage and current change in five plasmatrons in one of experiments is shown in Figure A2.5.69. The current changed in a range 240...300 A, and voltage changed in a range 45...70 V. Change of plasmatrons power in the same experiment is shown in Figure A2.5.70. Plasmatrons power was 14 ... 18 kW. The maximum power of five plasmatrons was 82 kW.

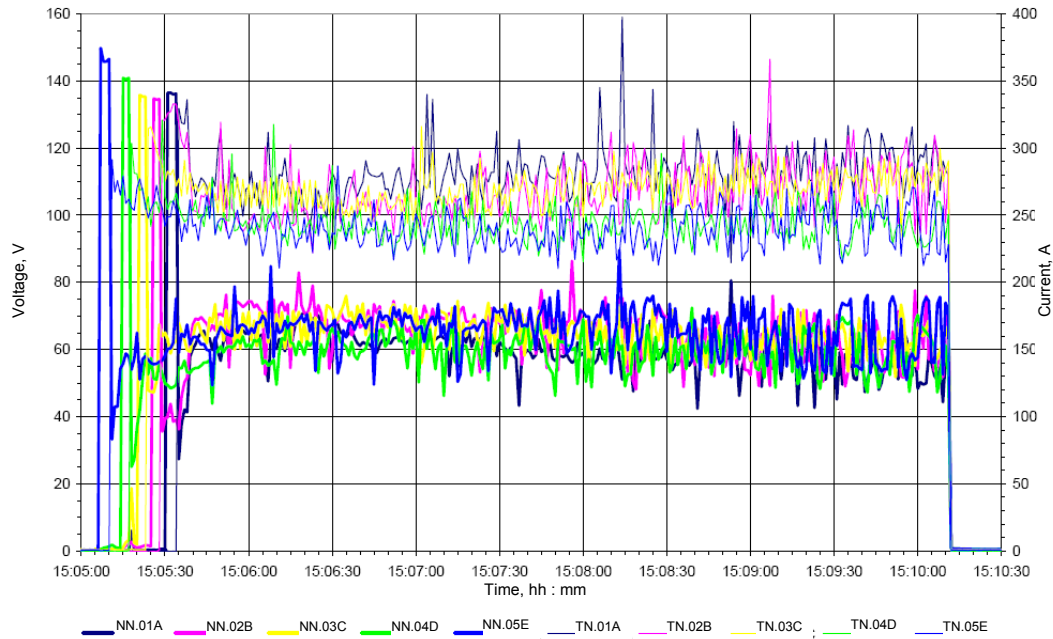


Figure A2.5.69 – Voltage and current of five plasmatrons in the course of 6<sup>th</sup> test

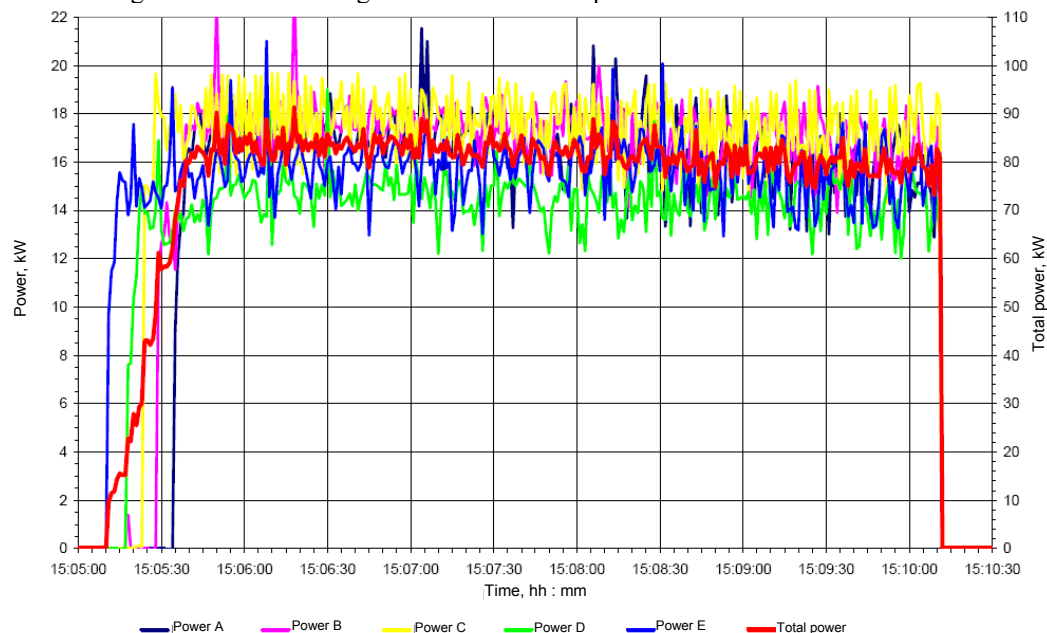


Figure A2.5.70 – Power of five plasmatrons in the course of 6<sup>th</sup> test

Change of temperature of water in cooling paths of plasmatrons in on six experiments is shown in Figures A2.5.71, A2.5.72. The maximum heating of water in plasmatrons cooling paths was equal to 18 °C.

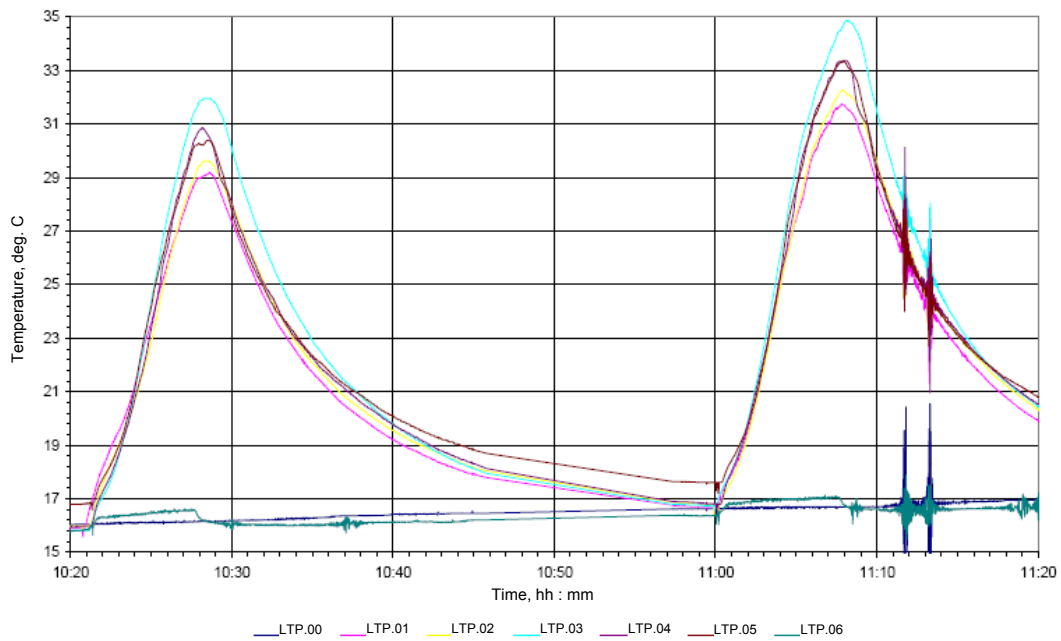


Figure A2.5.71 – Water temperature in the cooling paths in the course of 1<sup>st</sup> and 2<sup>nd</sup> tests

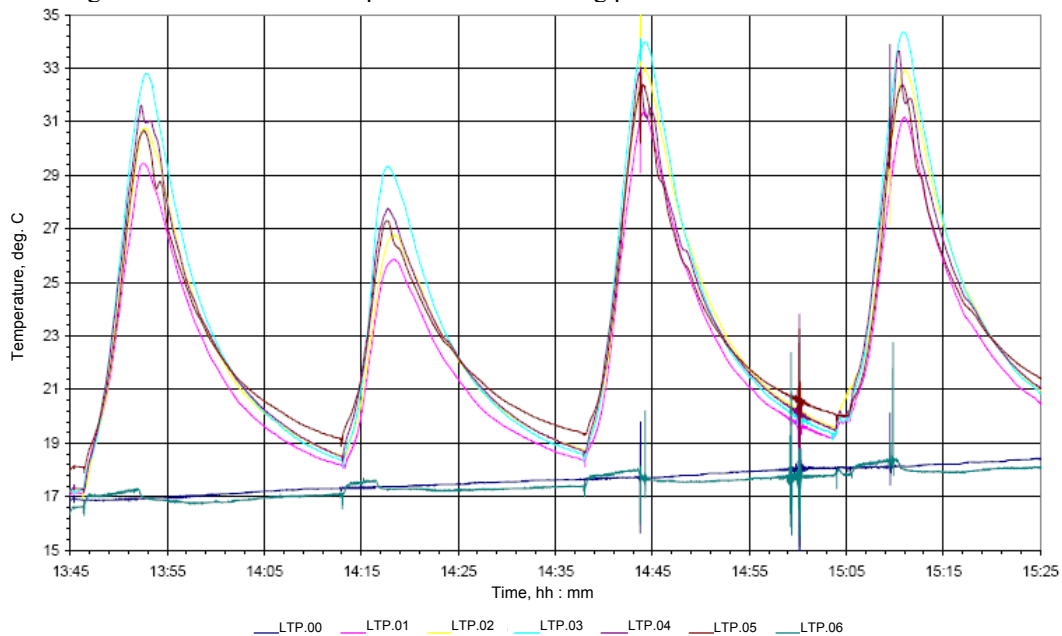


Figure A2.5.72 – Water temperature in the cooling paths in the course of 3<sup>rd</sup>, 4<sup>th</sup>, 5<sup>th</sup> and 6<sup>th</sup> tests

Change of temperature of a graphite nozzles and wall of RPV model in six experiments is shown in Figures A2.5.73, A2.5.74. On the fifth experiment thermocouple MDT.04 taking temperature of a graphite nozzle and standing on distance 70 mm from a nozzle end face has failed. The maximum temperature of a graphite nozzle was equal to 1600 °C. Temperature of a RPV model wall in the sixth experiment has exceeded 400 °C.

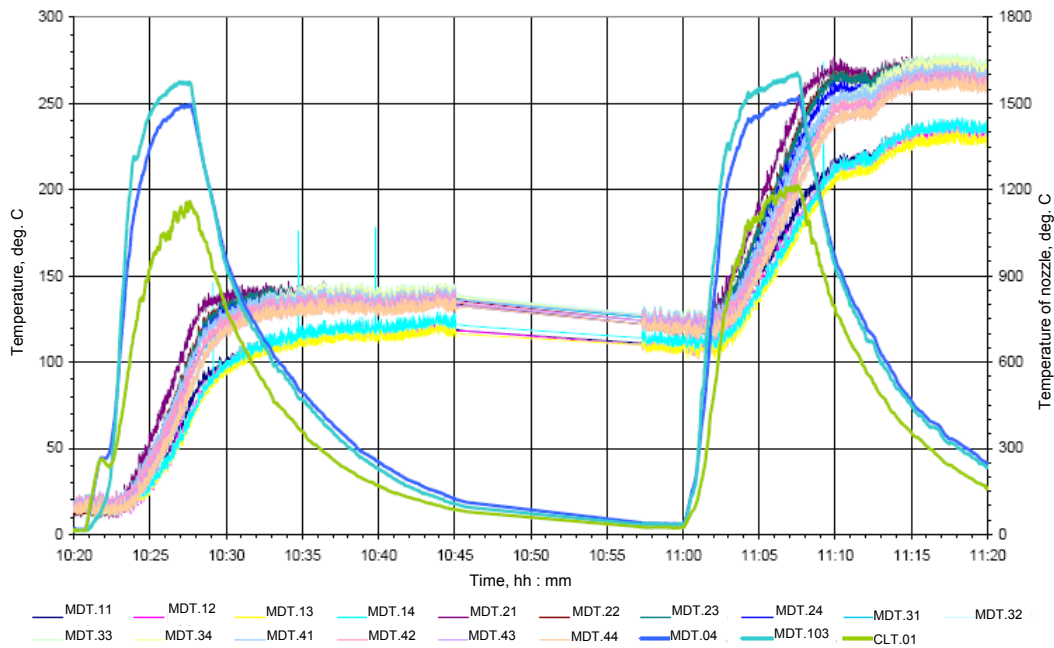


Figure A2.5.73 – Temperature of graphite nozzle and RPV model wall in the course of 1<sup>st</sup> and 2<sup>nd</sup> tests

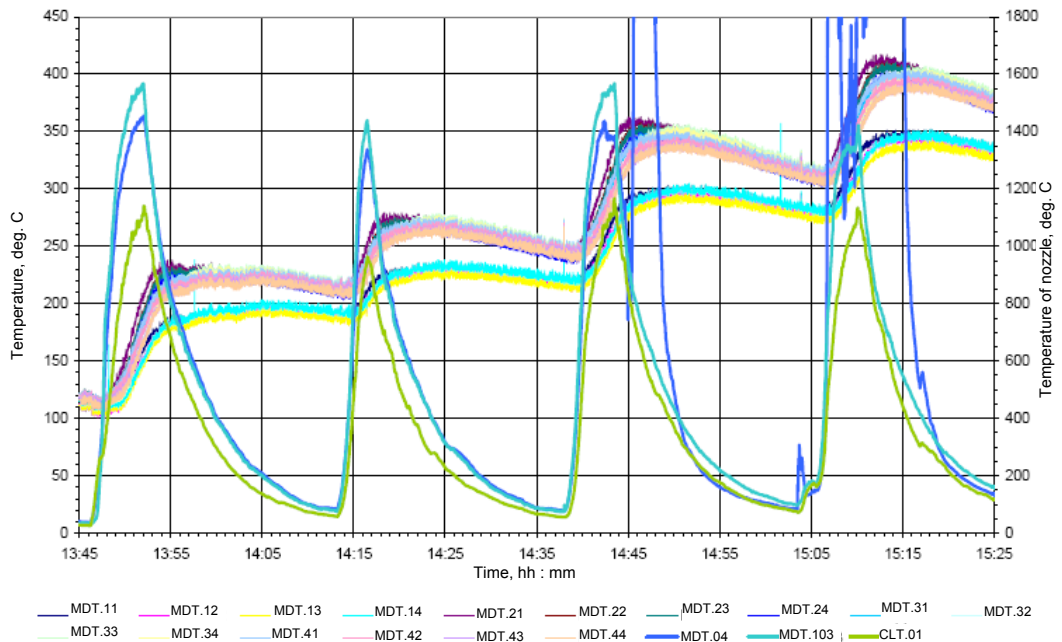


Figure A2.5.74 – Temperature of graphite nozzle and RPV model wall in the course of 3<sup>rd</sup>, 4<sup>th</sup>, 5<sup>th</sup> and 6<sup>th</sup> tests  
 Changes of total power of plasmatrons and power of heat leakages in cooling water during experiments No. 1...6 are shown in Figures A2.5.75, A2.5.76.  
 Changes of temperature of a graphite nozzle on distance of 110 mm from its end face (c.p. CLT.01) and changes of integral of power and integral of heat leakages in cooling water are shown also in Figures A2.5.75, A2.5.76. On last three experiments total power of plasmatrons sometimes exceeded 85 kW.



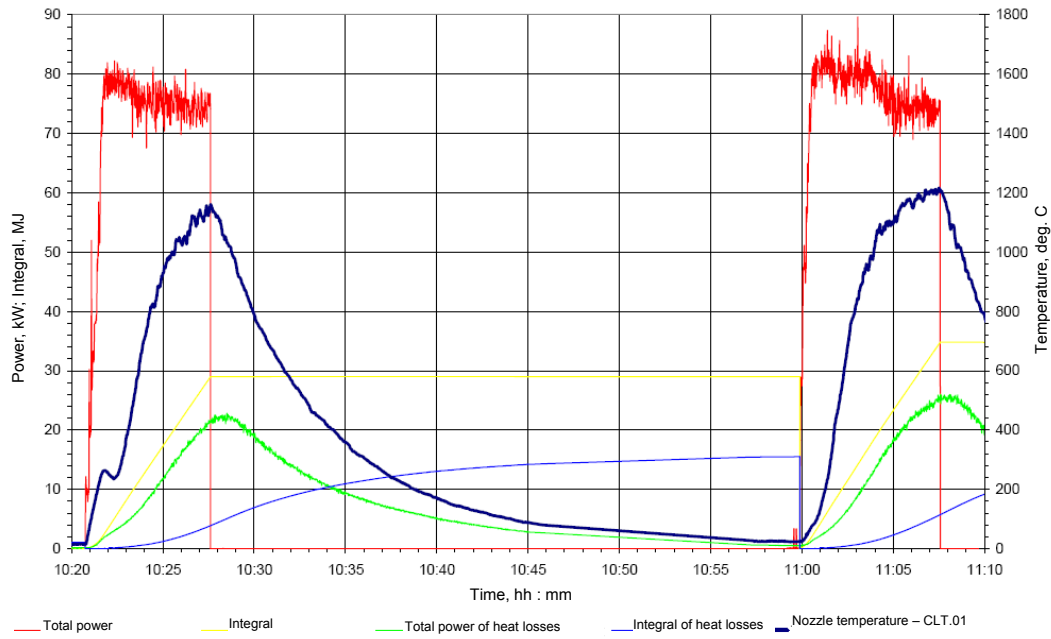


Figure A2.5.75 – Total power of 5 plasmatrons in the course of 1<sup>st</sup> and 2<sup>nd</sup> tests

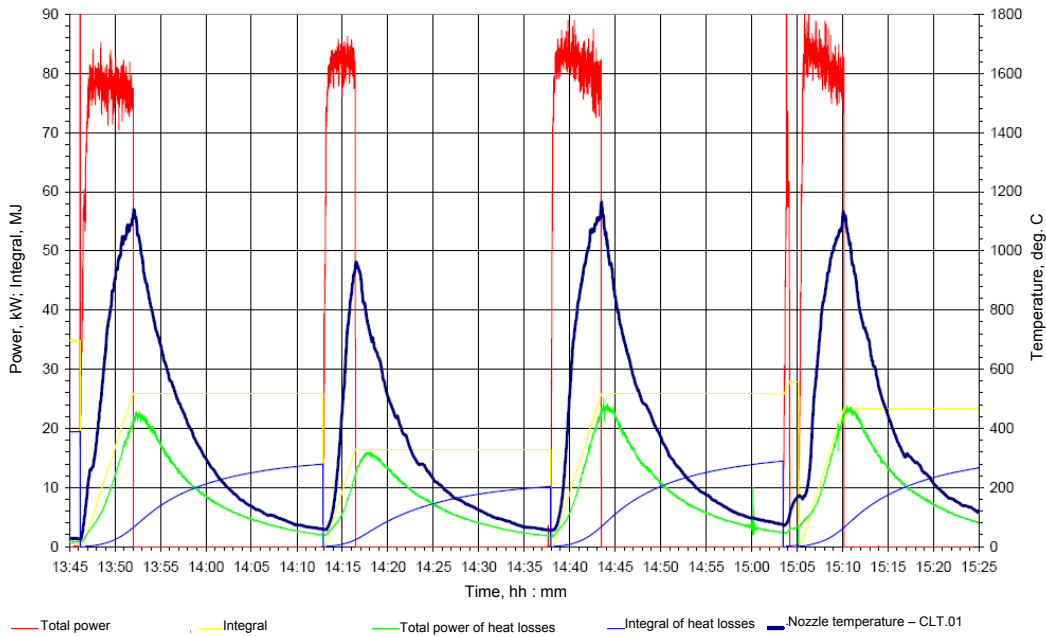


Figure A2.5.76 – Total power of 5 plasmatrons in the course of 3<sup>rd</sup>, 4<sup>th</sup>, 5<sup>th</sup> and 6<sup>th</sup> tests

Thermocouples are placed in RPV model by four groups in the locations of samples of RPV steel. The arrangement of thermocouples in each of samples is shown in Figure A2.5.77 - sections B and C-C. The first thermocouple of group is located on depth 30 mm from an external surface of RPV model. The second thermocouple is located on depth of 20 mm, the third - on depth of 12 mm, and the fourth - on depth of 2 mm from an external surface of RPV model.

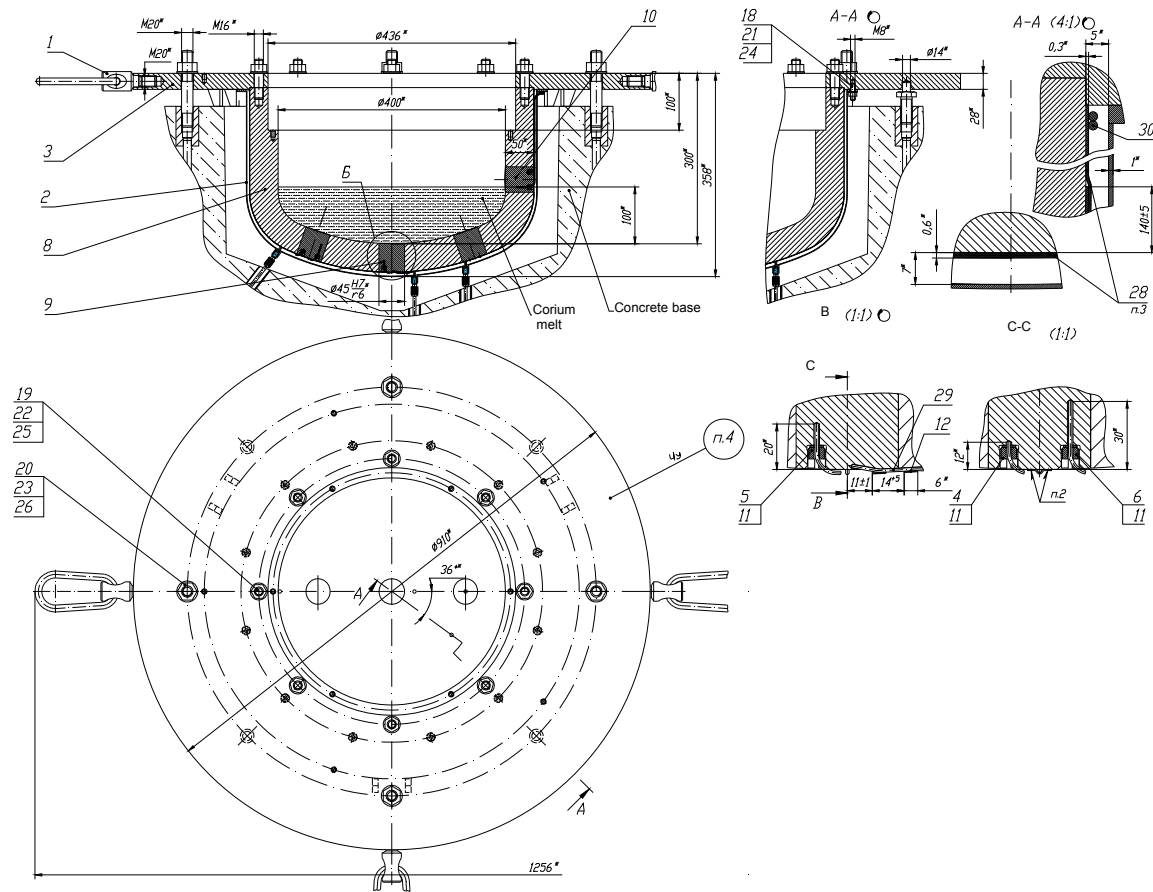


Figure A2.5.77 – Thermocouples placement in RPV model

### Conclusions

The integrated testing of the heat decay simulation in the corium for the integral tests demonstrated satisfactory operability of the device as a whole. Several faults in the plasmatrons electric supply system and instrumentation and measuring system are eliminated.

The device was running steady for 30 minutes. To avoid overheating of the vessel model wall, the duration of the test was not longer.

In the course of the testing maximum temperature of the vessel model wall did not exceed 100 °C due to internal insulation of the RPV model wall.

The integrated testing will be continued in 13<sup>th</sup> quarter after elimination of the revealed faults.